Implications of Shape Factors on Fate, Uptake, and Nanotoxicity of Gold Nanomaterials

Seyyed Mohammad Hossein Abtahi

Dissertation submitted to the faculty of the Virginia Polytechnic Institute and State University in partial fulfillment of the requirements for the degree of

Doctor of Philosophy

In

Civil Engineering

Peter J. Vikesland Chair

Richey M. Davis

Williams A. Ducker

Catherine J. Murphy

Linsey C. Marr

April 19, 2018

Blacksburg, VA 24061

Keywords:

Nanotechnology, nanomaterials, nanotoxicity, gold nanoparticles, gold nanorods, aggregation, colloidal stability, filter-feeders, *Corbicula fluminea*, fate and transport, Vis-NIR spectroscopy, TEM, Dynamic light scattering (DLS)

Implications of Shape Factors on Fate, Uptake, and Nanotoxicity of Gold Nanomaterials

Seyyed Mohammad Hossein Abtahi

ABSTRACT

Noble metal nanoparticles such as gold and silver are of interest because of the unique electro-optical properties (e.g., localized surface plasmon resonance [LSPR]) that originate from the collective behavior of their surface electrons. These nanoparticles are commonly developed and used for biomedical and industrial application. A recent report has predicted that the global market for gold nanoparticles will be over 12.7 tons by year 2020. However, these surface-functionalized nanoparticles can be potential environmental persistent contaminants post-use due to their high colloidal stability in the aquatic systems. Despite, the environmental risks associated with these nanoparticles, just a few studies have investigated the effect of nanofeature factors such as size and shape on the overall fate/transport and organismal uptake of these nanomaterials in the aquatic matrices.

This study presents a comprehensive approach to evaluate the colloidal stability, fate/transport, and organismal uptake of these nanoparticles while factoring in the size and shape related properties. We demonstrate the importance and effect of anisotropicity of a gold nanoparticle on the colloidal behavior and interaction with ecologically susceptible aquatic biota. We also show how readily available characterization techniques can be utilized to monitor and assess the fate/transport of this class of

nanoparticles. We further describe and investigate the relationship between the aspect ratio (AR) of these elongated gold nanoparticles with clearance mechanisms and rates from the aquatic suspension columns including aggregation, deposition, and biopurification. We illustrate how a fresh water filter-feeder bivalve, *Corbicula fluminea*, can be used as a model organism to study the size and shape-selective biofiltration and nanotoxicity of elongated gold nanoparticles. The results suggest that biofiltration by *C. fluminea* increases with an increase in the size and AR of gold nanoparticle. We develop a simple nanotoxicity assay to investigate the short-term exposure nanotoxicity of gold nanoparticles to *C. fluminea.* The toxicity results indicate that for the tested concentration and exposure period that gold nanoparticles were not acutely toxic (i.e., not lethal). However, gold nanoparticles significantly inhibited the activities of some antioxidant enzymes in gill and digestive gland tissues. These inhibitions could directly affect the resistance of these organisms to a secondary stressor (temperature, pathogens, hypoxia etc.) and threaten organismal health.

Implications of Shape Factors on Fate, Uptake, and Nanotoxicity of Gold Nanomaterials

Seyyed Mohammad Hossein Abtahi

GENERAL AUDIENCE ABSTRACT

Nanoparticles are fine particles that cannot be seen with naked eye and possess unique chemical and physical properties. Gold and silver nanoparticles are specifically of interest due to tunable optical properties and are commonly developed and used for biomedical and industrial applications. Unfortunately, these metallic nanoparticles can be potential environmental persistent contaminants post-use in the soil and aquatic systems. Despite, the environmental risks associated with these metallic nanoparticles, just a few studies have investigated the effect of size and shape of these nanoparticles on their interaction and transportation in the surrounding environment and with existing organisms.

This study presents a comprehensive approach to evaluate the stability, transportation, and organismal uptake of these nanoparticles while factoring in the size and shape related properties. We also show how readily available detection techniques can be utilized to monitor and assess the presence and transport of this class of nanoparticles. We illustrate how a fresh water bivalve, *Corbicula fluminea*, can be used as a model organism to study the size and shape-selective uptake and toxicity of gold nanoparticles. The results suggest that nanoparticles uptake by *C. fluminea* increases with an increase in the size of gold nanoparticle. We develop a simple toxicity assay to investigate the

short-term exposure toxicity of gold nanoparticles to *C. fluminea.* The toxicity results suggest that for the tested concentration and exposure period that gold nanoparticles were not acutely toxic (i.e., not lethal) but affect the resistance of these organisms to an environmental change (temperature, pathogens, hypoxia etc.) and threaten organismal health.

Dedication

Dedicated to Farzaneh Heidary and Sadegh Abtahi, my parents—thank you for your love and support these past five years, and the countless sacrifices you've made so that I can have this opportunity.

Acknowledgements

I am grateful to the people who made it possible for me to do my doctoral research at Virginia Tech. Foremost, I would like to express my sincere gratitude to my advisor Prof. Peter Vikesland for the continuous support of my Ph.D. study and research, for his patience, motivation, enthusiasm, and immense knowledge. His guidance helped me in all the time of research and writing of this dissertation. Special thanks to Prof. Richey Davis, my committee member and my M.Sc. advisor and to committee members Prof. Linsey Marr, Prof. Catherine Murphy, and Prof. William Ducker whose encouragement and critical research insights have been invaluable these past five years. I express much gratitude to the National Science Foundation (NSF) and Environmental Engineering programs, the Center for Environmental Implications of Nanotechnology (CEINT) at Duke University, and the VT Institute for Critical Technology and Applied Science (ICTAS) for generous funding support and creating opportunities for interdisciplinary research and professional development. Special thanks to Beth Lucas, and Bonnie Franklin in CEE Department. Special thanks to past and present labmates particularly Dr. Weinan Leng, Dr. Matt Chan, Dr. Haoran Wei, and Dr. Marjorie Willner. Thank you to my collaborators and friends across the VT campus: Steve McCartney, Christopher Winkler, and Jeffery Parks. Many thanks to my collaborators at Dr. Di Giulio's lab at Duke university specially Dr. Rafael Trevisan who helped with the toxicity studies. A special thank you to my parents, Farzaneh and Sadegh Abtahi, who taught me the value of hard work and compassion towards others.

Table of Contents

List of Figures

List of Tables

Chapter 1. Introduction

1.1 Background

Gold nanoparticles. Nanoparticles do naturally exist in the environment such as salt crystals, or can be produced through natural phenomena like volcanic activities. In this study we focus on engineered nanomaterials (ENMs) that have been designed and produced for a specific application. ENMs can be defined as particles having at least one dimension smaller than 100 nm with unique physiochemical properties that originates from their size and structural characteristics[1]. According to a recent report by the Centers for Disease Control and Prevention (CDC), current ENMs can be classified in four different groups based on their composition, which are elemental carbon, carbon compound, metal and metal oxides, and ceramics[2]. Metal and metal oxide ENMs are commonly used in industry among which gold and titanium dioxide are the most produced nanomaterials. The Radiant Insight report has predicted that the global market for gold nanoparticles will be 12.7 tons by year 2020 with medical industry as the first and electronics as the second application fields[3].Gold is commonly believed to be non-reactive in environmentally relevant conditions and consequently gold nanoparticles (AuNPs) are generally considered safe[4]. It's a long time that AuNPs are used for jewelry, art, decoration, and biomedical purposes. Chrysotherapy, using gold complexes in treating arthritis[5], and dietary supplement are two common examples in biomedical applications of AuNPs. Environmental fate and transport of ENMs has been broadly investigated and evaluated in the published research[6-12]. Nevertheless, a majority of current research focuses on spherical shaped nanoparticles and does not consider the

effect of shape[7, 11-14]. Currently there is a lack of knowledge on the environmental implications of elongated nanoparticles such as rods, tubes, and wires. This class of highly anisotropic ENMs are interesting due to their unique physiochemical properties and are commonly used in everyday consumer products[15-20]. Based on a recent report, metallic nanorods and nanowires are the most commonly fabricated ENMs after carbon nanotubes (CNTs)[21]. CNTs are the exception in the elongated nanomaterials category in that they are well studied for their environmentally relevant implications and concerns [22-26]. However, recent studies have shown some level of toxicity associated with gold nanorods (AuNRs) under certain conditions[27-31].

Elongated shape gold nanoparticles. Anisotropic metal and metal oxide nanoparticles such as nanorods are commonly tested and used in variety of applications. ZnO nanorods possess unique optical bandgap and are widely used to fabricate nanoscale electronic devices such as field effect transistor, ultraviolet photodetector, Schottky diode, and ultra-bright light-emitting diodes (LEDs)[16, 19, 32]. Silver nanorods are used in antimicrobial applications, sensors, and conductors[33-36]. Titanium dioxide nanorods are used in electro catalysis, photo catalysis, energy storage, and solar cells[37-39]. AuNRs are mainly used in biomedical applications such as biosensors, cancer therapy, and drug and gene delivery[40, 41]. Presently there are two approaches to produce elongated metal and metal oxide nanorods, wet chemistry seed-mediated bottom-up and hard template top-down. In the case of AuNRs, gold salt reduction by a mild reducing agent such as ascorbic acid in the presence of shape-directing agents such as cetyltrimethylammonium bromide (CTAB) is the main production approach. CTAB is a positively charged cationic surfactant that covers the AuNR surface as a vesicle-like bilayer and its primary goal is

to protect nanoparticles from aggregation under low ionic strength conditions. CTAB toxicity to living cells is well-known[42] and therefore excess CTAB in colloidal suspension is normally removed by centrifugal washing or dialysis. The remaining CTAB on the surface remains toxic and methods like layer by layer coating of GNR with a negatively charged polymer such as PAA (poly acrylic acid) and PVP (poly vinyl chloride) have been shown to be effective in reducing toxicity. If a positive surface charge is desired, then negatively charged polymer coated CTAB AuNR is coated in an extra layer of PAH (poly allylamine hydrochloride). Replacing CTAB with a more biocompatible polymer such as PEG (poly ethyleneglychol) or covering CTAB with a thick silica layer are other promising methods in biomedical applications. Production of AuNRs in the 1-20 aspect ratio (AR; length to width) range is achievable by controlling growth conditions. Adjusting the amount of introduced silver nitrate ($AgNO_3$) or stepwise growth of gold crystal in the presence of a cosurfactant such as dodecyltrimethylammonium bromide (DTAB) are commonly applied methods to tune the AR of produced AuNRs.

Aspect ratio associated toxicity. Prior studies have shown the toxicity of elongated-shape AuNRs to living cells under certain biological conditions. AR related cellular apoptosis and necrosis of cells have been reported while binding of AuNRs to cellular DNA has been shown to influence transcription and potentially induce inflammatory response and apoptosis in liver cells[5, 43]. The chemically non-reactive nature of gold is in contrast with the finding in the recent studies and raises the concern of shape and size driven ecotoxicity of AuNRs in the environment.

Aggregation rate, deposition mechanism, and interaction of anisotropic nanoparticles. There is a wide body of research on aggregation and deposition of ENMs

in aquatic systems, but unfortunately only a few of these studies have focused on the role of anisotropicity and AR. Petosa et.al recently reviewed the aggregation and deposition of various ENMs in aquatic environments including carbon nanotubes, fullerenes, metallic nanoparticles such as gold and iron, metal oxide nanoparticles such as titanium dioxide and ZnO plus quantum dots[44]. None of the studies reviewed in this paper systematically investigated the effect of shape and AR. To the best of our knowledge currently there are only two environmentally relevant published studies on ZnO nanorods[45] and GNRs[46] aggregation and interactions in which spheres and rods undergo different interactions and show different aggregation kinetics.

The presence of huge and accessible surface areas makes the collision and interaction of two different types of nanoparticles rare. Therefore, in environmental aquatic systems homoaggregation, AuNR-AuNR interaction, is addressed as aggregation while heteroaggregation, AuNR-other surfaces interaction, is addressed as deposition. Both of these phenomena are a function of the NP type and the aquatic exposure (suspension) medium characteristics. The main NP characteristics can be listed as material, size, shape, surface chemistry, particle concentration while for the aquatic medium they are pH, ionic strength, available surface area (media collector area). Knowing these parameters, Derjaguin-Landau-Verwey-Overbeek (DLVO) and filtration theories can be applied to theoretically study aggregation and deposition of NPs in aquatic systems. However, the applicability of these theories to elongated nanorods in environmental systems has not been well studied yet. Both DLVO and filtration theories have limitations for cylindrical geometries such as nanorods. For example, calculation of electrostatic interactions using the Poisson-Boltzmann equation and van der Waals (vdW) interaction based on Hamaker's constant are hindered by non-spherical geometries. Derjaguin

assumptions and mapping between cylindrical versus spherical geometry can theoretically help in easing these challenges. While in reality there is no experimental study to back up these assumptions in complex environmental systems.

The longitudinal LSPR band is highly sensitive to the colloidal stability of individual AuNRs. A slight changes in the number concentration of single AuNRs or the formation of a few agglomerates in suspension can noticeably change the absorption intensity, width, as well as result in red or blue shifting of the longitudinal band. In the case of anisotropic AuNRs, three different aggregation structures are possible; end-to-end, side-by-side, and random assemblies. Each of these assembly configurations affect the LSPR bands differently. End-to-end assembly enhances uniaxial plasmon coupling resulting in a red shift of the longitudinal band while the transverse band will almost remain unchanged. However, side-by-side assembly will reduce the overall AR of the agglomerate causing a blue shift of the longitudinal band and red shifting of the transverse band. For random assemblies, the behavior of the LSPR bands will depend on the overall structure of the agglomerate.

C. fluminea freshwater bivalve. Bivalves are column water and sediment filter feeders and can be found in both freshwater and marine habitats. Filter feeders are a sub-group of organisms that feed by straining suspended matter and food particles from water, typically by passing the water over a specialized filtering structure. As a result, they are highly susceptible to environmental pollutants such as heavy metals, organic pollutants, ENMs, etc[47]. This filtration mechanism makes them a good candidate to monitor and investigate a wide variety of contaminants in environmental studies. For example *Corbicula fluminea* has been used by scientists as an aquatic contaminant biodetector for

many decades[48]. *C. fluminea* is of an Asian origin and thus it is often commonly called the Asian clam or Asiatic clam. The species has been introduced into many parts of the world, including North American and Europe. They feed primarily on phytoplankton (algae), which they filter from the sandy or muddy bottoms of streams, lakes, or canals. According to the USGS, *C. fluminea* is known as an invasive species and likely will continue to expand its North American range until it reaches its lower temperature tolerance. *C. fluminea* has the highest filtration rate of freshwater bivalves and filters 45 L water/ g (dry weight)/day[49]. This exceptionally high filtration rate and ease of access and collecting from riverine ecosystems are the main reasons that they are used in many studies as contaminant biodetector organism. Prior studies have suggested that *C. fluminea* can uptake and accumulate ENMs based on size[50-52]. However, none of these studies have investigated the effect of anisotropicity and AR of ENMs on uptake rate.

1.2 Research Objectives

Objective 1. Synthesis of colloidally stable AuNRs with different aspect ratios and surface coatings

AuNRs with different aspect ratios of 1, 4, and 8 were synthesized. Synthesized CTAB coated AuNRs were latterly coated by bovine serum albumin (BSA). Vis-NIR spectroscopy, electrophoretic mobility measurements, and transmission electron microscopy (TEM) were used to characterize AuNRs.

Hypothesis.

H1.1) AuNRs with a fixed diameter and aspect ratios of 1, 4, and 8 (with 10% standard deviation in dimension) can be synthesized and be readily used.

H1.2) Surface coated AuNRs are well-dispersed and colloidally stable in nanopure DI water

Objective 2. Aggregation kinetics, and aggregation assembly study on AuNRs

The aggregation and agglomeration rate of AuNRs were kinetically studied through exposure of AuNRs to different ionic strength and salt composition aquatic environments. The effect of AR and surface coating were further evaluated by comparing results. The kinetics of aggregation were investigated using Vis-NIR spectroscopy while the structural conformation of aggregates were determined by TEM. A simple extended DLVO theory model was developed. The observed data from experiments were compared to modeling outputs to further investigate the aggregation kinetics and mechanism.

Hypothesis.

H2.1) The blue shifting and red shifting of transverse and longitudinal bands in Vis-NIR spectroscopy represent the formation of new suspended agglomeration or aggregates in the suspension

H2.2) Appearance of a new LSPR band at a different wavelength than transverse and longitudinal band of single AuNR in Vis-NIR spectroscopy shows the formation of a new nanoparticle agglomerate species

H2.3) Decrease in the intensity of a particular LSPR band in Vis-NIR spectroscopy is linearly related to the decrease in number concentration of that nanoparticle species.

H2.4) CTAB coated AuNRs are protected with a dense vesicle-like bilayer of CTAB on the sidewall facets while tip facets are covered with a nondense CTAB coating.

H2.5) Increasing ionic strength of suspension increases aggregation rate.

Objective 3. AuNRs and AuNPs uptake and nanotoxicity study on C. fluminea filter-feeding bivalve clam

Organismal uptake of suspended AuNRs and AuNPs by *C. fluminea* filter feeding bivalves in an environmentally relevant freshwater microcosms was studied. The overall uptake was determined and evaluated by the whole-body organism burden that was later normalized by body mass while the residue of NPs in the suspension was monitored in real time during the time course of experiment by Vis-NIR spectroscopy. The uptake per body mass for each set of experiment was determined and its relation to the tested AuNRs and AuNPs dimensional such as size and AR was developed. The protein damage and antioxidant enzyme activity reduction of *C. fluminea* cells that were associated to the gold nanoparticles exposure were studied by taking sample tissues from dissected clams post exposure to AuNRs and AuNPs. The relationship between NP physical characteristics such as shape and AR and the extent of protein damage and antioxidant enzyme activity reduction were further evaluated.

Hypothesis.

H3.1) AuNRs uptake by clams is size and aspect ratio dependent

H3.2) BSA coated AuNRs and AuNPs are colloidally stable in suspension and do not aggregate during the time course of experiment

H3.3) During organismal uptake and tissue fixation, AuNRs and AuNPs retain their physiochemical structure

H3.4) BSA coated AuNRs and AuNPs at an environmentally relevant concentration do not expose an immediate life threat to the clams.

1.3 Dissertation Outline

This dissertation contains a total of five chapters including this introductory chapter.

Chapter 2 describes a comprehensive evaluation of the size and shape-selective uptake of BSA coated gold nanomaterials by the Asian clam (*Corbicula fluminea*), to expand our knowledge on how collidally stable nanoparticles are processed by these aquatic filter-feeders. Chapter 3 describes how the aggregation assembly of elongated gold nanoparticles can be influenced by individual ions present in the aquatic solutions. Chapter 4 presents our efforts to apply characterization techniques particularly UV-vis spectroscopy, to evaluate the aggregation kinetics of gold nanoparticles and nanorods in environmentally relevant electrolyte solutions. Chapter 5 shows our general conclusions regarding the fate/transport and organismal interaction of gold nanoparticles in aquatic systems with a specific emphasis on the effects of nanoparticle anisotropicity.

1.4 References

1. Rotello, V.M., *Nanoparticles: building blocks for nanotechnology*. 2004: Springer Science & Business Media.
2. Topmiller, J.L. and K.H. Dunn, *Current strategies for engineering controls in nanomaterial production and downstream handling processes.* 2013.
3. Cooper, S., *Gold Nanoparticles Market Analysis by Application (Medical & Dentistry, Electronics, Catalysis and Sensors & Probes) And Segment Forecasts To 2020*. December, 2014, Radiant Insights.
4. Cho, W.-S., et al., *Comparison of gene expression profiles in mice liver following intravenous injection of 4 and 100nm-sized PEG-coated gold nanoparticles.* Toxicology letters, 2009. **191**(1): p. 96-102.
5. Merchant, B., *Gold, the noble metal and the paradoxes of its toxicology.* Biologicals, 1998. **26**(1): p. 49-59.
6. Lin, D., et al., *Fate and transport of engineered nanomaterials in the environment.* Journal of Environmental Quality, 2010. **39**(6): p. 1896-1908.
7. Praetorius, A., M. Scheringer, and K. Hungerbühler, *Development of Environmental Fate Models for Engineered Nanoparticles□ A Case Study of TiO2 Nanoparticles in the Rhine River.* Environmental science & technology, 2012. **46**(12): p. 6705-6713.
8. Lowry, G.V., et al., *Environmental occurrences, behavior, fate, and ecological effects of nanomaterials: an introduction to the special series.* Journal of environmental quality, 2010. **39**(6): p. 1867-1874.

9. Cornelis, G., et al., *Fate and bioavailability of engineered nanoparticles in soils: a review.* Critical Reviews in Environmental Science and Technology, 2014. **44**(24): p. 2720-2764.

10. Dale, A.L., et al., *Modeling nanomaterial environmental fate in aquatic systems.* Environmental science & technology, 2015. **49**(5): p. 2587-2593.

11. Lowry, G.V., et al., *Long-term transformation and fate of manufactured Ag nanoparticles in a simulated large scale freshwater emergent wetland.* Environmental science & technology, 2012. **46**(13): p. 7027-7036.

12. Gottschalk, F., et al., *Modeled environmental concentrations of engineered nanomaterials (TiO2, ZnO, Ag, CNT, fullerenes) for different regions.* Environmental science & technology, 2009. **43**(24): p. 9216-9222.

13. Aiken, G.R., H. Hsu-Kim, and J.N. Ryan, *Influence of dissolved organic matter on the environmental fate of metals, nanoparticles, and colloids.* Environmental science & technology, 2011. **45**(8): p. 3196-3201.

14. Hoecke, K.V., et al., *Fate and effects of CeO2 nanoparticles in aquatic ecotoxicity tests.* Environmental science & technology, 2009. **43**(12): p. 4537-4546.

15. Yang, P. and C.M. Lieber, *Nanorod-superconductor composites: a pathway to materials with high critical current densities.* Science, 1996. **273**(5283): p. 1836.

16. Park, W.I., et al., *Fabrication and electrical characteristics of high-performance ZnO nanorod field-effect transistors.* Applied Physics Letters, 2004. **85**(21): p. 5052-5054.

17. Dickerson, E.B., et al., *Gold nanorod assisted near-infrared plasmonic photothermal therapy (PPTT) of squamous cell carcinoma in mice.* Cancer letters, 2008. **269**(1): p. 57-66.

18. Law, M., et al., *Nanowire dye-sensitized solar cells.* Nature materials, 2005. **4**(6): p. 455-459.

19. Wan, Q., et al., *Fabrication and ethanol sensing characteristics of ZnO nanowire gas sensors.* Applied Physics Letters, 2004. **84**(18): p. 3654-3656.

20. Kolmakov, A., et al., *Detection of CO and O2 using tin oxide nanowire sensors.* Advanced Materials, 2003. **15**(12): p. 997-1000.

21. *consumer product inventories*. Woodrow Wilson international center for scholars: Washington DC.

22. Petersen, E.J., et al., *Potential release pathways, environmental fate, and ecological risks of carbon nanotubes.* Environmental science & technology, 2011. **45**(23): p. 9837-9856.

23. Helland, A., et al., *Reviewing the environmental and human health knowledge base of carbon nanotubes.* Ciência & Saúde Coletiva, 2008. **13**(2): p. 441-452.

24. Saleh, N.B., L.D. Pfefferle, and M. Elimelech, *Aggregation kinetics of multiwalled carbon nanotubes in aquatic systems: measurements and environmental implications.* Environmental science & technology, 2008. **42**(21): p. 7963-7969.

25. Lam, C.-w., et al., *A review of carbon nanotube toxicity and assessment of potential occupational and environmental health risks.* Critical reviews in toxicology, 2006. **36**(3): p. 189-217.

26. Petersen, E.J., et al., *Biological uptake and depuration of carbon nanotubes by Daphnia magna.* Environmental science & technology, 2009. **43**(8): p. 2969-2975.

27. Goodman, C.M., et al., *Toxicity of gold nanoparticles functionalized with cationic and anionic side chains.* Bioconjugate chemistry, 2004. **15**(4): p. 897-900.

28. Hauck, T.S., A.A. Ghazani, and W.C. Chan, *Assessing the effect of surface chemistry on gold nanorod uptake, toxicity, and gene expression in mammalian cells.* Small, 2008. **4**(1): p. 153-159.

29. Wang, S., et al., *Challenge in understanding size and shape dependent toxicity of gold nanomaterials in human skin keratinocytes.* Chemical physics letters, 2008. **463**(1): p. 145-149.

30. Schaeublin, N.M., et al., *Does shape matter? Bioeffects of gold nanomaterials in a human skin cell model.* Langmuir, 2012. **28**(6): p. 3248-3258.

31. Pan, Y., et al., *Size-dependent cytotoxicity of gold nanoparticles.* Small, 2007. **3**(11): p. 1941-1949.

32. Park, W., et al., *Schottky nanocontacts on ZnO nanorod arrays.* Applied Physics Letters, 2003. **82**(24): p. 4358-4360.

33. Chaney, S.B., et al., *Aligned silver nanorod arrays produce high sensitivity surface-enhanced Raman spectroscopy substrates.* Applied Physics Letters, 2005. **87**(3): p. 031908.

34. Abdullayev, E., et al., *Natural tubule clay template synthesis of silver nanorods for antibacterial composite coating.* ACS applied materials & interfaces, 2011. **3**(10): p. 4040-4046.

35. Yang, X., et al., *Preparation and properties of a novel electrically conductive adhesive using a composite of silver nanorods, silver nanoparticles, and modified epoxy resin.* Journal of Materials Science: Materials in Electronics, 2012. **23**(1): p. 108-114.

36. Langley, D., et al., *Flexible transparent conductive materials based on silver nanowire networks: a review.* Nanotechnology, 2013. **24**(45): p. 452001.

37. Barea, E., et al., *Origin of efficiency enhancement in Nb 2 O 5 coated titanium dioxide nanorod based dye sensitized solar cells.* Energy & Environmental Science, 2011. **4**(9): p. 3414-3419.

38. Kandiel, T.A., et al., *Tailored titanium dioxide nanomaterials: anatase nanoparticles and brookite nanorods as highly active photocatalysts.* Chemistry of materials, 2010. **22**(6): p. 2050-2060.

39. Chen, X. and S.S. Mao, *Titanium dioxide nanomaterials: synthesis, properties, modifications, and applications.* Chem. Rev, 2007. **107**(7): p. 2891-2959.

40. Pérez-Juste, J., et al., *Gold nanorods: synthesis, characterization and applications.* Coordination Chemistry Reviews, 2005. **249**(17): p. 1870-1901.

41. Huang, X., S. Neretina, and M.A. El-Sayed, *Gold nanorods: from synthesis and properties to biological and biomedical applications.* Advanced Materials, 2009. **21**(48): p. 4880.

42. Isomaa, B., J. Reuter, and B. Djupsund, *The subacute and chronic toxicity of cetyltrimethylammonium bromide (CTAB), a cationic surfactant, in the rat.* Archives of toxicology, 1976. **35**(2): p. 91-96.

43. Akiyama, Y., et al., *The effects of PEG grafting level and injection dose on gold nanorod biodistribution in the tumor-bearing mice.* Journal of Controlled Release, 2009. **139**(1): p. 81-84.

44. Petosa, A.R., et al., *Aggregation and deposition of engineered nanomaterials in aquatic environments: role of physicochemical interactions.* Environmental science & technology, 2010. **44**(17): p. 6532-6549.

45. Zhou, D. and A.A. Keller, *Role of morphology in the aggregation kinetics of ZnO nanoparticles.* Water research, 2010. **44**(9): p. 2948-2956.

46. Afrooz, A.N., et al., *Spheres vs. rods: The shape of gold nanoparticles influences aggregation and deposition behavior.* Chemosphere, 2013. **91**(1): p. 93-98.

47. Baun, A., et al., *Ecotoxicity of engineered nanoparticles to aquatic invertebrates: a brief review and recommendations for future toxicity testing.* Ecotoxicology, 2008. **17**(5): p. 387-395.

48. Doherty, F.G., *The Asiatic clam, Corbicula spp., as a biological monitor in freshwater environments.* Environmental monitoring and assessment, 1990. **15**(2): p. 143-181.

49. McLeod, P.B., S.N. Luoma, and R.G. Luthy, *Biodynamic modeling of PCB uptake by Macoma balthica and Corbicula fluminea from sediment amended with activated carbon.* Environmental Science & Technology, 2007. **42**(2): p. 484-490.

50. Hull, M.S., et al., *Filter-feeding bivalves store and biodeposit colloidally stable gold nanoparticles.* Environmental science & technology, 2011. **45**(15): p. 6592-6599.

51. Pan, J.-F., et al., *Size dependent bioaccumulation and ecotoxicity of gold nanoparticles in an endobenthic invertebrate: the Tellinid clam Scrobicularia plana.* Environmental pollution, 2012. **168**: p. 37-43.

52. Renault, S., et al., *Impacts of gold nanoparticle exposure on two freshwater species: a phytoplanktonic alga (Scenedesmus subspicatus) and a benthic bivalve (Corbicula fluminea).* Gold bulletin, 2008. **41**(2): p. 116-126.

Chapter 2. Implications of Aspect Ratio on Uptake and Nanotoxicity of Gold Nanomaterials

S.M.H. Abtahi,[1, 2, 3] Rafael Trevisan,[3, 4] Richard Di Giulio, [3, 4] Catherine J. Murphy,[5] Navid B. Saleh,[6] and Peter J. Vikesland[1, 2, 3]*

[1.]Virginia Tech, Department of Civil and Environmental Engineering, Blacksburg, VA, USA

[2.]Virginia Tech, Institute for Critical Technology and Applied Science (ICTAS) Center for Sustainable Nanotechnology (VTSuN), Blacksburg, VA, USA

[3.]Center for the Environmental Implications of Nanotechnology (CEINT), Duke University, Durham, NC, USA

[4.] Nicholas School of the Environment, Duke University, Durham, NC, 27710, USA

[5.]Department of Chemistry, University of Illinois at Urbana-Champaign, 600 S. Matthews Ave., Urbana, IL, 61801, USA

[6.]The University of Texas at Austin, Department of Civil, Architectural and Environmental Engineering, Austin, TX 78712, USA

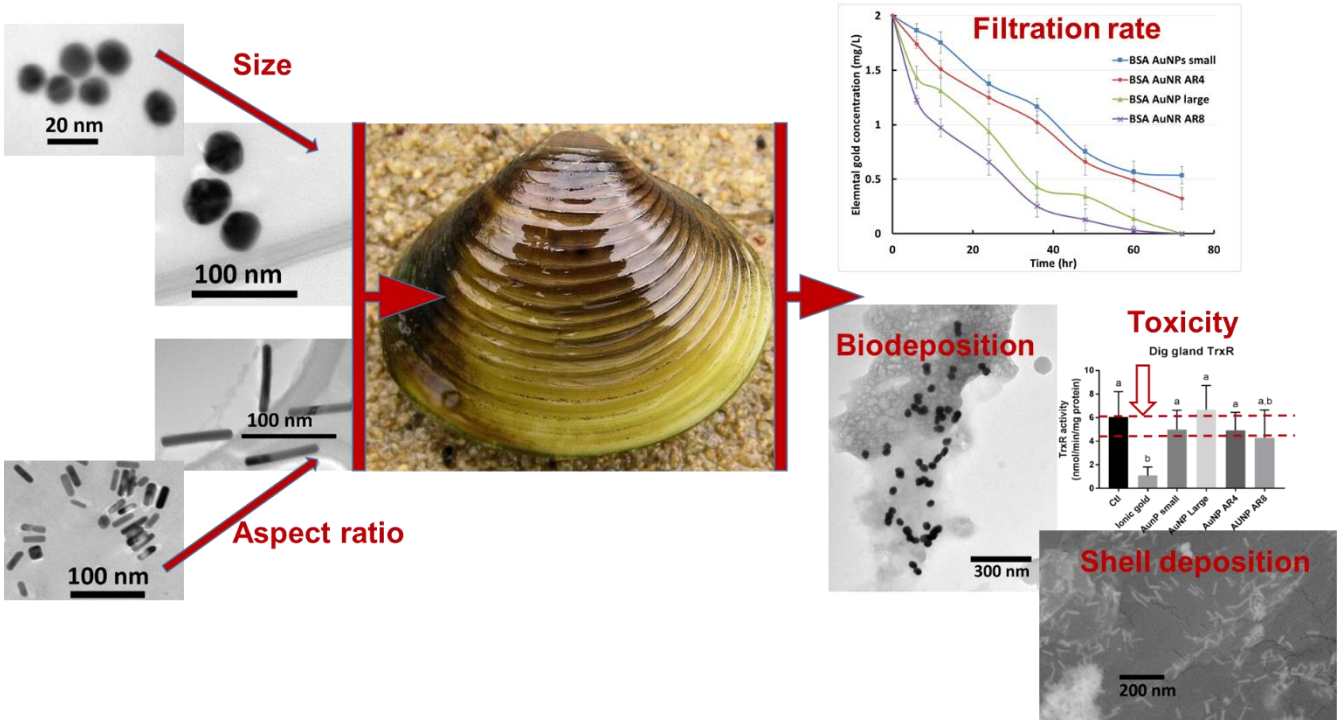

2.1 Abstract

Colloidally stable gold nanoparticles are commonly used for biomedical and industrial applications due to their unique physicochemical properties. However, the post-application fate of these nanoparticles is an environmental question that requires consideration. In this study, we evaluated how nanoparticle size and shape impact the uptake and toxicity of gold nanoparticles to the filter-feeding bivalve, *Corbicula fluminea*. Our results indicate that the organismal uptake rate increases with an increase in nanoparticle size and anisotropicity. Both spherical and elongated gold nanoparticles were readily detected in the digestive glands, gills, (pseudo)feces, and on the clamshell exterior following exposure. The presence of nanoparticles in non-digestive tissues suggest that the nanoparticles were internalized and consumed by *C. fluminea*. The toxicity results indicate that for the tested concentration and exposure period that gold

nanoparticles were not acutely toxic (i.e., not lethal). However, gold nanoparticles significantly inhibited the activity of some antioxidant enzymes in gill and digestive gland tissues. This inhibition could affect the resistance of these organisms to a secondary stressor (e.g., temperature, pathogens, and hypoxia) and threaten organismal health.

2.2 Introduction

The environmental fate, transport, and toxicity of engineered nanomaterials (ENMs) have been broadly investigated and discussed in the literature [1-7]. Nevertheless, a majority of the research published to date has focused on spherical nanoparticles and has not explicitly considered the effects of shape [2, 6-9]. Currently there is a general lack of knowledge with respect to the environmental implications of elongated nanoparticles such as rods, tubes, and wires. This class of highly anisotropic ENMs are interesting due to their unique physiochemical properties and are being incorporated in everyday consumer products [10-15]. Metallic nanorods and nanowires are the most commonly fabricated ENMs after carbon nanotubes (CNTs) [16]. Gold is commonly believed to be non-reactive under environmentally relevant conditions and consequently gold nanoparticles are generally considered safe [17]. For many years, gold nanoparticles (GNPs) have been used for jewelry, art, decorative, and biomedical purposes. Chrysotherapy, using gold complexes to treat arthritis [18], and dietary supplements are two examples of the biomedical applications of GNPs. Their unique optical properties and their ease of manufacturing and shape-tuning make GNPs good candidates for industrial applications such as catalysis and biosensing [19]. However, recent studies have shown some toxicity is imparted by gold nanorods (AuNRs) under certain conditions [20-25] and has raised concerns about the inertness of gold nanoparticles.

Freshwater *Corbicula fluminea* bivalves are water column and sediment filter feeders and can be found in both freshwater and marine habitats [26]. Filter feeders are a group of organisms that feed by straining suspended matter and food particles from water, typically by passing the water over a specialized filtering structure. As a result, they are highly susceptible to environmental pollutants such as heavy metals, organic pollutants, and ENMs [27] and as such they have been used by scientists as aquatic contaminant biodetectors for decades [28]. *C. fluminea* is an invasive organism introduced to North America from Asia. *C. fluminea* feeds primarily on phytoplankton (algae) that it filters from the sandy or muddy bottoms of streams, lakes, or canals. Interestingly, *C. fluminea* has the highest filtration rate of freshwater bivalves and filters approximately 45 L water/g (dry weight)/day [29]. This exceptionally high filtration rate and the relative ease of access for collection from riverine ecosystems are the primary reasons that they are used in many studies as a contaminant biodetector. Prior studies have suggested that *C. fluminea* can uptake and accumulate ENMs [30-32]. Our previous study indicated that the biofiltration rates of colloidally stable gold nanoparticles were related to the size and concentration of nanoparticles, with larger particles exhibiting a higher rate of filtration. Gold nanoparticles were easily detected in the digestive glands and pseudo(feces) of exposed clams [30]. However, none of the existing studies investigated the effect of anisotropicity and aspect ratio (AR) on ENM uptake. Prior studies suggest that shape-related parameters such as AR can significantly affect colloidal behavior, aggregation rates[33], and biotoxicity [22, 34]. As a result, we hypothesized that shape and AR will affect the biofiltration and biotoxicity of these AuNPs. The objective of this study was to investigate the shape related uptake and potential associated toxicity of gold nanoparticles to *C. fluminea*.

2.3 Materials and Methods

Gold Nanoparticle Synthesis. 19 nm citrate stabilized gold nanoparticles (citrate-AuNP) were prepared using the method of Jana et al. [35] that is based upon that of Turkevich [36]. 45 nm citrate-AuNPs were prepared using the seed-mediated method of Frens [37]. In both synthesis processes, citrate was used as the reducing agent and colloidal stabilizer. Post synthesis, the AuNP suspensions were filter sterilized (0.2 μm) and then stored in amber glass vials at 4 °C.

Aspect ratio 4 (AR4) CTAB coated gold nanorod synthesis. AR4 AuNRs were synthesized via the well-established seed-mediated surfactant-directed method [38-40]. In brief, 4 nm spherical gold seeds were prepared through the reduction of chloroauric acid ($HAuCl_4$) by the addition of ice-cooled and freshly prepared sodium borohydride in the presence of cetyltrimethylammonium bromide (CTAB). AR4 AuNRs were then grown from an aqueous growth solution consisting of CTAB, $HAuCl_4$, and $AgNO_3$ using ascorbic acid as the reducing agent. Gold seeds were added to the growth solution and the mixture was left undisturbed for 2 hours till growth completion. Post synthesis, other shape gold nanoparticles, such as spheres and cubes, were removed by centrifugation (25 min at 8,000 x g) repeated five times with pellet resuspension in 800 μM CTAB.

Aspect ratio 8 (AR8) CTAB coated gold nanorod synthesis. AR8 AuNRs were synthesized following the method of Nikoobakht et al. [39] with a few modifications. Gold seed nanoparticles were prepared following the process described for AR4 AuNRs. The growth solution consisted of $HAuCl_4$, $AgNO_3$, ascorbic acid, CTAB, and benzyldimethylammonium chloride (BDAC). The molar ratio of BDAC/CTAB was adjusted to 2.7. It has been shown that ratios between 2 and 5.5 favor decreased formation of

spherical particles. To further increase the yield of AR8 AuNRs, 200 µL of 1 M HCl was added to 10 mL growth solution. The mixture was left undisturbed for 24 hours in a 30 ºC water bath until growth completion. Post synthesis, the suspension was centrifuged at 2,000 x g for 5 min. The supernatant primarily consisting of AR8 gold nanorods was separated by a pipette from the pellet that primarily contained large nanoparticle byproducts.

Bovine serum albumin (BSA) coating of AuNPs and AuNRs. BSA coated AuNPs were prepared by incubating citrate-AuNP with 0.1 mg BSA/mL. The pH of the mixture was adjusted to 9.0 by addition of 1 M NaOH. The mixture was left undisturbed for 24 hours and centrifuged at 10,000 x g for 30 minutes to remove excess unreacted BSA and citrate. BSA coating of AR4 and AR8 AuNRs was done following the protocol of Tebbe et.al. [41]. In brief, for AR4 the CTAB and for AR8 the CTAB/BDAC concentration of the suspension was reduced to <0.1 mM by centrifugation and by replacing the supernatant with DI water. The AuNRs are not colloidally stable at this low surfactant concentration for more than 30 min. Accordingly, this step was done immediately prior to ligand exchange. The suspension was added to a concentrated BSA solution (10 mg/mL) at pH 7 under vigorous stirring and bath sonicated for 30 minutes. The volume ratio of BSA solution to AuNR suspension was 3:1. The mixture was then centrifuged and the supernatant was replaced by 1 mg/mL BSA solution at pH 12 and left undisturbed for 24 hours. Excess BSA and detached CTAB and BDAC were removed by several sequential centrifugal wash steps.

Gold NPs and NRs characterization. The size, shape, and quality of the synthesized nanoparticles were characterized by dynamic light scattering (DLS), vis-NIR

spectroscopy, inductively coupled plasma mass spectroscopy (ICP-MS), scanning electron microscopy (SEM), and transmission electron microscopy (TEM). The primary intensity particle size distributions of the GNPs were measured using a Malvern Zetasizer NanoZS DLS based on analysis of the correlation functions using the General Purpose algorithm and a non-negative least squares fit[42]. The Malvern NanoZS is equipped with a 4mW He-Ne 633 nm laser and a 175° angle backscattering detector. A Philips EM420 conventional electron microscope equipped with a CCD camera was used to measure the size and shape of the AuNRs and AuNPs. TEM samples were prepared using a drop-cast technique. In brief, a 10 µL droplet of sample was dropped onto a 300 mesh carbon coated copper TEM grid in a well ventilated hood and dried for 24 hours. The elemental gold content of the synthesized gold nanoparticles was measured using an Agilent 7500ce ICP-MS. For this purpose, 1 mL of synthesized gold NPs and NRs was washed twice using consecutive centrifugal washes at 10000 x g for 20 min and diluted 100x. Later the sample was transferred to a polystyrene tube followed by addition of 200 µL aqua regia (1:3, Trace metal grade HNO_3:HCl) and after 2 hours brought to 10 mL volume by addition of DI water. The absorption intensity and plasmon band (transverse and longitudinal) locations were characterized using a Cary 5000 UV-Vis-NIR spectrometer. The presence of gold nanoparticles on the clam shell was imaged using a LEO (Zeiss) 1550 field-emission scanning electron microscope.

***C. fluminea* clam collection and preparation**. The collected adult *C. fluminea* (Asian clam) on average were 17.7 ± 0.6 mm long and 12.3 ± 0.4 mm thick (the noted errors reflect 95% confidence intervals based on n=20 measurements). Clams were collected from the Eno River (Longitude 36.0701855, Latitude -78.9112751), Durham, NC in mid-

summer and acclimated for 10 days to laboratory conditions. In this acclimation period, the clams were stored under ample aeration and starved in 10 gallon glass aquarium tanks. Each tank contained 75 clams kept in freshly prepared moderately hard standard EPA synthetic water (Table S1 provides solution composition). The water was changed on a daily basis to assure that (pseudo)feces and other suspended particles did not accumulate in the gills and digestive glands of the clams.

AuNP and AuNR uptake and clearance assays with *C. fluminea* clams. Microcosm reactors consisted of 100 mL glass beakers. Each microcosm contained two clams exposed to 40 mL of ~2 mg (elemental gold)/L BSA coated AuNP or AuNR suspensions for 72 hours. Seven replicate microcosms were used per experiment to assure data quality. Test solutions were prepared by quantitative addition of AuNP or AuNR suspension to moderately hard synthetic EPA water followed by addition to microcosms. To evaluate deposit feeding by *C. fluminea* bivalves an artificial bed consisting of glass beads was added to a few of microcosms prior to addition of AuNR suspension. Two types of controls were conducted in parallel to the experiments. A positive control where the microcosm only contained dissolved gold having the same atomic concentration as used in the nanoparticle uptake experiments, and a negative control that did not have any dissolved gold or nanoparticles in it. We note that previous studies have shown that nanoparticles easily adhere to the *C. fluminea* shells. Therefore, organismal uptake as well as deposition to the glass beads and the bivalve shell surfaces are possible nanoparticle removal mechanisms. To investigate deposition on either glass beads or shells the following control experiments were conducted. A beaker containing glass beads and AuNR suspension was subjected to the same procedure as the actual experiment.

In the other control, two clams were dissected, their tissue and shells separated, the shells glued back together, and then these shells were exposed to the same concentration nanoparticle suspensions while the water column was tested accordingly.

Vis-NIR spectroscopy and ICP-MS were used to monitor the absorption intensity and elemental gold concentration of the water columns at 0, 6, 12, 24, 36, 48, 60, and 72 hour time-points during the time course of the experiments. Water column aliquots of 1 mL were removed by pipette and transferred to a 10 mm pathlength plastic cuvette. The sample was then characterized by vis-NIR spectroscopy in the wavelength range of 400-1300 nm prior to being returned to the microcosm. For ICP-MS sample preparation, 50 µL sample was taken and transferred to a polystyrene tube to which 200 mL of aqua regia (1:3, Trace metal grade HNO_3:HCl) was added and then left undisturbed for 2 hours. Finally the mixture was brought to 10 mL volume by addition of ultrapure DI water. Upon termination of the experiment, clams were removed from the microcosms and dissected. The dark tissue (digestive glands and gills) was separated from the rest of the tissue. Tissue segments and shells were separately wet digested [43] and the elemental gold content was measured by ICP-MS. In brief, 5 mL of trace metal grade HNO_3 was added to 0.5 g of the wet tissue or shell sample in a 20 mL beaker and left undisturbed for 24 hours. The mixture was heated in a 60°C water bath for an hour and then cooled at room temperature. Next 2 mL 30% H_2O_2 was added and the mixture was heated in a 60°C water bath for an hour. Finally, the sample was diluted to a volume of 25 mL by adding ultrapure DI water. In addition, (pseudo)feces samples were collected from the bottom of the microcosm using a 10 µL pipette. TEM samples of (pseudo)feces were prepared by the drop cast technique on a 300 mesh carbon coated copper grid. Clam shells were

crushed into tiny pieces and mounted on top of SEM stubs using carbon conductive tape for SEM characterization of AuNP and AuNR deposition on shells.

Toxicity Measurement Assay. For protein damage and antioxidant enzyme activity measurements, clams were exposed to 2 mg/L AuNP and AuNR suspensions at room temperature, as previously described. A 100 mL beaker containing 4 clams and 40 mL gold nanoparticle suspension was used as a microcosm for the 72 hour time course of an exposure experiment. To assure measurement consistency, three replicates and two controls were conducted. Control 1 in which the clams were exposed to 40 mL medium hard EPA water not containing any gold nanoparticles, and control 2 where the clams were exposed to 2 mg/L $HAuCl_4$. It should be noted that control 1 was carried out as the background for blank measurements, while control 2 directly measured the toxicity associated with ionic gold. At the end of the exposure, clams were weighed, the gills and digestive glands were dissected and then immediately frozen in liquid nitrogen and stored at -80°C.

Gills and digestive glands were individually homogenized in 200 µL of 50 mM potassium phosphate buffer pH 7.0 containing 0.5 mM EDTA (KPB50) supplemented with protease inhibitor cocktail (#P8340, MilliporeSigma - St. Louis, US). The homogenates were centrifuged at 15,000 x g for 15 minutes at 4 °C, and the supernatant was collected and stored as aliquots at -80°C until further analysis, as described below.

Protein damage assays. For protein thiol levels (P-SH), 20 µL of sample (approximately 100 µg protein) was added to 10 µL of KPB50 buffer and incubated with 300 µM monobromobimane (mBrB, #B4380, MilliporeSigma – St. Louis, US) for 4 hours at room temperature in the dark. The non-fluorescent dye mBrB specifically binds to reduced

sulfhydryl groups, after which it becomes fluorescent [44]. After the incubation, proteins were extracted using cold acetone (150 µL) and incubated overnight at -20°C. Samples were centrifuged at 15,000 x g for 10 min at 4°C, and the protein extracts were then further washed with cold acetone at least 3×, until no residual color from mBrB was visible. Proteins were resuspended in 25 µL of 25 mM pH 7.0 TRIS buffer containing 8 M urea and 2% SDS, and the protein concentration was determined by the bicinchoninic acid assay using the Pierce™ BCA protein assay kit (23225, ThermoFisher Scientific – Waltham, US). A standard curve of bovine serum albumin (BSA) was used containing urea and SDS concentrations equivalent to the samples. For the fluorescence measurements, 10 µg of protein were added to 384 well solid black plates and the volume of each well was adjusted to 100 µL with 25 mM TRIS buffer at pH 7.0 containing 8 M urea and 2% SDS. Samples were read at 340-10nm (excitation) and 520 nm (emission). Wells containing buffer, but no sample were used as blanks. The fluorescence of each sample was subtracted from the blank and normalized by the average for the control group.

For protein carbonyl groups (P-CO), samples were treated similar to the P-SH assay, except by replacing mBrB with 200 µM coumarin hydrazide (7-(diethylamino)-coumarin-3-carbohydrazide, 36798, MilliporeSigma, St. Loius - US). This non-fluorescent dye binds specifically to carbonyl groups, after which it becomes fluorescent.[45] Samples were analyzed at 400-10 nm (excitation) 470-12 (emission), and data were analyzed as described for the P-SH assay.

Enzyme assays. For glutathione reductase (GR) activity, samples were analyzed at 340 nm to measure = NADPH consumption by the reduction of disulfide glutathione in 100

mM potassium phosphate buffer pH 7.0 containing 1 mM EDTA, 200 µM NADPH, and 1 mM oxidized glutathione [46].

For glutathione peroxidase (GPx) activity, samples were analyzed at 340 nm to measure NAPDH consumption associated with peroxide breakdown in 50 mM potassium phosphate buffer pH 7.0 containing 0.5 mM EDTA, 200 µM NADPH, 1 mM reduced glutathione, 0.2 U/mL purified baker's yeast glutathione reductase, and 0.5 mM cumene hydroperoxide [47].

For catalase (Cat) activity, samples were analyzed at 240 nm to measure hydrogen peroxide consumption in 50 mM potassium phosphate buffer pH 7.0 containing 0.5 mM EDTA, 0.01% Triton x-100 and 10 mM hydrogen peroxide [48].

For thioredoxin reductase (TrxR) activity, samples were analyzed at 412 nm to measure the 5,5'-dithio-bis-(2-nitrobenzoic acid) (DTNB) reduction in 100 mM potassium phosphate buffer pH 7.0 containing 10 mM EDTA, 5 mM DTNB, 0.2 mg/ml BSA and 200 µM NADPH [49].

Specific enzyme activity was calculated by normalizing enzyme activity by the protein content, which was determined using the Pierce™ BCA protein assay kit (23225, ThermoFisher Scientific – Waltham, US) and BSA as standard.

Statistics. Data were analyzed for normality distribution using the Kolmogorov-Smirnov test and outliers were removed using the Grubs test. Data were further analyzed by one-way ANOVA and Tukey's post hoc or Kruskal-Wallis and Dunn's post hoc tests when appropriate. Significant differences were accepted when $p < 0.05$.

2.4 Results and Discussion

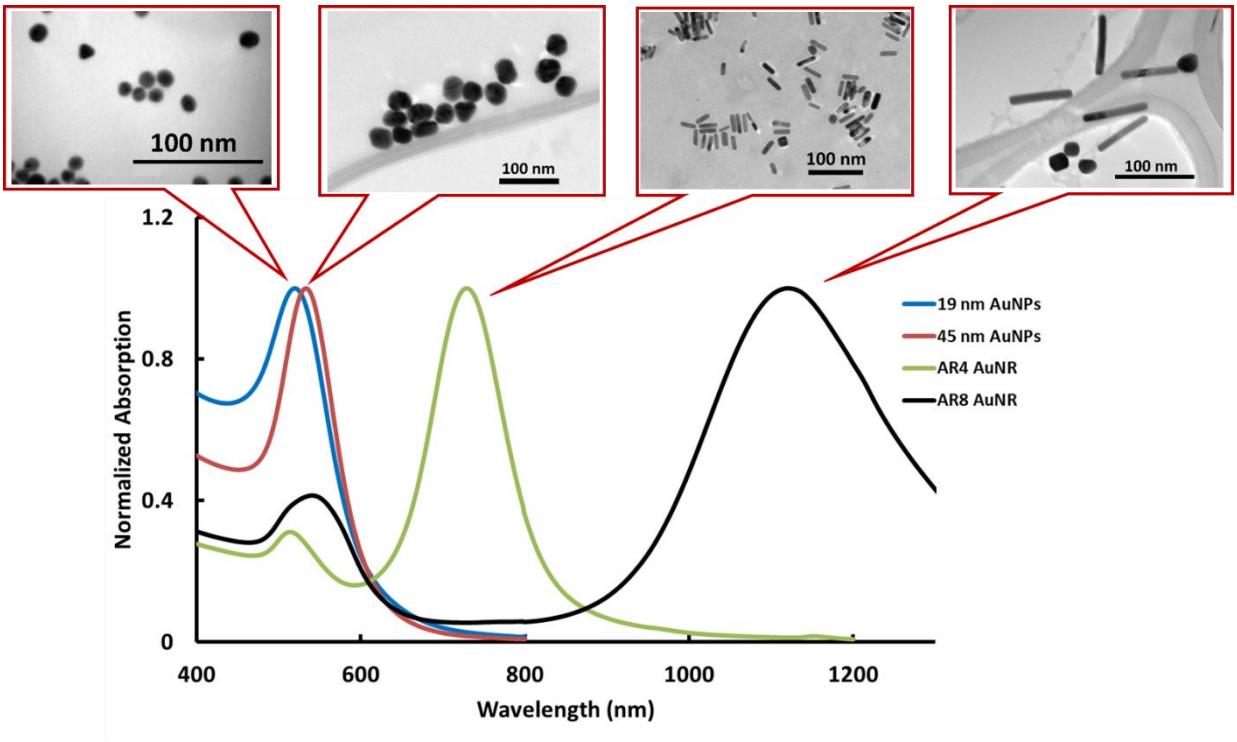

Figure 2.1. Vis-NIR normalized absorption and TEM images of synthesized AuNPs and AuNRs prior to BSA coating.

Vis-NIR and corresponding TEM images of synthesized AuNPs and AuNRs are shown in Figure 2.1 (Additional TEM images and particle size distributions of the nanoparticles are provided in Figures 2.S1-S2). Citrate-AuNPs were 19.2 ± 0.2 and 45.3 ± 0.1 nm average diameter, while CTAB coated AR4 and CTAB/BDAC coated AR8 AuNRs were 43 ± 0.1 nm and 84 ± 0.3 nm long and 11± 0.1 nm and 10 ± 0.2 nm in diameter, respectively (the noted errors reflect 95% confidence interval based on n=30 measurements of TEM images obtained using ImageJ). The average AR values were 3.9 ± 0.1 and 8.4 ± 0.2, but for simplicity we refer to these AuNRs as AR4 and AR8. Following

BSA treatment, the coated AuNPs and AuNRs retained their shapes while the plasmon bands red shifted due to the change in local dielectric constant ε_m. The relative impacts of medium dielectric constant are well-developed and previously described in the literature [40, 50] The plasmon band location of the nanoparticles before and after BSA coating are presented in Table 2.1.

Table 2.1. Plasmon band wavelengths of AuNPs and AuNRs before and after BSA coating

	Initial coating		BSA coating	
	Transverse band (nm)	Longitudinal band (nm)	Transverse band (nm)	Longitudinal band (nm)
Small AuNP (19 nm)	520	N.A.	526	N.A.
Large AuNP (45 nm)	533	N.A.	537	N.A.
AR4 AuNR	514	728	517	733
AR8 AuNR	530	1120	535	1128

Nanoparticles did not aggregate within the time course of the ligand exchange and *C. fluminea* exposure experiment. As a result, any reported changes in absorption intensity of the plasmon bands can be directly related to particle concentration changes in the water column using the Beer-Lambert law [51, 52].

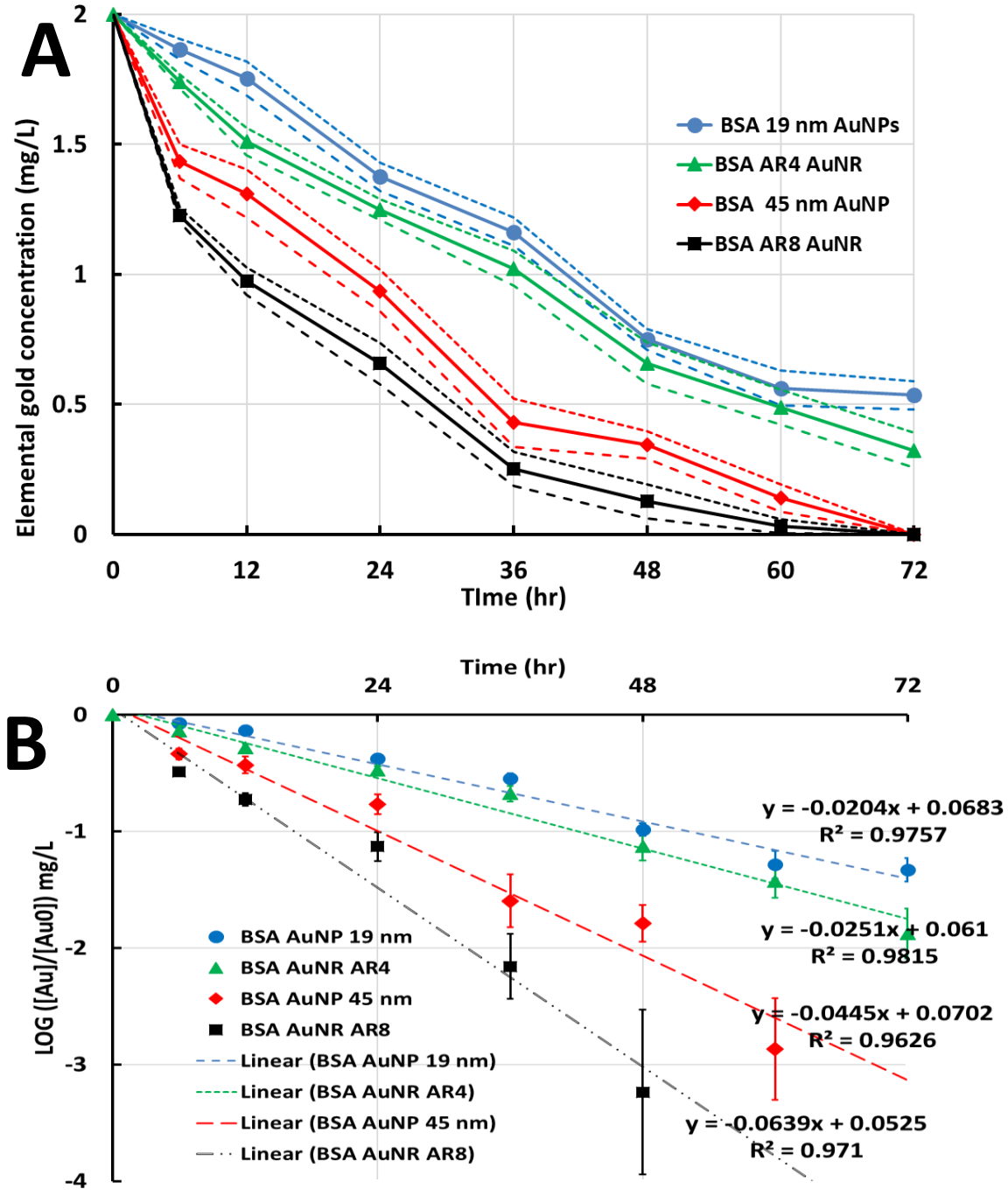

Figure 2.2. A) Elemental gold concentration in suspension column versus time within the 72 hour time course of the uptake study. The dashed lines indicate the upper and lower 95% confidence intervals. The data points are connected with straight lines to illustrate the depletion of nanoparticles from the suspension column. **B)** Clearance rate

calculations as fitted by first order kinetic rate modeling. The linear regressions and line equations represent the first order kinetic expressions.

Figure 2.2A indicates how the 2 mg/L initial gold nanoparticle concentration in suspension changes within the 72 hour exposure period of each experiment. Each reported value represents the average of seven replicates and the associated 95% confidence intervals for each measurement are presented as dashed lines. Data points were calculated by directly measuring the absorption intensity of the plasmon bands and linearly relating them to the elemental gold concentration in the suspension column. The results shown in Figure 2.2A are not surprising based upon our previous work[30] that showed the clearance efficiency of nanoparticles is size related. After 72 hours, the removal efficiencies for 19 nm AuNP, AR4 AuNR, 45 nm AuNP, and AR8 AuNR from the suspension column were 73, 84, 100, and 100%, respectively. To compare results obtained with the high AR AuNRs to the spherical AuNPs, the equivolume spherical diameter was calculated (the shape conversion calculations are presented in the SI). The equivolume spherical diameters of the AR4 and AR8 AuNRs were 16 and 19 nm, respectively. The kinetics of nanoparticle clearance were evaluated using a first-order model, since the clearance of each size particle follows a logarithmic pattern with a sharp drop within the first 12 hours and a linear drop over the remainder of the experiment. Our prior study has shown that nanoparticle removal via filter-feeding is most appropriately characterized by a first-order model [30]. As shown in Figure 2.2B and summarized in Table 2.2, the kinetic coefficients range from 0.020 ± 0.002 to 0.064 ± 0.012 h^{-1} and are size and shape dependent (calculation details are presented in the SI).

In general, the clearance rates increase with an increase in the nanoparticle size. AR8 AuNRs had the highest clearance rate (=0.064 h^{-1}) among all tested nanoparticles despite having a smaller equivolume spherical diameter than the 45 nm AuNPs. The clearance rate of the AR8 AuNRs was 45% higher than 45 nm AuNPs. AR4 AuNRs followed the same trend with a 25% higher clearance rate compared to 19 nm GNPs. We found out that AuNRs despite having a smaller equivolume spherical diameter compared to spherical AuNPs have a higher clearance rate due to elongation along one axis. A clear pattern relating clearance rates and shape-related nanoparticle size was observed, if these rates are sorted based on the longest axis (nanoscale feature) of these nanoparticles rather than apparent spherical size, Table 2.2. Accordingly, these results suggest that not only size, but shape-related features such as AR play an important role in the filtration of nanoparticles by *C. fluminea*. *C. fluminea* is generally known as a non-selective filter-feeder with a filtration mechanism that is mainly based on the quantity and the size of particulates rather than quality[53, 54]. Filter-feeders such as *C. fluminea* suck in and expel water through siphons for feeding and respiration. The water is pushed through the organism by the collective movement of millions of hairlike fibers called cilia on the gills. Simultaneously, cilia strain food (mainly particles) from the influent water and transport it into the clam[26, 55]. The net removal rate of particles via these fibers are governed by the following mechanisms 1) direct interception, 2) inertial impaction, 3) gravitational deposition, 4) diffusion, and 5) electrostatic attraction[56]. Due to the high fluid velocity inside the gills, diffusion and gravitational deposition are generally negligible compared to other mechanisms. The magnitudes of direct interception, inertial impaction, and electrostatic attractions are directly related to the available surface area of the

colloidal particles. Consequently, nanoparticles with a higher surface area to volume ratio are removed at a higher rate. High AR gold nanorods with a long axis unlike equivolume spherical particles have a larger surface area to volume ratio and are subjected to higher preferential filtration rates by *C. fluminea*. AR4 AuNR and 45 nm AuNP have almost the same size long axis, 43 nm vs 45 nm, while the clearance rate of 45 nm AuNP is close to 2× higher than AR4 AuNR. 45 nm AuNP has 2 equally sized 45 nm long axes due to its circular shape compared to a 43 nm long axis and a short 11 nm axis in AR4 AuNR. As a result, 45 nm AuNP has a higher probability to be filtered out by the clam's gills relative to AR4 AuNR.

Table 2.2. The overall first-order clearance rates for gold nanoparticles over a 72 hour exposure to *C. fluminea* clam as sorted by longest axis of gold nanoparticles

	Longest axis (nm)	Clearance rate (h^{-1})
19 nm AuNP	19	0.020 ± 0.002
AR4	43	0.025 ± 0.003
45 nm AuNP	45	0.044 ± 0.008
AR8	84	0.064 ± 0.012

The percentage of gold present in different tissues and adsorbed to the clam shell versus the initial mass of gold in the suspension is reported in Figure 2.3. These values were quantified after experiment termination by ICP-MS. The largest gold nanoparticle internal accumulations were observed in the gills and the digestive glands of the clams due to the high rate of water filtration by these species. Increasing the size and AR enhance internalization and gold nanoparticle uptake. These results show that larger and higher AR nanoparticles are filtered out at a higher rate compared to smaller

nanoparticles. As a result, they are more available for the clams to be taken up as a potential food source. These measurements are consistent with the vis-NIR spectroscopy measurements (Figure 2.2A). Much lower amounts of gold nanoparticles were detected in other tissues including anterior and posterior adductor muscles and the foot. It should be noted that due to the small size of these tissue compartments and very low concentration of gold nanoparticles in them, we did not investigate each tissue separately. After separating the gills and digestive glands, the rest of the tissues were wet digested and sampled as a collective unit. There is an inherent error in the gold values reported for (pseudo)feces that originates from the difficulty associated with retrieving all of the (pseudo)feces after the experiment termination. This error is due to the stickiness and fine size of the (pseudo)feces. Moreover, (pseudo)feces are exposed to gold nanoparticles present within the suspension and gold nanoparticle sorption to these organic matrices is feasible. However, the overall mass balance accuracies of gold nanoparticle fate within these exposure experiments fall in the range of 88.6-106.7% (calculations and details are provided in the SI). Since the collected amount and the elemental gold mass concentration in (pseudo)feces are much smaller than other specimens, its associated inaccuracy should not noticeably change the overall mass balance.

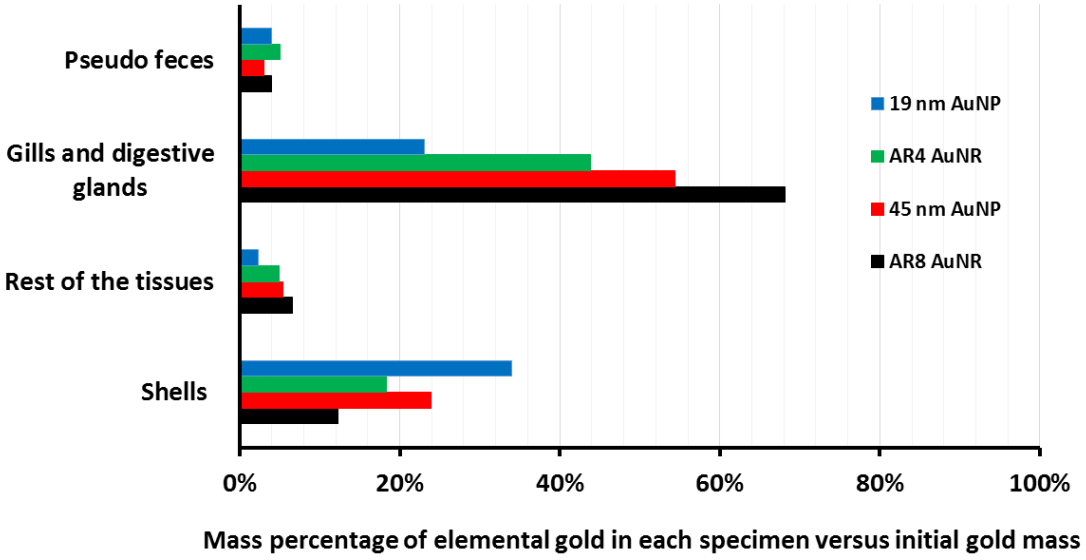

Figure 2.3. Elemental gold ICP-MS measurements presenting the gold content present in different tissues and on the top of the clam shells as expressed in mass percentages versus the initial gold mass.

Elemental gold ICP-MS measurements suggest that nanoparticles are not only internalized in the digestive glands of clams, but are also internally taken up and consumed by the clams. In all sets of experiments, a noticeably large drop in the Vis-NIR absorption intensity of plasmon bands of control 2 (microcosm containing nanoparticle suspension and glued shells of dissected clams) was observed, confirming nanoparticle adsorption to the shells. These plasmon band intensity drops were converted to adsorption percentages and the final values are reported in Table 2.S2. We believe that the presence of a thick organic biolayer on the top of the shells facilitates sorption of BSA coated gold nanoparticles. This biolayer mainly consists of natural organic matter (NOM), organic waste (pseudo)feces, and other organic materials present in the system. As indicated in Figure 2.3 and Table 2.S2, 45 and 19 nm AuNPs showed a higher affinity

and adsorption, almost twice compared to elongated nanoparticles, to the biolayer on the clam shell. We attribute this lower adsorption to the decreased Brownian motion of higher AR AuNRs. Colloidal particles with more rapid Brownian movement collide more with other particles and surfaces in their proximity. Higher numbers of collisions increase the overall probability of heteroaggregation and adsorption of these colloidal particles[57]. In general, the Brownian motion of nanoparticles is decreased with an increase in nanoparticle size. Moreover, AuNRs exhibit a more complicated Brownian motion pattern. Elongated nanoparticles unlike spherical particles undergo rotational diffusion as well as translational diffusion[58, 59]. Increasing the AR significantly reduces the transitional Brownian motion of nanoparticles[60, 61]. As a result, higher AR nanorods have fewer collisions with adjacent surfaces and particles compared to spherical particles and thus exhibit lower surface adsorption. Unlike control 2, no drop in the absorption intensity of the plasmon bands was observed for control 1 (microcosm containing nanoparticle suspension and glass beads, no clams) illustrating the colloidal stability of BSA coated AuNPs and AuNRs against attachment to the beaker and glass bead surfaces. SEM images taken from the top layer on the shells for each set of experiment are presented in Figure 2.4. These images qualitatively show a larger number of adsorbed BSA coated AuNPs (Figure 2.5A-B) versus BSA coated AuNRs (Figure 2.5C-D), and are consistent with ICP-MS and Vis-NIR spectroscopy observations in Figure 2.2, Figure 2.4, and Table S2. It should be noted that the SEM images were taken at 10.00 kV using a Rutherford backscattering detector. Gold nanoparticles could not be imaged using the conventional InLens detector due to being deeply embedded inside the biolayer matrix on top of the clam shell.

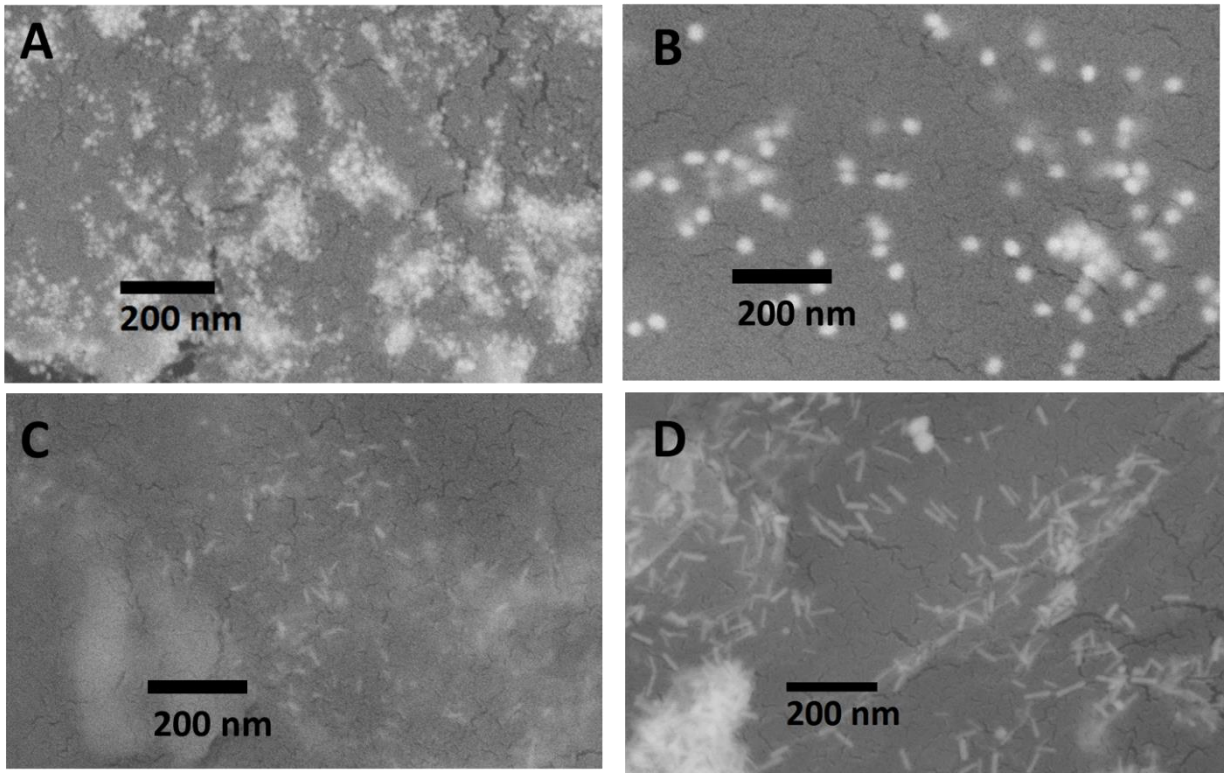

Figure 2.4. Rutherford backscattering SEM images of BSA coated AuNPs and AuNRs adsorbed on the clams' shells. A) 19 nm AuNPs B) 45 nm AuNPs C) AR4 AuNRs D) AR8 AuNRs

TEM images taken of the collected (pseudo)feces after termination of each experiment are provided in Figure 2.5. AuNPs and AuNRs have retained their shape and size, and nanoparticles are found in big cluster-like aggregates embedded in an organic material matrix. These aggregates were larger in size and denser in the case of AuNRs compared to similarly sized AuNPs. The presence of a higher number of elongated gold nanoparticles in the (pseudo)feces (Figure 2.6C-D) compared to spherical shaped gold nanoparticles (Figure 2.6A-B) further illustrates that shape-affects filtration and uptake of nanoparticles by *C. fluminea*.

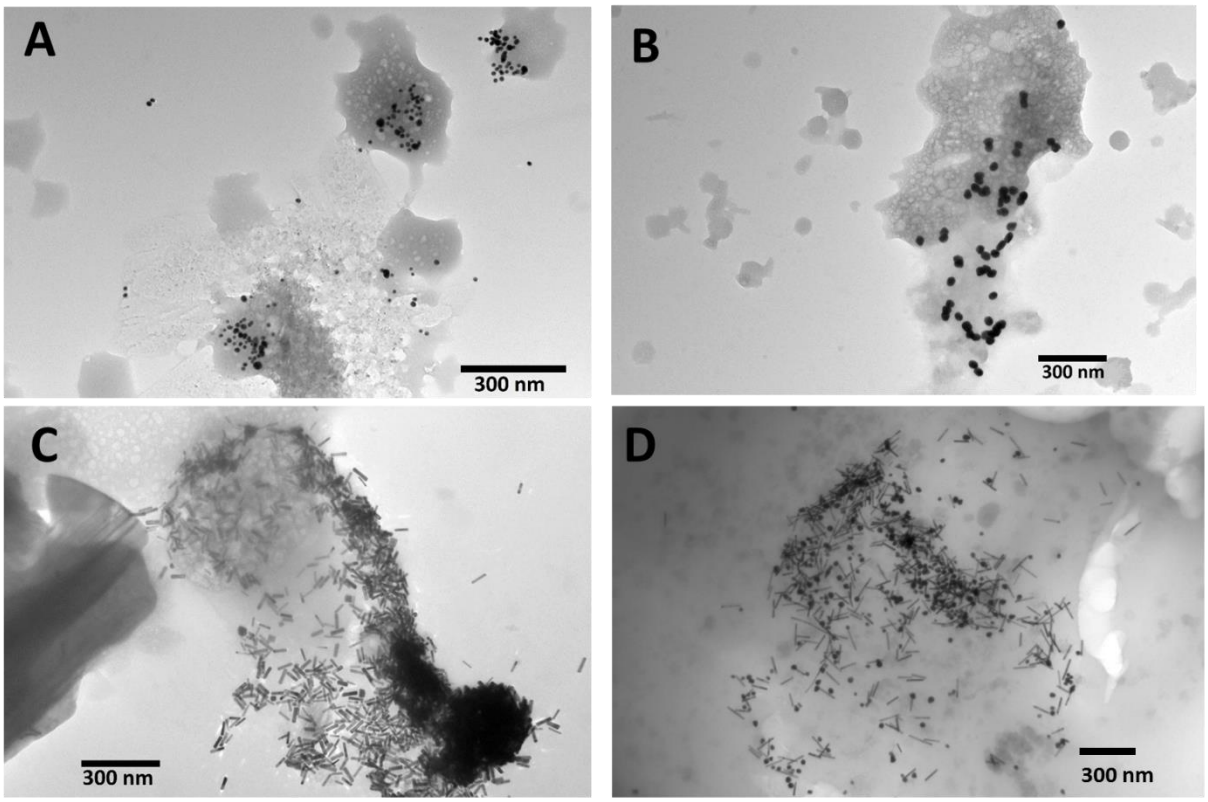

Figure 2.5. TEM images of AuNPs and AuNRs present in the clam's organic wastes. The samples are collected after experiment termination and prepared by drop cast technique A) 19 nm AuNP B) 45 nm AuNP C) AR4 AuNR D) AR8 AuNR

Toxicity assay results.

To investigate the possible nanotoxicity of AuNPs and AuNRs to *C. fluminea*, the activities of four different antioxidant enzymes and the levels of protein oxidative damage were analyzed in the gills and digestive gland of the clams at the end of the exposure. Together with peroxiredoxins, GPx and Cat are the main enzymes responsible for peroxide breakdown [62] and therefore they are considered major first-line antioxidants. No significant differences were detected for both Cat and GPx in all the different tissues

and exposure conditions, despite the fact that larger nanoparticles such as AR8 AuNR and 45 nm AuNPs exhibited higher clearance rates and biodeposition, as shown in Figure 2.6.

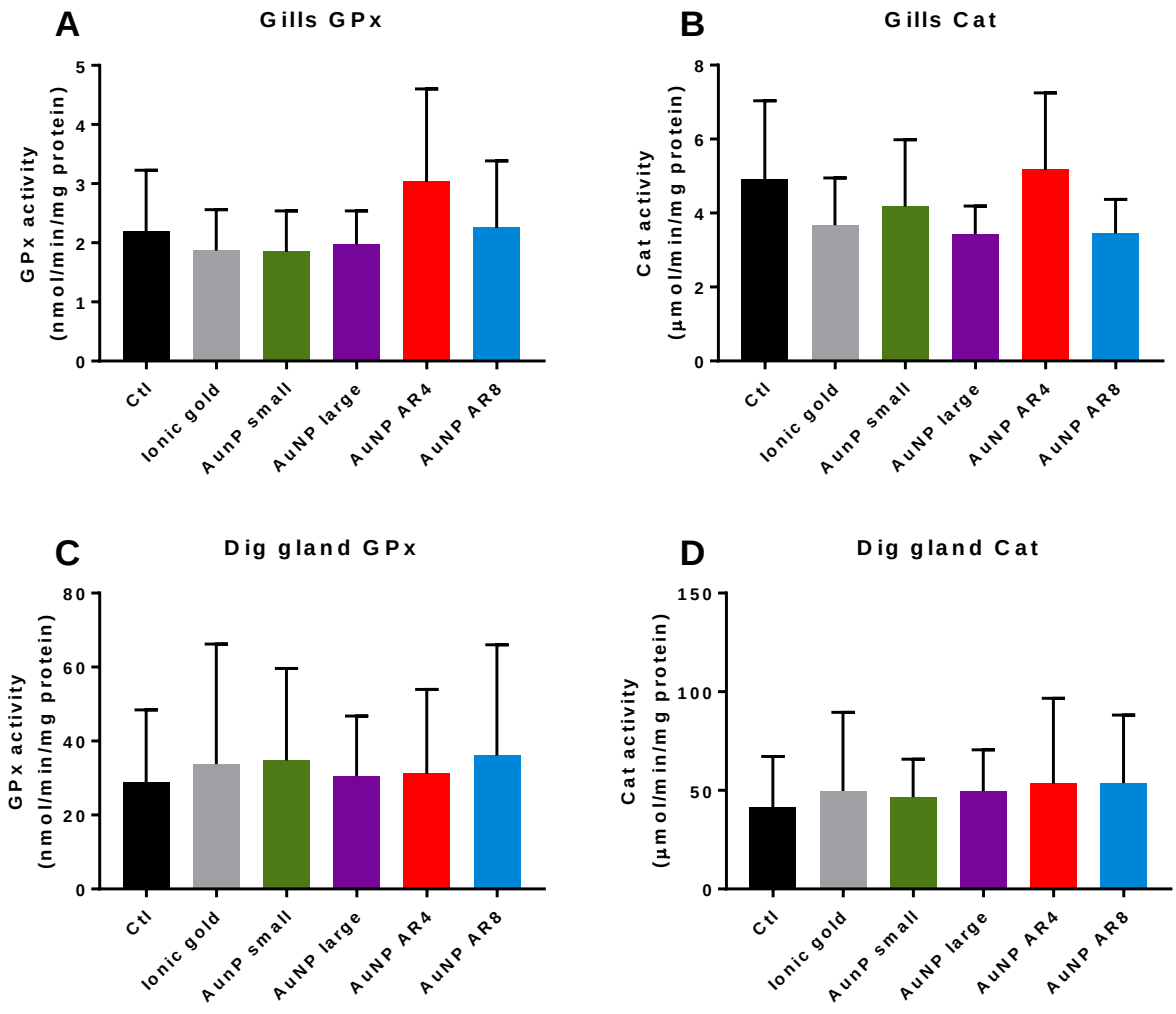

Figure 2.6. Activity of antioxidant enzymes related to peroxide breakdown in clams exposed to ionic gold and different types of gold nanoparticles. Activities of glutathione peroxidase (GPx, A and C) and catalase (Cat, B and D) were analyzed in the gills (left) and digestive gland (right). Data were analyzed by one-way ANOVA and Tukey's post hoc or Kruskal-Wallis and Dunn's post hoc tests, when appropriate. No significant differences were detected ($p > 0.05$, $n = 10$-12).

The activities of the thiol reductase enzymes GR and TrxR were also analyzed, as they are key antioxidant ancillary enzymes [62]. GR is responsible for the reduction of the oxidized form of glutathione and plays a role in peroxide breakdown mediated by GPx. Similarly, TrxR reduces the oxidized form of thioredoxin, which is an electron donor for peroxide breakdown by peroxiredoxins. As shown in Figure 2.7, GR activity decreased in the gills after exposure to AR4 and AR8 AuNRs (Figure 2.7A), but not in the digestive gland (Figure 2.7B). This result reflects the higher the number of elongated nanoparticles captured in the gills relative to the amounts transported into the digestive gland. Regarding TrxR activity, ionic gold had a strong inhibitory (80-90% inhibition) effect in both tissues, which was expected since many gold complexes are known inhibitors of this enzyme [63]. This same effect was detected in gills after exposure to Large (45 nm) AuNPs, AR4, and AR8 AuNRs (Figure 2.7C), but at lower levels (25-30% inhibition). The observed lack of inhibition of TrxR activity in the case of small (19 nm) AuNPs is consistent with the ICP-MS observations of lower concentration of 19 nm AuNP in the gills, Figure 2.3. In the digestive gland, only partial inhibition was detected in the digestive gland (30%) after exposure to AR8 AuNRs (Figure 2.7D), as TrxR activity was similar to both the control and ionic gold group. It should be noted that AR8 AuNRs had the highest rate of filtration and accumulation in the digestive gland and gills, Figure 2.3. Thus, observed partial inhibition can be correlated to the higher presence of AR8 AuNRs in these tissues.

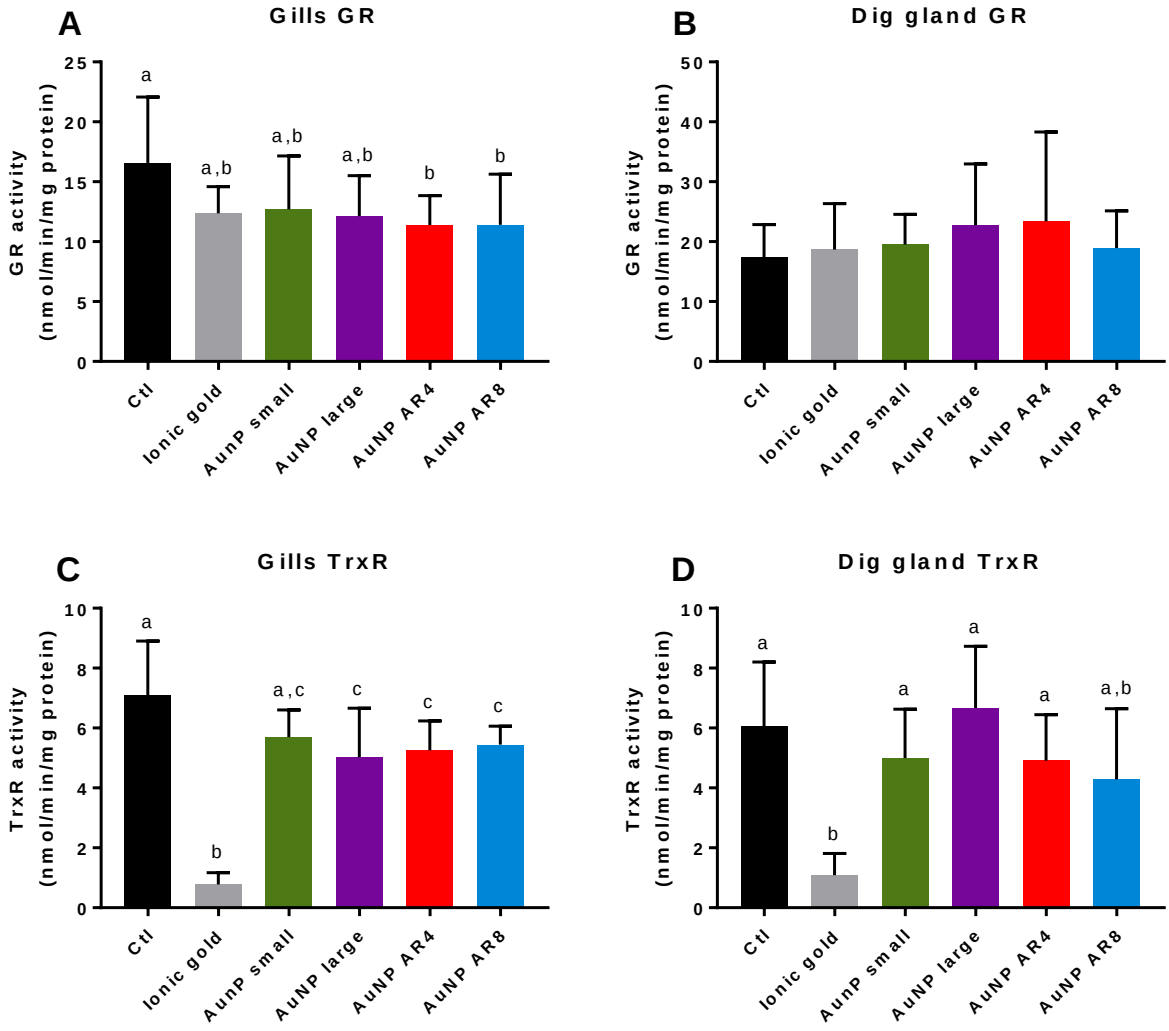

Figure 2.7. Activity of thiol reductase antioxidant enzymes in clams exposed to ionic gold and different types of gold nanoparticles. Activities of glutathione reductase (GR, A and C) and thioredoxin reductase (TrxR, B and D) were analyzed in the gills (left) and digestive gland (right). Data were analyzed by one-way ANOVA and Tukey's post hoc or Kruskal-Wallis and Dunn's post hoc tests, when appropriate. Groups not sharing letters are significantly different ($p<0.05$, n=10-12).

It is unclear if inhibition of GR and TrxR by the different gold nanoparticles was related to intracellular gold dissociation after nanoparticle uptake. BSA-coated nanoparticles were found in the shell and feces of the animals at the end of the exposure (Figures 2.4 and 2.5) while retaining their initial shapes, an indication of the high stability of these

nanomaterials. In addition, the mode of action for the TrxR inhibition by gold(I) and gold(III) complexes is not dependent on the release of ionic gold, but by the direct binding to the TrxR selenol group[63]. Due to the lack of a selenol group, GR activity is not as sensitive to gold exposure as TrxR, which is in accordance to our data. Nevertheless, GR and TrxR inhibition was evident in animals exposed to AuNR and to large (45 nm) AuNP, which were also the groups with the highest gold bioaccumulation in the digestive gland and gills (Figure 2.3).

To account for the role of oxidative damage as one of the mechanisms of toxicity for metal nanoparticles [64], protein oxidation in gills and digestive gland was assessed using fluorescent-labeling techniques. As shown in Figure 2.8, P-SH levels remained unaltered in the gills, but increased 76% in the digestive gland (Figure 2.8C), suggesting higher levels of reduced protein sulfhydryl groups. For P-CO levels, no significant effects were observed in both tissues. These data suggest a low reactivity and probably lower toxicity of BSA coated gold nanomaterials, as already shown in vitro with cell cultures [65]. Such increases in P-SH can be indicative of synthesis of sulfhydryl–containing proteins. For instance, metallothioneins are sulfhydryl-rich proteins with the ability to bind to and dispose gold [66, 67] and can be upregulated by AuNP exposure in other invertebrates.[31] Interestingly, the increase in P-SH levels was detected only in the digestive gland of clams exposed to small AuNP, which was the group with the lowest gold bioaccumulation (Figure 2.3). This may indicate that different signaling pathways related to cellular defenses and stress response could be activated depending not only on the size and type of gold nanomaterial, but also on their uptake and body burden, which remains to be elucidated.

Despite no signs of increased oxidative damage detected in this study, the inhibition of GR and TrxR by gold nanoparticles can cause further consequences to the organisms when exposed to additional stressors, what is usually the case when taking into consideration an environmental scenario. For instance, inhibition of GR and TrxR in the gills of brown mussels *Perna perna* and oysters *Crassostrea gigas* decreases their survival rate to quinone and peroxide exposure, as well as their *in vivo* peroxide breakdown rate [68, 69]. This is indicative of the importance of these enzymes for the maintenance of the cellular redox environment, cell function and survival. An interesting example of how these antioxidant enzymes can be associated with cellular function was found in oyster immune cells: depletion of glutathione and inhibition of GR and TrxR in hemocytes causes loss of important cellular functions associated with pathogen recognition and clearance [70], such as cellular adhesion, phagocytosis and oxidative burst. Additional studies with these AuNP and AuNR in the presence of temperature or hypoxic stress, pathogen exposure, or even other pro-oxidant chemicals, could help to clarify this scenario.

It is also important to note that this study focused only on the antioxidant system and protein oxidative damage to investigate the potential toxicity of these nanomaterials. Yet, different types of gold nanomaterials have caused other effects on bivalve species: loss of hemocyte or digestive cell lysosomal membrane integrity [71, 72]; changes on cellular element composition and tissue histological changes [73] and inflammation [74]. In addition, mitochondrial TrxR is known to be inhibited by gold complexes, as well as mitochondrial enzyme complexes [63]. In fact, the mitochondrial effects of nanoparticles in bivalves are still poorly understood, and apparently the mitochondrial

TrxR/peroxiredoxin system could be a target for gold nanomaterial in bivalves. Bivalve mitochondria were already shown to uptake and are sensitive to different nanoparticles, such as glass wool [75], silver [76], and zinc oxide [77], and have been considered an important target for nanotoxicity in bivalves.

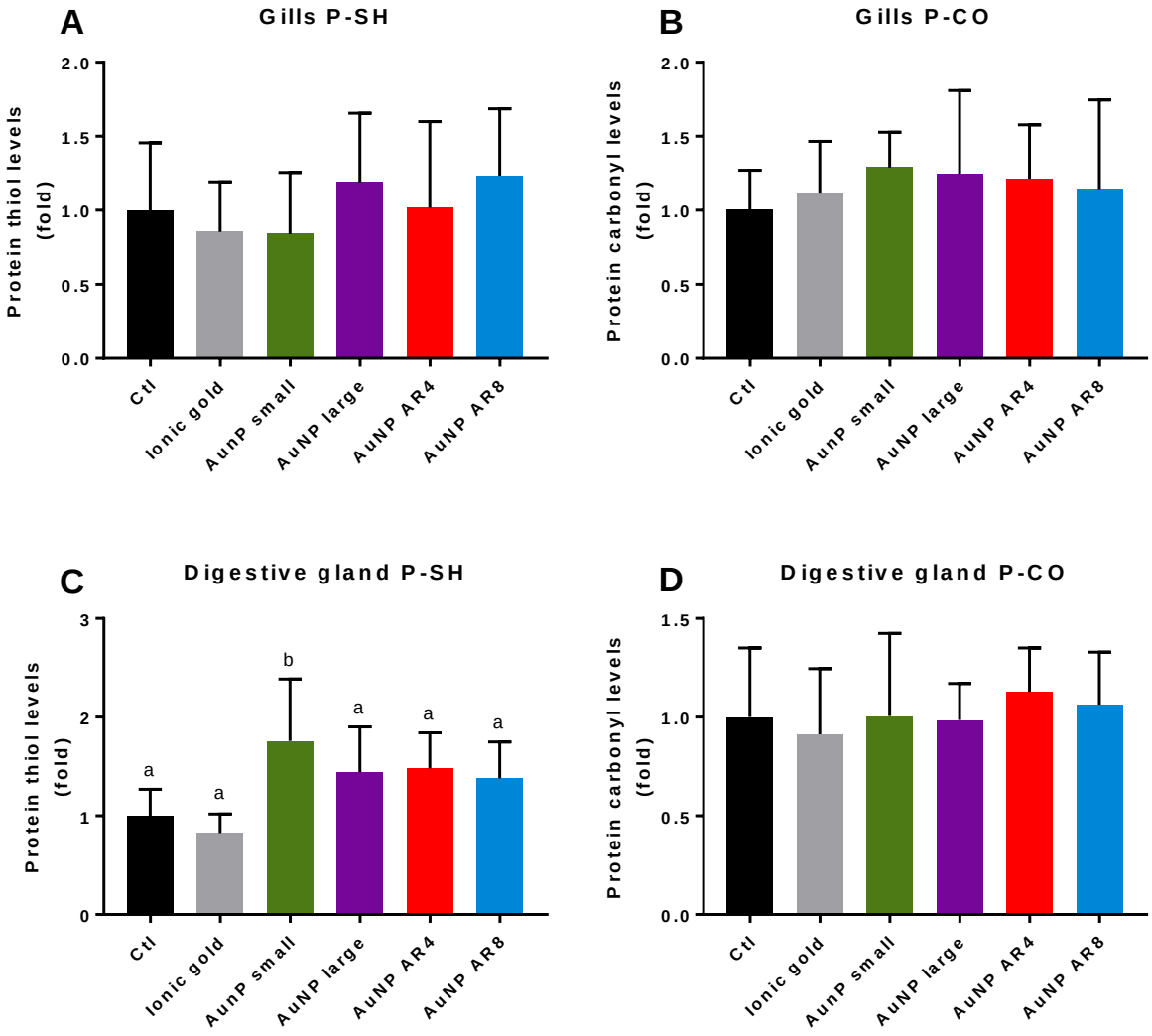

Figure 2.8. Protein damage in gills and digestive gland of clams exposed to ionic gold and different types of gold nanoparticles. The levels of reduced protein thiols (P-SH, A and C) and protein carbonyl groups (P-CO, B and D) were analyzed in the gills (left) and digestive gland (right). Data were analyzed by one-way ANOVA and Tukey's post hoc or Kruskal-Wallis and Dunn's post hoc tests, when appropriate. Groups not sharing letters are significantly different ($p<0.05$, n=9-12).

2.5 Conclusions

This study has shown that AR affects gold nanomaterial uptake and biodeposition by the filter feeder *C. fluminea*. To the best of our knowledge, this study was the first to investigate the impact of nanoparticle elongation on the fate and nanotoxity to *C. fluminea*, and establishing a mass distribution balance. As shown, on a mass basis the highest AR nanomaterials were retained more effectively than lower AR nanomaterials in the gills and digestive glands. On the basis of an equivolume sphere calculation it is apparent that elongated rods are filtered more effectively than equivolume spheres, while spherical BSA coated gold nanoparticles exhibited higher sorption onto the organic biolayer of the shells. This result suggests that the elongated rods are preferentially removed due to a better association with the gills or other tissues during the filter feeding process. Based on the analysis of antioxidant enzyme responses and protein oxidations, the toxicological impacts of nanoparticle uptake were generally minor, with a higher impact in the case of higher AR elongated nanorods, but other physiological consequences may not be ruled out.

2.6 References

1. Lin, D., et al., *Fate and transport of engineered nanomaterials in the environment.* Journal of Environmental Quality, 2010. **39**(6): p. 1896-1908.
2. Praetorius, A., M. Scheringer, and K. Hungerbühler, *Development of Environmental Fate Models for Engineered Nanoparticles□ A Case Study of TiO2 Nanoparticles in the Rhine River.* Environmental science & technology, 2012. **46**(12): p. 6705-6713.
3. Lowry, G.V., et al., *Environmental occurrences, behavior, fate, and ecological effects of nanomaterials: an introduction to the special series.* Journal of environmental quality, 2010. **39**(6): p. 1867-1874.
4. Cornelis, G., et al., *Fate and bioavailability of engineered nanoparticles in soils: a review.* Critical Reviews in Environmental Science and Technology, 2014. **44**(24): p. 2720-2764.
5. Dale, A.L., et al., *Modeling nanomaterial environmental fate in aquatic systems.* Environmental science & technology, 2015. **49**(5): p. 2587-2593.
6. Lowry, G.V., et al., *Long-term transformation and fate of manufactured Ag nanoparticles in a simulated large scale freshwater emergent wetland.* Environmental science & technology, 2012. **46**(13): p. 7027-7036.
7. Gottschalk, F., et al., *Modeled environmental concentrations of engineered nanomaterials (TiO2, ZnO, Ag, CNT, fullerenes) for different regions.* Environmental science & technology, 2009. **43**(24): p. 9216-9222.

8. Aiken, G.R., H. Hsu-Kim, and J.N. Ryan, *Influence of dissolved organic matter on the environmental fate of metals, nanoparticles, and colloids.* Environmental science & technology, 2011. **45**(8): p. 3196-3201.

9. Hoecke, K.V., et al., *Fate and effects of CeO2 nanoparticles in aquatic ecotoxicity tests.* Environmental science & technology, 2009. **43**(12): p. 4537-4546.

10. Yang, P. and C.M. Lieber, *Nanorod-superconductor composites: a pathway to materials with high critical current densities.* Science, 1996. **273**(5283): p. 1836.

11. Park, W.I., et al., *Fabrication and electrical characteristics of high-performance ZnO nanorod field-effect transistors.* Applied Physics Letters, 2004. **85**(21): p. 5052-5054.

12. Dickerson, E.B., et al., *Gold nanorod assisted near-infrared plasmonic photothermal therapy (PPTT) of squamous cell carcinoma in mice.* Cancer letters, 2008. **269**(1): p. 57-66.

13. Law, M., et al., *Nanowire dye-sensitized solar cells.* Nature materials, 2005. **4**(6): p. 455-459.

14. Wan, Q., et al., *Fabrication and ethanol sensing characteristics of ZnO nanowire gas sensors.* Applied Physics Letters, 2004. **84**(18): p. 3654-3656.

15. Kolmakov, A., et al., *Detection of CO and O2 using tin oxide nanowire sensors.* Advanced Materials, 2003. **15**(12): p. 997-1000.

16. *consumer product inventories*. Woodrow Wilson international center for scholars: Washington DC.

17. Cho, W.-S., et al., *Comparison of gene expression profiles in mice liver following intravenous injection of 4 and 100nm-sized PEG-coated gold nanoparticles.* Toxicology letters, 2009. **191**(1): p. 96-102.

18. Merchant, B., *Gold, the noble metal and the paradoxes of its toxicology.* Biologicals, 1998. **26**(1): p. 49-59.

19. Daniel, M.-C. and D. Astruc, *Gold nanoparticles: assembly, supramolecular chemistry, quantum-size-related properties, and applications toward biology, catalysis, and nanotechnology.* Chemical reviews, 2004. **104**(1): p. 293-346.

20. Goodman, C.M., et al., *Toxicity of gold nanoparticles functionalized with cationic and anionic side chains.* Bioconjugate chemistry, 2004. **15**(4): p. 897-900.

21. Hauck, T.S., A.A. Ghazani, and W.C. Chan, *Assessing the effect of surface chemistry on gold nanorod uptake, toxicity, and gene expression in mammalian cells.* Small, 2008. **4**(1): p. 153-159.

22. Wang, S., et al., *Challenge in understanding size and shape dependent toxicity of gold nanomaterials in human skin keratinocytes.* Chemical physics letters, 2008. **463**(1-3): p. 145-149.

23. Schaeublin, N.M., et al., *Does shape matter? Bioeffects of gold nanomaterials in a human skin cell model.* Langmuir, 2012. **28**(6): p. 3248-3258.

24. Pan, Y., et al., *Size-dependent cytotoxicity of gold nanoparticles.* Small, 2007. **3**(11): p. 1941-1949.

25. Metch, J.W., et al., *Metagenomic analysis of microbial communities yields insight into impacts of nanoparticle design.* Nature nanotechnology, 2018: p. 1.

26. Sousa, R., C. Antunes, and L. Guilhermino. *Ecology of the invasive Asian clam Corbicula fluminea (Müller, 1774) in aquatic ecosystems: an overview*. in *Annales de Limnologie-International Journal of Limnology*. 2008. EDP Sciences.

27. Baun, A., et al., *Ecotoxicity of engineered nanoparticles to aquatic invertebrates: a brief review and recommendations for future toxicity testing.* Ecotoxicology, 2008. **17**(5): p. 387-395.

28. Doherty, F.G., *The Asiatic clam, Corbicula spp., as a biological monitor in freshwater environments.* Environmental monitoring and assessment, 1990. **15**(2): p. 143-181.

29. McLeod, P.B., S.N. Luoma, and R.G. Luthy, *Biodynamic modeling of PCB uptake by Macoma balthica and Corbicula fluminea from sediment amended with activated carbon.* Environmental Science & Technology, 2007. **42**(2): p. 484-490.

30. Hull, M.S., et al., *Filter-feeding bivalves store and biodeposit colloidally stable gold nanoparticles.* Environmental science & technology, 2011. **45**(15): p. 6592-6599.

31. Pan, J.-F., et al., *Size dependent bioaccumulation and ecotoxicity of gold nanoparticles in an endobenthic invertebrate: the Tellinid clam Scrobicularia plana.* Environmental pollution, 2012. **168**: p. 37-43.

32. Renault, S., et al., *Impacts of gold nanoparticle exposure on two freshwater species: a phytoplanktonic alga (Scenedesmus subspicatus) and a benthic bivalve (Corbicula fluminea).* Gold bulletin, 2008. **41**(2): p. 116-126.

33. Guo, Z., et al., *Shape separation of colloidal gold nanoparticles through salt-triggered selective precipitation.* Chemical Communications, 2011. **47**(14): p. 4180-4182.

34. Albanese, A. and W.C. Chan, *Effect of gold nanoparticle aggregation on cell uptake and toxicity.* ACS nano, 2011. **5**(7): p. 5478-5489.

35. Jana, N.R., L. Gearheart, and C.J. Murphy, *Wet chemical synthesis of high aspect ratio cylindrical gold nanorods.* The Journal of Physical Chemistry B, 2001. **105**(19): p. 4065-4067.

36. Turkevich, J., P.C. Stevenson, and J. Hillier, *A study of the nucleation and growth processes in the synthesis of colloidal gold.* Discussions of the Faraday Society, 1951. **11**: p. 55-75.

37. Frens, G., *Controlled nucleation for the regulation of the particle size in monodisperse gold suspensions.* Nature, 1973. **241**(105): p. 20-22.

38. Murphy, C.J., et al., *Gold nanorod crystal growth: from seed-mediated synthesis to nanoscale sculpting.* Current Opinion in Colloid & Interface Science, 2011. **16**(2): p. 128-134.

39. Nikoobakht, B. and M.A. El-Sayed, *Preparation and growth mechanism of gold nanorods (NRs) using seed-mediated growth method.* Chem. Mater, 2003. **15**(10): p. 1957-1962.

40. Abtahi, S., et al., *Sulfate-Mediated End-to-End Assembly of Gold Nanorods.* Langmuir, 2017. **33**(6): p. 1486-1495.

41. Tebbe, M., et al., *Colloidally stable and surfactant-free protein-coated gold nanorods in biological media.* ACS applied materials & interfaces, 2015. **7**(10): p. 5984-5991.

42. Lawson, C.L. and R.J. Hanson, *Solving least squares problems*. Vol. 15. 1995: Siam.

43. Miekeley, N., M.D. Carneiro, and C.P. da Silveira, *How reliable are human hair reference intervals for trace elements?* Science of the total environment, 1998. **218**(1): p. 9-17.

44. Fahey, R.C., et al., *Analysis of biological thiols: quantitative determination of thiols at the picomole level based upon derivatization with monobromobimanes and separation by cation-exchange chromatography.* Analytical biochemistry, 1981. **111**(2): p. 357-365.

45. Vemula, V., Z. Ni, and M. Fedorova, *Fluorescence labeling of carbonylated lipids and proteins in cells using coumarin-hydrazide.* Redox biology, 2015. **5**: p. 195-204.

46. Carlberg, I. and B. Mannervik, *[59] Glutathione reductase.* Methods in enzymology, 1985. **113**: p. 484-490.

47. Wendel, A., *[44] Glutathione peroxidase.* Methods in enzymology, 1981. **77**: p. 325-333.

48. Aebi, H., *[13] Catalase in vitro.* Methods in enzymology, 1984. **105**: p. 121-126.

49. Arnér, E.S., L. Zhong, and A. Holmgren, *Preparation and assay of mammalian thioredoxin and thioredoxin reductase.* Methods in enzymology, 1999. **300**: p. 226-239.

50. Link, S., M. Mohamed, and M. El-Sayed, *Simulation of the optical absorption spectra of gold nanorods as a function of their aspect ratio and the effect of the medium dielectric constant.* The Journal of Physical Chemistry B, 1999. **103**(16): p. 3073-3077.

51. Jain, P.K., et al., *Calculated absorption and scattering properties of gold nanoparticles of different size, shape, and composition: applications in biological imaging and biomedicine.* J. Phys. Chem. B, 2006. **110**(14): p. 7238-7248.

52. Schneider, L., H.J. Schmid, and W. Peukert, *Influence of particle size and concentration on the second-harmonic signal generated at colloidal surfaces.* Applied Physics B: Lasers and Optics, 2007. **87**(2): p. 333-339.

53. Boltovskoy, D., I. Izaguirre, and N. Correa, *Feeding selectivity of Corbicula fluminea (Bivalvia) on natural phytoplankton.* Hydrobiologia, 1995. **312**(3): p. 171-182.

54. Atkinson, C.L., et al., *Suspended material availability and filtration–biodeposition processes performed by a native and invasive bivalve species in streams.* Hydrobiologia, 2011. **667**(1): p. 191-204.

55. Way, C.M., et al., *Dynamics of filter feeding in Corbicula fluminea (Bivalvia: Corbiculidae).* Canadian Journal of Zoology, 1990. **68**(1): p. 115-120.

56. Rubenstein, D.I. and M. Koehl, *The mechanisms of filter feeding: some theoretical considerations.* The American Naturalist, 1977. **111**(981): p. 981-994.

57. Barton, L.E., et al., *Theory and methodology for determining nanoparticle affinity for heteroaggregation in environmental matrices using batch measurements.* Environmental Engineering Science, 2014. **31**(7): p. 421-427.

58. Maeda, H. and Y. Maeda, *Direct observation of brownian dynamics of hard colloidal nanorods.* Nano letters, 2007. **7**(11): p. 3329-3335.

59. Han, Y., et al., *Brownian motion of an ellipsoid.* Science, 2006. **314**(5799): p. 626-630.

60. Lehner, D., H. Lindner, and O. Glatter, *Determination of the translational and rotational diffusion coefficients of rodlike particles using depolarized dynamic light scattering.* Langmuir, 2000. **16**(4): p. 1689-1695.

61. Sharma, V., K. Park, and M. Srinivasarao, *Colloidal dispersion of gold nanorods: Historical background, optical properties, seed-mediated synthesis, shape separation and self-assembly.* Materials Science and Engineering: R: Reports, 2009. **65**(1-3): p. 1-38.

62. Sies, H., C. Berndt, and D.P. Jones, *Oxidative stress.* Annual review of biochemistry, 2017. **86**: p. 715-748.

63. Rigobello, M.P., et al., *Gold complexes inhibit mitochondrial thioredoxin reductase: consequences on mitochondrial functions.* Journal of inorganic biochemistry, 2004. **98**(10): p. 1634-1641.

64. Huang, Y.-W., M. Cambre, and H.-J. Lee, *The Toxicity of Nanoparticles Depends on Multiple Molecular and Physicochemical Mechanisms.* International journal of molecular sciences, 2017. **18**(12): p. 2702.

65. Khullar, P., et al., *Bovine serum albumin bioconjugated gold nanoparticles: synthesis, hemolysis, and cytotoxicity toward cancer cell lines.* The Journal of Physical Chemistry C, 2012. **116**(15): p. 8834-8843.

66. Sharma, R., *Role of metallothionein in cellular uptake and disposition of gold sodium thiomalate.* European journal of drug metabolism and pharmacokinetics, 1984. **9**(1): p. 57-64.

67. Schmitz, G., et al., *The binding of gold (I) to metallothionein.* Journal of inorganic biochemistry, 1980. **12**(4): p. 293-306.

68. Trevisan, R., et al., *Antioxidant deficit in gills of Pacific oyster (Crassostrea gigas) exposed to chlorodinitrobenzene increases menadione toxicity.* Aquatic toxicology, 2012. **108**: p. 85-93.

69. Trevisan, R., et al., *The biological importance of glutathione peroxidase and peroxiredoxin backup systems in bivalves during peroxide exposure.* Marine environmental research, 2014. **101**: p. 81-90.

70. Mello, D.F., et al., *How important are glutathione and thiol reductases to oyster hemocyte function?* Fish & shellfish immunology, 2015. **46**(2): p. 566-572.

71. Tedesco, S., et al., *Oxidative stress and toxicity of gold nanoparticles in Mytilus edulis.* Aquatic Toxicology, 2010. **100**(2): p. 178-186.

72. Jimeno-Romero, A., et al., *Lysosomal responses to different gold forms (nanoparticles, aqueous, bulk) in mussel digestive cells: a trade-off between the toxicity of the capping agent and form, size and exposure concentration.* Nanotoxicology, 2017. **11**(5): p. 658-670.

73. Sellami, B., et al., *Toxicity assessment of ZnO-decorated Au nanoparticles in the Mediterranean clam Ruditapes decussatus.* Aquatic Toxicology, 2017. **188**: p. 10-19.

74. Volland, M., et al., *Citrate gold nanoparticle exposure in the marine bivalve Ruditapes philippinarum: uptake, elimination and oxidative stress response.* Environmental Science and Pollution Research, 2015. **22**(22): p. 17414-17424.

75. Koehler, A., et al., *Effects of nanoparticles in Mytilus edulis gills and hepatopancreas–a new threat to marine life?* Marine environmental research, 2008. **66**(1): p. 12-14.

76. Gomes, T., et al., *Differential protein expression in mussels Mytilus galloprovincialis exposed to nano and ionic Ag.* Aquatic toxicology, 2013. **136**: p. 79-90.

77. Trevisan, R., et al., *Gills are an initial target of zinc oxide nanoparticles in oysters Crassostrea gigas, leading to mitochondrial disruption and oxidative stress.* Aquatic toxicology, 2014. **153**: p. 27-38.

78. Weber, C.I., *Methods for measuring the acute toxicity of effluents and receiving waters to freshwater and marine organisms*. 1991: Environmental Monitoring Systems Laboratory, Office of Research and Development, US Environmental Protection Agency Cincinnati, Ohio.

2.7 Supporting Information

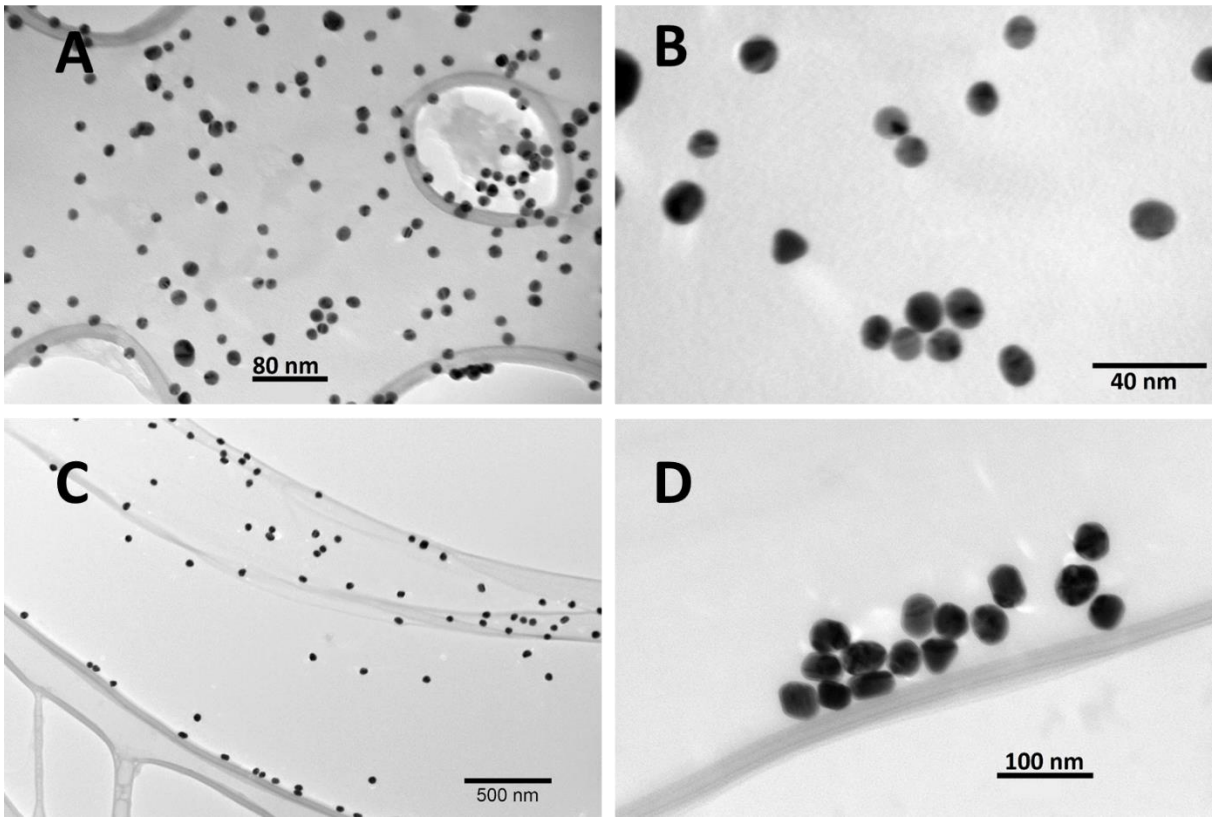

Figure 2.S1. TEM images of synthesized citrate coated A&B) Small GNPs (19 nm) C&D) large GNPs (45 nm)

Table 2.S1. Preparation of synthetic fresh water using reagent grade chemicals[78]

	Reagent Added (mg/L)[1]				Approximate Final Water Quality		
	$NaHCO_3$	$CaSO_4\ 2H_2O$	$MgSO_4$	KCl	pH[2]	Hardness[3]	Alkalinity[3]
Very soft	12	7.5	7.5	0.5	6.4-6.8	10-13	10-13
Soft	48	30	30	2	7.2-7.6	40-48	30-35
Moderately hard	96	60	60	4	7.4-7.8	80-100	57-64
Hard	192	120	120	8	7.6-8.0	160-180	110-120
Very Hard	384	240	240	16	8.0-8.4	280-320	225-245

1. Add reagent grade chemicals to deionized water.
2. Approximate equilibrium pH after 24 h of aeration.
3. Expressed as mg $CaCO_3$/L.

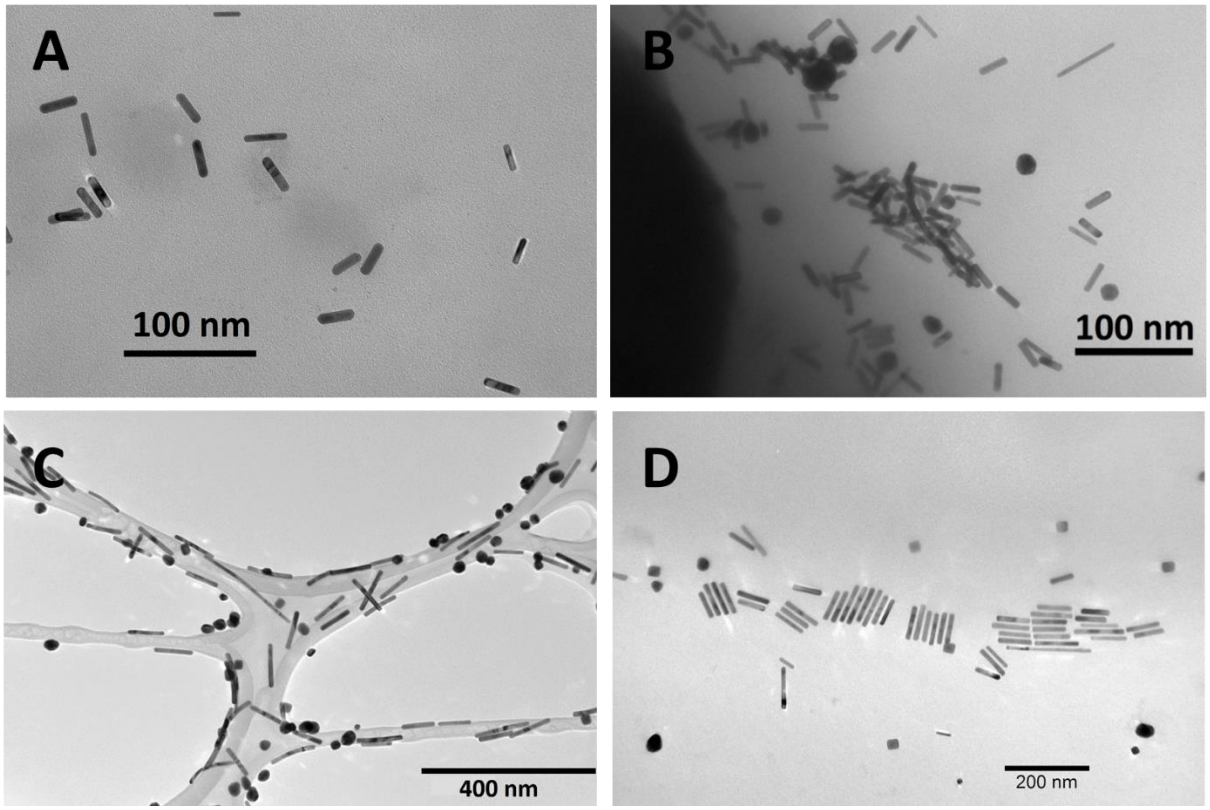

Figure 2.S2. TEM images of synthesized A&B) CTAB coated AR4 AuNRs C&D) CTAB/BDAC AR8 AuNRs

Table 2.S2. Final adsorption percentage of gold nanoparticles adsorbed to the biolayer on the top of the shells observed in control 2 microcosms. These values are calculated by converting the plasmon band absorption intensity drop to number concentration of nanoparticles using Lambert-Beer's law.

	Overall Adsorption percentage on clam shells
Small GNPs (19 nm)	34%
Large GNPs (45 nm)	24%
AR4 AuNRs	18%
AR8 AuNRs	12%

First order clearance kinetic rate modeling:

$\frac{-d[C]}{dt} = k[C]$ After integration $\ln(\frac{[C]}{[C_0]}) = -kt$

Where:

[C]= Elemental gold concentration at time t mg/L

$[C_0]$= Elemental gold concentration at time zero (2 mg/L)

k= First order clearance rate (1/hr)

Equivolume spherical diameter conversion for a cylinder shape:

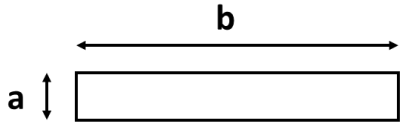

$V_c = (\frac{\pi a^2}{4})b$

$V_c = V_s \Longrightarrow d = \sqrt[3]{\frac{3a^2 b}{2}}$

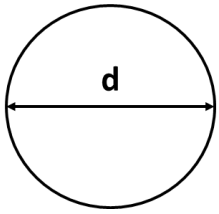

$V_s = \frac{\pi d^3}{6}$

	Diameter a (nm)	Length b (nm)	Equivolume spherical diameter d (nm)
AR4 AuNR	11	43	16
AR8 AuNR	10	84	19

Overall gold nanoparticles mass balance in exposure experiments

Initial gold mass = Initial suspension column volume x Initial gold concentration = 40 mL x 2 mg/L= 80 µg

	ICPMS readings (microgram gold/gram wet tissue)			
	Shells	Other tissues	Gills and digestive glands	Pseudo feces
19 nm AuNP	8.18	7.11	50.04	213.82
45 nm AuNP	4.80	16.35	108.88	329.20
AR4 AuNR	6.52	18.30	136.00	144.70
AR8 AuNR	3.82	25.15	178.47	323.27

	Tissue mass per 2 clams (mg)			
	Shells	Other tissues	Gills and digestive glands	Pseudo feces
19 nm AuNP	3377.6	265	375.4	15.2
45 nm AuNP	3288	258.5	346.8	13.1
AR4 AuNR	3253.2	264.3	354.6	18.4
AR8 AuNR	3013.8	245.6	358.1	11.6

	Elemental gold mass (micro gram)						
	Shells	Other tissues	Gills and digestive glands	Pseudo feces	Summation	Clearance percentage out of initial 80 μg	Mass balance accuracy
19 nm AuNP	27.64	1.88	18.78	3.25	51.56	73%	$=\frac{51.56}{80\frac{73}{100}}\times 100=88.3\%$
45 nm AuNP	15.78	4.22	37.76	4.31	62.08	84%	$=\frac{62.08}{80\frac{84}{100}}\times 100=92.4\%$
AR4 AuNR	21.21	4.84	48.23	2.66	76.94	100%	$=\frac{76.94}{80\frac{100}{100}}\times 100=96.2\%$
AR8 AuNR	11.52	6.18	63.91	3.75	85.36	100%	$=\frac{85.36}{80\frac{100}{100}}\times 100=106.7\%$

	Mass percentage (micro gram gold/80 micro gram initial gold)*100%			
	Shells	Other tissues	Gills and digestive glands	Pseudo feces
19 nm AuNP	34.02	2.32	23.12	4.06
45 nm AuNP	18.3	4.9	43.78	5.39
AR4 AuNR	23.9	5.45	54.34	3.33
AR8 AuNR	12.29	6.59	68.17	4.69

Chapter 3. Sulfate Mediated End-to-End Assembly of Gold Nanorods

S.M.H. Abtahi,[1, 2, 3] Nathan D. Burrows,[4] Fred A. Idesis,[4] Catherine J. Murphy,[4] Navid B. Saleh,[5] and Peter J. Vikesland[1, 2, 3]*

[1.]Virginia Tech, Department of Civil and Environmental Engineering, Blacksburg, VA, USA

[2.]Virginia Tech, Institute for Critical Technology and Applied Science (ICTAS) Center for Sustainable Nanotechnology (VTSuN), Blacksburg, VA, USA

[3.]Center for the Environmental Implications of Nanotechnology (CEINT), Duke University, Durham, NC, USA

[4.]Department of Chemistry, University of Illinois at Urbana-Champaign, 600 S. Matthews Ave., Urbana, IL, 61801, USA

[5.]The University of Texas at Austin, Department of Civil, Architectural and Environmental Engineering, Austin, TX 78712, USA

Langmuir, **2017**, *33* (6), pp 1486–1495

DOI: 10.1021/acs.langmuir.6b04114

Publication Date (Web): January 18, 2017

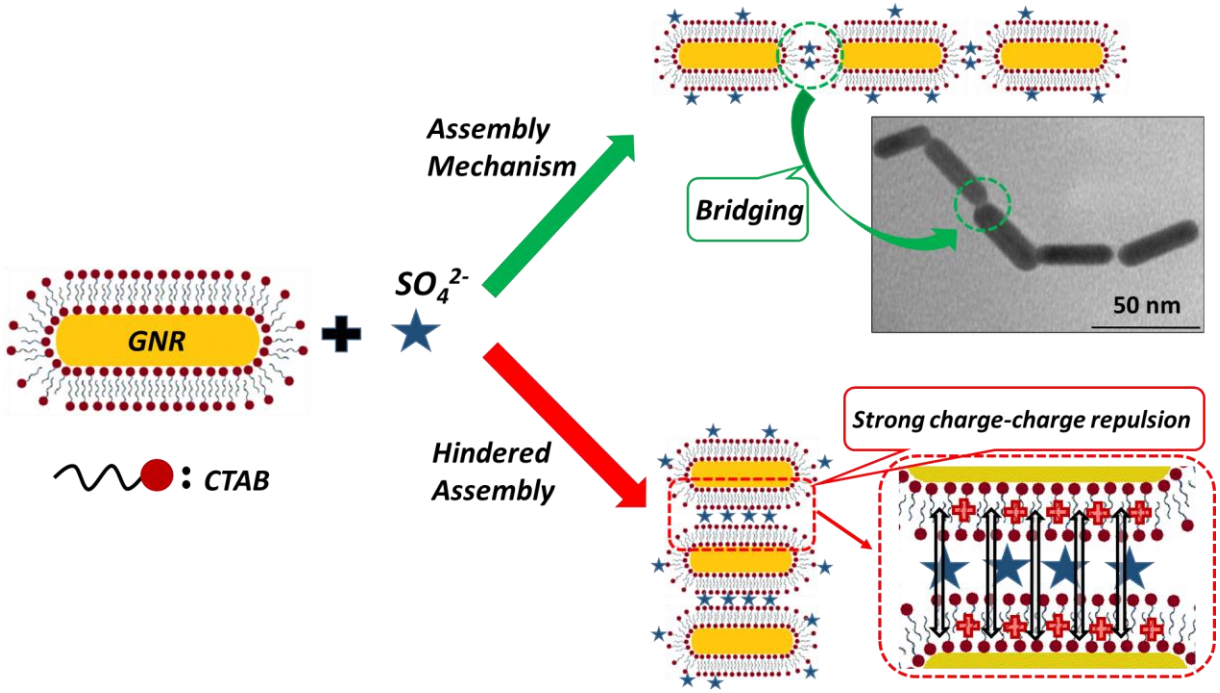

3.1 Abstract

There is interest in the controlled aggregation of gold nanorods (GNRs) for the production of extended nanoassemblies. Prior studies have relied upon chemical modification of the GNR surface to achieve a desired final aggregate structure. Herein, we illustrate that control of electrolyte composition can facilitate end-to-end assembly of cetyltrimethylammonium bromide (CTAB) coated GNRs. By adjusting either the sulfate anion concentration or the exposure time it is possible to connect GNRs in chain-like assemblies. In contrast, end-to-end assembly was not observed in control experiments using monovalent chloride salts. We attribute the end-to-end assembly to the localized association of sulfate with exposed quaternary ammonium head groups of CTAB at the nanorod tip. To quantify the assembly kinetics, visible-near infrared extinction spectra

were collected over a pre-determined time period and the colloidal behavior of the GNR suspensions was interpreted using plasmon band analysis. Transmission electron microscopy and atomic force microscopy results support the conclusions reached via plasmon band analysis and the colloidal behavior is consistent with Derjaguin-Landau-Verwey-Overbeek (DLVO) theory.

3.2 Introduction

Gold and silver nanoparticles are of interest because of the unique electro-optical properties (e.g., localized surface plasmon resonance [LSPR])[1-5] that originate from the collective behavior of their surface electrons. In the case of LSPR, visible-infrared light interacts with a noble metal nanoparticle smaller than the incident radiation wavelength[1, 6] and resonant interactions result in the coherent oscillation of the nanoparticle's conduction band electrons. The LSPR is a function of the local dielectric environment as well as the size and shape of the nanoparticle.[1, 2, 7-12] A peak is observed in the extinction spectrum at the wavelength where the frequency of the incident light matches the frequency at which the conduction electrons oscillate.[1, 6, 8, 13] Peak location is dependent on nanoparticle size and shape and shifts to longer wavelengths with an increase in particle size.[14-16] Anisotropic nanoparticles, such as gold nanorods (GNRs), exhibit two different plasmon oscillations: one along the short axis (the transverse oscillation) and the other along the long axis (the longitudinal oscillation).[5, 17-21] Each of these oscillations exhibits its own specific LSPR band. The transverse LSPR band typically occurs at a wavelength between 500-550 nm and shifts to longer wavelengths with an increase in diameter. The longitudinal LSPR band is aspect ratio (AR: length/diameter) sensitive, and occurs at longer wavelengths for

GNRs with higher AR.[19, 22, 23] The extinction (absorbance + scattering) of these peaks is linearly related to the concentration of nanoparticles in suspension. Changes in the number concentration, the AR, or the local dielectric environment can be detected by a change in extinction or by the shift of these two plasmon peaks.[14, 24]

The electro-optical properties of GNRs can be significantly altered by nanoparticle assembly. We use the term controlled assembly to refer either to end-to-end, end-to-side, or side-by-side assembly.[25, 26] End-to-end assemblies couple the longitudinal plasmon preferentially and are of particular interest for sensing technologies that rely on large electric fields.[26-28] Extended end-to-end GNR assemblies have previously been produced by manipulation of GNR surface chemistry,[29-32] by alteration of the chemistry of the solution in which the GNRs are suspended,[13, 30, 33, 34] by applying polystyrene and surface enhanced Raman spectroscopy (SERS) markers,[35] or by attachment of pH-responsive DNA[36] to the GNR surface. Side-by-side assemblies of GNRs have been prepared by cysteine conjugated GNRs in the presence of lead[37] and in adiptic acid treated GNR suspensions.[38] Interchangeable end-to-end and side-by-side assemblies of GNRs have been prepared by addition of tetrahydrofuran,[39] dithiol polyethylene glycol,[40] bifunctional poly(ethylene glycol, PEG),[26] or antibodies,[25] onto GNR surfaces where the final assembled configuration is controlled by the concentration of the organic molecule. Each of these approaches requires extensive nanoparticle functionalization.

In this work, we illustrate a simple method in which sulfate ions are used to facilitate end-to-end GNR assembly in aqueous suspension. The coordinating activity of sulfate anions enables conversion of >80% of well-dispersed GNRs in a suspension into

extended structures (chains of dimers, trimers, tetramers, etc.). For these experiments we used cetyltrimethylammonium bromide capped GNRs (CTAB-GNRs) because CTAB is the *de facto* GNR capping agent in GNR synthesis[5, 18, 41-44]. Visible-near infrared (Vis-NIR) extinction spectra were collected over a pre-determined time period and the colloidal behavior of the GNR suspensions was interpreted using plasmon band analysis. Transmission electron microscopy (TEM) and atomic force microscopy (AFM) were used to further characterize the samples. These results are self-consistent and can be explained by Derjaguin-Landau-Verwey-Overbeek (DLVO) theory.

3.3 Materials and Methods

Preparation of CTAB-coated GNRs

GNRs were synthesized via the well-established seed-mediated surfactant-directed method.[45, 46] In brief, 3-4 nm spherical gold nanoparticle seeds were produced through the reduction of chloroauric acid ($HAuCl_4 \bullet 3H_2O$, 2.5×10^{-4} M in aqueous solution) in the presence of CTAB ($[CH_3(CH_2)_{15}N(CH_3)_3]^+Br^-$, 0.10 M) by addition of ice-cooled and freshly prepared sodium borohydride ($NaBH_4$, 0.010 M). A rapid color change to light brown indicated seed formation. In the next step, GNRs of aspect ratio 4.4 were grown from an aqueous growth solution consisting of 0.10 M CTAB, 5.0×10^{-4} M $HAuCl_4$, 8.0×10^{-5} M $AgNO_3$, and 5.5×10^{-4} M ascorbic acid, which became colorless upon acid addition. Once the gold seeds were added to the growth solution, it changed color to dark brown over 1-2 h indicating GNR formation. Spheres, cubes, and other shaped byproducts (minor component) and chemical byproducts were removed by centrifugation (25 min at 8000 rcf), repeated 5 times with pellet

resuspension in 800 μM CTAB, yielding CTAB-GNRs. ICP-MS measurements indicated that the GNR stock had a 41.0±0.3 mg/L atomic gold concentration. Accordingly, a concentration of 2.1×10^{14} GNRs/L was calculated based on the density of gold (19.3 g/cm^3)[47] and the TEM determined average GNR size of 28.8 ± 0.1 nm length and 6.6 ± 0.1 nm diameter.

End-to-end linkage of CTAB-GNRs in $CaSO_4$ and $MgSO_4$

Suspensions of CTAB-GNRs (1.1×10^{14} GNRs/L) were incubated over a range of $CaSO_4$ and $MgSO_4$ concentrations (1-5 mM) for 24 h. To initiate an experiment, CTAB-GNRs were washed by centrifugation (20 min at 11000 rcf) and 90% of the supernatant was replaced with DI water, followed by bath sonication for 1 min. The resuspended GNRs were readily dispersed and were colloidally stable 2-. This step removed excess CTAB from the GNR suspension. Following a second centrifugation step (20 min at 11000 rcf), 90% of the supernatant was replaced with a given $CaSO_4$ or $MgSO_4$ solution followed by 1 min of bath sonication. The GNR suspensions were then transferred to Vis-NIR cuvettes that were used for colloidal stability monitoring over 24 h. During the first hour, 10 min sampling intervals were used. Subsequently, one-hour intervals were used for the remaining 23 h. Vis-NIR extinction spectra were collected between 400-1200 nm. TEM samples were prepared after 3 and 10 h of exposure to salt solutions. To quantitatively capture the temporal changes in the extinction of the GNR suspensions, individual peaks within the Vis-NIR spectrum were fit with Lorentzian distributions[48, 49] using Grams/AI software (Thermo-Fisher, Waltham, MA).

TEM samples were prepared by submerging 200 mesh carbon film coated copper grids in a given GNR suspension and then fast dried by putting the grid on top of

an 80 °C hot plate for 10 s. An AFM sample was prepared following 3 h GNR exposure to salt solutions. Negatively charged AFM metal specimen discs were submerged vertically in a petri dish containing 5 mL GNR suspension sample for half an hour followed by DI water rinsing prior to AFM measurement.

Instrumentation

An Agilent Cary 5000 spectrometer (Santa Clara, CA) and disposable polystyrene cuvettes (10 mm pathlength) were used for Vis-NIR extinction spectroscopy. TEM images were taken using a Philips (Thermo-Fisher, Waltham, MA) EM420 conventional transmission electron microscope. A Malvern (Worcestershire, UK) Zetasizer Nano-ZS was used for electrophoretic mobility measurements. A Bruker (Billerica, MA) Nanoscope IIIa AFM and Ted Pella (Redding, CA) 15 mm metal specimen discs were used for atomic force microscopy. Sonication was performed using a Fisher Scientific FS20H bath sonicator. DI water (18.2 MΩ) was produced by a Thermo Scientific Barnstead nanopure system.

3.4 Results and Discussion

GNR characterization

The GNRs were characterized via TEM, Vis-NIR spectroscopy, electrophoretic mobility, and ICP-MS measurements. The GNRs (inset to Figure 3.1; Figure 3.S1) have an average length of 28.8 ± 0.1 nm and an average diameter of 6.6 ± 0.1 nm (the noted errors reflect 95% confidence interval based on n = 2104 measurements obtained using ImageJ). These relative dimensions result in an average AR of 4.4 ± 0.1. These GNRs exhibit a transverse extinction band at 518 nm and a longitudinal band at 756 nm, which

are the expected wavelengths for GNRs of these dimensions.[45] The electrophoretic mobility of the GNRs in DI water was determined to be +3.58 µm•cm/V•s. Applying Henry's equation while considering Smoluchowski equation for Henry's constant resulted in calculated ζ-potential of +45.6 mV. We note that for the GNRs and the range of ionic strengths tested in this study, κa (is 1/Debye length in 1/nm and "a" is the nanoparticle effective diameter in nm) varies from 4.09 to 9.13. Because $\kappa a >> 1$, the Smoluchowski equation is an acceptable 2- approximation of ζ-potential (details and example calculations are presented in SI; pages 2-3).[50, 51], [52] These values are consistent with the literature and illustrate that the rods have a positive effective surface charge.[44, 51]

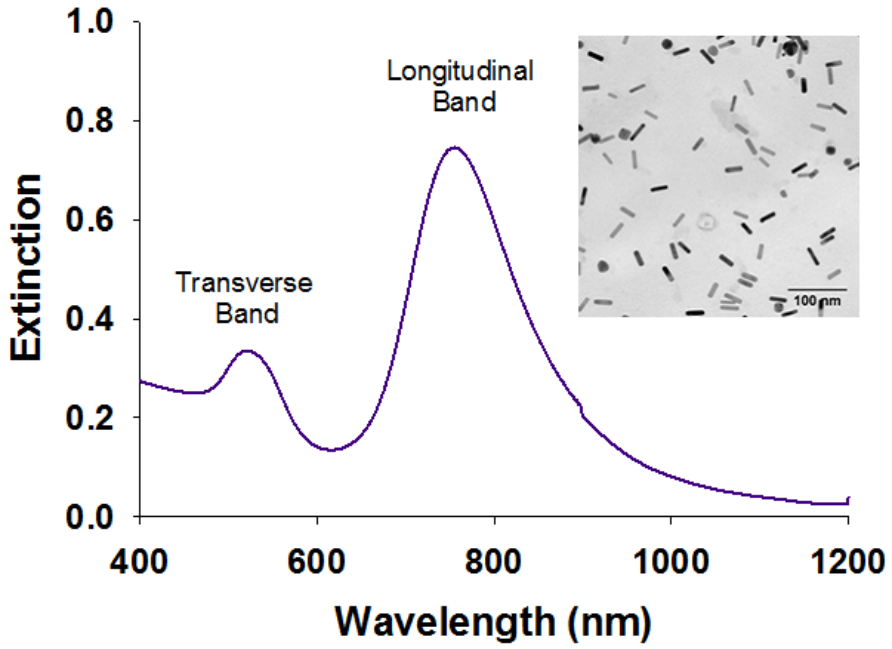

Figure 3.1. Vis-NIR extinction spectrum for the synthesized CTAB-GNRs after centrifugal purification and washing. Inset: Transmission electron micrograph of CTAB-GNRs.

End-to-end assembly of CTAB-coated gold nanorods in $CaSO_4$ and $MgSO_4$

The in situ development of GNR assemblies was probed via Vis-NIR extinction spectroscopy. It has been shown previously that during side-to-side and end-to-side assemblies, the extinction of the initial transverse LSPR band increases and the band slightly red shifts to higher wavelengths; while the extinction of the longitudinal band decreases and blue shifts to lower wavelengths, thus resulting in the convergence of the two bands.[26] The calculated extinction intensity change versus incident light wavelength and corresponding transverse and longitudinal bands of these two assemblies are presented in Table 3.S3 and Figure 3.S6. These calculations are developed based on our experiment parameters while employing extended Mie theory modeling. In end-to-end assembly the bands behave quite differently. For aggregates with this configuration, neither the transverse nor the longitudinal band shifts; however, the extinction of the longitudinal band significantly decreases as the total average length of the GNR chain increases. Under these conditions, a third plasmon band appears at wavelengths larger than that of the original longitudinal band, Figure 3.S5. Because of extended plasmonic coupling this new plasmon band red shifts to longer and longer wavelengths as the GNR chain length increases.[22, 26, 53-55]

To evaluate the aggregation behavior of the GNRs, CTAB-GNR suspensions were exposed to 1, 2, and 5 mM $CaSO_4$ or $MgSO_4$. We observed salt concentration dependent changes in the visual characteristics of the suspensions. In the presence of

DI water the suspension is brownish in color, while at higher salt concentrations the color darkens. At a salt concentration of 5 mM the colloidal stability of the suspension was lost within 24 h (Figure 3.S2). As illustrated in representative plots for 2 mM $CaSO_4$ and 2 mM $MgSO_4$ (Figure 3.2) there are readily observable declines in the intensities of both the transverse and longitudinal bands and additional bands appear at longer wavelengths. Such behavior is consistent with the previously described end-to-end aggregation process. Qualitatively similar results were observed at the other salt concentrations.

To quantify the declines in peak intensity we plotted the change in extinction for both the transverse and longitudinal bands for each salt concentration. As shown in Figure 3.2C-F, a sharp drop in the longitudinal peak intensity was observed within the first hour of exposure of the GNRs to all concentrations of $CaSO_4$ and $MgSO_4$, accompanied by a slower decrease in intensity over the next 23 h. In contrast, the transverse band intensity did not change as noticeably. To interpret the temporal changes in the longitudinal and transverse bands we fitted our collected data using a simple second order aggregation model[56, 57] (details are presented in the SI; page 4):

$$\frac{d[rod]}{dt} = -k[rod]^2 \quad (1)$$

Where [rod] is the number concentration of individual, fully dispersed rods and *k* is the observed second order rate constant. Other more complex aggregation models may be more appropriate for this system due to its complexity; however, our purpose in using this model is to capture the differential behavior of the two extinction bands. Number concentration-based rate constants and associated 95% confidence intervals for single

CTAB-GNRs in the presence of $CaSO_4$ and $MgSO_4$ are presented in Table 3.1. We note that for 5 mM $CaSO_4$ the second order model did not fit the collected data as well as it did for other experimental conditions. We attribute this behavior to the more rapid aggregation observed with $CaSO_4$ and the greater degree of colloidal instability.

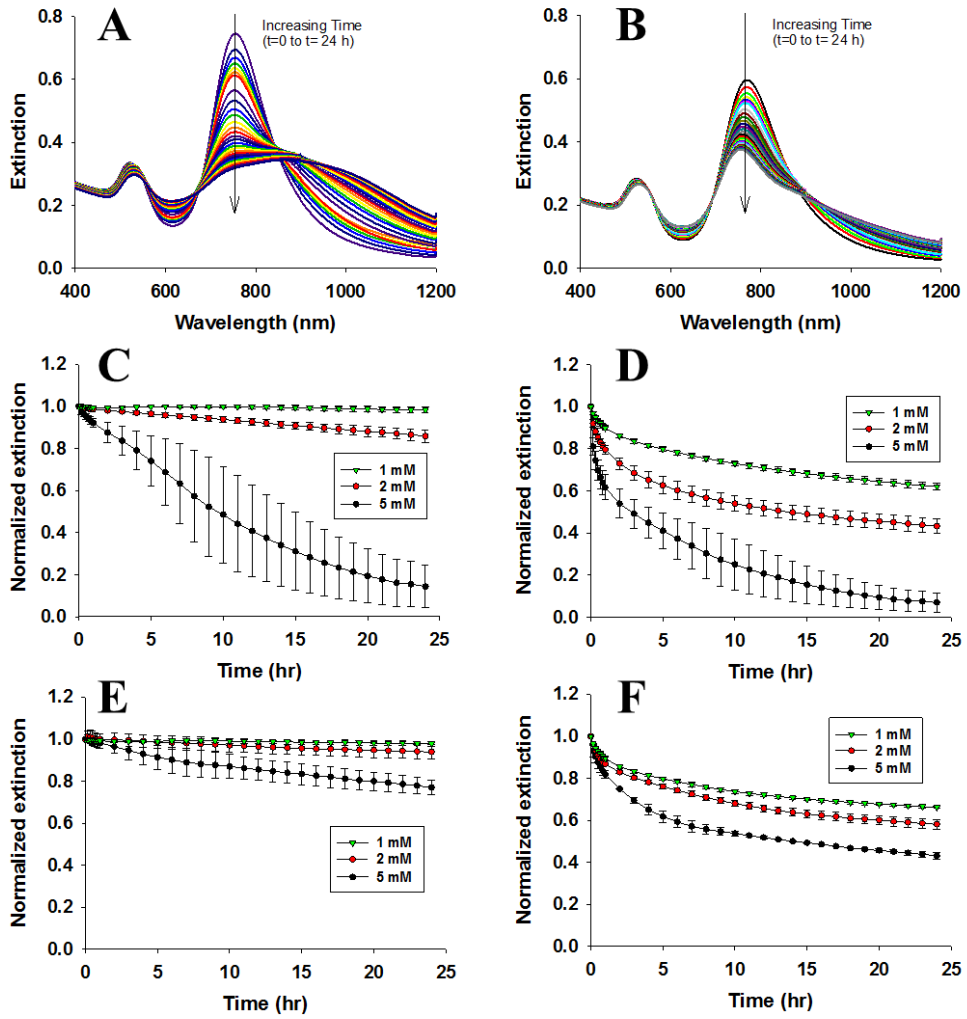

Figure 3.2. Vis-NIR extinction spectra of 1.1×1014 GNRs/L exposed to A) 2 mM CaSO4 and B) 2 mM MgSO4 from zero hours (red spectra) to 24 hours (blue spectra). Changes in the average normalized transverse band and longitudinal band extinction maxima of CTAB-GNRs (1.1×1014 GNRs/L) in 1-5 mM CaSO4 and MgSO4 solutions as a function of exposure time. (C) Transverse band-CaSO4 (D) Longitudinal band-CaSO4 (E) Transverse band-MgSO4 (F) Longitudinal band- MgSO4.

Table 3.1. Second order number concentration rate constants ($\frac{L}{1.07\times10^{14}(goldnanorods).\ S}$) for single CTAB-GNRs in the presence of different concentrations of CaSO4 and MgSO4. Both the changes in the transverse band and the longitudinal band are provided. Errors are reported at the ±95% confidence intervals.

Salt Concentration	Transverse band		Longitudinal band	
(mM)	$CaSO_4$	$MgSO_4$	$CaSO_4$	$MgSO_4$
1	0.0006 ± 0.0001	0.0007 ± 0.0001	0.025 ± 0.0020	0.019 ± 0.0021
2	0.0065 ± 0.0000	0.0032 ± 0.0001	0.05 ± 0.0051	0.028 ± 0.0026
5	0.22 ± 0.049	0.012 ± 0.0006	0.49 ± 0.072	0.051 ± 0.0053

An increase in ionic strength significantly increased the rate at which the GNRs assembled. In all cases, the rate of change of the longitudinal band was greater than that of the transverse band (Table 3.1). Over the 24 h period that the GNRs were exposed to 1 mM and 2 mM of $CaSO_4$ and $MgSO_4$ there was minimal change in the transverse band intensity, while simultaneously there was a 40-60% decline in the longitudinal band intensity. If the assemblies were colloidally unstable 2- and were precipitating out of suspension and leaving only single GNRs behind then the rate constants for the change in the transverse and longitudinal bands of single GNRs should be equal (Table 3.S1 and Figure 3.S3). However, the much slower change in the transverse band relative to the longitudinal band supports the conclusion that the GNRs are assembling into extended structures. In end-to-end nanoparticle assembly the transverse band is not expected to shift, while the longitudinal band will decrease in intensity and red-shift.

Following exposure of the GNRs to $CaSO_4$ or $MgSO_4$ a new shoulder with an extinction maximum at a wavelength greater than the longitudinal band appears. The

intensity of this shoulder increases and red-shifts to longer wavelengths over time and at increased salt concentrations. Formation of this shoulder is consistent with the assembly of GNRs to produce new structures with elongated AR (i.e., end-to-end assemblies). Past studies have illustrated that chain-like assemblies of GNRs display the formation of an extinction band at longer wavelengths compared to individual rods.[25, 26, 30, 34] The peak wavelength is strongly related to the number of linked rods and shifts to longer wavelengths as the chains become increasingly extended over time.

TEM and AFM images consistent with formation of end-to-end assemblies are shown in Figure 3.3. Both the TEM and AFM images illustrate the formation of end-to-end linkages. The AFM images unlike the TEM images were collected *in situ* without sample drying. Observation of an extended end-to-end assembly in the AFM image supports the argument that the presence of these assemblies in the TEM images is not necessarily a result of drying mediated artifacts. TEM images taken at different times and salt concentrations suggest that the end-to-end chains of GNRs grow longer over time and with an increase in ionic strength (Figure 3.3B-C, Figure 3.S4).

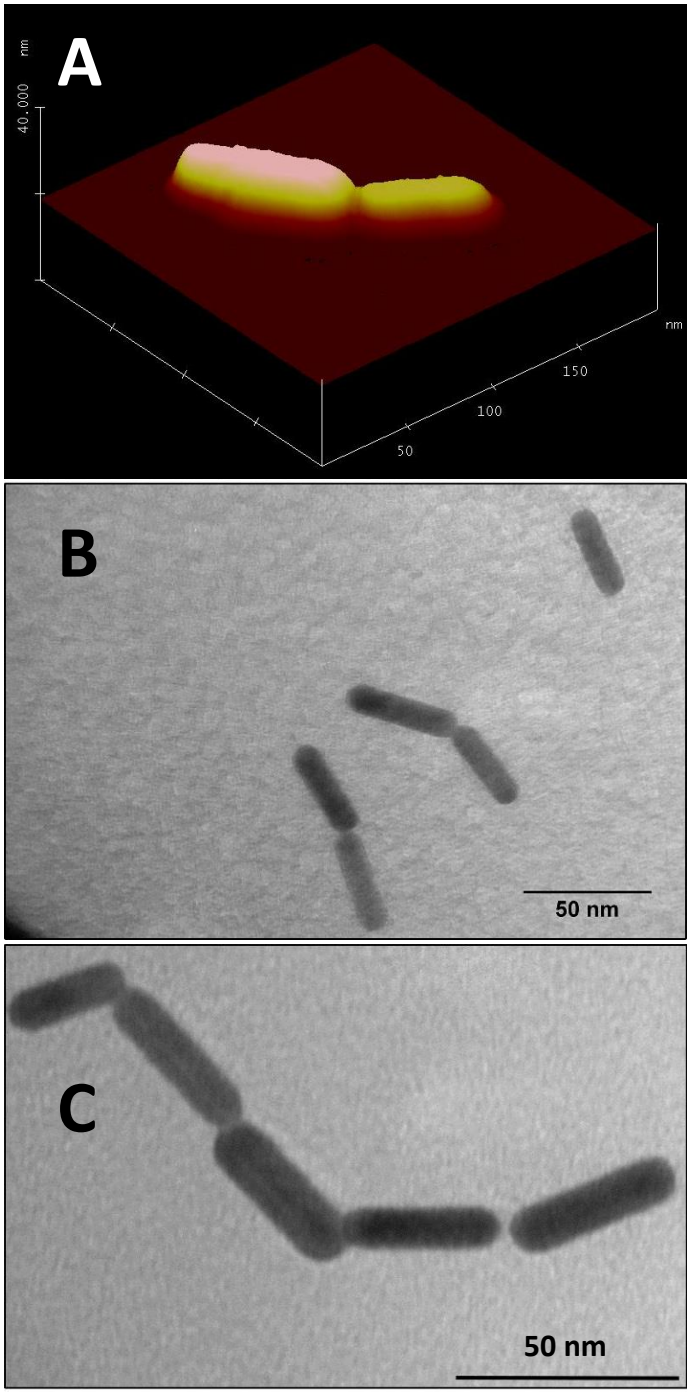

Figure 3.3. A) Representative AFM image of CTAB-GNRs after 3 h exposure to 2 mM CaSO4, B) TEM image of CTAB-GNRs after 3 h exposure to 2 mM CaSO4, C) TEM image of CTAB-GNRs after 10 h exposure to 2 mM CaSO4.

Extinction spectra peak fitting

Prior studies have established that there is a linear relationship between the peak wavelength location and AR.[22, 58]Theoretical peak wavelengths for end-to-end GNR assemblies of different length can be estimated by application of extended Mie theory (see SI for details).[22, 58-61] Knowing the physical and chemical properties of the GNRs and the solution chemistry employed herein, we were able to calculate the expected location of the extinction band for each end-to-end configuration (see SI for details of calculations). Our GNRs have an AR of 4.4, therefore the calculated λ_{max} values for dimer (AR=8.8), trimer (AR=13.2), and tetramer (AR=17.6) end-to-end linked AuNRs are 860, 965, and 1070 nm, respectively (Figure 3.4A). These values are qualitatively similar to those theoretically calculated for end-to-end assemblies of GNRs of similar AR.

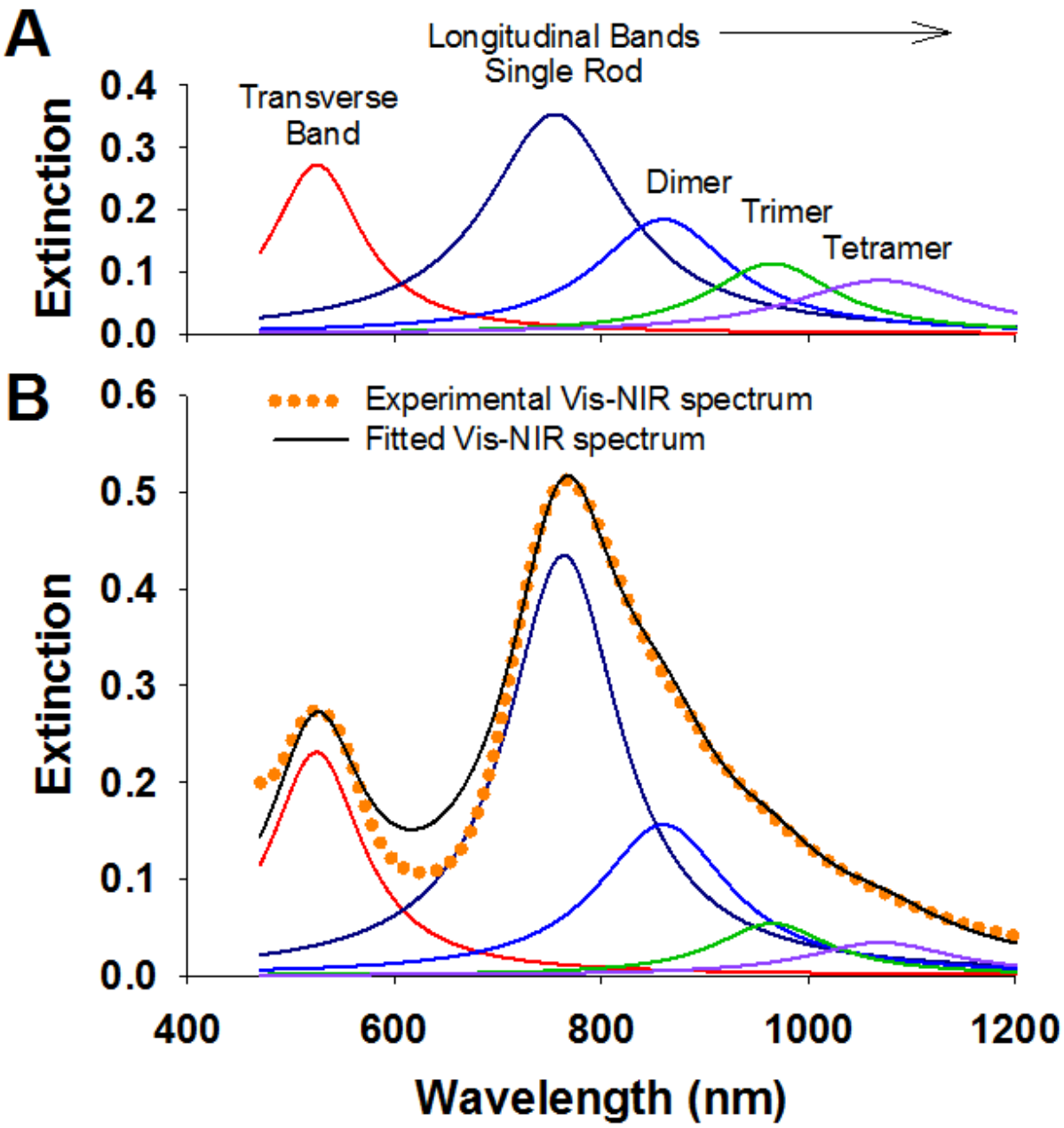

Figure 3.4. A) Plasmon band wavelengths of different GNR end-to-end assemblies as calculated by extended Mie theory. B) Exemplary Figure 3.illustrating quality of fit for experimental vs. fitted Vis-NIR spectrum for GNRs exposed to 5 mM MgSO4 after 1 hr. The magnitudes of individual extinction bands are illustrated.

Based upon these wavelengths we used a non-linear least squares iterative[62] procedure (within GRAMS/AI) to fit the collected Vis-NIR spectra for each experiment as the summation of five separate Lorentzian bands that correspond to the transverse band and the longitudinal band for single, dimer, trimer, and tetramer GNRs. Lorentzian distribution can be explained as a Fourier-transform of exponentially decaying oscillations[63]. The extended Mie modeling that is used in this study to calculate the extinction intensity changes versus incident light wavelength and to locate plasmon bands of different end-to-end assemblies is a Lorentzian function in nature[22] (refer to SI page 7 for details). As a result Lorentzian distribution has been applied for curve fitting. In this exercise, the center of each peak is fixed while the amplitude (height) and width are unknown parameters. Using this constrained fitting approach, we are able to fit and reproduce the collected Vis-NIR spectra quite readily (Figure 3.4B). By fitting each of the spectra collected over the course of an experiment we can probe the relative numbers of single, dimer, trimer, and tetramer assemblies present at any time. Figure 3.5 illustrates the temporal changes in each Lorentzian distribution band for the $CaSO_4$ experiments, while the results for the $MgSO_4$ experiments are shown in Figure 3.S7.

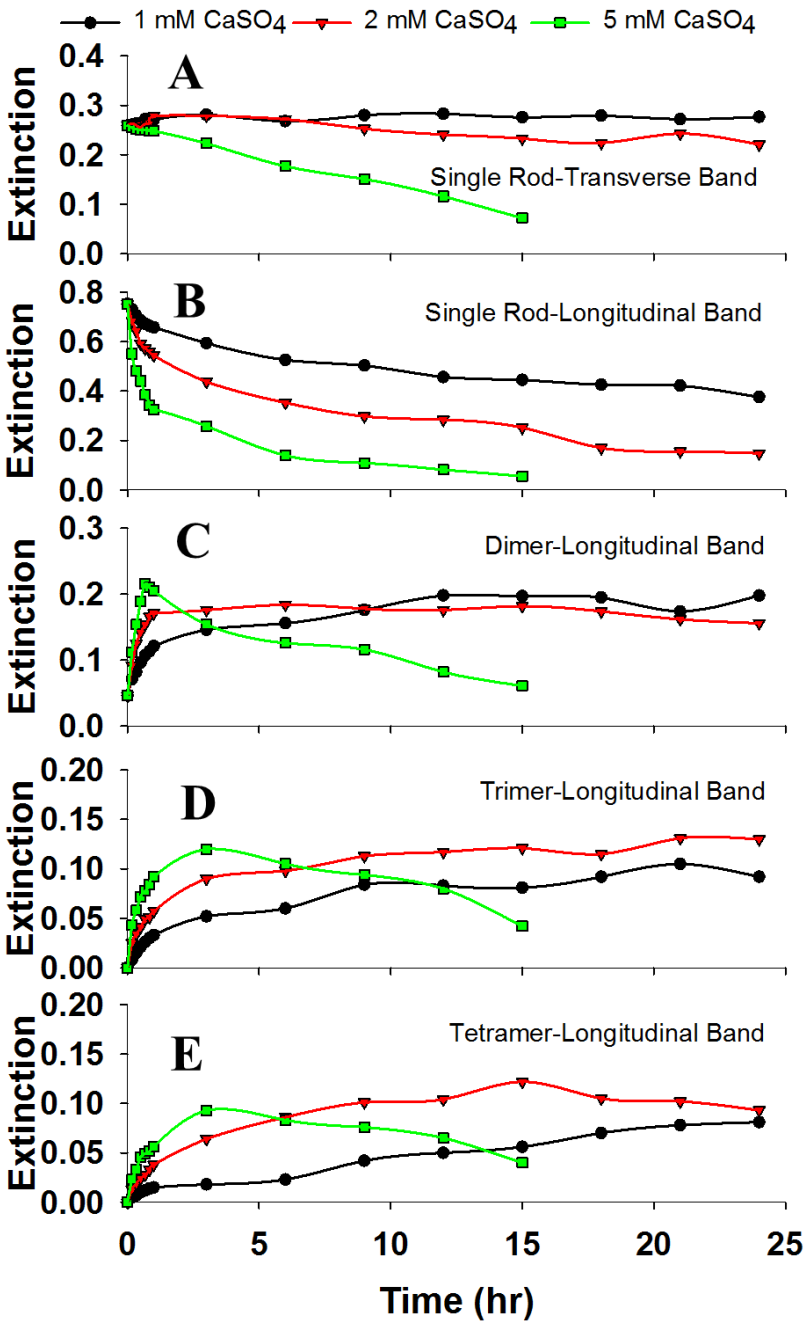

Figure 3.5. Extinction intensities of different Lorentzian distribution band end-to-end assemblies of GNRs exposed to three different CaSO4 concentrations A) Transverse bands of single rod B) Longitudinal bands of single rod C) Longitudinal bands of dimer D) Longitudinal bands of trimer E) Longitudinal bands of tetramer

With an increase in salt concentration increasing numbers of GNRs participate in end-to-end assembly and there is a concomitant decrease in the extinction of the

longitudinal band that represents single GNRs (Figure 3.5B). At 1 and 2 mM $CaSO_4$, the extinction of the dimer band at 860 nm increases rapidly and then plateaus, while at 5 mM it increases and then decreases with time (Figure 3.5C). At 5 mM $CaSO_4$, the dimer, trimer, and tetramer extinction intensities rapidly increase but then decrease over extended time. These results collectively show that at high salt concentrations the end-to-end GNRs assemblies that are formed initially, grow further to be colloidally unstable 2-, and finally undergo precipitation. This precipitation trend is consistent with visual observation of large dark pellets at the bottom of the sample cuvette (Figure 3.S2).

The validity of our curve fitting technique was studied by analyzing 36 TEM images taken from one sample (GNRs exposed to 2 mM $CaSO_4$) at three different time periods (3, 10, and 24 h). A total of 270 GNRs were counted via TEM image analysis. Figure 3.6 shows the change in percentage of these assemblies as a function of time. As expected, the length of the end-to-end assemblies generally increase over time. As an example, after 3 h almost 50% of GNRs are in the dimer form and no tetramers were found; but after 24 h 50% of GNRs are in the tetramer form while only 12% single GNRs were observed. Because of the potential for drying mediated artifacts and the potential effects of the TEM substrate on aggregate formation the results presented in Figure 3.6 cannot be directly compared to the plasmon band analyses; however, the general trend is the same with longer and longer assemblies forming with extended time.

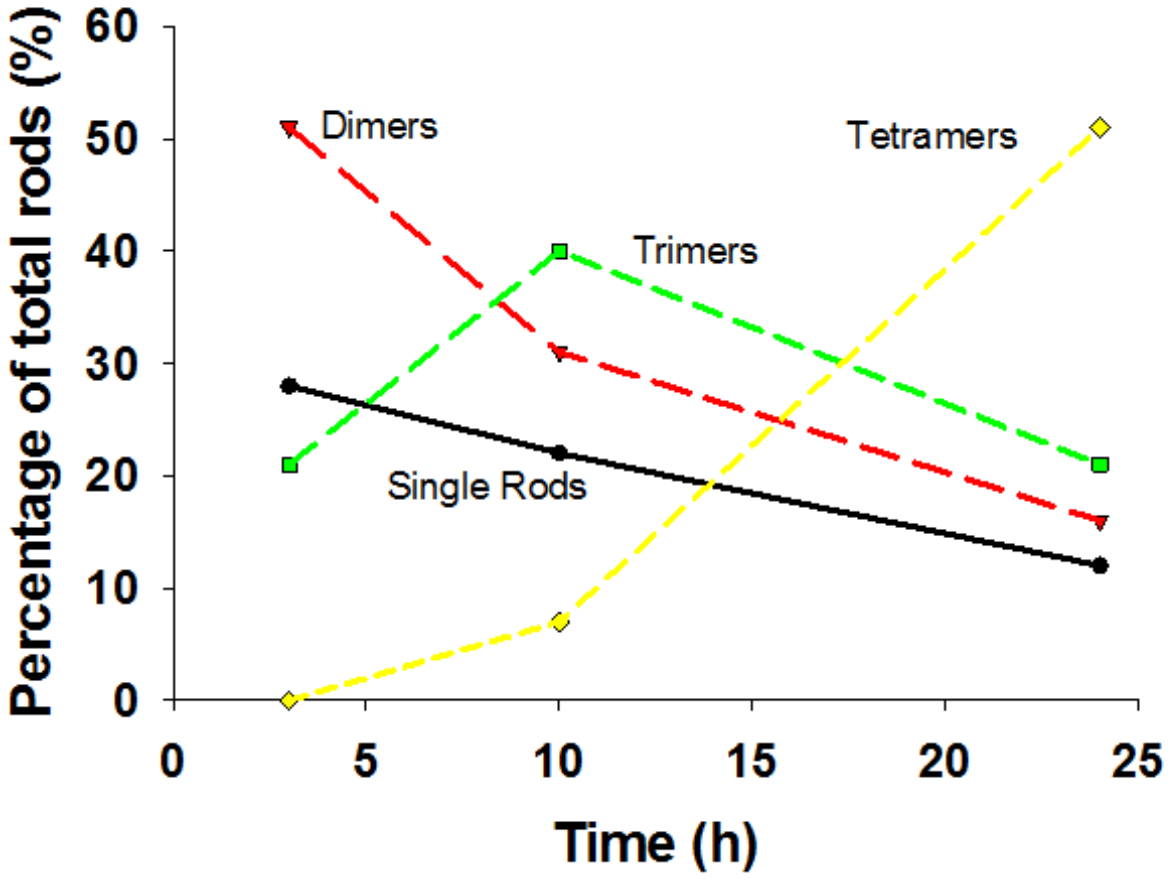

Figure 3.6. Percentage of GNRs forming different end-to-end assemblies. Analysis of 36 TEM images taken from GNRs exposed to 2 mM CaSO4 at three different time periods. Representative TEM images are shown Figure 3.S4.

Anion identity and valence dictate assembly

Past studies have suggested that CTAB forms a dense 3.5 nm thick vesicle-like bilayer on the GNR side facets, while it may not fully coat the ends.[44, 64, 65] The presence of the positively charged vesicle-like bilayer around the side facets protects the GNRs from undergoing side-by-side aggregation. To investigate the chemistry underlying the observed end-to-end assembly we exposed CTAB-GNRs to $CaCl_2$, $MgCl_2$, NaCl, and Na_2SO_4 salts at the same ionic strength used in the $CaSO_4$ and

$MgSO_4$ experiments. The collected Vis-NIR extinction spectra over a period of 24 h are shown in Figures S8 and S9. The decline in the transverse and longitudinal absorption bands is shown in Figures S10 and S11.

No change in the extinction of the transverse band, a <15% drop in the longitudinal band, and no new absorption band at wavelengths longer than the longitudinal band occurred when CTAB-GNRs were exposed to non-sulfate salts. These observations collectively suggest that CTAB-GNRs are colloidally stable 2- and exhibit no significant aggregation when exposed to $CaCl_2$, $MgCl_2$, and NaCl over the range of ionic strengths considered in this study. ζ-potential measurements of CTAB-GNRs exposed to salts show that unlike SO_4^{2-} the interaction of Cl^- with CTAB is weak, resulting in a much smaller change in measured potential (Table 3.2). Over this ionic strength range the ζ-potential values of CTAB-GNRs are close to the value of CTAB-GNRs in DI water. TEM images taken for CTAB-GNRs exposed to $CaCl_2$, $MgCl_2$, and NaCl salts over the concentration range of 1-5 mM show no apparent GNR aggregation (Figure 3.S12), which is consistent with the Vis-NIR and ζ-potential measurements. On the other hand, TEM images taken from CTAB-GNRs exposed to Na_2SO_4 exhibit a similar end-to-end assembly pattern as $CaSO_4$ and $MgSO_4$, but with shorter end-to-end chain length.

As reported in Table 3.2 CTAB-GNRs exposed to salt solutions containing SO_4^{2-} ions have significantly lower ζ-potential values compared to other salts. The measured values are approximately 50% of the measured ζ potentials for the non-sulfate salts. Previous studies have shown that increasing the salt concentration of a CTAB solution reduces the CTAB CMC (critical micelle concentration) and produces larger micelles

due to a shape change from spherical to cylindrical.[66-69] We note, however, that the reported CMC is ~0.9 mM, while our free CTAB concentration was only 4 μM and thus well-below the point at which micelle formation can be expected. Collectively these studies suggest that the observed reduction in ζ-potential values in our study is not caused by the desorption of CTAB from the gold surface.

Sulfate as a divalent anion interacts with the quaternary ammonium head group of CTAB and significantly reduces the measured surface charge of the GNRs in DI water (45.6 mV) to 20.3±0.8 mV for sulfate concentrations of 1-5 mM (Figure 3.S13). Our hypothesis is that when two GNR tips with a non-dense bilayer of CTAB are in close proximity to each other, sulfate effectively bridges adjacent GNRs to form an end-to-end assembly. By increasing the concentration of the $CaSO_4$ or $MgSO_4$ solutions from 1 mM to 5 mM, the ionic strength increases and the electrostatic double layer thickness (i.e., the Debye length) surrounding the GNRs decreases thus enhancing the overall end-to-end assembly of the GNRs. Changes in ζ-potential and Debye length with ionic strength are shown in **Table 3.2.**

Table 3.2. Zeta potential and electrophoretic mobility values of CTAB coated gold nanorod suspensions in 1-5 mM concentrations of CaSO4, MgSO4, Na2SO4, CaCl2, MgCl2, and 3-15 mM of NaCl solutions. The Smoluchowski formulation was used to calculate zeta potential values.

		Ionic Strength (M)	Debye Length (nm)	Electrophoretic Mobility (μmcm/Vs)	ζ-Potential (mV)
$CaSO_4$	**1 mM**	3.71×10^{-3}	4.8	1.69	20.9
	2 mM	6.88×10^{-3}	3.4	1.67	20.6
	5 mM	1.54×10^{-2}	2.15	1.71	21.3
$MgSO_4$	**1 mM**	3.78×10^{-3}	4.8	1.57	19.5
	2 mM	7.08×10^{-3}	3.4	1.58	19.5
	5 mM	1.61×10^{-2}	2.15	1.62	20.1
Na_2SO_4	**1 mM**	2.98×10^{-3}	4.85	2.17	26.84
	2 mM	5.94×10^{-3}	3.43	2.01	24.9
	5 mM	1.47×10^{-2}	2.18	1.72	21.31
$CaCl_2$	**1 mM**	3.00×10^{-3}	4.85	3.51	44.0
	2 mM	6.00×10^{-3}	3.43	3.45	43.3
	5 mM	1.50×10^{-2}	2.17	3.41	42.8
$MgCl_2$	**1 mM**	3.00×10^{-3}	4.85	3.48	42.6
	2 mM	6.00×10^{-3}	3.43	3.40	41.7
	5 mM	1.50×10^{-2}	2.17	3.34	41.1
NaCl	**3 mM**	3.00×10^{-3}	4.85	4.41	56.4
	6 mM	6.00×10^{-3}	3.43	3.99	51.1
	15 mM	1.50×10^{-2}	2.17	2.62	33.6

The evidence suggests that end-to-end assembly of GNRs is enabled by sulfate bridges between adjacent nanorod tips. Due to the strong charge interaction between the quaternary ammonium head group of CTAB on the GNR surface and sulfate anions, electrostatic repulsion between particles is noticeably reduced while the attractive van der Waals (vdW) forces are roughly constant. As DLVO theory based simulations suggest (discussed in the next section), charge repulsion between adjacent GNR side facets (having a high density CTAB coating) is strong enough to prevent side-to-side

assembly. Compared to the side facets, the tip facets are expected to have CTAB coverage and therefore charge-charge repulsion between the tip facets of two adjacent GNRs is weaker. Consequently, strong vdW interactions overcome charge repulsion and favor end-to-end assembly. A noticeable difference in ζ-potential was observed when di-valent versus mono-valent cation counter-ions were present. Such a result is due to the lower dielectric constant of the medium in the presence of divalent cations as compared to monovalent cations at equivalent ionic strength. The decreased dielectric constant of the medium favors the instability of the colloidal suspension toward larger extended end-to-end assemblies of GNRs. As a result, in case of Na_2SO_4 where no divalent cation is present, the end-to-end linkage of CTAB-GNRs occurs less frequently compared to $CaSO_4$ and $MgSO_4$.

DLVO interaction potential energy simulations

We developed a DLVO based particle-particle interaction model that considers both van der Waals attractive forces as well as electrostatic repulsion (Details are presented in SI; Pages 13-15). We note that more complicated models considering additional attractive or repulsive forces could have been considered; however, such models require assumptions with unknown applicability to elongated nanostructures.[70, 71] DLVO modeling results for CTAB-GNRs in 2 mM $CaSO_4$ are shown in Figure 3.7.

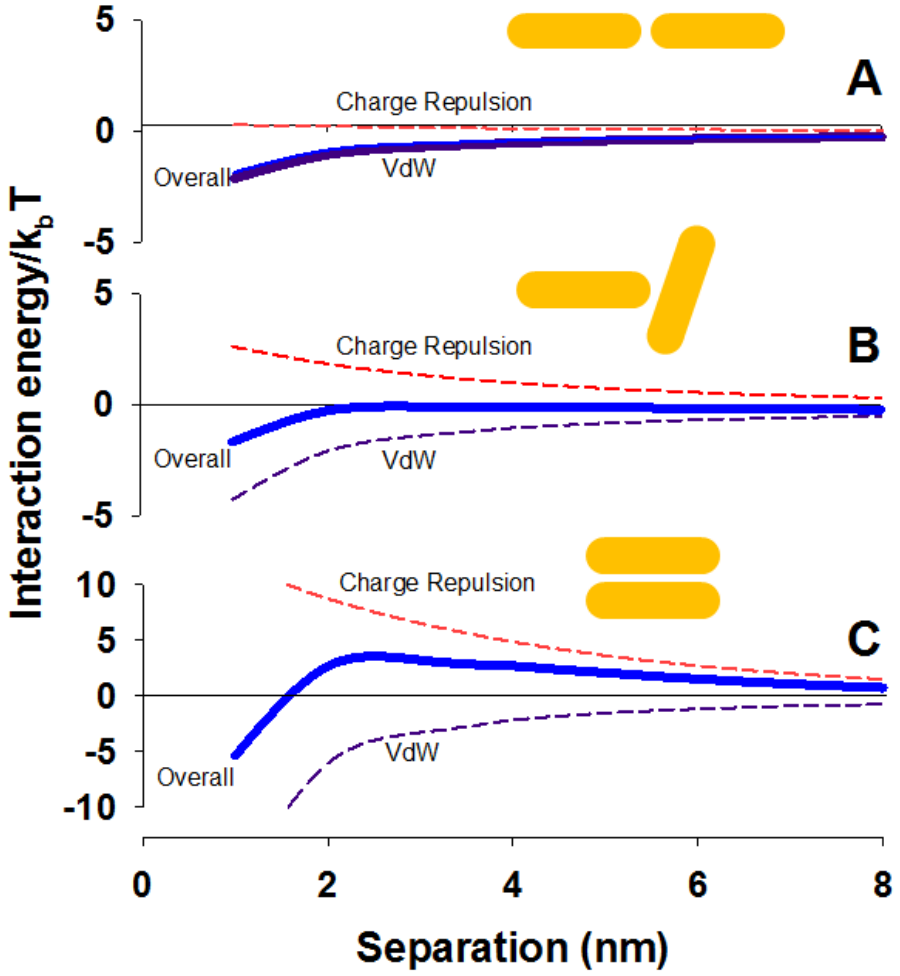

Figure 3.7. DLVO modeling of GNR particle-particle interaction potential energy for the illustrated possible orientations of assembled CTAB-GNRs in 2 mM CaSO4 solution: (A) End-to-End assembly, (B) End-to-Side assembly, and (C) Side-by-Side assembly.

The DLVO modeling results are consistent with our Vis-NIR spectroscopy, TEM, and AFM experimental observations. When two CTAB-GNRs are located in proximity to one another, the end-to-end configuration is calculated to be the most probable and dominant form of interaction. For this configuration the attractive van der Waals (vdW) forces are stronger than the repulsive electrostatic forces at all separation distances. As a result, at a 2 nm end-to-end separation, the overall interaction energy is greater than

$-k_BT$ (=4.1×10^{-21} J) and stable 2- end-to-end assemblies are favorable. Modeling of the end-to-side configuration shows neither strong attraction nor repulsion for separations over 2 nm. In this range, vdW and electrostatic repulsive interactions are of comparable strength. For separations smaller than 2 nm, the overall interaction energy becomes theoretically strong enough to form end-to-side assemblies; however, the presence of a dense CTAB bilayer on the side facets prevents the nanorods from getting that close to one another. Modeling of the side-to-side configuration shows a large charge repulsion between the positively charged CTAB bilayer of each side facet compared to attractive vdW interactions. Similar to the end-to-side assembly, the overall interaction energy becomes attractive at separation distances shorter than the expected length of the CTAB bilayer (~3.5 nm)[72, 73]. Therefore, as observed in the TEM and AFM images, the end-to-end assembly is the dominant configuration, followed by the occasional end-to-side assembly. Side-by-side assembly was not observed at low salt concentrations.

For CTAB-GNRs in 5 mM $CaSO_4$ or $MgSO_4$, although end-to-end assembly is the primary expected configuration, the increase in the number of dimer end-to-end assemblies increases the accessible side facet surface area. Due to the high salt concentration and low electrostatic repulsion, these side facets are subject to side-by-side assembly. Consequently, a 6 nm red shift in the transverse peak and an 11 nm blue shift in the longitudinal peak were observed, while the new end-to-end peak increased and red shifted to longer wavelengths. The drop in the height of the longitudinal peak followed by convergence of the transverse and longitudinal peaks, show side-by-side assembly compared to end-to-end and end-to-side assemblies. Suspension color change and precipitated GNRs were consistent with Vis-NIR

extinction observations at higher salt concentrations. Neither a shift in the longitudinal and transverse peaks, nor a change in suspension color was observed in other concentrations of $CaSO_4$ or $MgSO_4$. At high salt concentrations (i.e., 5 mM $CaSO_4$ and $MgSO_4$), end-to-end, end-to-side, and side-by-side assemblies were frequently observed in TEM images.

3.5 Conclusions

In this paper we introduced a simple one step mechanism to produce chain like end-to-end assemblies of CTAB coated GNRs. We propose that sulfate as a divalent anion effectively interacts with the quaternary ammonium head group of CTAB on the GNRs surface and bridges the tip facets of adjacent rods. This bridging produces chainlike end-to-end assemblies of GNRs and the length of assembly can be controlled by sulfate ion concentration, GNR concentration, and exposure time. In contrast to end-to-end assembly, side-by-side and end-to-side assemblies are hindered by strong electrostatic repulsion between the dense CTAB bilayers present on the side facets. Our simple DLVO model supports the observed assembly trend. Furthermore, we showed that by analyzing the UV-Vis extinction spectrum and knowing the absorption band of each order of assembly that we can separately track the formation and growth of these assemblies over time.

It has been shown that end-to-end assembly of GNRs produces a strong SERS (surface enhanced Raman spectroscopy) template,[35, 74] and can be used in bio-sensing and contaminant detection.[25, 75] The majority of prior studies to produce elongated assemblies involve complex, laborious antibody or polymer involved chemical reactions while in our work only exposure to a simple divalent anion, sulfate, triggers

and enhances formation of these chain-like assemblies. Isolating these assemblies and protecting them with a stable 2- coatings such as silica may make them a good choice for SERS based detection strategies.

3.6 Acknowledgements

Funding for this study was provided by the US National Science Foundation (NSF; CBET 1236005 and 1133736) and the Virginia Tech Institute for Critical Technology and Applied Science. Additional funding was provided by NSF and the Environmental Protection Agency under NSF Cooperative Agreement EF-0830093, Center for the Environmental Implications of NanoTechnology (CEINT). With special thanks to Dr. Samuel Lohse for his contribution to this study at the beginning phase. Any opinions, findings, conclusions or recommendations expressed in this material are those of the authors and do not necessarily reflect the views of the NSF or the EPA. This work has not been subjected to EPA review and no official endorsement should be inferred.

3.7 References

1. Kelly, K.L., et al., *The optical properties of metal nanoparticles: the influence of size, shape, and dielectric environment.* The Journal of Physical Chemistry B, 2003. **107**(3): p. 668-677.
2. Sosa, I.O., C. Noguez, and R.G. Barrera, *Optical properties of metal nanoparticles with arbitrary shapes.* The Journal of Physical Chemistry B, 2003. **107**(26): p. 6269-6275.
3. McConnell, W.P., et al., *Electronic and optical properties of chemically modified metal nanoparticles and molecularly bridged nanoparticle arrays.* The Journal of Physical Chemistry B, 2000. **104**(38): p. 8925-8930.
4. Yu, Y.-Y., et al., *Gold nanorods: electrochemical synthesis and optical properties.* The Journal of Physical Chemistry B, 1997. **101**(34): p. 6661-6664.
5. Murphy, C.J., et al., *Anisotropic metal nanoparticles: synthesis, assembly, and optical applications.* The Journal of Physical Chemistry B, 2005. **109**(29): p. 13857-13870.
6. Willets, K.A. and R.P. Van Duyne, *Localized surface plasmon resonance spectroscopy and sensing.* Annu. Rev. Phys. Chem., 2007. **58**: p. 267-297.
7. Hornyak, G.L., C.J. Patrissi, and C.R. Martin, *Fabrication, characterization, and optical properties of gold nanoparticle/porous alumina composites: the nonscattering Maxwell-Garnett limit.* The Journal of Physical Chemistry B, 1997. **101**(9): p. 1548-1555.

8. Link, S. and M.A. El-Sayed, *Spectral properties and relaxation dynamics of surface plasmon electronic oscillations in gold and silver nanodots and nanorods.* The Journal of Physical Chemistry B, 1999. **103**(40): p. 8410-8426.
9. Kottmann, J.P., et al., *Dramatic localized electromagnetic enhancement in plasmon resonant nanowires.* Chemical Physics Letters, 2001. **341**(1): p. 1-6.
10. Imura, K., T. Nagahara, and H. Okamoto, *Plasmon mode imaging of single gold nanorods.* Journal of the American Chemical Society, 2004. **126**(40): p. 12730-12731.
11. Elghanian, R., et al., *Selective colorimetric detection of polynucleotides based on the distance-dependent optical properties of gold nanoparticles.* Science, 1997. **277**(5329): p. 1078-1081.
12. Afrooz, A.N., et al., *Mechanistic heteroaggregation of gold nanoparticles in a wide range of solution chemistry.* Environmental science & technology, 2013. **47**(4): p. 1853-1860.
13. Ghosh, S.K. and T. Pal, *Interparticle coupling effect on the surface plasmon resonance of gold nanoparticles: from theory to applications.* Chemical Reviews, 2007. **107**(11): p. 4797-4862.
14. Haiss, W., et al., *Determination of size and concentration of gold nanoparticles from UV-vis spectra.* Analytical chemistry, 2007. **79**(11): p. 4215-4221.
15. Liu, X., et al., *Extinction coefficient of gold nanoparticles with different sizes and different capping ligands.* Colloids and Surfaces B: Biointerfaces, 2007. **58**(1): p. 3-7.

16. Amendola, V. and M. Meneghetti, *Size evaluation of gold nanoparticles by UV−vis spectroscopy.* The Journal of Physical Chemistry C, 2009. **113**(11): p. 4277-4285.

17. Gou, L. and C.J. Murphy, *Fine-tuning the shape of gold nanorods.* Chemistry of materials, 2005. **17**(14): p. 3668-3672.

18. Jana, N.R., L. Gearheart, and C.J. Murphy, *Wet chemical synthesis of high aspect ratio cylindrical gold nanorods.* The Journal of Physical Chemistry B, 2001. **105**(19): p. 4065-4067.

19. Pérez-Juste, J., et al., *Gold nanorods: synthesis, characterization and applications.* Coordination Chemistry Reviews, 2005. **249**(17): p. 1870-1901.

20. Prescott, S.W. and P. Mulvaney, *Gold nanorod extinction spectra.* Journal of applied physics, 2006. **99**(12): p. 123504.

21. Afrooz, A.N., et al., *Spheres vs. rods: The shape of gold nanoparticles influences aggregation and deposition behavior.* Chemosphere, 2013. **91**(1): p. 93-98.

22. Link, S., M. Mohamed, and M. El-Sayed, *Simulation of the optical absorption spectra of gold nanorods as a function of their aspect ratio and the effect of the medium dielectric constant.* The Journal of Physical Chemistry B, 1999. **103**(16): p. 3073-3077.

23. Eustis, S. and M.A. El-Sayed, *Determination of the aspect ratio statistical distribution of gold nanorods in solution from a theoretical fit of the observed inhomogeneously broadened longitudinal plasmon resonance absorption spectrum.* Journal of applied physics, 2006. **100**(4): p. 044324.

24. Kim, T., et al., *Kinetics of gold nanoparticle aggregation: experiments and modeling.* Journal of colloid and interface science, 2008. **318**(2): p. 238-243.

25. Wang, L., et al., *Side-by-Side and End-to-End Gold Nanorod Assemblies for Environmental Toxin Sensing.* Angewandte Chemie International Edition, 2010. **49**(32): p. 5472-5475.

26. Zhong, L., et al., *Rational design and SERS properties of side-by-side, end-to-end and end-to-side assemblies of Au nanorods.* Journal of Materials Chemistry, 2011. **21**(38): p. 14448-14455.

27. Jain, P.K., S. Eustis, and M.A. El-Sayed, *Plasmon coupling in nanorod assemblies: optical absorption, discrete dipole approximation simulation, and exciton-coupling model.* The Journal of Physical Chemistry B, 2006. **110**(37): p. 18243-18253.

28. Funston, A.M., et al., *Plasmon coupling of gold nanorods at short distances and in different geometries.* Nano letters, 2009. **9**(4): p. 1651-1658.

29. Chen, H. and E. Ruckenstein, *Controlling Nanorod Oligomer Aggregation in Solutions.* The Journal of Physical Chemistry C, 2016.

30. Leung, F.C.-M., et al., *Metal–Metal and π–π Interactions Directed End-to-End Assembly of Gold Nanorods.* Journal of the American Chemical Society, 2016. **138**(9): p. 2989-2992.

31. Wang, Y., et al., *End-to-end assembly of gold nanorods by means of oligonucleotide–mercury (II) molecular recognition.* Chemical Communications, 2010. **46**(8): p. 1332-1334.

32. Jain, T., et al., *End-to-end assembly of gold nanorods via oligopeptide linking and surfactant control.* Journal of colloid and interface science, 2012. **376**(1): p. 83-90.

33. Gordel, M., et al., *End-to-end self-assembly of gold nanorods in isopropanol solution: experimental and theoretical studies.* Journal of Nanoparticle Research, 2015. **17**(12): p. 1-12.

34. Wang, Y., et al., *Solvent-mediated end-to-end assembly of gold nanorods.* The Journal of Physical Chemistry Letters, 2010. **1**(18): p. 2692-2698.

35. Stewart, A.F., et al., *Rational design for the controlled aggregation of gold nanorods via phospholipid encapsulation for enhanced Raman scattering.* ACS nano, 2014. **8**(6): p. 5462-5467.

36. Zhao, D., et al., *Reversible gold nanorod assembly triggered by pH-responsive DNA nanomachine.* Applied Physics Letters, 2013. **102**(12): p. 123101.

37. Cai, H.-H., et al., *Controlled side-by-side assembly of gold nanorods: A strategy for lead detection.* Sensors and Actuators B: Chemical, 2014. **196**: p. 252-259.

38. Orendorff, C.J., P.L. Hankins, and C.J. Murphy, *pH-triggered assembly of gold nanorods.* Langmuir, 2005. **21**(5): p. 2022-2026.

39. Ke, S., et al., *Controlled assembly of gold nanorods using tetrahydrofuran.* RSC Advances, 2013. **3**(8): p. 2690-2696.

40. Liu, J., et al., *End-to-end and side-by-side assemblies of gold nanorods induced by dithiol poly (ethylene glycol).* Applied Physics Letters, 2014. **104**(25): p. 253105.

41. Gao, J., C.M. Bender, and C.J. Murphy, *Dependence of the gold nanorod aspect ratio on the nature of the directing surfactant in aqueous solution.* Langmuir, 2003. **19**(21): p. 9065-9070.

42. Nikoobakht, B. and M.A. El-Sayed, *Preparation and growth mechanism of gold nanorods (NRs) using seed-mediated growth method.* Chemistry of Materials, 2003. **15**(10): p. 1957-1962.

43. Smith, D.K. and B.A. Korgel, *The importance of the CTAB surfactant on the colloidal seed-mediated synthesis of gold nanorods.* Langmuir, 2008. **24**(3): p. 644-649.

44. Nikoobakht, B. and M.A. El-Sayed, *Evidence for bilayer assembly of cationic surfactants on the surface of gold nanorods.* Langmuir, 2001. **17**(20): p. 6368-6374.

45. Murphy, C.J., et al., *Gold nanorod crystal growth: from seed-mediated synthesis to nanoscale sculpting.* Current Opinion in Colloid & Interface Science, 2011. **16**(2): p. 128-134.

46. Lohse, S.E. and C.J. Murphy, *The quest for shape control: a history of gold nanorod synthesis.* Chemistry of Materials, 2013. **25**(8): p. 1250-1261.

47. Haynes, W.M., *CRC handbook of chemistry and physics*. 2014: CRC press.

48. Li, Z., et al., *Absorption Spectroscopy of Single Optically Trapped Gold Nanorods.* Nano letters, 2015. **15**(11): p. 7731-7735.

49. Scolari, M., et al., *Surface enhanced Raman scattering of carbon nanotubes decorated by individual fluorescent gold particles.* The Journal of Physical Chemistry C, 2008. **112**(2): p. 391-396.

50. Israelachvili, J.N., *Intermolecular and surface forces: revised third edition*. 2011: Academic press.

51. Dougherty, G.M., et al., *The zeta potential of surface-functionalized metallic nanorod particles in aqueous solution.* Electrophoresis, 2008. **29**(5): p. 1131-1139.

52. Ohshima, H., *Theory of colloid and interfacial electric phenomena*. Vol. 12. 2006: Academic Press.

53. Thomas, K.G., et al., *Uniaxial plasmon coupling through longitudinal self-assembly of gold nanorods.* The Journal of Physical Chemistry B, 2004. **108**(35): p. 13066-13068.

54. Vigderman, L., B.P. Khanal, and E.R. Zubarev, *Functional Gold Nanorods: Synthesis, Self-Assembly, and Sensing Applications.* Advanced Materials, 2012. **24**(36): p. 4811-4841.

55. Payne, E.K., et al., *Multipole plasmon resonances in gold nanorods.* The Journal of Physical Chemistry B, 2006. **110**(5): p. 2150-2154.

56. Lebovka, N.I., *Aggregation of charged colloidal particles*, in *Polyelectrolyte Complexes in the Dispersed and Solid State I*. 2014, Springer. p. 57-96.

57. Gregory, J., *Particles in water: properties and processes*. 2005: CRC Press.

58. Link, S. and M.A. El-Sayed, *Shape and size dependence of radiative, non-radiative and photothermal properties of gold nanocrystals.* International Reviews in Physical Chemistry, 2000. **19**(3): p. 409-453.

59. Papavassiliou, G.C., *Optical properties of small inorganic and organic metal particles.* Progress in Solid State Chemistry, 1979. **12**(3): p. 185-271.

60. Kerker, M., *The scattering of light*. 1969, Academic Press, New York.

61. Bohren, C.F. and D.R. Huffman, *Absorption and scattering of light by small particles*. 2008: John Wiley & Sons.

62. Antonov, L. and D. Nedeltcheva, *Resolution of overlapping UV–Vis absorption bands and quantitative analysis.* Chemical Society Reviews, 2000. **29**(3): p. 217-227.

63. Schärtl, W., C. Roos, and K. Gohr, *Oscillating time correlation functions from dynamic light scattering of gold-labeled tracers.* The Journal of chemical physics, 1998. **108**(22): p. 9594-9597.

64. Wang, Z., et al., *Surface reconstruction of the unstable {110} surface in gold nanorods.* The Journal of Physical Chemistry B, 2000. **104**(23): p. 5417-5420.

65. Wang, Z., et al., *Crystallographic facets and shapes of gold nanorods of different aspect ratios.* Surface science, 1999. **440**(1): p. L809-L814.

66. Zhang, W., et al., *Effect of KBr on the micellar properties of CTAB.* Chinese Science Bulletin, 2000. **45**(20): p. 1854-1857.

67. Goyal, P., et al., *Form factors for different aggregation models of micelles.* Physica B: Condensed Matter, 1991. **174**(1): p. 192-195.

68. Kuperkar, K., et al., *Formation and growth of micelles in dilute aqueous CTAB solutions in the presence of NaNO3 and NaClO3.* Journal of Surfactants and Detergents, 2010. **13**(3): p. 293-303.

69. Cates, M. and S. Candau, *Statics and dynamics of worm-like surfactant micelles.* Journal of Physics: Condensed Matter, 1990. **2**(33): p. 6869.

70. Choi, J., et al., *Electrical Repulsive Energy between Two Cylindrical Particles with Finite Length: Configuration Dependence.* BULLETIN-KOREAN CHEMICAL SOCIETY, 2008. **29**(6): p. 1131.

71. Min, Y., et al., *The role of interparticle and external forces in nanoparticle assembly.* Nature materials, 2008. **7**(7): p. 527.

72. Gomez-Grana, S., et al., *Surfactant (bi) layers on gold nanorods.* Langmuir, 2011. **28**(2): p. 1453-1459.

73. Hore, M.J., et al., *Probing the Structure, Composition, and Spatial Distribution of Ligands on Gold Nanorods.* Nano letters, 2015. **15**(9): p. 5730-5738.

74. Caswell, K., et al., *Preferential end-to-end assembly of gold nanorods by biotin-streptavidin connectors.* Journal of the American Chemical Society, 2003. **125**(46): p. 13914-13915.

75. Zhu, Y., et al., *Gold nanorod assembly based approach to toxin detection by SERS.* Journal of Materials Chemistry, 2012. **22**(6): p. 2387-2391.

3.8 Supporting Information for

Sulfate Mediated End-to-End Assembly of Gold Nanorods

S.M.H. Abtahi,[1, 2, 3] Nathan D. Burrows,[4] Fred A. Idesis,[4] Catherine J. Murphy,[4] Navid B. Saleh,[5] and Peter J. Vikesland[1, 2, 3]*

[1.]Virginia Tech, Department of Civil and Environmental Engineering, Blacksburg, VA, USA

[2.]Virginia Tech, Institute for Critical Technology and Applied Science (ICTAS) Center for Sustainable Nanotechnology (VTSuN), Blacksburg, VA, USA

[3.]Center for the Environmental Implications of Nanotechnology (CEINT), Duke University, Durham, NC, USA

[4.]Department of Chemistry, University of Illinois at Urbana-Champaign, 600 S. Matthews Ave., Urbana, IL, 61801.

[5.]The University of Texas at Austin, Department of Civil, Architectural, and Environmental Engineering, Austin, TX 78750, USA

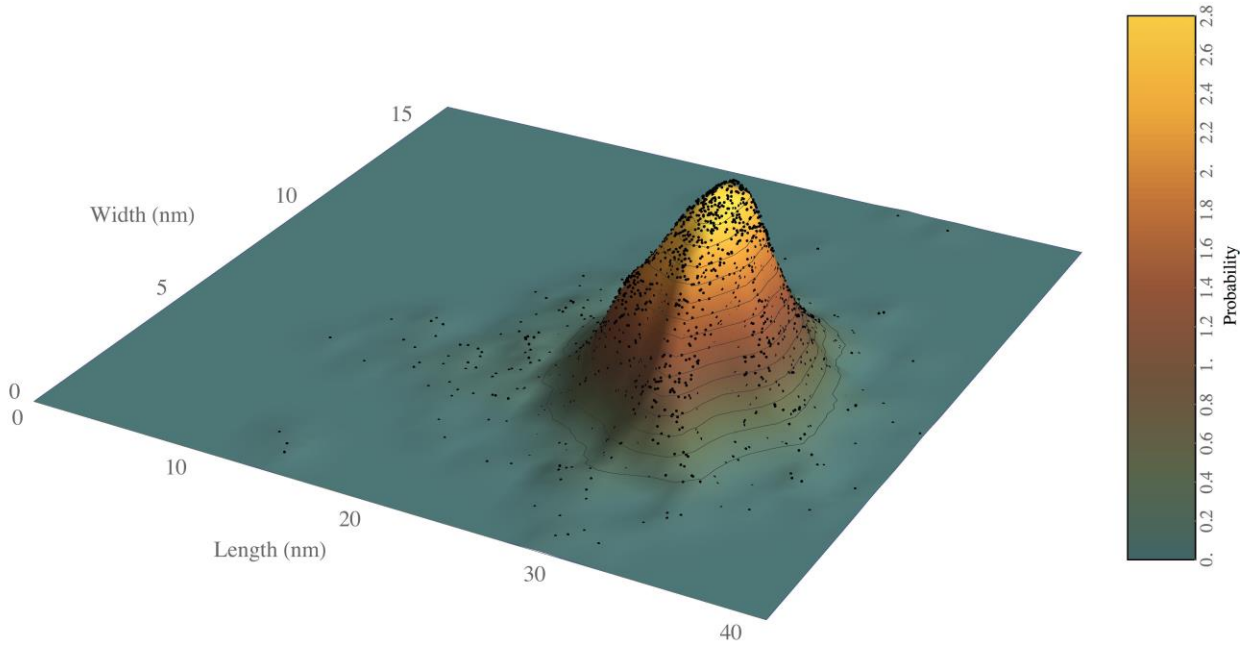

Figure 3.S1. TEM image analysis of synthesized GNRs. The GNRs have an average length of 28.8 ± 0.1 nm and an average diameter of 6.6 ± 0.1 nm (the noted errors reflect the 95% confidence interval based on n = 2104 measurements obtained using ImageJ)

Henry Equation

Zeta potential value can be directly calculated from measured electrophoretic mobility by means of Henry equation. Knowing the medium and nanoparticle characteristics and appropriate Henry's constant value are the keys parameters in this calculation.

$$U_E = \frac{2\varepsilon\zeta f(\kappa a)}{3\eta}$$

U_E: $Electrophoretic\ mobility$

ε: $Dielectric\ constant$

ζ: $Zeta\ potential$

$f(\kappa a)$: $Henry's\ constant$

η: $Viscosity$

$a: Radius\ of\ particle$

$1/\kappa : Double\ layer\ thickness$

Smoluchowski equation

Smoluchowski equation is an approximation for Henry's constant (f(κa)=1.5). This approximation works best if the particles are fairly large while suspended in an aqueous medium with moderate electrolyte concentration. In order to justify the application of Smoluchowski approximation during zeta potential calculations, It is suggested that the κa>>1 condition should be met.

$If \kappa a \gg 1\ then\ f(\kappa a) = 1.5$

$$\kappa = \left(\frac{2Ie^2}{\varepsilon_0 \varepsilon_r k_B T}\right)^{1/2}$$

$\varepsilon_0: Permittivity\ of\ vacuum$

$\varepsilon_r: Relative\ static\ permittivity\ of\ solution$

$I: Ionic\ strength\ of\ solution$

$e: Charge\ of\ an\ electron$

$k_B: Boltz - mann\ constant$

$T: Temperature$

Synthesized GNRs have cylindrical shape with 28.8 nm length and 6.6 nm diameter. An equivolume sphere will have a radius of 19.65 nm. All calculation and measurements occurred at 20°C and DI water was the solvent.

$a = 19.65\ nm$

$5\ mM\ CaSO_4;\ I = 1.54 \times 10^{-2}\ mol/L,\ therefore\ \ \kappa = 4.65 \times 10^8\ 1/m\ and\ \ \kappa a = 9.13$

$1\ mM\ CaSO_4; I = 3.71 \times 10^{-3}\ {}^{mol}/_{L}$, *therefore* $\kappa = 2.08 \times 10^{8}\ {}^{1}/_{m}$ *and* $\kappa a = 4.09$

At all ranges of ionic strengths in this study, $\kappa a \gg 1$ always , therefore Smoluchowski model for zeta potential measurements is valid.

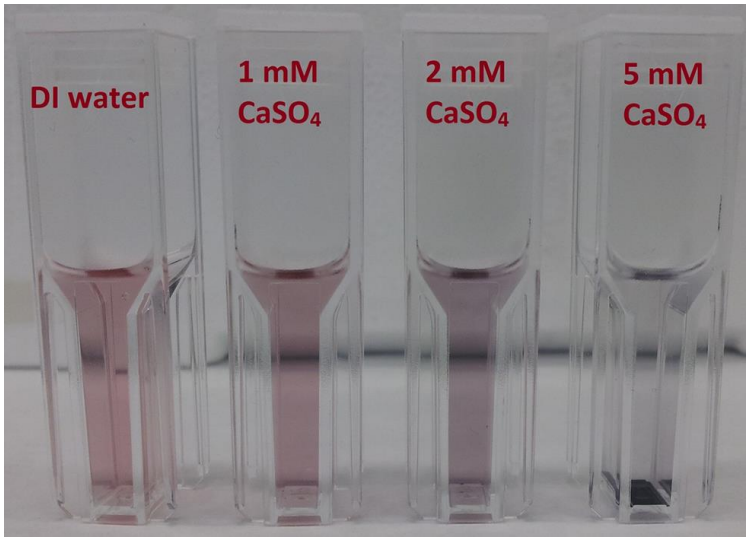

Figure 3.S2. Image of 20 mg/L CTAB-GNRs in DI water and in the presence of different concentrations of CaSO4 after 24 hours of exposure.

Second Order GNR aggregation rate:

In this study the aggregation rate of gold nanorods, decay in single GNRs number concentration, at different experiments is calculated based on a second order kinetics rate. Beer-Lambert law suggests that change in the measured extinction intensity of the single GNRs longitudinal band is linearly related to the change in the GNRs number concentration. The reported aggregation rates are calculated based on plotting the inverse of single GNRs longitudinal band extinction intensity versus time.

$A = Extinction\ intensity \qquad t = time$

$k = \ second\ rate\ constant \qquad C = \ single\ GNR\ number\ concentration$

$I = \ incident\ light\ intensity \quad \varepsilon = \ molar\ extinction\ coefficient$

$L = Incident\ light\ pathlength$

Beer-Lambert law:

$A = \varepsilon LC = Log\frac{I_0}{I}$ therefore $A \propto C\ C_0 = 1.07 \times 10^{14}\ goldnanorods/L$ $\frac{d[C]}{dt} = k[C]^2$;

$\frac{1}{[C]} = \frac{1}{[C]_0} + kt$; $\frac{1}{[A]} = \frac{1}{[A]_0} + kt$ K values for each set of experiment is determined by plotting $1/[A]$ vs. t

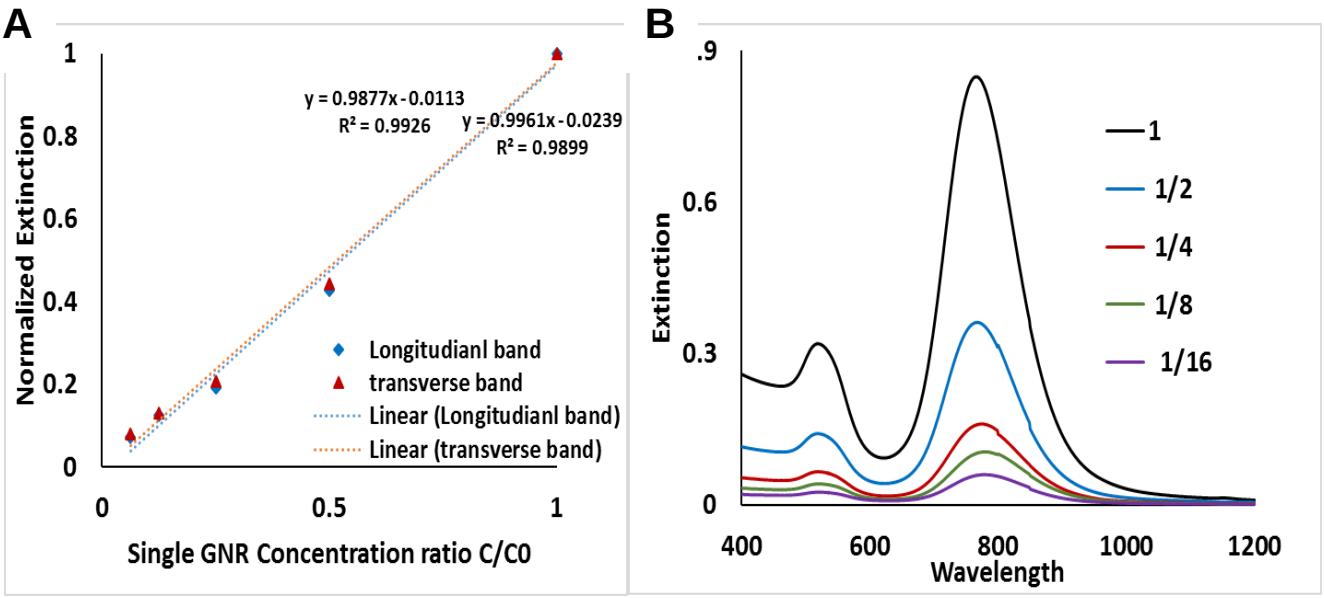

Figure 3.S3. A) Normalized Extinction intensity of transverse band and longitudinal band of single GNRs suspension in DI water at different concentrations B) Vis-NIR extinction intensity of single GNRs suspension in DI water at different concentrations (Note: C0=1.1×1014 gold nanorods/L ; spectra 1 in graph B represents this concentration)

Table 3.S1: Normalized and non-normalized transverse band and longitudinal band extinction intensities of single GNR suspensions in DI water at different concentrations

			Normalized	
Single GNR Concentration (x 1.07×10^{14} gold nanorods/L)	Transverse band	Longitudinal band	Transverse band	Longitudinal band
1	0.319	0.849	1	1
0.5	0.141	0.362	0.442	0.426
0.25	0.065	0.161	0.205	0.189
0.125	0.041	0.105	0.130	0.123
0.0625	0.025	0.060	0.079	0.070

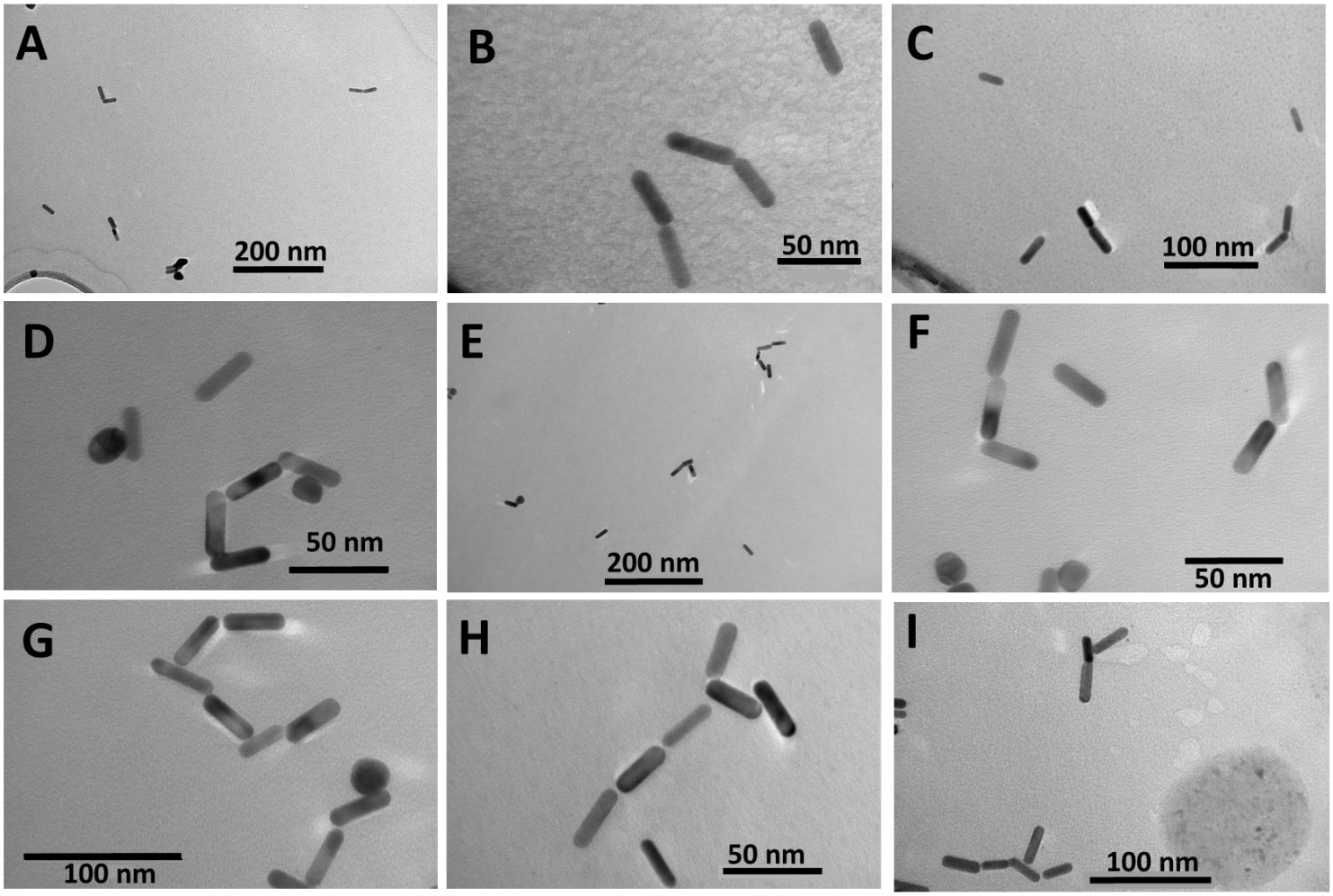

Figure 3.S4. TEM images of end-to-end assemblies of GNRs exposed to 2 mM CaSO4 after A,B,C) 3 hours; D,E,F) 10 hours; G,H,I) 24 hours.

Calculation of absorption spectra based on incident light wavelength λ and aspect ratio of gold nanorod assemblies by extended Mie theory

Mie theory predicts the extinction and scattering of electromagnetic wave (light) by a homogenous spherical particle and is not accurate in the case of anisotropic GNRs. Therefore a modeified and extended version of Mie theory has been used in this study to model and predict the extinction intensities of different assemblies based on their aspect ratios. The corresponding wavelengths of the extinction bands can be determined by finding the local maximum extinction intensities in the range of incident light wavelengths.

$$\gamma = \frac{2\pi NV\varepsilon_m^{3/2}}{3\lambda}\sum_j \frac{(1/P_j^2)\varepsilon_2}{(\varepsilon_1 + \frac{1-P_j}{P_j}\varepsilon_m)^2 + \varepsilon_2^2}$$

$$P_A = \frac{1-e^2}{e^2}\left[\frac{1}{2e}\ln(\frac{1+e}{1-e}) - 1\right]$$

$$P_B = P_C = \frac{1-P_A}{2} \qquad e = \sqrt{1-(\frac{2R}{L})^2}$$

Where $Aspectratio = \frac{L}{2R}$

$$\varepsilon_1(\lambda) = n(\lambda)^2 - k(\lambda)^2$$

$$\varepsilon_2(\lambda) = \sqrt{(n(\lambda)^2 + k(\lambda)^2) - \varepsilon_1(\lambda)^2}$$

ϒ= Extinction intensity

λ= Wavelength of incident light

n= Refractive index of gold

k= Extinction coefficient of gold

ε_1 and ε_2 = dielectric constants of gold

P_A, P_B and P_c = depolarization factors of GNR

ε_m = dielectric constant of surrounding medium

N= number of particles per unit volume

V= Volume of each particle

Example: Calculation of longitudinal band wavelength for dimer GNR end-to-end assembly (AR=8.8)

$$L = 57.6nm \qquad R = 3.3nm \qquad Aspectratio = \frac{L}{2R} = 8.8 \quad e = \sqrt{1-(\frac{2R}{L})^2} = 0.994 \qquad \varepsilon_m = 0.65$$

$$P_A = \frac{1-e^2}{e^2}\left[\frac{1}{2e}\ln(\frac{1+e}{1-e}) - 1\right] = 0.023 \qquad P_B = P_C = \frac{1-P_A}{2} = 0.488$$

Since N,V, and ε_m are constant then:

$$\gamma = X\gamma'' \text{ Where } \quad \gamma'' = \frac{1}{\lambda}\sum_j \frac{(1/P_j^2)\varepsilon_2}{(\varepsilon_1 + \frac{1-P_j}{P_j}\varepsilon_m)^2 + \varepsilon_2^2} \text{ and } X = \frac{2\pi NV\varepsilon_m^{3/2}}{3} = constant$$

ε_1 and ε_2 can be calculated knowing the values of n and k at each wavelength (λ). Using $\varepsilon_1, \varepsilon_2, P_A, P_B$, and P_C one can calculate ϒ (extinction) versus λ(wavelength). The values of n and k at each incident light wavelengths and the calculated $\varepsilon_1, \varepsilon_2$, and ϒ" are

reported at Table 3.S2. Υ" is linearly related to the extinction intensity (Υ) and represents the magnitude of light absorption at that specific incident light wavelength. Figure 3.S5 shows how these calculated extinction intensities change versus incident light wavelengths.

Table 3.S2. n (refractive index) and k (extinction coefficient) of gold, calculated $\varepsilon_1, \varepsilon_2$, and Υ" values for dimer GNRs end-to-end assembly versus incident light wavelength. (n and k values are derived from McPeak, Kevin M., et al. "Plasmonic films can easily be better: rules and recipes." ACS photonics 2.3 (2015): 326-333)

wavelength (λ)	n	k	ε1	ε2	Υ"
800	0.104	5.224	-27.2794	1.086592	0.072452
810	0.106	5.313	-28.2167	1.126356	0.103348
820	0.104	5.407	-29.2248	1.124656	0.156777
830	0.104	5.492	-30.1512	1.142336	0.255183
840	0.107	5.577	-31.0915	1.193478	0.480281
845	0.109	5.619	-31.5613	1.224942	0.690112
850	0.111	5.66	-32.0233	1.25652	0.994327
855	0.111	5.705	-32.5347	1.26651	1.42718
860	0.111	5.75	-33.0502	1.2765	1.714754
865	0.112	5.791	-33.5231	1.297184	1.545007
870	0.112	5.831	-33.988	1.306144	1.164572
875	0.113	5.872	-34.4676	1.327072	0.809401
880	0.114	5.913	-34.9506	1.348164	0.565538
890	0.116	5.993	-35.9026	1.390376	0.307517
900	0.117	6.082	-36.977	1.423188	0.177924
910	0.117	6.164	-	1.442376	0.11712

			37.9812		
920	0.119	6.242	-38.9484	1.485596	0.084741
930	0.121	6.329	-40.0416	1.531618	0.062182
940	0.122	6.41	-41.0732	1.56404	0.048034
950	0.124	6.492	-42.1307	1.610016	0.038353

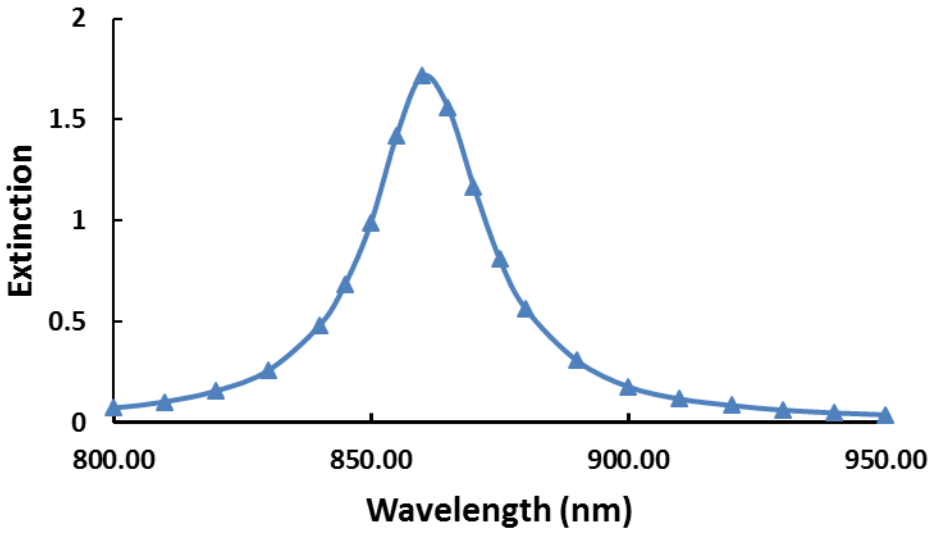

Figure 3.S5. Calculated extinction intensity of dimer GNRs end-to-end assembly versus wavelength (nm) of incident light using extended Mie theory.

The longitudinal band occurs at 860 nm.

Example: Calculation of extinction intensity changes versus incident light wavelength for GNR side-by-side and end-to-side assembly
Side-by-side assembly

$$L = 28.8nm \qquad R = 6.6nm \qquad Aspectratio = \frac{L}{2R} = 2.18 \quad e = \sqrt{1-(\frac{2R}{L})^2} = 0.888 \qquad \varepsilon_m = 0.65$$

$$P_A = \frac{1-e^2}{e^2}\left[\frac{1}{2e}\ln(\frac{1+e}{1-e})-1\right] = 0.158 \qquad P_B = P_C = \frac{1-P_A}{2} = 0.421$$

Side-by-side assembly

$$L = 35.4nm \qquad R = 14.4nm \qquad Aspectratio = \frac{L}{2R} = 1.23 \quad e = \sqrt{1-(\frac{2R}{L})^2} = 0.582 \qquad \varepsilon_m = 0.65$$

$$P_A = \frac{1-e^2}{e^2}\left[\frac{1}{2e}\ln(\frac{1+e}{1-e})-1\right] = 0.280 \qquad P_B = P_C = \frac{1-P_A}{2} = 0.360$$

Table 3.S3. n (refractive index) and k (extinction coefficient) of gold, calculated $\varepsilon_1, \varepsilon_2$, and ϒ" values for GNRs side-by-side and end-to-side assemblies versus incident light wavelength. (n and k values are derived from McPeak, Kevin M., et al. "Plasmonic films can easily be better: rules and recipes." ACS photonics 2.3 (2015): 326-333)

					Side-by-side	End-to-side
Wavelength (λ)	n	k	ε1	ε2	ϒ"	ϒ"
450	1.538	1.910	-1.2845	5.8787	0.005545	0.005191
460	1.475	1.872	-1.3291	5.5244	0.005495	0.005117
470	1.386	1.827	-1.4187	5.0673	0.005501	0.005067
480	1.252	1.782	-1.6061	4.4656	0.005636	0.005071
490	1.064	1.767	-1.9925	3.7633	0.006096	0.005246
500	0.848	1.828	-2.6227	3.1025	0.007212	0.005814
510	0.661	1.964	-3.4216	2.5996	0.009169	0.007104
520	0.529	2.129	-4.2558	2.2538	0.010813	0.00948
530	0.438	2.299	-5.0751	2.0106	0.009894	0.013414
540	0.3	2.451	-	1.826	0.00726	0.018379

	72		5.8719	5		
550	0.323	2.597	-6.6403	1.6826	0.00513	0.020352
560	0.284	2.738	-7.4208	1.561	0.003839	0.018317
570	0.254	2.871	-8.183	1.4593	0.003181	0.018288
580	0.228	2.999	-8.9447	1.3734	0.002907	0.019917
590	0.207	3.121	-9.6999	1.293	0.002886	0.015388
600	0.188	3.241	-10.473	1.224	0.003112	0.008703
610	0.172	3.359	-11.238	1.1596	0.003599	0.004923
620	0.160	3.465	-11.985	1.1095	0.004476	0.003053
630	0.146	3.577	-12.778	1.0473	0.00609	0.001962
640	0.135	3.685	-13.568	0.99829	0.009317	0.001348
650	0.125	3.792	-14.366	0.95187	0.016752	0.000965
660	0.117	3.896	-15.166	0.91818	0.036847	0.000722
670	0.111	3.999	-15.984	0.88884	0.06737	0.000554
680	0.105	4.102	-16.821	0.86768	0.035392	0.000437
690	0.101	4.205	-17.672	0.8537	0.013971	0.000353
700	0.098	4.305	-18.524	0.84903	0.006856	0.000292
710	0.097	4.403	-19.384	0.8613	0.004016	0.00025
720	0.098	4.499	-20.233	0.88745	0.002678	0.00022
730	0.096	4.595	-21.112	0.8907	0.001854	0.00019
740	0.099	4.687	-21.96	0.93241	0.001426	0.000173
750	0.098	4.781	-22.849	0.94223	0.001089	0.000153

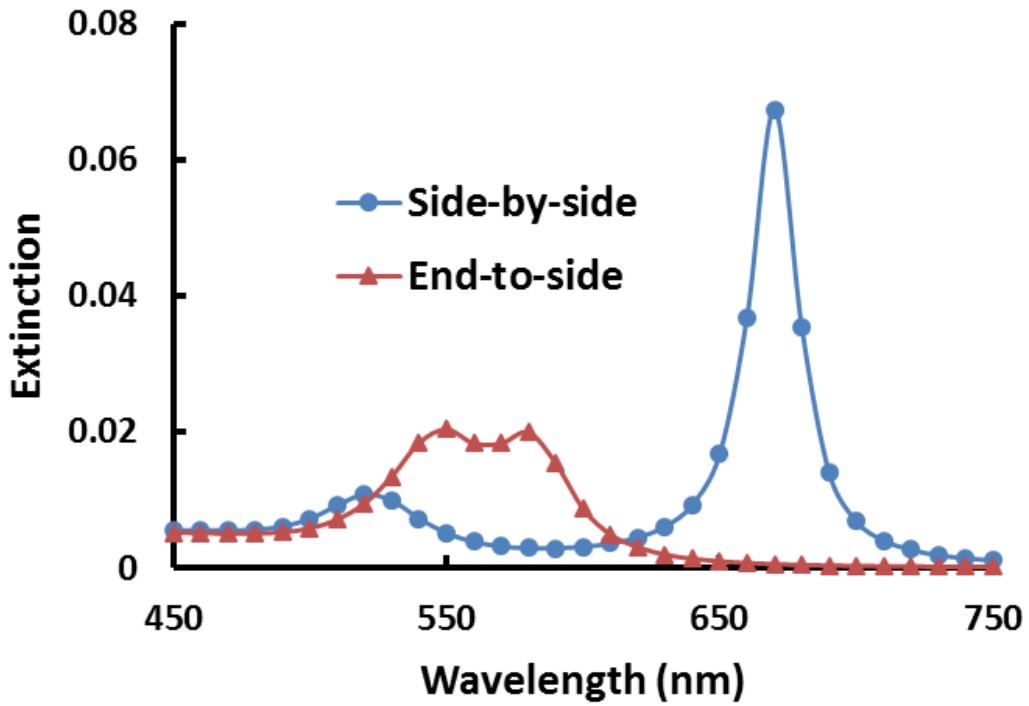

Figure 3.S6. Calculated extinction intensity of side-by-side and end-to-side GNRs assemblies versus wavelength (nm) of incident light using extended Mie theory

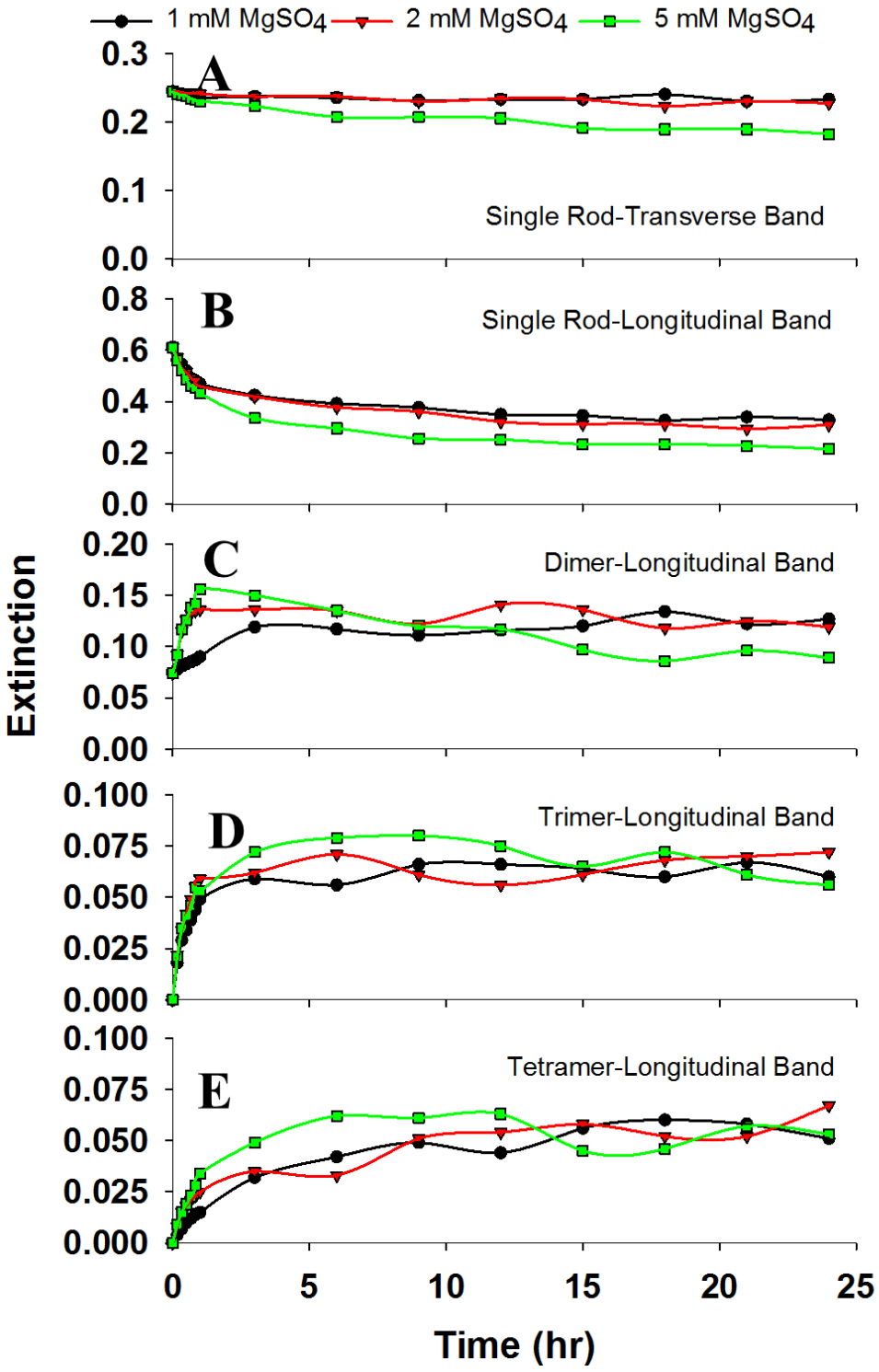

Figure 3.S7. Extinction intensities of different Lorentzian distribution band end-to-end assemblies of GNRs exposed to three different MgSO4 concentrations A) Transverse bands of single rod B) Longitudinal bands of single rod C) Longitudinal bands of dimer D) Longitudinal bands of trimer E) Longitudinal bands of tetramer

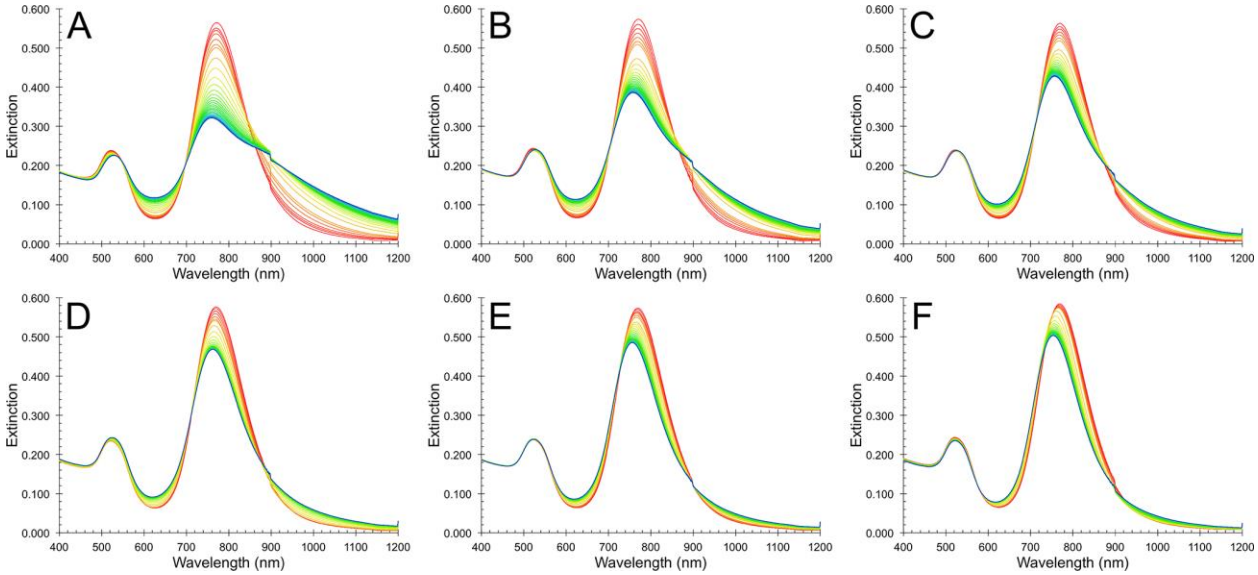

Figure 3.S8. Vis-NIR extinction spectra of 4 µM CTAB-GNRs (1.1×1014 gold nanorods/L) exposed to different concentrations of Na2SO4 and NaCl from t=0 hours (red spectrum) to t=24 hours (blue spectrum). (A) 5 mM Na2SO4, (B) 2 mM Na2SO4, (C) 1 mM Na2SO4, (D) 15 mM NaCl, (E) 6 mM NaCl, and (F) 3 mM NaCl.

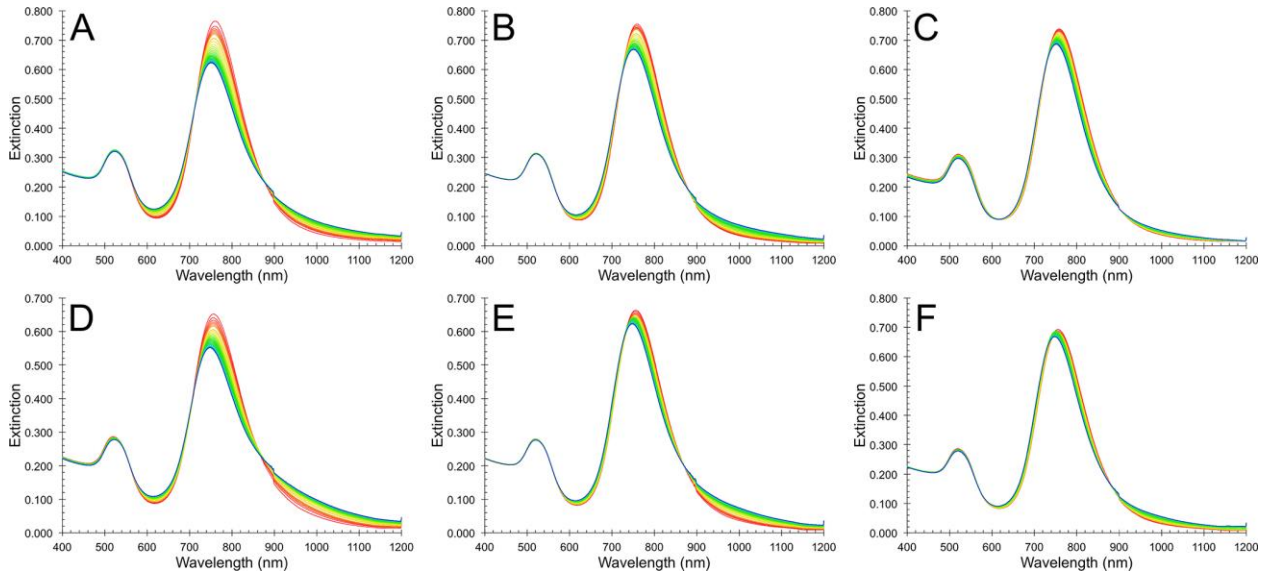

Figure 3.S9. Vis-NIR extinction spectra of 4 µM CTAB-GNRs (1.1×1014 gold nanorods/L) exposed to different concentrations of CaCl2 and MgCl2 solutions from t=0 hours (red spectrum) to t=24 hours (blue spectrum). (A) 5 mM CaCl2, (B) 2 mM CaCl2, (C) 1 mM CaCl2, (D) 5 mM MgCl2, (E) 2 mM MgCl2, and (F) 1 mM MgCl2.

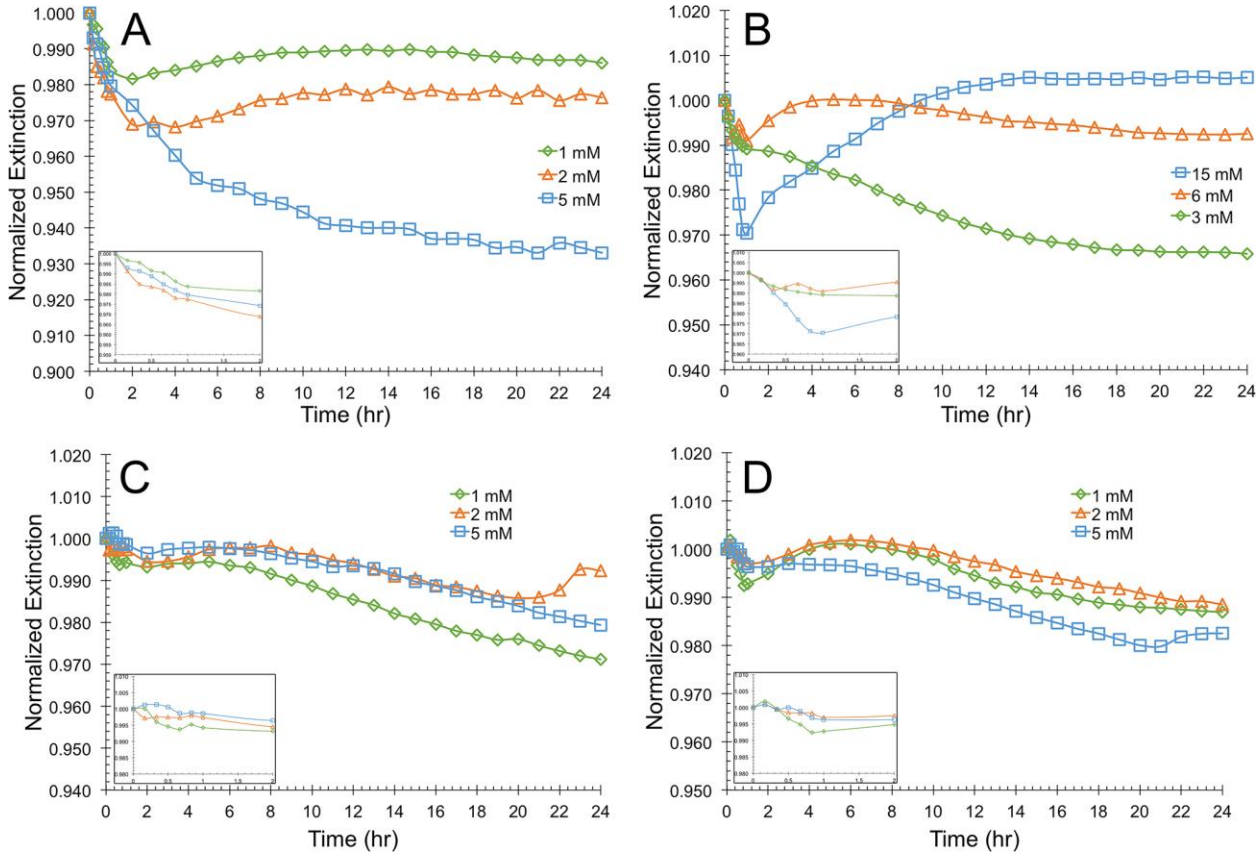

Figure 3.S10. Normalized transverse band extinction maxima of 4 µM CTAB-GNRs (1.1×1014 gold nanorods/L) in different (A) Na2SO4, (B) NaCl, (C) CaCl2, and (D) MgCl2 solutions as a function of exposure time. Insets show an expanded view of 0 to 2 hours exposure.

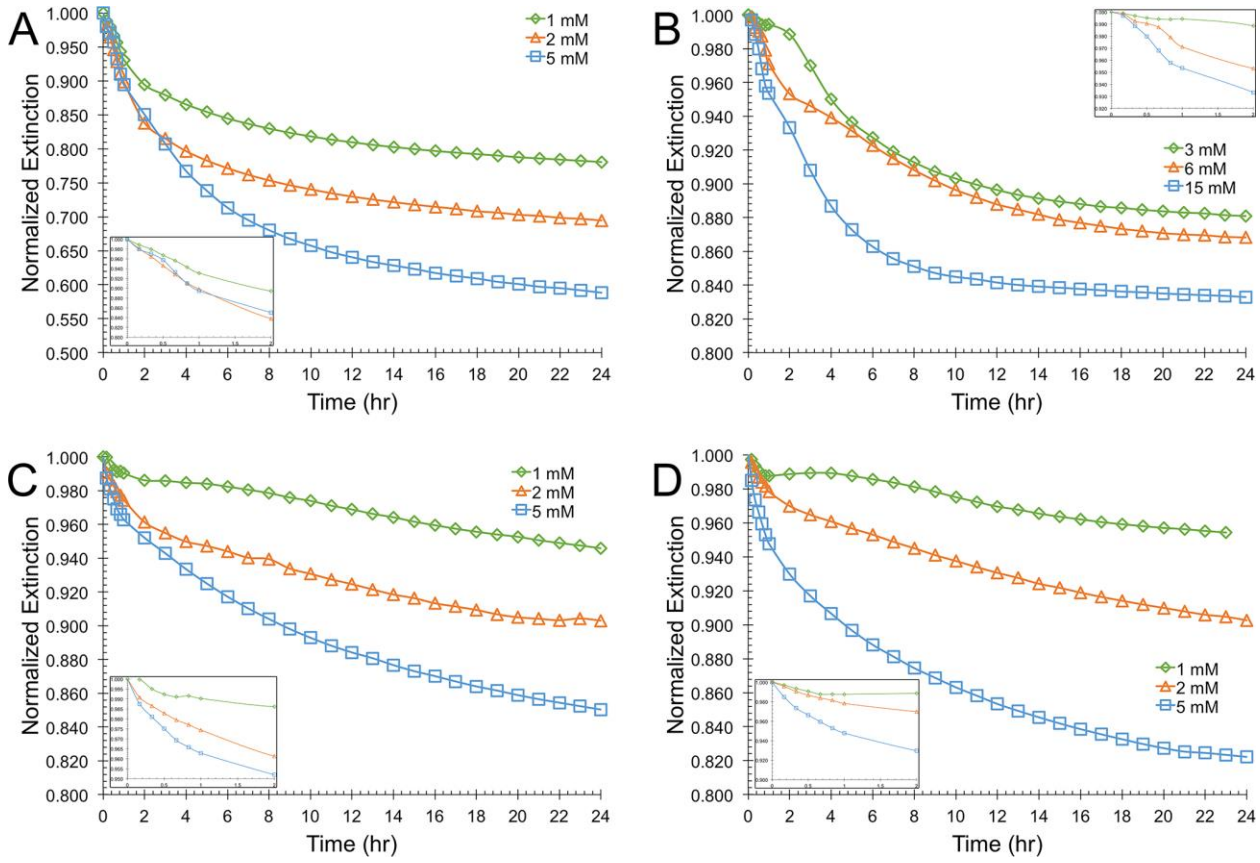

Figure 3.S11. Normalized longitudinal band extinction maxima of 4 µM CTAB-GNRs (1.1×1014 gold nanorods/L) in different (A) Na2SO4, (B) NaCl, (C) CaCl2, and (D) MgCl2 solutions as a function of exposure time. Insets show an expanded view of 0 to 2 hours exposure.

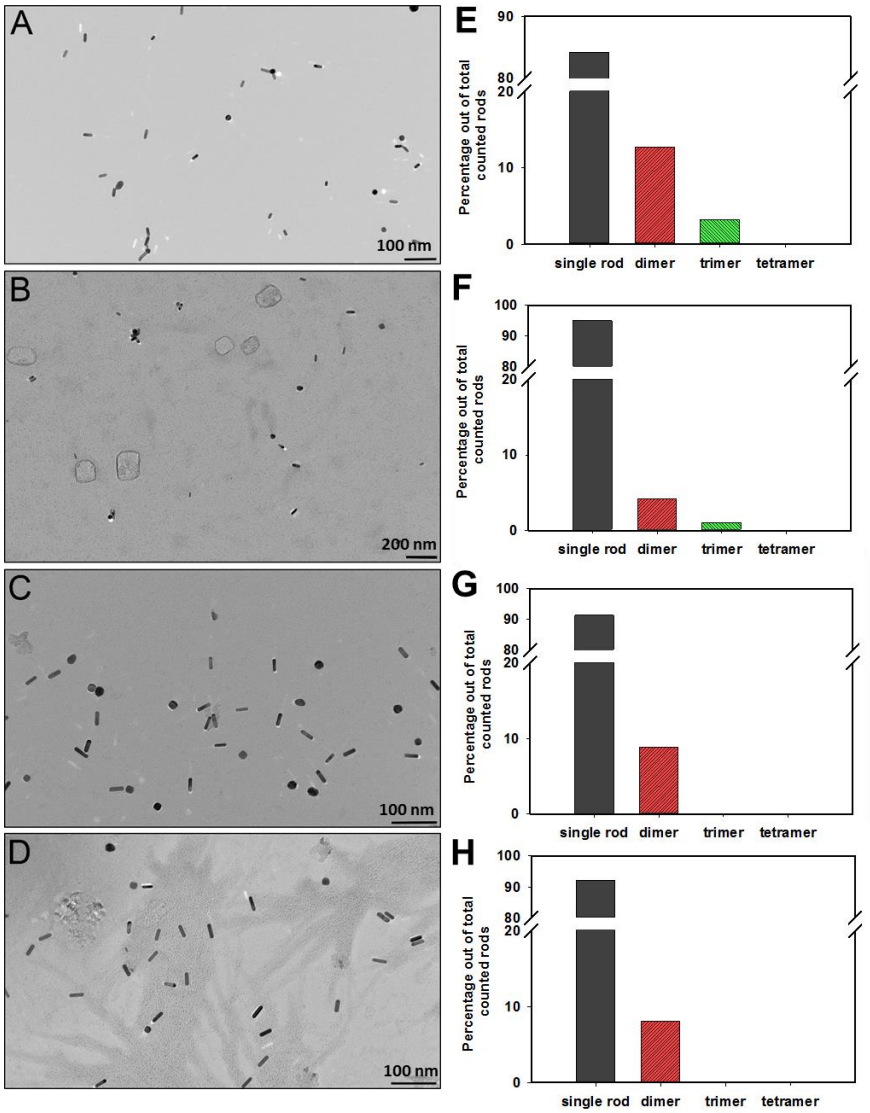

Figure 3.S12. A-D: TEM image of CTAB-GNRs taken after 10 h exposure to (A) 5 mM Na2SO4, (B) 15 mM NaCl, (C) 5 mM CaCl2, and (D) 5 mM MgCl2 solutions. All scale bars represent 100 nm. E-H: Percentage of counted GNRs forming different end-to-end assemblies. Analysis from E) 4 TEM images taken from GNRs exposed to 5 mM Na2SO4, (F) 7 TEM images taken from GNRs exposed to 15 mM NaCl, (G) 3 TEM images taken from GNRs exposed to 5 mM CaCl2, and (H) 4 TEM images taken from GNRs exposed to 5 mM MgCl2 solutions.

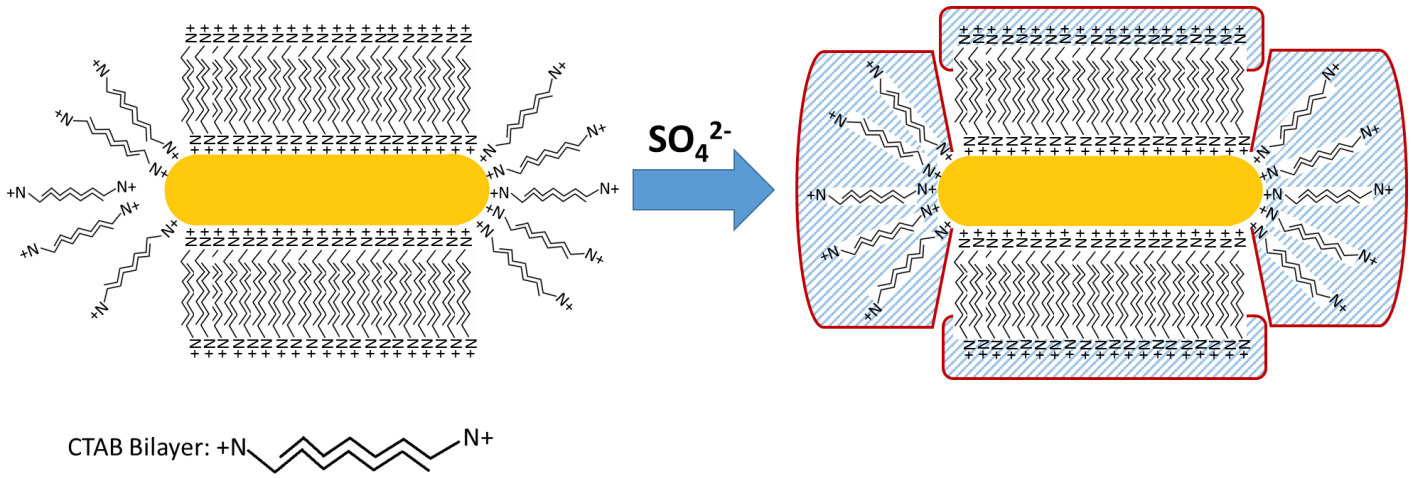

Figure 3.S13. Sulfate ion interaction with CTAB's quaternary ammonium head group on GNR surface

DLVO particle-particle interaction modeling

The introduced DLVO model here accounts van der Waals attraction and charge-charge repulsion as the dominant particle-particle interaction forces. Based on the relative positions (end-to-end, side-by-side, and end-to-side) of two adjacent GNRs the corresponding vdW attraction and charge repulsion equations are developed. Note that for end-to-end GNRs interaction, the tips of GNRs are modeled as two spheres having the same diameter as the GNRs. For end-to-side interaction one of the rods is modeled as an infinite plate while the other rod's tip is modeled as a sphere having the same diameter. For side-by-side interaction, both nanorods are modeled as cylinders having the same length and diameter as the GNR. We note that different facets of CTAB coated gold nanorods do have different surface charges. However, modeling this difference is challenging because at present there is no readily available technique to directly measure the surface charge of the side and tip facets of gold nanorods. The

value used in the modeling was based upon the measured zeta potential value as obtained using Malvern Zetasizer and by the application of the Smoluchowski equation.

This is a simplified DLVO model and more complex model can be developed. However, the results predicted by this model is in compliance with observed results from the actual experiment.

$$\phi_{net} = \phi_{VdW} + \phi_{ER}$$

Parameters

$T = 293\ K$

$\varepsilon = 80.1$

$\varepsilon_0 = 8.854\times10^{-24}\ {}^{C}/_{V\cdot m}$

$e = 1.602\times10^{-19}\ C$

$k_B = 1.38\times10^{-23}\ {}^{m^2\cdot kg}/_{s^2\cdot K}$

$L = 28.8\ nm$

$R = 3.3\ nm$

$\psi = \zeta = 20.6\ mV$

$I = 6.88\times10^{-3}\ {}^{mol}/_{L}$

$\kappa = \frac{1}{\lambda_D} = \sqrt{\frac{2Ie^2}{\varepsilon_0 \varepsilon k_B T}} = 2.94\times10^{8}\ {}^{1}/_{m}$

End-to-End Model

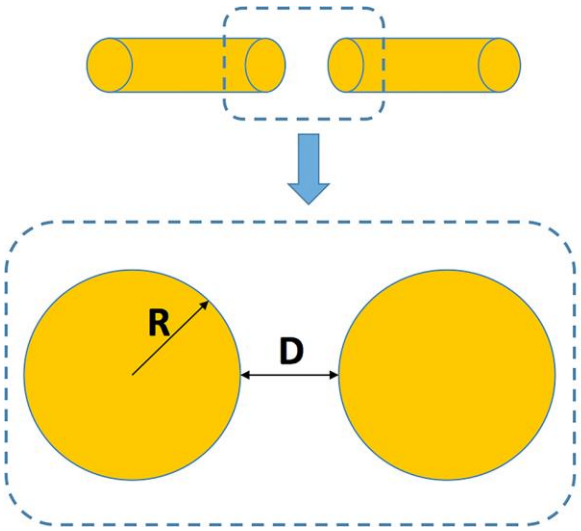

$$\phi_{VdW} = \frac{-AR}{12D}$$

$$A = 3.2\times10^{-20}\ J$$

$$\phi_{ER} = 32\pi\varepsilon_0\varepsilon R\left(\frac{k_B T}{ze}\right)^2 tanh^2\left(\frac{1}{4}\psi_s\right) exp(-\kappa D)$$

End-to-Side Model

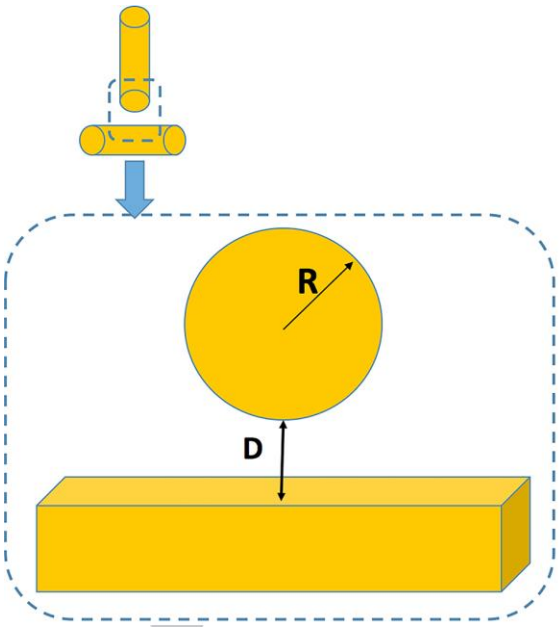

$$\phi_{vdw} = \frac{-AR}{6D}$$

$$A = 3.2\times10^{-20}\,J$$

$$\phi_{ER} = 4\pi\varepsilon\varepsilon_0 R\left(\psi^2 \exp(-\kappa D) + \frac{1}{4}\psi^2 \frac{R}{R+D}\exp(-2\kappa D)\right)$$

Side-by-Side Model

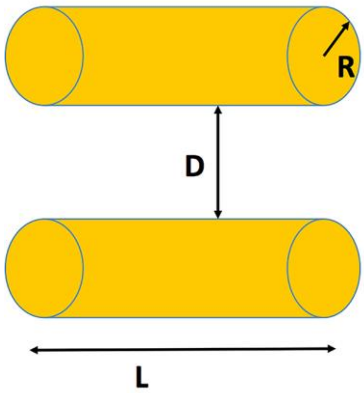

$$\phi_{vdw} = \frac{-ALR^{\frac{1}{2}}}{24D^{\frac{3}{2}}}$$

$$A = 3.2\times10^{-20}\,J$$

$$\phi_{ER} = 128\pi\varepsilon\varepsilon_0\left(\frac{k_B T}{ze}\right)^2 \frac{\gamma^2}{[1+\{1-(1-\beta^2)\gamma^2\}^{\frac{1}{2}}]^2}$$

$$\text{where, } \beta = \frac{K_0(\kappa R)}{K_1(\kappa R)} \text{ and } \gamma = \tanh\left(\frac{ez\psi}{4K_B T}\right) \text{ and}$$

$$K_i(x) = \text{zero and first order Bessel function of the second kind}$$

Chapter 4. Size, Shape, and Surface Coating Impacts on the Colloidal Stability and Aggregation Rate of Gold Nanoparticles in Aquatic Matrices

S.M.H. Abtahi[1, 2, 3, 4], Catherine J. Murphy[5], Navid B. Saleh[6], and P. J. Vikesland[1, 2, 3, 4]

1. Virginia Polytechnic Institute and State University, Department of Civil and Environmental Engineering, Blacksburg, Virginia, USA
2. Virginia Polytechnic Institute and State University, Institute for Critical Technology and Applied Science (ICTAS), Blacksburg, Virginia, USA
3. Virginia Polytechnic Institute and State University, Center for Sustainable Nanotechnology (VT SuN), Blacksburg, Virginia, USA
4. Center for the Environmental Implications of Nanotechnology (CEINT), USA
5. University of Illinois at Urbana-Champaign, Department of Chemistry, Champaign, Illinois, USA.
6. The University of Texas at Austin, Department of Civil, Architectural, and Environmental Engineering, Austin, Texas, USA

4.1 Abstract

GoId nanoparticles with different shapes and surface coatings are being developed for biomedical and industrial applications because of their unique properties. However, these nanoparticles can be a potential environmental contaminants post-use due to their high colloidal stability. In this study, the impacts of size, aspect ratio (AR), and surface coating on the colloidal stability of these gold nanoparticles in aquatic matrices were evaluated. Gold nanoparticles were exposed to synthetic fresh water solutions with ionic compositions ranging from very soft to very hard and the colloidal stability and aggregation rates of the particles were characterized by UV-VIS spectroscopy and ICP-MS (inductively coupled plasma mass spectrometry). As expected, the results suggest that for citrate coated AuNP, CTAB coated AR4 AuNR, and CTAB/BDAC coated AR8 AuNR the colloidal stabilities were reduced with an increase in ionic strength. Aggregation rates were evaluated using both first and second order kinetic rate equations. Moreover, the changes in aggregation rate versus solution hardness were determined for each type of gold nanoparticle. The collected results were consistent with electrolyte mediated double layer compression. For BSA coated gold nanoparticles of different shapes where the steric repulsion is strong, colloidal stability was not hindered by ionic strength of the solution and no aggregation was observed.

4.2 Introduction

ENMs (engineered nanomaterials) can be defined as particles that possess at least one dimension smaller than 100 nm and that possess unique physiochemical properties that originate from their size and structural characteristics[1]. According to a recent report by

the Centers for Disease Control and Prevention (CDC), current ENMs can be classified into four different groups based on their composition: elemental carbon, carbon compounds, metals and metal oxides, and ceramics[2]. Metal and metal oxide ENMs, among which gold and titanium dioxide are the most widely produced nanomaterials, are commonly used in industry. The Radiant Insights has predicted that the global market for gold nanoparticles will be approximately 13 tons by year 2020 with the medical industry as the first and electronics as the second largest application fields[3]. Noble metal nanoparticles such as gold are of interest for their potential application in biomedicine and electronics due to their unique electro-optical properties [4-8]. These properties result from the collective resonance of free surface electrons during their interaction with an electromagnetic field whose incident wavelength is longer than the size of the nanoparticle[4, 9]. This local coherent oscillation of conductive free electrons is termed LSPR (localized surface plasmon resonance) and is highly dependent on the size and shape of the nanoparticle [4, 5, 10-14]. The LSPR spectrum of gold nanospheres (AuNPs) shows a distinctive band at 500-550 nm within the visible range. The location of this band is size dependent and red shifts to higher wavelengths with an increase in size [15-17]. Unlike spherical nanoparticles, elongated nanoparticles such as gold nanorods (AuNRs), show two separate conduction electron oscillations along both the short axis (transverse oscillation) and the long axis (longitudinal oscillation) [8, 18-21]. The longitudinal plasmon band is highly aspect ratio (AR) dependent and red shifts to longer wavelengths with an increase in AR [20, 22, 23]. The Beer-Lambert equation (provided in the SI) suggests that the extinction intensity of these plasmon bands are linearly related to the suspension

nanoparticle concentration [15, 24]. As a result, aggregation rates can be determined based upon the decrease in the longitudinal and transverse plasmon bands with time.

There is a wide body of research examining the aggregation and deposition of ENMs in aquatic systems, but unfortunately only a few of these studies have focused on the roles of anisotropicity and AR. Petosa et.al recently reviewed the aggregation and deposition of various ENMs in aquatic environments including carbon nanotubes, fullerenes, metallic nanoparticles such as gold and iron, metal oxide nanoparticles such as titanium dioxide and ZnO plus quantum dots[25]. None of the studies reviewed in this paper systematically investigated the effects of shape and AR. To our best knowledge, in addition to our previous study on the aggregation kinetics and assembly of AuNRs[26] currently there are only two other environmentally relevant published studies on ZnO nanorods[27] and GNR[28] aggregation and interactions in which spheres and rods undergo different interactions and show different aggregation kinetics.

This study focused on the investigation of the impacts of size, shape, and surface coating of nanoparticles on their colloidal stability, fate, and aggregation rates in complex environmentally relevant aquatic matricies. Citrate coated AuNPs, cetyltrimethylammonium bromide (CTAB) coated AuNRs with different AR, and BSA (Bovine serum albumin) coated versions of these nanoparticles were used to carry out the experiments. Citrate and CTAB were chosen because they are commonly used during synthesis of AuNPs and AuNRs and are the primary coatings on these nanoparticle surfaces [8, 19, 29-32]. The effects of the aquatic matrix ionic strength on the colloidal stability of these nanoparticles were investigated by UV-Vis absorbance spectroscopy.

4.3 Materials and Methods

Gold Nanoparticle Synthesis. 19 nm citrate stabilized (citrate-AuNP) were prepared following the technique introduced by Jana et al. [19] based upon that originally developed by Turkevich [33].

Aspect ratio 4 (AR4) CTAB coated gold nanorod synthesis. AR4 AuNRs were synthesized via the seed-mediated surfactant-directed method [26, 34, 35]. Initially, 4 nm spherical gold seeds were synthesized through the reduction of chloroauric acid ($HAuCl_4$) in a 10 mM solution of cetyltrimethylammonium bromide (CTAB) by the addition of freshly prepared and ice-cooled sodium borohydride. AR4 AuNRs were then grown by a surfactant directed method in a growth solution consisting of CTAB, $HAuCl_4$, $AgNO_3$, and ascorbic acid. After addition of the gold seeds to the growth solution, the mixture was left undisturbed at 25°C for 2 hours. Other shape gold nanoparticle by-products such as spheres and cubes were removed by five sequential centrifugal wash (25 min at 8,000 x g) and pellet resuspension in 800 µM CTAB steps.

Aspect ratio 8 (AR8) CTAB coated gold nanorod synthesis. The Nikoobakht et al. synthesis method was used to synthesize AR8 AuNRs [35]. However, a few modifications were done to tune the size and overall yield of the AuNRs. 4 nm gold nanoseeds were prepared following the same process as for AR4 AuNRs, but the growth solution had a different combination consisting of $HAuCl_4$, $AgNO_3$, ascorbic acid, CTAB, and benzyldimethylammonium chloride (BDAC). The molar ratio of BDAC/CTAB was adjusted to 2.7 because it has been shown that ratios ranging from 2-5.5 result in less spherical nanoparticle byproducts. Moreover, 200 µL of 1 M HCl was added to 10 mL growth solution to further increase the yield of AR8 AuNRs. The growth solution was left

undisturbed in a 30 ºC water bath for 24 hours. Post synthesis, the mixture was centrifuged at 2,000 x g for 5 min. AR8 gold nanorods were primarily suspended in the supernatant, while the large spherical nanoparticles were precipitated as a pellet. Supernatant and pellet were later separated by pipette.

Bovine serum albumin (BSA) coating of AuNP and AR4 & AR8 AuNRs. BSA coating of AuNPs was done by incubating citrate-AuNP with a solution of 0.1 mg BSA/mL. The pH was adjusted to 9.0 by addition of 1 M NaOH. The mixture was then left undisturbed for 24 hours at 25°C. Excess unreacted BSA and citrate were removed by centrifugation at 10,000 x g for 30 minutes. AR4 and AR8 AuNR coating by BSA was done following the protocol developed by Tebbe et.al. [36]. For AR4 the CTAB and for AR8 the CTAB/BDAC concentrations were reduced to <0.1 mM by sequential centrifugal washing and replacement of the supernatant with DI water. It should be noted that the AuNRs were colloidally stable at this low surfactant concentration for just half an hour. Therefore, the residual surfactant reduction step was done immediately prior to ligand exchange. Afterwards, the gold nanoparticle suspension was added to a 10 mg/mL BSA solution under vigorous stirring. The volume ratio of BSA solution to AuNR suspension was 3:1. The pH of the mixture was adjusted to 7.0 and kept in a bath sonicator for 30 minutes. The mixture was centrifuged at 10,000 x g for 20 minutes and the supernatant was replaced by 1 mg/mL BSA solution at pH 12 and left undisturbed for 24 hours. The detached CTAB and BDAC and unreacted BSA were further separated by several sequential centrifugal washings.

Gold NP and NR characterization. The monodispersity, size distribution, and shape of the synthesized nanoparticles were characterized by dynamic light scattering (DLS), vis-

NIR spectroscopy, inductively coupled plasma mass spectroscopy (ICP-MS), and transmission electron microscopy (TEM). The primary intensity particle size distributions and monodispersity of the GNPs were assessed using a Malvern Zetasizer NanoZS DLS based on analysis of the correlation functions using the General Purpose algorithm and a non-negative least squares fit[37]. The Malvern NanoZS is equipped with a 175° angle backscattering detector and a 4 mW He-Ne 633 nm laser. The elemental gold content of the synthesized gold nanoparticles was measured using an Agilent 7500ce ICP-MS. In brief, a 1 mL sample of synthesized gold NPs and NRs was washed twice using sequential centrifugal washing at 10,000 x g for 20 min followed by 100× dilution in DI water. The sample was then transferred to a polystyrene tube where a 200 µL aliquot of aqua regia (1:3, Trace metal grade HNO_3:HCl) was added. After 2 hours digestion, the total volume was brought to 10 mL by addition of DI water. A Philips EM420 conventional electron microscope equipped with a CCD camera was used to measure the size distribution and shape of the AuNRs and AuNPs. In brief, TEM samples were prepared by drop-cast technique. A 10 µL droplet of sample was put on a 300 mesh carbon coated copper TEM grid and left undisturbed in a ventilated hood for 24 hours to dry. A Cary 5000 UV-Vis-NIR spectrometer and disposable 10 mm pathlength polystyrene cuvettes were used to measure the absorption intensity and plasmon band (transverse and longitudinal) locations of the AuNPs and AuNRs. DI water with a resistivity of 18.2 MΩ was produced by a Thermo Scientific Barnstead nanopure system. 10-100 µL and 100-1000 µL micropipettes with disposable tips were used during all sets of experiments.

Colloidal stability assay of AuNPs and AuNRs in different ionic strength solutions. 2 mg/L elemental gold concentration of AuNPs and AuNRs with different surface coatings

were exposed to freshly prepared synthetic EPA standard waters of various hardness for 24 hours. The detailed water chemistries of these waters are described in **Table 4.S1**.

To initiate an experiment, non-BSA and BSA coated AuNPs and AuNRs were washed by centrifugation at 10,000 x g for 15 min and replacement of 95% of the supernatant with DI water prior to resuspension. Nanoparticles were resuspended in DI water by bath sonication for 1 min. Resuspended AuNRs and AuNPs were readily redispersed and colloidally stable in suspension without any perceptible aggregation. Following a second centrifugation step, the supernatant was replaced with a predetermined volume of given EPA standard water solutions ranging from very soft to very hard hardness to achieve a final 2 mg/L elemental gold concentration. The nanoparticle suspensions were transferred to vis-NIR plastic cuvettes that were used for 24-hour colloidal stability tests. 20 min sampling intervals and 1 hr intervals were used for the first hour and the rest of the time course of the experiments. Vis-NIR extinction spectra ranging from 400-800 nm, 400-1050 nm, and 400-1350 nm were used to collect absorption intensities of 19 nm AuNPs, AR4 AuNRs, and AR8 AuNRs, respectively.

4.4 Results and discussion

Gold nanoparticle characterization. Nanoparticles were primarily characterized by TEM, UV-Vis-NIR, electrophoretic mobility, and ICP-MS measurements. TEM images of these nanoparticles are shown as insets in Figure 4.1 along with the associated vis-NIR absorption spectra. Additional TEM images are provided in Figure 4.S1. Citrate-AuNPs were 19.2 ± 0.2 nm while AR4 and AR8 AuNRs had average lengths of 42.1 ± 0.3 and 83.4 ± 0.2 nm and diameters of 11.2 ± 0.1 and 10.5 ± 0.3 nm, respectively. The noted

errors reflect the 95% confidence interval of n = 30 measurements obtained using ImageJ). The average ARs of the elongated nanoparticles were 3.76 ± 0.2 and 7.94 ± 0.3, but for simplicity they are addressed as AR4 and AR8 AuNRs in this paper.

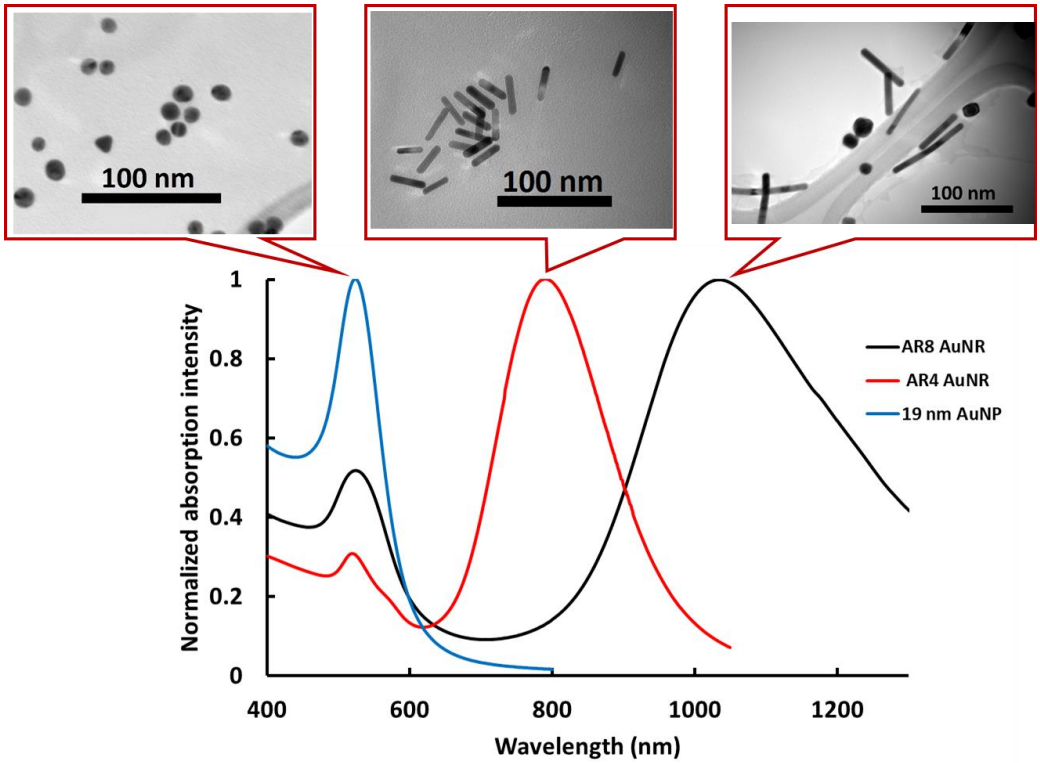

Figure 4.1. Vis-NIR normalized absorption and TEM images of synthesized AuNP and AR4 and AR8 AuNRs prior to BSA coating

Post BSA coating, the AuNP, AR4, and AR8 AuNRs retained their shapes, but the plasmon bands red-shifted to higher wavelengths. This shift happens due to changes in the local dielectric constant of the medium after BSA coating and has been previously described in the literature[22, 26]. Table 4.1 shows the plasmon band wavelengths and zeta potential values for citrate AuNPs and CTAB and CTAB/BDAC coated AuNRs before and after BSA coating. Zeta potential values were calculated based on electrophoretic mobility measurements and the application of Henry's equation (details in the SI). The Henry's constants for different sizes and ARs of AuNP and AuNRs were calculated based

on Ohshima's correction[38, 39]. The reported values are the average of 3 measurements of 15 runs each. ICP-MS measurements indicate that the stock suspension of AuNP, AR4 AuNR, and AR8 AuNR had 93.6 ± 0.1, 41.1 ± 0.3, and 19.4 ± 0.2 mg/L elemental gold concentrations.

Table 4.1. Plasmon band wavelengths, Zeta potential, and electrophoretic mobility (EM) values of citrate AuNP, CTAB AR4 AuNR, and CTAB/BDAC coated AR8 AuNR suspension in DI water before and after BSA coating

	Initial coating				BSA coating			
	Transverse band (nm)	Longitudinal band (nm)	Zeta potential (mv)	EM (μm.cm/V.s)	Transverse band (nm)	Longitudinal band (nm)	Zeta potential (mv)	EM (μm.cm/V.s)
AuNP 19 nm	523	N.A.	-36.0 ± 2.2	-2.90 ± 0.12	529	N.A.	-45.3 ± 1.2	-3.78 ± 0.02
AR4 AuNR	510	798	+39.2 ± 3.1	3.45 ± 0.09	513	803	-29.4 ± 0.6	-2.46 ± 0.15
AR8 AuNR	524	1044	+41.4 ± 0.8	4.18 ± 0.18	529	1052	-21.5 ± 1.1	-1.91 ± 0.07

Gold nanoparticle colloidal stability and aggregation rates in EPA standard waters.

The changes in the monomer (colloidally stable single nanoparticle) concentrations in the suspensions over the 24-hour time course of the experiments are presented in Figure 4.2. As we reported before, these graphs were created by considering a linear correlation between the change in the plasmon band absorption intensities and changes in the mass concentration of nanoparticles, based upon the Beer-Lambert law[26]. As expected, citrate coated AuNPs, CTAB coated AR4 AuNRs, and CTAB/BDAC coated AR8 AuNRs become increasingly unstable with an increase in solution hardness. The harder the water, the more rapidly the nanoparticles aggregate and there was a concomitant decrease in both the transverse and longitudinal bands, Figure 4.S2-4. For non-BSA coated AuNPs and AuNRs, electrostatic repulsion among the adjacent nanoparticles is the main deterrent to aggregation. By increasing the ionic strength of the solution from

4.69×10^{-4} M in the case of very soft to 1.51×10^{-2} M for very hard, the electrostatic double layer surrounding the nanoparticles is compressed. The presence of large amounts of divalent cations and anions such as Ca^{2+}, Mg^{2+}, CO_3^{2-}, and SO_4^{2-} in the high ionic strength solutions along with monovalent cations and anions such as Na^+, K^+, and Cl^- strongly facilitates the reduction of the diffuse layer thickness[40-43]. Divalent anions and cations such as Ca^{2+}, Mg^{2+}, and SO_4^{2-} can contribute to the aggregation of nanoparticles via another mechanism termed bridging[44-47]. Our prior study showed the end-to-end assembly formation of CTAB coated AR4 AuNRs mediated by divalent SO_4^{2-} present in the solution[26]. The length of the assembly increased with an increase in the sulfate concentration. This significant compression of double layer results in a measurable decrease in zeta potential. The measured zeta potential values of the gold nanoparticle suspensions for each ionic strength EPA water are listed in Table 4.2. Consequently, the net charge-charge repulsion forces between these nanoparticles decrease while these nanoparticles are moving via Brownian motion and coming in proximity of one another. Minimal electrostatic repulsion leads to enhanced collision of the adjacent nanoparticles and the formation of aggregates. The size of the aggregates increases with time and they eventually become colloidally unstable and precipitate.

Unlike the non-BSA coated nanoparticles, the BSA coated AuNP, AR4, and AR8 AuNR were colloidally stable at all ranges of ionic strengths employed in these sets of experiments (as evinced by a time invariant UV-Vis spectrum and elemental gold concentration in the suspension), Figure 4.S5A-C. BSA coated nanoparticles benefited from both charge and steric repulsion anti-aggregation mechanisms[43, 48, 49]. Increasing the ionic strength of the solution decreased the electrostatic repulsion forces

among these nanoparticles due to the decrease of the zeta potential values, Table 4. 2. However, steric repulsion forces originating from the thick polymeric layer of BSA covering these nanoparticles were unaffected and strong enough to keep these nanoparticles colloidally stable at all ranges of ionic strengths[48, 50-52].

An intense sharp drop in both the transverse and longitudinal peak intensities were observed within the first hour of exposure of non-BSA coated nanoparticles to EPA waters in almost all cases, Figure 4.S2-4, Figure 4.2A-C. This decreasing trend smoothly and less-intensely continues for the remaining 23 hours in the case of elongated AuNRs. Unlike AuNRs, the plasmon band intensity of citrate AuNP kept dropping intensely for the first 10 hours and smoothed-out for the remaining 14 hours for very hard, hard, and moderately hard EPA waters, Figure 4.2A. These consistent sharp drops indicate that citrate AuNPs are more substantially affected by higher ionic strength solutions compared to elongated AuNRs. Zeta potential measurements of these nanoparticles over the time course of the experiment further prove that citrate coated nanoparticles had lower zeta potential values at moderately hard, hard, and very hard ionic strength solutions, Table 4. 2. Moreover, elongated gold nanorods have an extra rotational diffusion mechanism as compared to gold nanospheres that only have transitional diffusion[53, 54]. The diffusion coefficient of AuNP and the transitional and rotational diffusion coefficients of the AuNRs were calculated based on physical parameters used in the experiment (details in the SI). The diffusion coefficient of the AuNPs was 11.2 x 10^{-11} (m^2/S). The transitional diffusion coefficients of AR4 AuNR and AR8 AuNR were, 10.7 x 10^{-11} and 4.14 x 10^{-11}(m^2/S), respectively. The transitional diffusion coefficient of AR4 AuNR was comparable in magnitude to AuNP while AR8 AuNR had the smallest transitional diffusion coefficient. A

similar pattern was observed for both parallel and perpendicular rotational diffusion coefficients of the AuNRs. The parallel and perpendicular diffusion coefficients of AR4 AuNR were 3.52 x 10^3 and 1.39 x 10^3 (S^{-1}) while for AR8 AuNR were decreased to 2.72 x 10^3 and 0.21 x 10^3 (S^{-1}). Both transitional and rotational diffusion coefficients were noticeably decreased with an increase in AR. The extra rotational movement and elongation along one axis reduce the mean square distance (MSD) random walk of nanorods compared to nanospheres and result in fewer collisions among adjacent nanorods. Having lower zeta potential values and faster Brownian motion of AuNPs relative to AuNRs, resulted in higher aggregation rates.

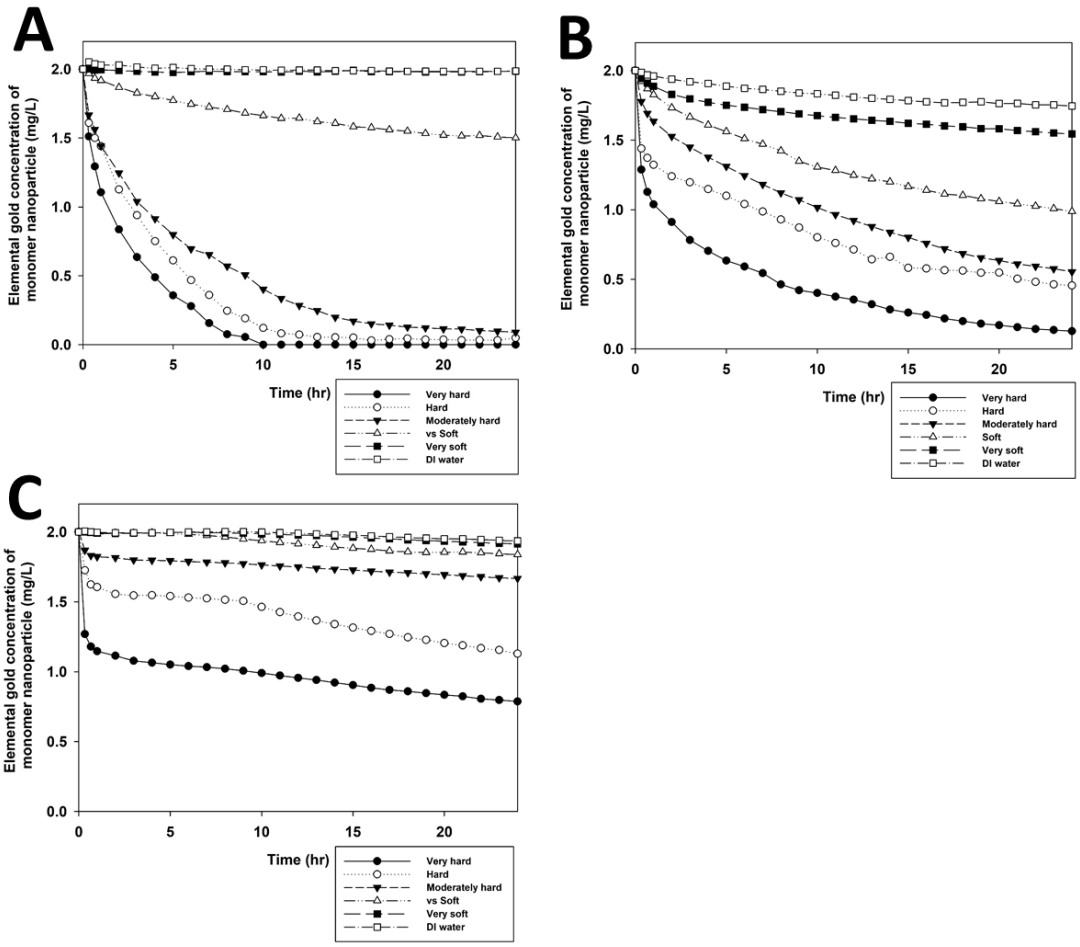

Figure 4.2. Elemental gold concentration changes of monomer (colloidally stable single nanoparticles) nanoparticles in the suspension versus time A) Citrate coated AuNP B) CTAB coated AR4 AuNR C) CTAB/BDAC coated AR8 AuNR

Table 4.2. Zeta potential measurements of AuNP and AuNRs having different surface coating exposed to EPA waters ranging from very soft to very hard.

	Non-BSA coated			BSA coated		
	AuNP	AR4 AuNR	AR8 AuNR	AuNP	AR4 AuNR	AR8 AuNR
DI water	-36.0 ± 2.2	+39.2 ± 3.1	+41.4 ± 0.8	-45.3 ± 1.2	-29.4 ± 0.6	-21.5 ± 1.1
Very soft	-31.5 ± 1.3	+34.0 ± 0.6	+40.3 ± 2.3	-40.2 ± 0.8	-24.4 ± 1.1	-18.6 ± 0.1
Soft	-21.4 ± 2.0	+30.2 ± 1.5	+33.2 ± 1.7	-28.4 ± 2.0	-19.5 ± 0.6	-14.3 ± 1.2
Moderately hard	-12.1 ± 0.8	+21.2 ± 1.0	+26.2 ± 0.6	-18.5 ± 0.6	-13.2 ± 1.4	-11.2± 0.2
Hard	-9.0 ± 1.1	+15.1 ± 0.3	+19.1 ± 1.4	-11.2 ± 1.4	-8.8 ± 0.2	-7.4 ± 2.2
Very hard	-5.1 ± 0.11	+9.2 ± 1.6	+12.6 ± 0.3	-8.3 ± 0.6	-4.3 ± 1.5	-3.2 ± 1.1

Aggregation rates were calculated based on the change in the elemental mass concentration of colloidally stable individual nanoparticles in the suspension. Citrate coated AuNP followed a fist order aggregation kinetics rate while CTAB AR4 AuNR and CTAB/BDAC AR8 AuNR were best fit by second-order aggregation kinetics. The calculation details are provided in the SI. The overall kinetic aggregation rates for non-BSA coated nanoparticles are presented in Figure 4.3.

The first order aggregation rate for citrate AuNP has a different unit compared to second order rate of AuNRs, hr^{-1} vs. $L.mg^{-1}.hr^{-1}$. To be able to compare these rates, aggregation rate half-times for each nanoparticle concentration were derived for the different solution hardness values that they were exposed to and are plotted in Figure 4.4, half-time equations for each aggregation rate order are provided in SI. Having a smaller aggregation rate half-time at a specific solution hardness represents a larger aggregation

rate of that nanoparticle. For all non-BSA coated gold nanoparticles the aggregation rates increased with the increase in the hardness of the solutions, Table 4.3.

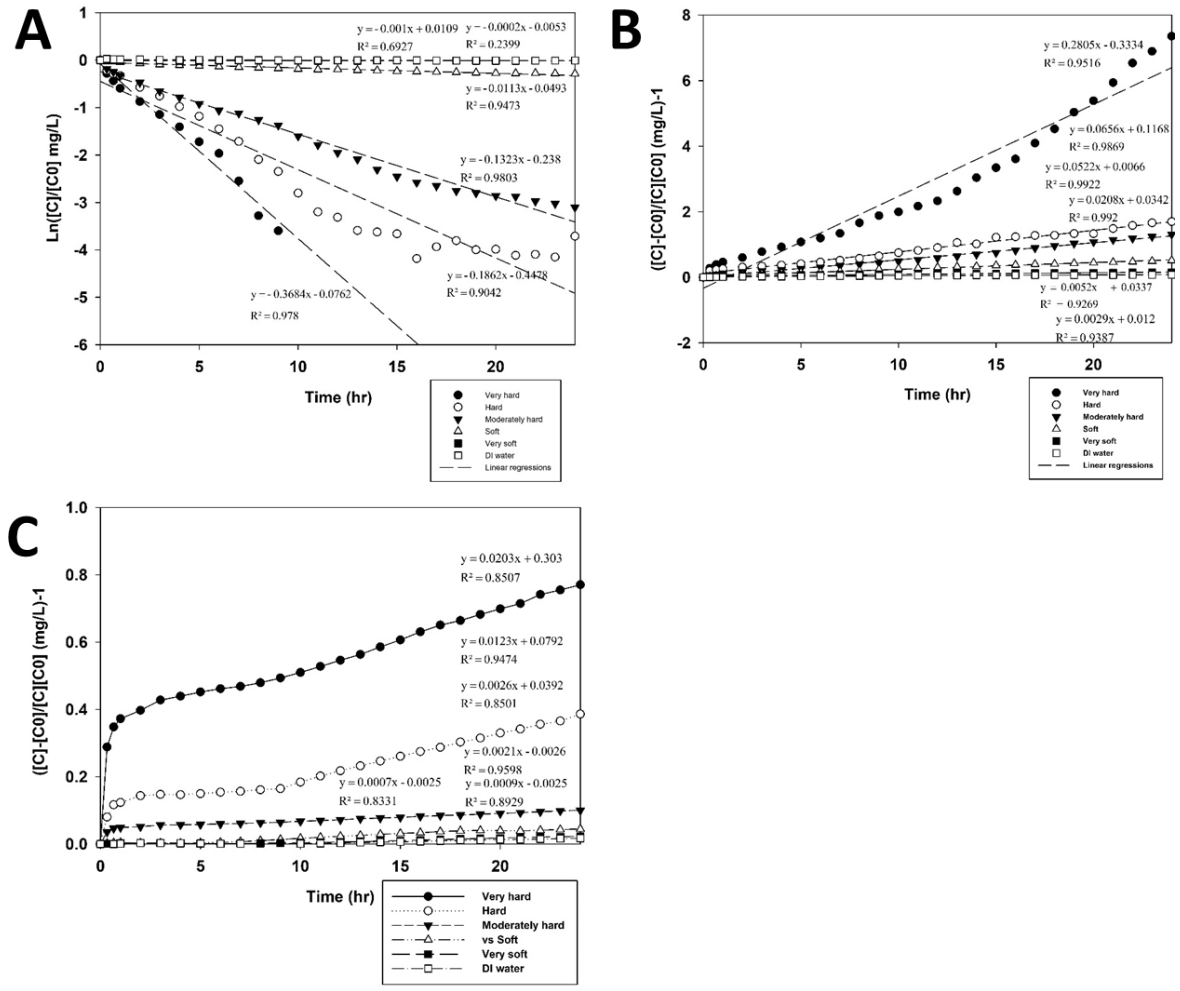

Figure 4.3. Aggregation rates for different ionic strength solutions. A) First-order aggregation rates for citrate AuNP B) Second order aggregation rate for CTAB AR4 AuNR C) Second order aggregation rate for CTAB/BDAC AR8 AuNR

Table 4.3. Calculated aggregation rates for non-BSA coated AuNP and AR4 and AR8 AuNRs in different EPA waters with various ionic strength hardness

		Aggregation rate		
	Hardness (mg $CaCO_3$/L)	AuNP (1/hr)	AR4 AuNR (L/mg.hr)	AR8 AuNR (L/mg.hr)
Very hard	300	0.368 ± 0.020	0.280 ± 0.015	0.020 ± 0.003
Hard	170	0.186 ± 0.015	0.065 ± 0.005	0.012 ± 0.002
Moderately hard	90	0.132 ± 0.012	0.052 ± 0.004	0.003 ± 0.000
Soft	44	0.011 ± 0.003	0.020 ± 0.004	0.002 ± 0.000
Very soft	12	0.001 ± 0.000	0.005 ± 0.000	0.001 ± 0.000
DI water	0	0.000 ± 0.000	0.003 ± 0.000	0.001 ± 0.000

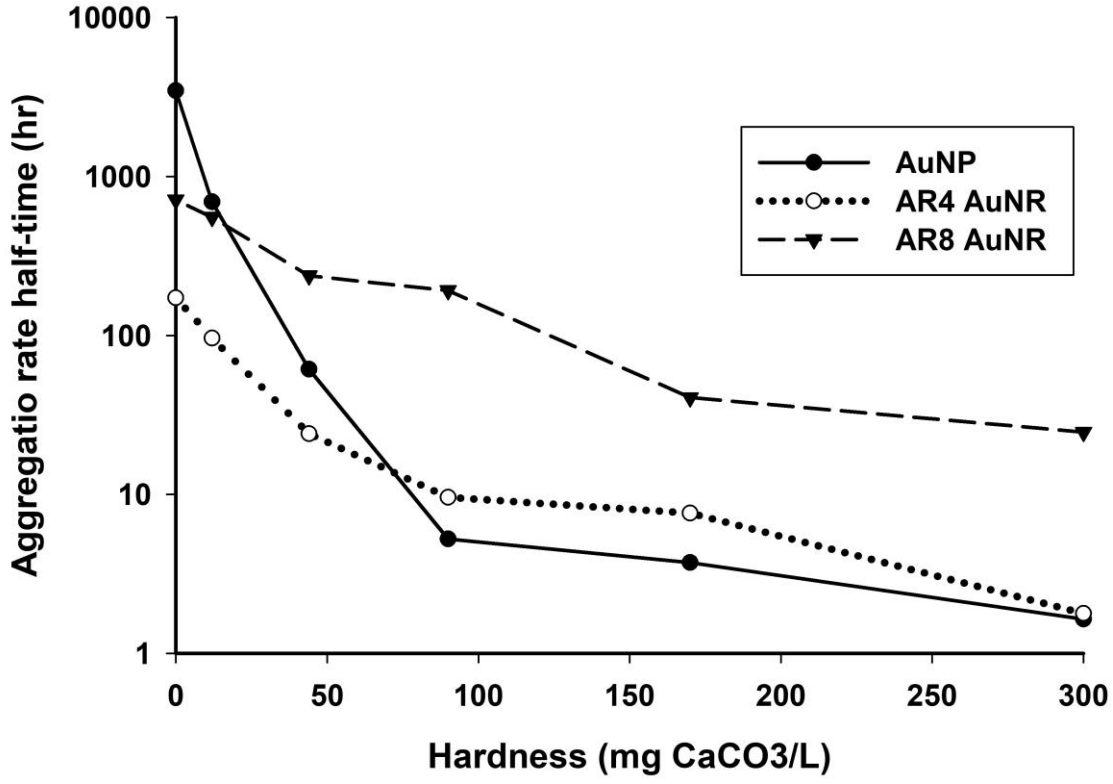

Figure 4.4. Aggregation rate half times for different non-BSA coated gold nanoparticles versus the hardness of the exposure solutions

Citrate AuNPs had the shortest aggregation rate half-times and the highest aggregation rates due to their lower zeta potential values at higher ionic strength solutions and more rapid Brownian motion as explained previously. AR4 AuNRs had longer half-times in high ionic strength solutions and shorter half times in low ionic strength solutions compared to Citrate AuNPs. This means that CTAB coated AR4 AuNRs are more stable in high ionic strength solutions and less stable in low ionic strength solutions relative to similarly sized Citrate AuNPs. AR8 AuNRs were relatively more colloidally stable than AR4 AuNRs by having the longest aggregation rate half-times. These results were not surprising since the larger AR8 AuNRs had lower Brownian motion due to the larger size and higher AR[54]. It should be noted that there are other interparticle attractive forces such as van-der-Waals forces, electromagnetic dipole-dipole interaction, and depletion interactions whose magnitudes increase with an increase in nanoparticle size[55-60]. The competition between repulsive forces (electrostatic and steric repulsion) and the mentioned attractive forces dictates the final colloidal stability state of nanoparticles in suspension. Attractive interparticle interactions can overcome repulsive interactions for larger sized nanoparticles and result in suspension colloidal instability and aggregation. Our findings in this study that is increasing colloidal stability with increase in AR of AuNRs is derived based upon specific ionic strength conditions, size, shape, and surface coatings of AuNRs. Therefore, it cannot be generalized to other sizes and ARs without factoring in other interparticle interactions.

Gold nanoparticle aggregation rates in environmentally relevant scenarios.

The water hardness map of the United States is depicted in Figure 4.5. States located on the East coast and the West coast have soft and moderately hard waters, while the

states located on central united states have hard and very hard waters with a relatively higher ionic strengths. The current study shows how the colloidal stability and aggregation rates of these gold nanoparticles with different size, shape, and surface coatings can have different environmental impacts depending on the exposure location in the US. In a same exposure scenario model, gold nanoparticles released into the surface waters located on east coast and west coast states stay colloidally stable for a longer period of time and can distribute farther compared to the surface waters located on the central united states. The current aggregation rate study can enhance the overall understanding and predicting abilities during an environmental exposure fate, and transport modeling for these gold nanoparticles.

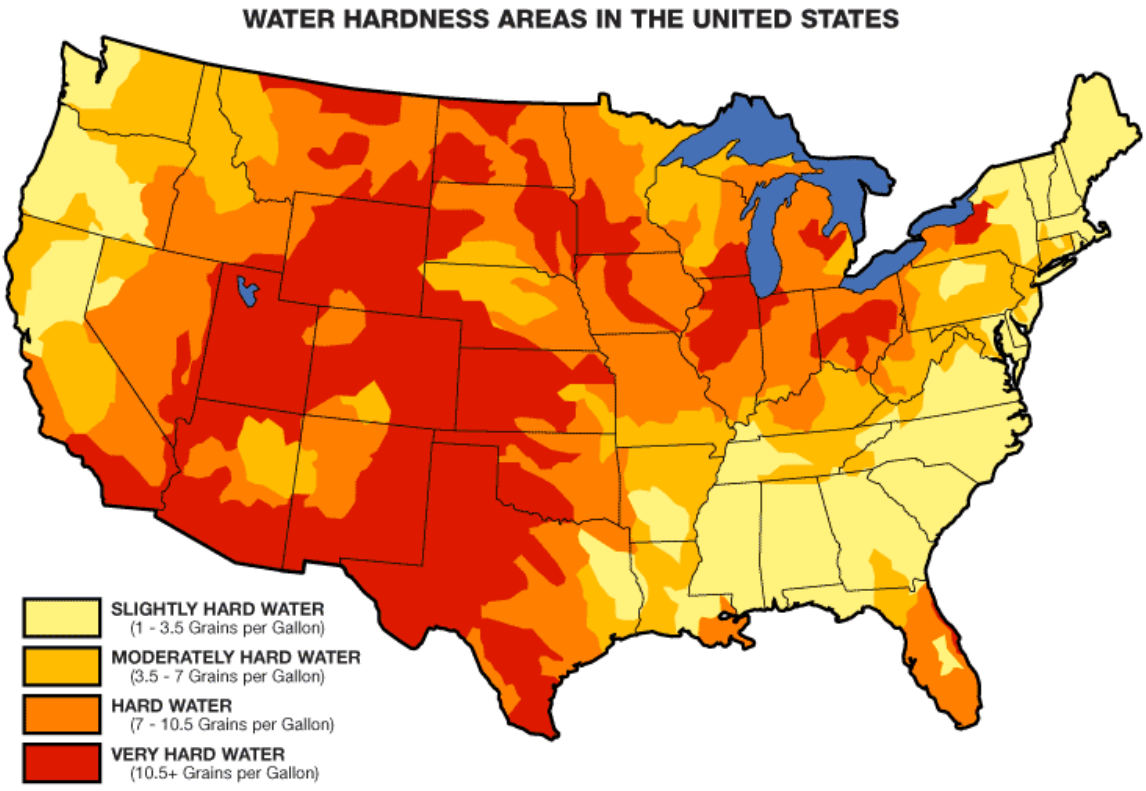

Figure 4.5. Water hardness distribution in the USA

4.5 References

1. Rotello, V.M., *Nanoparticles: building blocks for nanotechnology*. 2004: Springer Science & Business Media.
2. Topmiller, J.L. and K.H. Dunn, *Current strategies for engineering controls in nanomaterial production and downstream handling processes.* 2013.
3. Cooper, S., *Gold Nanoparticles Market Analysis by Application (Medical & Dentistry, Electronics, Catalysis and Sensors & Probes) And Segment Forecasts To 2020*. December, 2014, Radiant Insights.
4. Kelly, K.L., et al., *The optical properties of metal nanoparticles: the influence of size, shape, and dielectric environment.* The Journal of Physical Chemistry B, 2003. **107**(3): p. 668-677.
5. Sosa, I.O., C. Noguez, and R.G. Barrera, *Optical properties of metal nanoparticles with arbitrary shapes.* The Journal of Physical Chemistry B, 2003. **107**(26): p. 6269-6275.
6. McConnell, W.P., et al., *Electronic and optical properties of chemically modified metal nanoparticles and molecularly bridged nanoparticle arrays.* The Journal of Physical Chemistry B, 2000. **104**(38): p. 8925-8930.
7. Yu, Y.-Y., et al., *Gold nanorods: electrochemical synthesis and optical properties.* The Journal of Physical Chemistry B, 1997. **101**(34): p. 6661-6664.
8. Murphy, C.J., et al., *Anisotropic metal nanoparticles: synthesis, assembly, and optical applications.* The Journal of Physical Chemistry B, 2005. **109**(29): p. 13857-13870.

9. Willets, K.A. and R.P. Van Duyne, *Localized surface plasmon resonance spectroscopy and sensing.* Annu. Rev. Phys. Chem., 2007. **58**: p. 267-297.

10. Hornyak, G.L., C.J. Patrissi, and C.R. Martin, *Fabrication, characterization, and optical properties of gold nanoparticle/porous alumina composites: the nonscattering Maxwell-Garnett limit.* The Journal of Physical Chemistry B, 1997. **101**(9): p. 1548-1555.

11. Link, S. and M.A. El-Sayed, *Spectral properties and relaxation dynamics of surface plasmon electronic oscillations in gold and silver nanodots and nanorods.* The Journal of Physical Chemistry B, 1999. **103**(40): p. 8410-8426.

12. Kottmann, J.P., et al., *Dramatic localized electromagnetic enhancement in plasmon resonant nanowires.* Chemical Physics Letters, 2001. **341**(1): p. 1-6.

13. Imura, K., T. Nagahara, and H. Okamoto, *Plasmon mode imaging of single gold nanorods.* Journal of the American Chemical Society, 2004. **126**(40): p. 12730-12731.

14. Elghanian, R., et al., *Selective colorimetric detection of polynucleotides based on the distance-dependent optical properties of gold nanoparticles.* Science, 1997. **277**(5329): p. 1078-1081.

15. Haiss, W., et al., *Determination of size and concentration of gold nanoparticles from UV-vis spectra.* Analytical chemistry, 2007. **79**(11): p. 4215-4221.

16. Liu, X., et al., *Extinction coefficient of gold nanoparticles with different sizes and different capping ligands.* Colloids and Surfaces B: Biointerfaces, 2007. **58**(1): p. 3-7.

17. Amendola, V. and M. Meneghetti, *Size evaluation of gold nanoparticles by UV−vis spectroscopy.* The Journal of Physical Chemistry C, 2009. **113**(11): p. 4277-4285.

18. Gou, L. and C.J. Murphy, *Fine-tuning the shape of gold nanorods.* Chemistry of materials, 2005. **17**(14): p. 3668-3672.

19. Jana, N.R., L. Gearheart, and C.J. Murphy, *Wet chemical synthesis of high aspect ratio cylindrical gold nanorods.* The Journal of Physical Chemistry B, 2001. **105**(19): p. 4065-4067.

20. Pérez-Juste, J., et al., *Gold nanorods: synthesis, characterization and applications.* Coordination Chemistry Reviews, 2005. **249**(17): p. 1870-1901.

21. Prescott, S.W. and P. Mulvaney, *Gold nanorod extinction spectra.* Journal of applied physics, 2006. **99**(12): p. 123504.

22. Link, S., M. Mohamed, and M. El-Sayed, *Simulation of the optical absorption spectra of gold nanorods as a function of their aspect ratio and the effect of the medium dielectric constant.* The Journal of Physical Chemistry B, 1999. **103**(16): p. 3073-3077.

23. Eustis, S. and M.A. El-Sayed, *Determination of the aspect ratio statistical distribution of gold nanorods in solution from a theoretical fit of the observed inhomogeneously broadened longitudinal plasmon resonance absorption spectrum.* Journal of applied physics, 2006. **100**(4): p. 044324.

24. Kim, T., et al., *Kinetics of gold nanoparticle aggregation: experiments and modeling.* Journal of colloid and interface science, 2008. **318**(2): p. 238-243.

25. Petosa, A.R., et al., *Aggregation and deposition of engineered nanomaterials in aquatic environments: role of physicochemical interactions.* Environmental science & technology, 2010. **44**(17): p. 6532-6549.

26. Abtahi, S., et al., *Sulfate-Mediated End-to-End Assembly of Gold Nanorods.* Langmuir, 2017. **33**(6): p. 1486-1495.

27. Zhou, D. and A.A. Keller, *Role of morphology in the aggregation kinetics of ZnO nanoparticles.* Water research, 2010. **44**(9): p. 2948-2956.

28. Afrooz, A.N., et al., *Spheres vs. rods: The shape of gold nanoparticles influences aggregation and deposition behavior.* Chemosphere, 2013. **91**(1): p. 93-98.

29. Gao, J., C.M. Bender, and C.J. Murphy, *Dependence of the gold nanorod aspect ratio on the nature of the directing surfactant in aqueous solution.* Langmuir, 2003. **19**(21): p. 9065-9070.

30. Nikoobakht, B. and M.A. El-Sayed, *Preparation and growth mechanism of gold nanorods (NRs) using seed-mediated growth method.* Chemistry of Materials, 2003. **15**(10): p. 1957-1962.

31. Smith, D.K. and B.A. Korgel, *The importance of the CTAB surfactant on the colloidal seed-mediated synthesis of gold nanorods.* Langmuir, 2008. **24**(3): p. 644-649.

32. Nikoobakht, B. and M.A. El-Sayed, *Evidence for bilayer assembly of cationic surfactants on the surface of gold nanorods.* Langmuir, 2001. **17**(20): p. 6368-6374.

33. Turkevich, J., P.C. Stevenson, and J. Hillier, *A study of the nucleation and growth processes in the synthesis of colloidal gold.* Discussions of the Faraday Society, 1951. **11**: p. 55-75.

34. Murphy, C.J., et al., *Gold nanorod crystal growth: from seed-mediated synthesis to nanoscale sculpting.* Current Opinion in Colloid & Interface Science, 2011. **16**(2): p. 128-134.

35. Nikoobakht, B. and M.A. El-Sayed, *Preparation and growth mechanism of gold nanorods (NRs) using seed-mediated growth method.* Chem. Mater, 2003. **15**(10): p. 1957-1962.

36. Tebbe, M., et al., *Colloidally stable and surfactant-free protein-coated gold nanorods in biological media.* ACS applied materials & interfaces, 2015. **7**(10): p. 5984-5991.

37. Lawson, C.L. and R.J. Hanson, *Solving least squares problems*. Vol. 15. 1995: Siam.

38. Park, S., N. Sinha, and K. Hamad-Schifferli, *Effective size and zeta potential of nanorods by Ferguson analysis.* Langmuir, 2010. **26**(16): p. 13071-13075.

39. Ohshima, H., *Henry's function for electrophoresis of a cylindrical colloidal particle.* Journal of colloid and interface science, 1996. **180**(1): p. 299-301.

40. Stankus, D.P., et al., *Interactions between natural organic matter and gold nanoparticles stabilized with different organic capping agents.* Environmental science & technology, 2010. **45**(8): p. 3238-3244.

41. Baalousha, M., et al., *Effect of monovalent and divalent cations, anions and fulvic acid on aggregation of citrate-coated silver nanoparticles.* Science of the Total Environment, 2013. **454**: p. 119-131.

42. Lee, B.-T. and J.F. Ranville, *The effect of hardness on the stability of citrate-stabilized gold nanoparticles and their uptake by Daphnia magna.* Journal of hazardous materials, 2012. **213**: p. 434-439.

43. Pfeiffer, C., et al., *Interaction of colloidal nanoparticles with their local environment: the (ionic) nanoenvironment around nanoparticles is different from bulk and determines the physico-chemical properties of the nanoparticles.* Journal of The Royal Society Interface, 2014. **11**(96): p. 20130931.

44. Stover, R.J., et al., *Formation of small gold nanoparticle chains with high NIR extinction through bridging with calcium ions.* Langmuir, 2016. **32**(4): p. 1127-1138.

45. Wang, H., et al., *Effects of monovalent and divalent metal cations on the aggregation and suspension of Fe3O4 magnetic nanoparticles in aqueous solution.* Science of the Total Environment, 2017. **586**: p. 817-826.

46. Zhang, X., et al., *Potential of mean force between like-charged nanoparticles: Many-body effect.* Scientific reports, 2016. **6**: p. 23434.

47. Afrooz, A.N., et al., *Mechanistic heteroaggregation of gold nanoparticles in a wide range of solution chemistry.* Environmental science & technology, 2013. **47**(4): p. 1853-1860.

48. Hotze, E.M., T. Phenrat, and G.V. Lowry, *Nanoparticle Aggregation: Challenges to Understanding Transport and Reactivity in the Environment All rights reserved.*

 Journal of environmental quality, 2010. **39**(6): p. 1909-1924.

49. Nghiem, T.H.L., et al., *Synthesis, capping and binding of colloidal gold nanoparticles to proteins.* Advances in Natural Sciences: nanoscience and nanotechnology, 2010. **1**(2): p. 025009.

50. Dominguez-Medina, S., et al., *Adsorption of a protein monolayer via hydrophobic interactions prevents nanoparticle aggregation under harsh environmental conditions.* ACS sustainable chemistry & engineering, 2013. **1**(7): p. 833-842.

51. Sperling, R.A. and W.J. Parak, *Surface modification, functionalization and bioconjugation of colloidal inorganic nanoparticles.* Philosophical Transactions of the Royal Society of London A: Mathematical, Physical and Engineering Sciences, 2010. **368**(1915): p. 1333-1383.

52. Sapsford, K.E., et al., *Functionalizing nanoparticles with biological molecules: developing chemistries that facilitate nanotechnology.* Chemical reviews, 2013. **113**(3): p. 1904-2074.

53. Xiao, L., et al., *Imaging translational and rotational diffusion of single anisotropic nanoparticles with planar illumination microscopy.* Journal of the American Chemical Society, 2011. **133**(27): p. 10638-10645.

54. Glidden, M. and M. Muschol, *Characterizing gold nanorods in solution using depolarized dynamic light scattering.* The Journal of Physical Chemistry C, 2012. **116**(14): p. 8128-8137.

55. Rance, G.A., et al., *Van der Waals interactions between nanotubes and nanoparticles for controlled assembly of composite nanostructures.* ACS nano, 2010. **4**(8): p. 4920-4928.

56. Parsegian, V.A., *Van der Waals forces: a handbook for biologists, chemists, engineers, and physicists*. 2005: Cambridge University Press.

57. Gobre, V.V. and A. Tkatchenko, *Scaling laws for van der Waals interactions in nanostructured materials.* Nature communications, 2013. **4**: p. 2341.

58. Min, Y., et al., *The role of interparticle and external forces in nanoparticle assembly.* Nature materials, 2008. **7**(7): p. 527.

59. Tavares, F.W., et al., *Ion-Specific Effects in the Colloid− Colloid or Protein− Protein Potential of Mean Force: Role of Salt− Macroion van der Waals Interactions.* The Journal of Physical Chemistry B, 2004. **108**(26): p. 9228-9235.

60. Klimov, V. and A. Lambrecht, *Van der Waals forces between plasmonic nanoparticles.* Plasmonics, 2009. **4**(1): p. 31-36.

4.6 Supporting Information

Size, Shape, and Surface Coating Impacts on the Colloidal Stability and Aggregation Rate of Gold Nanoparticles in Aquatic Matrices

S.M.H. Abtahi[1, 2, 3, 4], Catherine J. Murphy[5], Navid B. Saleh[6], and P. J. Vikesland[1, 2, 3, 4]

1. Virginia Polytechnic Institute and State University, Department of Civil and Environmental Engineering, Blacksburg, Virginia, USA
2. Virginia Polytechnic Institute and State University, Institute for Critical Technology and Applied Science (ICTAS), Blacksburg, Virginia, USA
3. Virginia Polytechnic Institute and State University, Center for Sustainable Nanotechnology (VT SuN), Blacksburg, Virginia, USA
4. Center for the Environmental Implications of Nanotechnology (CEINT), USA
5. University of Illinois at Urbana-Champaign, Department of Chemistry, Champaign, Illinois, USA.
6. The University of Texas at Austin, Department of Civil, Architectural, and Environmental Engineering, Austin, Texas, USA

Table 4.S1. Chemical speciation, and chemical specifications of EPA standard waters

	Reagent Added mg/L				Approximate Final Water Quality		
	$NaHCO_3$	$CaSO_4+2H_2O$	$MgSO_4$	KCl	pH	Hardness[2]	Alkalinity[2]
18.9 MΩ (nanopure water)	0.00	0.00	0.00	0.00			
Very Soft	12.0	7.5	7.5	0.5	6.4 - 6.8	10 - 13	10 - 13
Soft	48.0	30.0	30.0	2.0	7.2 - 7.6	40 - 18	30 - 35
Moderately Hard	96.0	60.0	60.0	4.0	7.4 - 7.8	80 - 100	57 - 64
Hard	192.0	120.0	120.0	8.0	7.6 - 8.0	160 - 180	110 - 120
Very Hard	384.0	240.0	240.0	16.0	8.0 - 8.4	280 - 320	225 - 245

[1]Taken in part from Marking and Dawson (1973).

[2]Expressed as mg $CaCO_3$/L.

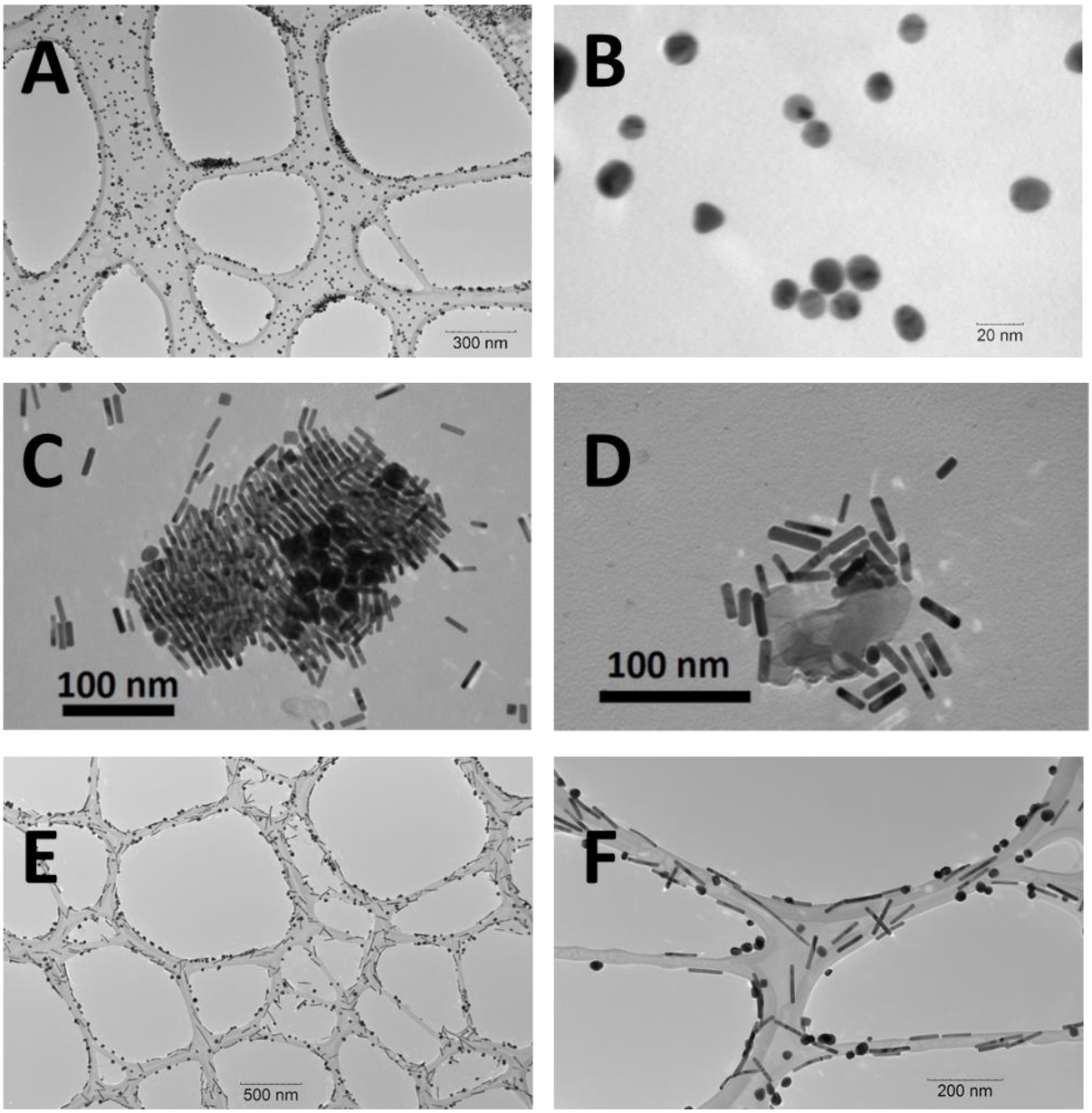

Figure 4.S1. TEM images of synthesized A-B) 19 nm citrate AuNPs C-D) CTAB AR4 AuNRs E-F) CTAB/BDAC AR8 AuNRs

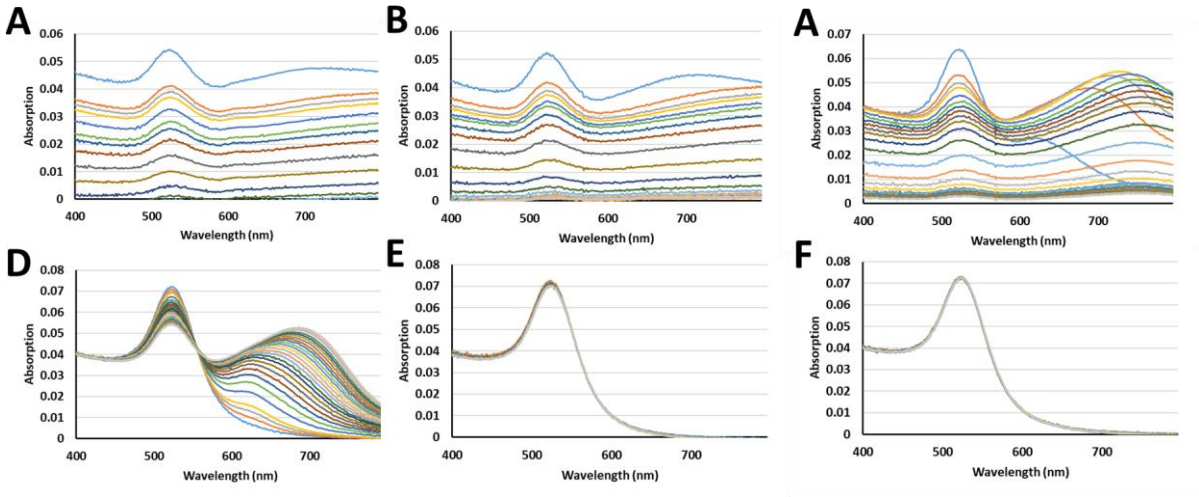

Figure 4.S2. Vis-NIR absorption spectra of 2 mg/L Citrate coated AuNP in different ionic strength EPA waters A) Very hard B) Hard C) Moderately hard D) Soft E) Very soft F) DI water

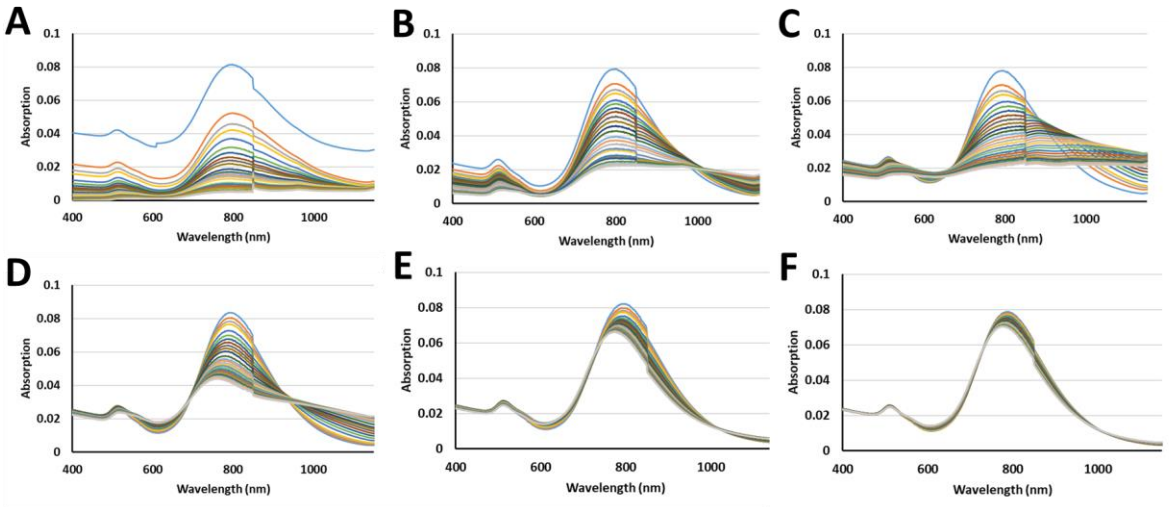

Figure 4.S3. Vis-NIR absorption spectra of 2 mg/L CTAB coated AR4 AuNR in different ionic strength EPA waters A) Very hard B) Hard C) Moderately hard D) Soft E) Very soft F) DI water

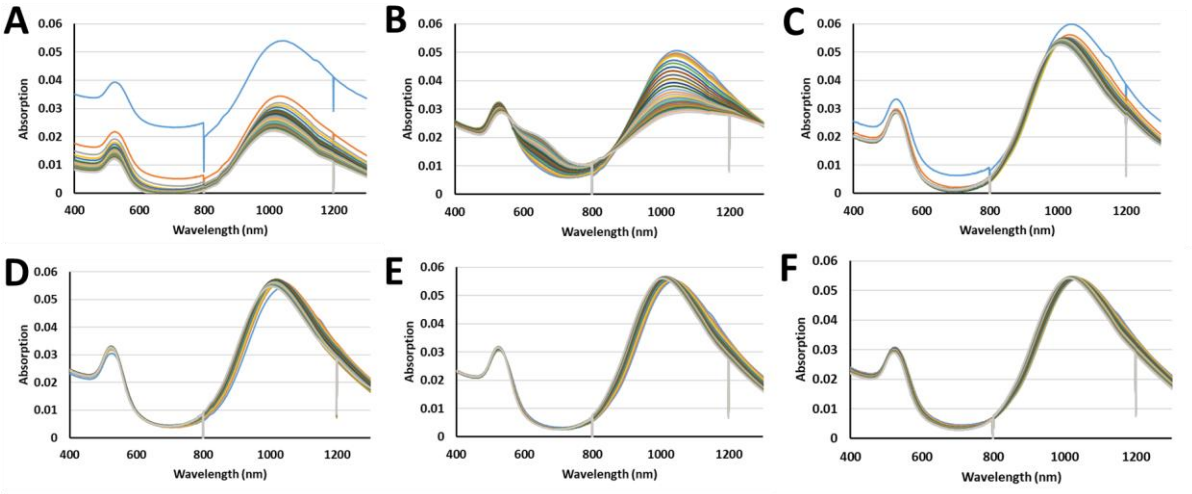

Figure 4.S4. Vis-NIR absorption spectra of 2 mg/L CTAB/BDAC coated AR8 AuNR in different ionic strength EPA waters A) Very hard B) Hard C) Moderately hard D) Soft E) Very soft F) DI water

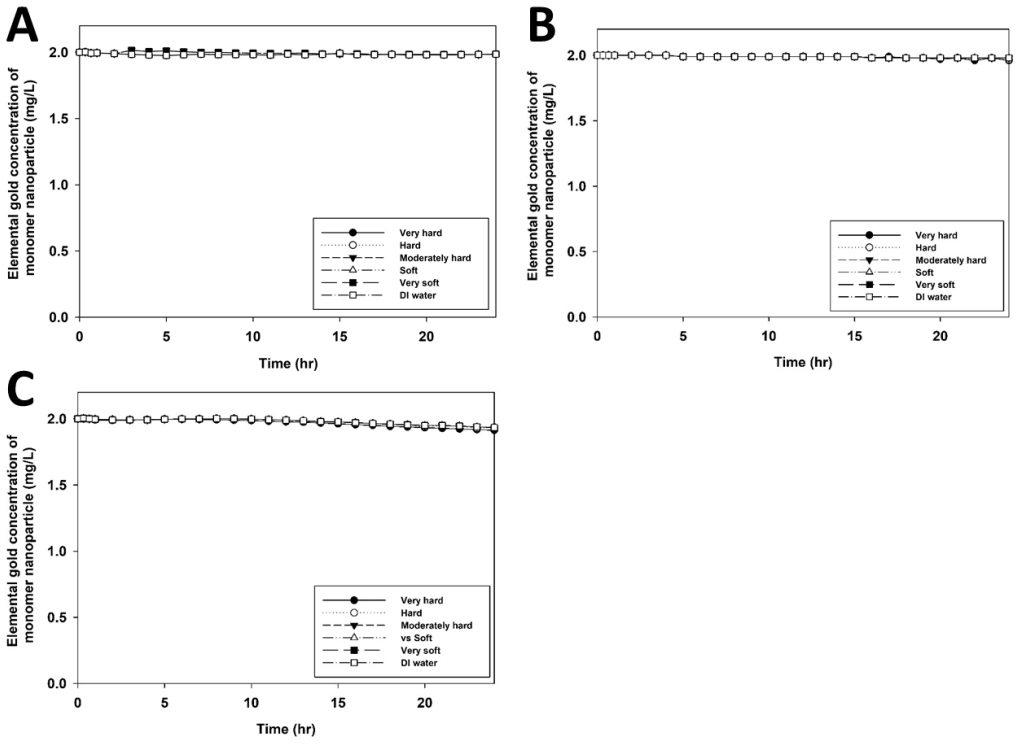

Figure 4.S5. Elemental gold concentration changes of monomer (colloidally stable single nanoparticles) BSA coated nanoparticles in the suspension versus time A) AuNP B) AR4 AuNR C) AR8 AuNR

Henry equation

$$U_E = \frac{2\varepsilon\zeta f(\kappa a)}{3\eta}$$

U_E: Electrophoretic mobility
ε: Dielectric constant
ζ: Zeta potential
$f(\kappa a)$: Henry's constant
η: Viscosity
a: Radius of particle
$1/\kappa$: Double layer thickness

Ohshima's correction to Henry's constant

$$\kappa = \left(\frac{2Ie^2}{\varepsilon_0 \varepsilon_r k_B T}\right)^{1/2}$$

ε_0: Permittivity of vacuum
ε_r: Relative static permittivity of solution
I: Ionic strength of solution
e: Charge of an electron
k_B: Boltz − mann constant
T: Temperature

For spherical particles:

$$f(ka) = 1 + \frac{1}{2}\left(1 + \frac{2.5}{ka}\right)^{-1}$$

For cylindrical particles:

$$f(ka) = 1 + \frac{1}{2}\left(1 + \frac{2.55}{ka(1+\exp(-ka))}\right)^{-2}$$

Examples for Henry's constant calculations

Synthesized AR4 AuNRs have cylindrical shape with 42.1 nm length and 11.2 nm diameter. Equivolume sphere will be 19.93 nm. All calculation and measurements occurred at 20°C and DI water was the solvent.

$a = 9.96\ nm$

Very hard EPA water; $I = 1.51 \times 10^{-2}\ {}^{mol}/_{lit}$; $\kappa = 4.0 \times 10^{8}\ {}^{1}/_{m}$; $\kappa a = 39.87$

$f(ka) = 1.41$

Very soft EPA water; $I = 4.69 \times 10^{-4}\ {}^{mol}/_{lit}$; $\kappa = 7.1 \times 10^{7}\ {}^{1}/_{m}$; $\kappa a = 7.07$

$f(ka) = 1.15$

Synthesized AR8 AuNRs have cylindrical shape with 83.4 nm length and 10.5 nm diameter. Equivolume sphere will be 23.98 nm. All calculation and measurements occurred at 20°C and DI water was the solvent.

$a = 11.99\,nm$

Very hard EPA water; $I = 1.51 \times 10^{-2}\ {}^{mol}/_{lit}$; $\kappa = 4.0 \times 10^{8}\ {}^{1}/_{m}$; $\kappa a = 47.96$

$f(ka) = 1.42$

Very soft EPA water; $I = 4.69 \times 10^{-4}\ {}^{mol}/_{lit}$; $\kappa = 7.1 \times 10^{7}\ {}^{1}/_{m}$; $\kappa a = 8.51$

$f(ka) = 1.19$

Beer-Lambert law:

$A = \varepsilon LC = Log\frac{I_0}{I}$ therefore $A \propto C$

$A = Absorption\ intensity$

$C = \ single\ GNR\ number\ concentration$

$I = \ incident\ light\ intensity$

$\varepsilon = \ molar\ extinction\ coefficient$

$L = Incident\ light\ pathlength$

First order kinetics aggregation rate.

$\frac{-d[C]}{dt} = k[C]$ After integration $\ln(\frac{[C]}{[C_0]}) = -kt$

$t_{0.5} = \frac{\ln(2)}{k}$

Where:

[C]= Elemental gold concentration at time t mg/L
[C_0]= Elemental gold concentration at time zero (2 mg/L)
k= First order aggregation rate (1/hr)

Second order kinetics aggregation rate.

$\frac{d[C]}{dt} = k[C]^2$; $\frac{1}{[C]} = \frac{1}{[C]_0} + kt$

$t_{0.5} = \frac{1}{k[C_0]}$

[C]= Elemental gold concentration at time t mg/L
[C_0]= Elemental gold concentration at time zero (2 mg/L)
k= Second order aggregation rate (L/mg.hr)

Diffusion coefficient for AuNP (Stokes-Einstein equation)

$D = \frac{K_b T}{6\pi\mu a}$ $D = 11.15 \times 10^{-11}\ {}^{m^2}/_{S}$

a= Diameter
T= Temperature = 293 k
K_b= Boltzmann constant
μ= Dynamic viscosity of medium at temperature 293 k

Rotational and Transitional diffusion coefficients calculations for AuNRs

$P = \frac{b}{a}$ Where b = Length; a = Diameter; P = Aspect ratio

$$G(P) = arctan(\sqrt{P^2 - 1})/\sqrt{P^2 - 1}$$

$$D_{\parallel}^{T} = \frac{K_b T}{8\pi\mu a}\frac{(2 - P^2)G(P) - 1}{1 - P^2}$$
$$D_{\perp}^{T} = \frac{K_b T}{16\pi\mu a}\frac{(2 - 3P^2)G(P) + 1}{1 - P^2}$$
$$D_{\parallel}^{R} = \frac{3K_b T}{16\pi\mu a^3 P^2}\frac{(1 - P^2)G(P)}{1 - P^2}$$
$$D_{\perp}^{R} = \frac{3K_b T}{16\pi\mu a^3}\frac{(2 - P^2)G(P) - 1}{1 - P^4}$$
$$D^{T} = \frac{D_{\parallel}^{T} + 2D_{\perp}^{T}}{3}$$

	Diameter, a (nm)	Length, b (nm)	Aspect Ratio, AR	D^T x 10^{-11} (m^2/s)	$D^R_\perp$ x 10^3 (1/s)	$D^R_\parallel$ x 10^3 (1/s)
AR4 AuNR	11.2 ± 0.1	42.1 ± 0.3	3.76 ± 0.2	10.72	3.52	1.39
AR8 AuNR	10.5 ± 0.3	83.4 ± 0.2	7.94 ± 0.3	4.14	2.72	0.21

Chapter 5. Environmental Implications and Future Work

5.1 Environmental implications

Given their stability in high ionic strength aquatic solutions, surface-functionalized gold nanoparticles can be a persistent aquatic nano-contaminent. Anisotropic gold nanoparticles such gold nanorods (AuNRs) are commonly tested and used in variety of applications due to their unique optical properties Environmental fate and transport of engineered nanomaterials (ENMs) has been broadly investigated and evaluated in the published research studies[1-7]. Nevertheless, majority of current researches focus on spherical shaped nanoparticles not considering the shape factor effects[2, 6-9]. The important objective of this study was to investigate the effects of nanoparticle anisotropicity and surface coating on the overall fate, transportation, deposition, and organismal uptake in aquatic matrices. To achieve this goal, we developed well-characterized stock suspensions of AuNPs and AuNRs with aspect ratios ranging from 1 to 8 having various surface coatings. The gold nanoparticles were characterized by complimentary characterization techniques such as Vis-NIR spectroscopy, transmission electron microscopy (TEM), dynamic light scattering (DLS), electrophoretic mobility measurements, and Inductively coupled plasmon mass spectrometry (ICP-MS).

At first, the colloidal stability and aggregation kinetic rates of these nanoparticles in environmentally relevant ionic strength solutions were studied and the results are reported in Chapter 4. In this chapter, we particularly focused on how the aggregation rate of elongated nanoparticles changed with altering the aspect ratio and surface coating of nanoparticles in EPA fresh waters. We found out that for citrate coated AuNP, CTAB

coated AR4 AuNR, and CTAB/BDAC coated AR8 AuNR the colloidal stabilities were reduced with an increase in ionic strength. Aggregation rates were evaluated using both first and second order kinetic rate equations. Moreover, the changes in aggregation rate versus solution hardness were derived for each type of gold nanoparticle. The collected results were consistent with electrolyte mediated double layer compression. For BSA coated gold nanoparticles of different shapes where the steric repulsion was strong, colloidal stability was not hindered by ionic strength of the solution and no aggregation was observed.

As the next step, the role and significance of individual monovalent and divalent ions in the solution on the kinetic aggregation rates and structural composition of aggregates were investigated. Our observations and findings are summarized in chapter 3. In brief, a simple one step mechanism to produce chain like end-to-end assemblies of CTAB coated AuNRs was introduced. We proposed that sulfate as a divalent anion effectively interacted with the quaternary ammonium head group of CTAB on the AuNR surface and bridged the tip facets of adjacent rods. The length of assembly were controlled by sulfate ion concentration, AuNR concentration, and exposure time. In contrast to end-to-end assembly, side-by-side and end-to-side assemblies were hindered by strong electrostatic repulsion between the dense CTAB bilayers present on the side facets. Our simple DLVO model supported the observed assembly trend. Furthermore, we showed that by analyzing the UV-Vis extinction spectrum and knowing the absorption band of each order of assembly that we could separately track the formation and growth of these assemblies over time.

At last we studied the shape characteristics and properties that govern the uptake and nanotoxicity of AuNPs and AuNRs to a model organism, *C. fluminea*. The presented results in chapter 2 indicate that the organismal uptake rate increased with increasing nanoparticle size and anisotropicity. Gold nanoparticles were readily detected in the digestive glands, gills, (pseudo)feces, and on top of the shells after exposure. The presence of nanoparticles in non-digestive tissues showed that the nanoparticles were internalized and consumed by clams. The toxicity results indicated that for the tested concentration and exposure period that gold nanoparticles were not acutely toxic (i.e., not lethal). However, gold nanoparticles significantly inhibited the activities of some antioxidant enzymes in gill and digestive gland tissues. These inhibitions could directly affect the resistance of these organisms to a secondary stressor (temperature, pathogens, hypoxia etc.) and threaten organismal health.

5.2 Summary and future work

In the current study we showed how shape-related characteristics of gold nanomaterials such as aspect ratio can affect their overall colloidal stability, fate, and organismal interaction in environmentally relevant aquatic matrices. We showed how the existing characterization techniques could be effectively utilized to monitor the colloidal behavior and fate of these elongated nanomaterials.

Prospects for future research in general can include the following:

- Studies on aggregation mechanism and governing parameters of gold nanomaterials should be expanded to hetroaggregation (deposition) since in this study we mainly focused on homoaggregation of these nanomaterials.

- Although the gold nanomaterials used in the current study were not found acutely toxic to test organism (*C. fluminea)* in a short-term exposure time, further studies are important to investigate the long-term exposure toxicity of elongated nanomaterials.

5.3 References

1. Lin, D., et al., *Fate and transport of engineered nanomaterials in the environment.* Journal of Environmental Quality, 2010. **39**(6): p. 1896-1908.

2. Praetorius, A., M. Scheringer, and K. Hungerbühler, *Development of Environmental Fate Models for Engineered Nanoparticles: A Case Study of TiO2 Nanoparticles in the Rhine River.* Environmental science & technology, 2012. **46**(12): p. 6705-6713.

3. Lowry, G.V., et al., *Environmental occurrences, behavior, fate, and ecological effects of nanomaterials: an introduction to the special series.* Journal of environmental quality, 2010. **39**(6): p. 1867-1874.

4. Cornelis, G., et al., *Fate and bioavailability of engineered nanoparticles in soils: a review.* Critical Reviews in Environmental Science and Technology, 2014. **44**(24): p. 2720-2764.

5. Dale, A.L., et al., *Modeling nanomaterial environmental fate in aquatic systems.* Environmental science & technology, 2015. **49**(5): p. 2587-2593.

6. Lowry, G.V., et al., *Long-term transformation and fate of manufactured Ag nanoparticles in a simulated large scale freshwater emergent wetland.* Environmental science & technology, 2012. **46**(13): p. 7027-7036.

7. Gottschalk, F., et al., *Modeled environmental concentrations of engineered nanomaterials (TiO2, ZnO, Ag, CNT, fullerenes) for different regions.* Environmental science & technology, 2009. **43**(24): p. 9216-9222.

8. Aiken, G.R., H. Hsu-Kim, and J.N. Ryan, *Influence of dissolved organic matter on the environmental fate of metals, nanoparticles, and colloids.* Environmental science & technology, 2011. **45**(8): p. 3196-3201.

9. Hoecke, K.V., et al., *Fate and effects of CeO2 nanoparticles in aquatic ecotoxicity tests.* Environmental science & technology, 2009. **43**(12): p. 4537-4546.

Appendix A. Plasmonic Colorimetric and SERS Sensors for Environmental Analysis

Haoran Wei [abc], **Seyyed M. Hossein Abtahi** [abc] **and Peter J. Vikesland** *[abc]

[a]*Department of Civil and Environmental Engineering, Virginia Tech, Blacksburg, Virginia, USA. E-mail: pvikes@vt.edu; Tel: (540) 231 3568*

[b]*Virginia Tech Institute of Critical Technology and Applied Science (ICTAS) Sustainable Nanotechnology Center (VTSuN), Blacksburg, Virginia, USA*

[c]*Center for the Environmental Implications of Nanotechnology (CEINT), Duke University, Durham, North Carolina, USA*

Received 22nd December 2014 , Accepted 9th March 2015

First published on 10th March 2015

The potential for water pollution outbreaks requires the development of rapid, yet simple detection methods for water quality monitoring. Plasmonic nanostructures such as gold (AuNPs) and silver (AgNPs) nanoparticles are compelling candidates for the development of highly sensitive biosensors due to their unique localized surface plasmon resonances (LSPRs). The LSPR of AuNPs and AgNPs lies in the visible and infrared light range and is sensitive to the composition, size, shape, surrounding medium, and aggregation state of these NPs. This plasmonic behavior provides the basis for fabrication of colorimetric sensors for environmental analyses. Furthermore, the LSPR also enhances the electromagnetic field near the NP surface, which provides the basis for surface-enhanced Raman spectroscopy (SERS) based detection. Organic or inorganic pollutants and

pathogens can be detected and differentiated based upon the finger-print spectra that arise when they enter SERS-active hot spots. In this tutorial review, we summarize progress made towards environmental analysis based on LSPR-based colorimetric and SERS detection. The problems and challenges that have hindered the development of LSPR-based nanosensors for real-world environmental pollutant monitoring are extensively discussed.

Haoran Wei

Haoran Wei received a MS (July 2013) in Environmental Engineering from Tsinghua University after receiving his BS (June 2010) in Environmental Engineering from Shandong University. He is currently a Ph.D. candidate in Civil and Environmental Engineering at Virginia Tech. His research interests are in the development of nanotechnology-based biosensors for detection of waterborne pathogens or contaminants.

Seyyed M. Hossein Abtahi

Seyyed Mohammad Hossein Abtahi received a second MS (December 2013) in Chemical Engineering from Virginia Tech after receiving his first MS (June 2008) and BS (June 2006) in Chemical Engineering from Sharif University of Technology. He is currently a Ph.D. candidate in Civil and Environmental Engineering at Virginia Tech. His research interests are to assess the colloidal stability, fate, transport, and organismal uptake of anisotropic nanomaterials in aquatic matrices.

Peter J. Vikesland

Peter J. Vikesland is a Professor of Civil and Environmental Engineering at Virginia Tech. He received his BA (1993) in Chemistry from Grinnell College and obtained his MS (1995) and Ph.D. (1998) in Civil and Environmental Engineering from the University of Iowa. After completing a postdoctoral fellowship at Johns Hopkins University he joined the faculty at Virginia Tech in 2002. Vikesland is a NSF CAREER awardee and currently serves as the Co-Director of the Virginia Tech ICTAS Sustainable Nanotechnology Center and the Director of the Virginia Tech Interdisciplinary Graduate Education Program. His research group is interested in the development of nanotechnology-based approaches for the protection of water and air.

Nano impact

The localized surface plasmon resonance (LSPR) of gold (AuNP) and silver nanoparticles (AgNP) enables rapid identification and detection of environmental pollutants. Using a LSPR-based colorimetric assay it is possible to detect contaminants either visually or *via* spectroscopic approaches. For even greater sensitivity, LSPR enabled surface-enhanced Raman spectroscopy (SERS) makes single molecule or single pathogen detection achievable.

A1.1. Introduction

One notorious side effect of global development is the ever-increasing number of gaseous and aqueous pollutants that pose ecosystem and human-health risks. Rapid pollutant recognition is vitally important in some emergent situations. For example, in the 2014 Elk River, WV incident in excess of 7500 gallons of 4-methylcyclohexanemethanol (4-MCHM) rapidly leaked into the Elk River such that the drinking water distribution system for the greater Charleston, WV area was heavily contaminated.[1]Similarly, in the summer of 2014 a massive algal bloom led to closure of the Toledo, OH drinking water treatment plant due to the contamination of the water by microcystin toxins.[2] In addition to outbreaks caused by chemicals, outbreaks of waterborne pathogens are also problematic. For example, the 1993 Milwaukee *Cryptosporidium* outbreak in drinking water caused 104 deaths in only two weeks.[3] In November 2010, *Cryptosporidium* infected ≈27 000 people in Östersund, Sweden *via*contaminated drinking water, and in December 2012 an

outbreak of waterborne norovirus caused acute gastrointestinal illness in a district containing 368 families in Denmark.[4,5] In addition to waterborne contaminants, airborne contaminants, such as dioxins from garbage incineration plants or potentially pandemic bird flu, also threaten people's health.[6,7]

To prevent contaminants from causing environmental catastrophes it would be ideal to detect such contamination events as quickly as possible in order to rapidly initiate remedial strategies. Unfortunately, the most commonly used detection methods for water and airborne contaminants such as gas/liquid chromatography-mass spectrometry, inductively coupled plasma mass spectroscopy, and quantitative polymerase chain reaction, although very sensitive and quantitative, require either laborious sample preparation procedures or onerous analysis methods and are thus very time-consuming. Besides, they all require expensive instruments and high level of expertise and thus cannot be conducted on site. Plasmonic nanostructures such as gold and silver nanoparticles (AuNPs and AgNPs) provide a promising avenue for the development of rapid, cost-effective and highly sensitive sensor platforms, which also exhibit the potential for onsite detection.[8] Many of the sensing capabilities enabled by AuNPs and AgNPs rely upon localized surface plasmon resonance (LSPR). When excited by light of a specific wavelength, the conduction electrons on the nanoparticle surface collectively oscillate and generate a significantly enhanced electromagnetic field or LSPR.[8–10] LSPR is an extremely sensitive optical transducer, which is dependent on the type, size, shape and aggregation state of plasmonic nanoparticles as well as the refractive index of the surrounding environment.[11–13] Changes in the LSPR result in color changes of the colloid

suspension. Based on this phenomenon, LSPR-based colorimetric sensors have been developed.[14–16]

When the incident light wavelength is coupled with the LSPR of plasmonic NPs the electromagnetic field near the NP surface is significantly enhanced.[17,18] When analytes closely associate with the NP surface, their Raman scattering cross-section increases substantially and this phenomenon is the basis for surface-enhanced Raman scattering (SERS).[18] SERS is an ultrasensitive sensing technique that has been shown to enable the detection of single molecules.[19–22] Compared with fluorescent techniques, SERS has greater potential for multiplex analysis due to the narrower peak widths in the collected Raman spectra. Because SERS is a vibrational spectroscopy method it provides chemical bonding information that facilitates differentiation of highly similar molecules and different molecular orientations.[23,24] Unlike other environmental analysis techniques such as inductively coupled plasmon atomic emission spectroscopy and gas chromatography-mass spectroscopy, SERS does not require complex sample pretreatment, sophisticated analytical method optimization, or advanced analyst training. During the last decade, the rapid development of nanotechnology has created a number of novel nanostructures that have the potential for ultrasensitive SERS detection of environmental contaminants.[25–27]

Ultrasensitive chemical analysis *via* SERS was reviewed in the late 1990s, with the focus on the mechanisms responsible for “single molecule detection”.[28,29] Subsequently, many review papers have appeared that describe the fundamental theories, material fabrication methods, and applications of SERS.[17,18,21,30–36] Reviews on colorimetric sensors that monitor the LSPR band location have also been produced.[37–39] However, relatively few of these reviews focus explicitly on environmental applications of LSPR based sensing.

A number of recent reviews discuss nanomaterial-based sensors for environmental monitoring.[40–45]However, these reviews covered either a broad suite of nanoparticles and sensing techniques or focused exclusively on SERS-based sensors. Herein we focus on the application of AuNPs and AgNPs for environmental sensing *via* either colorimetric or SERS approaches because these two related methods dominate much of the current literature. Readers interested in SPR sensors based on refractive index sensing are referred elsewhere.[46–48] This review is organized into five parts (including this introduction). The second part briefly introduces the photonic behavior responsible for LSPR-based colorimetric and SERS sensors. The third and fourth parts summarize recent progress in environmental analysis with colorimetric and SERS sensors, respectively. In the SERS portion of the review, we focus on organic pollutants, biomolecules, and pathogen detection. For SERS detection of inorganic analytes the reader is referred elsewhere.[49] The concluding part of this tutorial review discusses the extant challenges associated with ultimate application of these sensors in environmental samples.

A1.2. Background on photonics

Colloidal gold and silver nanoparticles exhibit intense colors due to a phenomenon known as surface plasmon resonance.[12,50–52]This phenomenon occurs when conduction band electrons undergo coherent oscillations following excitation by an electromagnetic field. The interaction between the electric field of the incoming light and NPs with dimension smaller than the incident wavelength causes polarization of the electrons in the nanoparticle relative to its heavier ionic core.[53] This net charge difference is confined to the nanoparticle surface and acts as a restoring force that causes the collective oscillation

of the surface electrons (*i.e.*, a surface plasmon).[53] The frequency at which these surface plasmons oscillate is known as the LSPR.

The LSPR bands for gold and silver are within the visible portion of the electromagnetic spectrum. For example, the LSPR of spherical 50 nm gold nanoparticles is at ≈530 nm, which falls into the green light range (495–570 nm). Accordingly, green light is absorbed and red light is transmitted thus causing suspensions of this size AuNP to exhibit red colors under visible light excitation. Similarly, the LSPR of spherical 50 nm silver nanoparticles is at ≈430 nm, which falls in the violet light range, leading suspensions of this size AgNP to exhibit green colors.[12,52] The exact location of the LSPR band is highly dependent on the identity, size, shape, and aggregation state of the noble metal nanoparticle, and the chemistry of the suspension medium.[12,50]Increases in size result in red-shifts (an absorption peak shift to a longer wavelength), while changes in shape result in more complicated effects. For example, the peak LSPR wavelength of 100 nm edge-length silver triangles is approximately 100 nm larger than that for 100 nm silver pentagons (pentagon length is defined as the distance between opposite corners), which is in turn 100 nm greater than that of 50 nm diameter silver spheres (Figure. 1).[12] Asymmetric gold nanorods exhibit two LSPR bands – one that corresponds to the longitudinal direction and the other the transverse direction of the rods.[54,55]

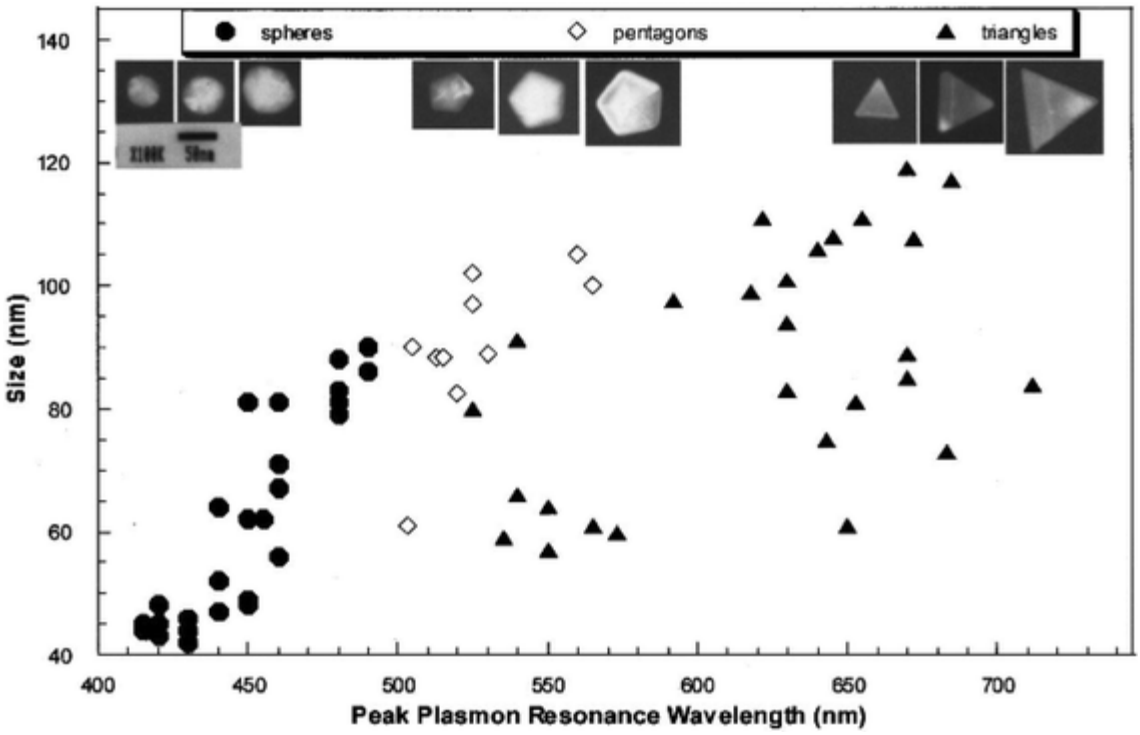

Figure A1.1. TEM images of silver spheres, pentagons, and triangles with different size (above) and their size-dependent peak LSPR wavelength. The size of a silver triangle is its edge length; the size of a silver pentagon is the distance between its opposite corners; the size of a silver sphere is its diameter.[12] Reprinted with permission from J. Mock, M. Barbic, D. Smith, D. Schultz and S. Schultz, *J. Chem. Phys.*, 2002, **116**, 6755–6759. Copyright 2014 American Institute of Physics.

In addition to shape mediated effects, changes in aggregation result in quantifiable red-shifts or blue-shifts.[56,57] The potential development of secondary LSPR bands at longer wavelengths has been observed in end-to-end assembly of gold nanorods and at shorter wavelengths in side-by-side assembly of gold nanorods.[56] Although the physics are quite complex, in simplistic terms the new LSPR band is the result of dipole alignment between adjacent particles.[58] A tunable LSPR is crucial for sensing applications. The overlap

between laser wavelength and the LSPR peak results in high SERS enhancement factors, which will be discussed later.[17] Changes in the LSPR band location can also elicit quantifiable color changes. Using 50 nm AuNPs as an example, aggregation results in the development of a new red-shifted peak at about 700 nm that falls in the red light range. Therefore, red light will be absorbed, while blue light will be scattered and the suspension color changes to blue. Because this color change is distinct and can be easily measured, it has been found to be highly useful for analyte detection.[14,38,59] A broad range of analytes have been detected solely on the basis of this color change.[15,59–61]

Surface-enhanced Raman scattering (SERS) is another phenomenon that arises due to LSPR. A schematic illustrating the basic working principle of SERS is shown in Figure. 2. Raman scattering is the inelastic scattering of photons by the vibrational chemical bonds of a molecule. The Raman spectrum is unique for each molecule due to the different vibrational modes present within it. Unfortunately, the Raman scattering signal is at most 10^{-7} of the total scattering, which makes it challenging to use Raman to detect low concentration analytes. When a molecule is adsorbed on AuNPs or AgNPs, its Raman cross section can be enhanced by several orders of magnitude due to SERS. Two primary mechanisms are responsible for SERS: electromagnetic and chemical. The former refers to the enhanced electromagnetic field near the nanoparticle surface, which is a long-range mechanism.[62]Long-range enhancements occur at greater distances away from the nanoparticle surface whose edge is schematically shown by the dotted red circle in Figure. 2. As shown in Figure. 2, analyte molecules located within the dotted red circle (position 2 and 3) exhibit clear Raman spectra, while analytes located outside the dotted red circle (position 1) exhibit no detectable Raman signal. For example, the SERS signal

of the CH_3 group of an alkanethiol molecule decreased by a factor of 2 when its distance from a SERS enhancing silver substrate increased from 0.8 nm to 2.5 nm.[63] The latter reflects charge transfer between the guest molecule and nanoparticle, which is a short-range mechanism.[62] Shorter-range enhancements only occur when an analyte is absorbed to a nanoparticle surface.

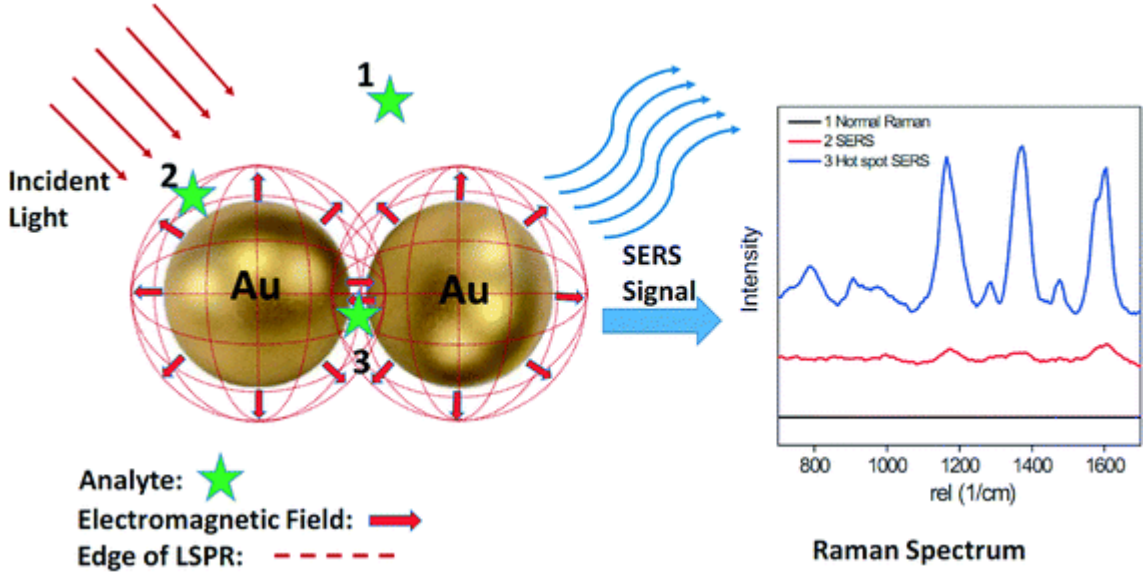

Figure A1.2. Schematic of SERS phenomenon for an organic analyte on AuNPs.

Studies to understand the SERS effect have shown that the largest SERS enhancements are produced by strongly interacting metal nanoparticles.[17,64] Clusters of two or more nanoparticles give rise to an extinction spectrum consisting of multiple peaks and facilitate single-molecule SERS.[19] This effect can be attributed to the coupling of the intense localized electromagnetic fields on each nanoparticle produced by incident light excitation of the appropriate wavelength and polarization. The long range coupling of the electromagnetic fields, although it decays exponentially with particle distance, can extend

to a distance of 2.5× the nanoparticle diameter.[64,65] It is generally thought that significant Raman enhancements primarily occur within gaps smaller than 10 nm although the exact distance is still a topic of debate.[66–68] These localized areas are often referred to as 'hotspots' (Figure. 2).[69] As shown in Figure. 2, analyte molecules located within the hot spot (position 3) exhibit a much stronger Raman signal than those located on an AuNP monomer surface (position 2). In addition to the gap between two adjacent nanoparticles, the sharp corners and tips of anisotropic plasmonic nanoparticles such as nanorods, nanoprisms, and nanostars produce another type of SERS “hot spot”.[70,71] A recent study demonstrated that isolated single gold nanorods can generate strong SERS signals that approach those obtained in the gap between spherical particles.[72] Because of the importance of hot spots for SERS application, a substantial body of research has focused on the creation and maximization of the number and location of SERS hot spots.[73–76]

Other than SERS hot spots, several additional factors significantly influence SERS, such as nanoparticle type, shape, size, solution pH and so on.[77–83] AgNPs can generate stronger SERS intensities than AuNPs because the extinction coefficient of AgNPs can be 4× larger than AuNPs of the same size and shape.[84,85] Anisotropic plasmonic nanoparticles show multiple LSPR modes and are suitable for use under different laser lines.[86–88] For example, gold nanostars (40 nm) show a second LSPR peak at 730 nm, while gold nanospheres (40 nm) show only one peak at 530 nm. Therefore, when excited by a 785 nm laser, the SERS intensity of gold nanostars is 2–3 orders of magnitude higher than that of gold nanospheres.[89] The size of a nanoparticle affects its LSPR, which determines its SERS intensity as well. A recent study shows even under random aggregation conditions, nanoparticle size still plays an important role in the Raman signal.

With 785 nm laser excitation, AuNPs with size between 46–74 nm showed the strongest Raman signal. It has been shown that for elongated shape gold nanoparticles such as rods that the aspect ratio (length/diameter) is an important factor. Results suggest that enhancement can be two orders of magnitude greater when the plasmon band of the gold nanorod overlaps with the excitation wavelength.[90] These results indicate that it is necessary to carefully choose nanoparticle size according to the excitation laser wavelength.[91] Solution pH influences analyte adsorption to the NP surface and can subsequently influence its SERS signal.[77] For example, diclofenac sodium only exhibited a clear SERS spectrum under acidic and neutral pH conditions and not under alkaline pH conditions due to electrostatic repulsion between its carboxylic group and the citrate-coated AgNP surface.[92]

Organic chemical detection is comparatively easy to achieve because small molecules can readily enter SERS hot spots. Pathogens, however, such as bacteria and viruses, are too large to enter SERS hot spots thus resulting in several orders of magnitude lower Raman enhancement factors. To circumvent this problem, a SERS tag is often employed.[31,93] A SERS tag includes a recognition element, Raman reporter, and a signal transducer.[45] AuNPs and AgNPs are most commonly used signal transducers, while dyes with large Raman cross-sections are used as Raman reporters. Specific antibodies or aptamers against the target pathogens are used as recognition elements. Generally, a protection layer is needed for the Raman reporter modified nanoparticle to prevent the leakage of Raman reporter and improve the stability of the nanoparticle.

A1.3. Colorimetric detection

Perhaps the most convenient mechanism for a rapid, field-deployable contaminant detection assay would be to observe color changes with our naked eye. Because the LSPRs of gold and silver colloids fall within the visible spectrum, color changes that occur due to changes in aggregation state have been exploited for colorimetric sensor fabrication. Colorimetric sensing of DNA using functionalized AuNPs was pioneered by Mirkin *et al.*[94] In that study, two batches of 13 nm AuNPs were functionalized with two non-complementary oligonucleotides and were then combined. After the addition of a target DNA duplex with two “sticky ends” (complementary to the oligonucleotides on each type of AuNP), the suspension color changed from red to purple due to DNA hybridization induced AuNP aggregation.[94] Both the oligonucleotide modification position and the AuNP size greatly influenced probe sensitivity. When the two batches of AuNPs were modified with 5′-oligonucleotide and 3′-oligonucleotide, respectively, single base imperfections could be detected.[59] Importantly, larger AuNPs (50 nm, 100 nm) were found to be more sensitive than smaller AuNPs (13 nm) because of their larger extinction coefficients.[95] In addition to oligonucleotide-gold nanoparticle (OGN) conjugates, oligonucleotide-silver nanoparticle (OSN) conjugates were also used as DNA probes. Because of the larger extinction coefficients of AgNPs compared with AuNPs, the detection limit for target DNA by the OSNs was 50× lower than with the OGNs.[96]

Aggregation induced by oligonucleotide hybridization is one example of a cross-linked colorimetric sensor. Similar sensor designs have been applied for detection of a range of biomolecules, heavy metal ions, and pathogens.[97] When the target directly binds to a recognition element on the nanoparticle surface, it induces aggregation and, in the e of

AuNPs, a red to blue color change. Alternatively, the target can induce dissociation of nanoparticle aggregates by competitively binding to the linker between nanoparticles. Under these conditions a blue to red color change is expected. For example, an aptamer-linked gold nanoparticle aggregate was developed for adenosine detection. Aptamers are single oligonucleotide strands of DNA or RNA that can bind pathogens, molecules, or even ions with high affinity and specificity.[98] Adenosine addition resulted in dissociation of the aptamer-linked aggregates due to its competitive binding to the aptamer linker between the two AuNPs. Following addition of adenosine, the suspension color changed from purple to red indicating the transformation from AuNP aggregates to monomers. This result was further indicated by the blue shift of the LSPR band in the UV–VIS spectrum from 700 to 522 nm.[99] A similar protocol was successfully applied for the fabrication of a cocaine sensor with a detection limit of 50–500 μM.[61] Recently this protocol was extended to development of a "smart hydrogel" sensor, where dissociation of the cross-linked hydrogel following addition of target resulted in the release of AuNPs to the solution and a change in color.[100]

In a non cross-linked detection protocol there is no hybridization between different gold/silver nanoparticles. In this e, aggregation/dissociation of the nanoparticles is achieved by decreasing/increasing the concentration of stabilizer on the nanoparticle surface. For example, an ultrasensitive colorimetric DNA probe (1 pM detection limit by eye) was developed by using a polyelectrolyte that forms conjugates with single stranded DNA. Following polyelectrolyte addition, AuNPs stabilized with single stranded DNA aggregated due to preferential binding between the aptamer and the polyelectrolyte, while AuNPs stabilized with target double stranded DNA remained stable.[15]

The detection protocols described above have been used for heavy metal detection due to their capacity to form strong complexes with chelators and other recognition agents. In this manner, a sensitive and selective probe for Hg^{2+} was fabricated by modifying the 13 nm AuNP surface with mercaptopropionic acid (MPA). Hg^{2+} forms complexes with the carboxylate groups of MPA and induces AuNP aggregation. After addition of 2,6-pyridinedicarboxylic acid (PDCA) into the probe suspension, the selectivity for Hg^{2+} relative to other heavy metals was significantly improved. This result was attributed to the 100× higher complexation coefficient of PDCA for Hg^{2+} than for other heavy metals. The combined method enabled quantitative detection of Hg^{2+} over a concentration range of 250–500 nM with a limit of detection of 100 nM.[60] In addition to using toxic organic compounds as recognition elements, urine can also be used for Hg^{2+} sensing. The uric acid and creatinine in urine can synergistically bind to AuNPs as well as selectively adsorb Hg^{2+}. In addition to the low cost sensor fabrication, a low detection limit of 50 nM was achieved in this manner.[16] It has been shown that Zn^{2+} and Cu^{2+} can be detected using agglomeration and the resulting suspension color change of 20 nm chitosan-capped gold nanoparticles.[101] Chitosan is a well-known chelating agent for heavy metals and the presence of Zn^{2+} and Cu^{2+} can cause colloidal instability and loose aggregation (agglomeration) of gold nanoparticles. This phenomenon causes a rapid color change that is directly related to the heavy metal concentration. Pb^{2+} with a tunable detection limit of 100 nM to 200 μM has been detected following an aggregation-dissociation protocol. The DNAzyme-directed assembly of gold nanoparticles cleaves in the presence of Pb^{2+} and results in a blue to red color change (Figure. 3A).

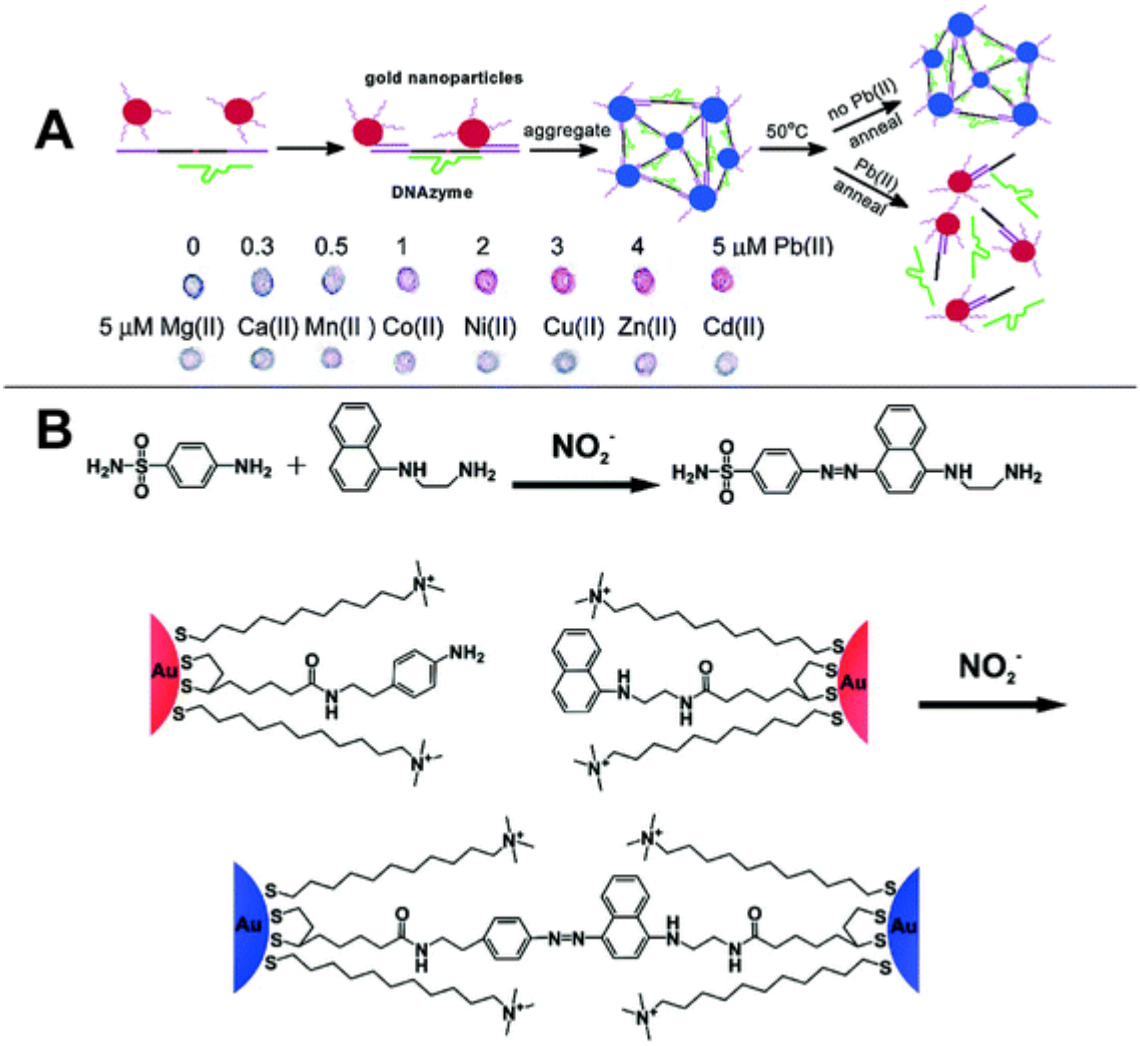

Figure A1.3 A) DNAzyme-directed assembly formation and cleavage of gold nanoparticles in a Pb^{+} colorimetric sensor;[102] Reprinted with permission from J. Liu and Y. Lu, *J. Am. Chem. Soc.*, 2003, **125**, 6642–6643. Copyright 2014 American Chemical Society. B) Schematic of the Griess reaction and Griess reaction induced aggregation of AuNPs.[14] Reprinted with permission from W. L. Daniel, M. S. Han, J. S. Lee and C. A. Mirkin, *J. Am. Chem. Soc.*, 2009, **131**, 6362–6363. Copyright 2014 American Chemical Society.

Nitrate and nitrite ions are two regulated contaminants in drinking water. A simple colorimetric method was developed for their detection based upon the Griess reaction (Figure. 3B). As shown in Figure. 3B, two batches of AuNPs were functionalized with 5-[1,2]dithiolan-3-yl-pentazoic acid [2-(4-amino-phenyl)ethyl]amide (DPAA) and 5-[1,2]dithiolan-3-yl-pentazoic acid [2-(naphthalene-1-ylamino)ethyl]amide, respectively. Following nitrite ion addition, the amino group and naphthalene group were linked *via* an azide linkage, which then resulted in AuNP aggregation and the fading of the suspension color. The color change threshold could be controlled by adjusting the incubation time and temperature to meet the EPA standard (1 ppm for nitrite ion). The same procedure was applied for nitrate detection after the nitrate ions were reduced to nitrite by nitrate reductase. The specificity of this probe is high enough that it is not affected by the presence of other inorganic ions (F^-, SO_4^{2-}, HCO_3^-, *etc.*) even when their concentrations are two orders of magnitude larger than that of nitrite.[14]

A majority of the plasmonic nanoparticle based colorimetric detection methods rely upon crosslinking. However, non-crosslinking methods are also sometimes employed. A homogeneous method for the selective detection of Hg^{2+} and Ag^+ using Tween 20-modified AuNPs has been developed. Citrate-capped AuNPs were modified with Tween 20. In the presence of silver and mercury ions, citrate ions reduce Hg^{2+} and Ag^+ to form Hg^0 and Ag^0 on the surface of the AuNPs. This phenomenon was followed by Tween 20 removal from the NP surface and aggregation of AuNPs. The detection limit can be as low as 0.1 μM in the presence of NaCl and EDTA.[103] In another study, a sensor for quantitative detection and differentiation of two nitroamine explosives – hexahydro-1,3,5-trinitro-1,3,5-triazine (RDX) and octahydro-1,3,5,7-tetranitro-1,3,5,7-tetrazocine (HMX)

was developed.[104] In this sensor, nitrite hydrolyzed from RDX and HMX reacted with 4-aminothiolphenol on AuNPs to form an azo dye with naphthylene diamine. Dye formation changed the LSPR of the AuNPs because of a charge-transfer interaction on the AuNP surface. The absence of a second LSPR peak indicated the color change was not due to AuNP aggregation, but instead due to dye formation. AuNPs improved the sensitivity of the probe, but the mechanism responsible for this behavior was not clearly elucidated.

Some special detection protocols have also been used for heavy metal ion detection. Cr^{6+} can selectively etch the tips of gold nanorods (AuNRs) due to its strong oxidation state. Shortening of the nanorod induces a blue shift in its longitudinal LSPR band and a corresponding color change. Using this approach a detection limit of 90 nM was obtained.[105] This method does not require aggregation or dissociation of nanoparticles and as such it can be described as a non-aggregation method. Cu^{2+} can also etch the tips of AuNRs in the presence of HBr. In this e, Au^0 was oxidized to Au^+ and Cu^{2+} was reduced to Cu^+, which was subsequently oxidized to Cu^{2+} by dissolved oxygen (Figure. 4A). The presence of cetyltrimethylammonium bromide (CTAB) was key to this redox reaction because it reduced the redox potential of Au^+/Au^0 from 0.93 V to less than 0.2 V. The decrease in aspect ratio due to etching resulted in a blue shift of the LSPR band and a color change from blue to red (Figure. 4A). With this method, 50 nM Cu^{2+} was detected by the naked eye and 0.5 nM Cu^{2+} was detectable by UV–VIS.[106] A similar protocol was applied for Hg^{2+} detection. In the presence of ascorbic acid, Hg^{2+} was reduced to Hg^0 and deposited on AuNRs, which induced a color change from purple to blue green. The detection limit of Hg^{2+} was 800 pM. The Hg^0–AuNR can subsequently be used as a S^{2-} sensor because S^{2-} can exfoliate Hg^0 from the AuNR surface.[107]

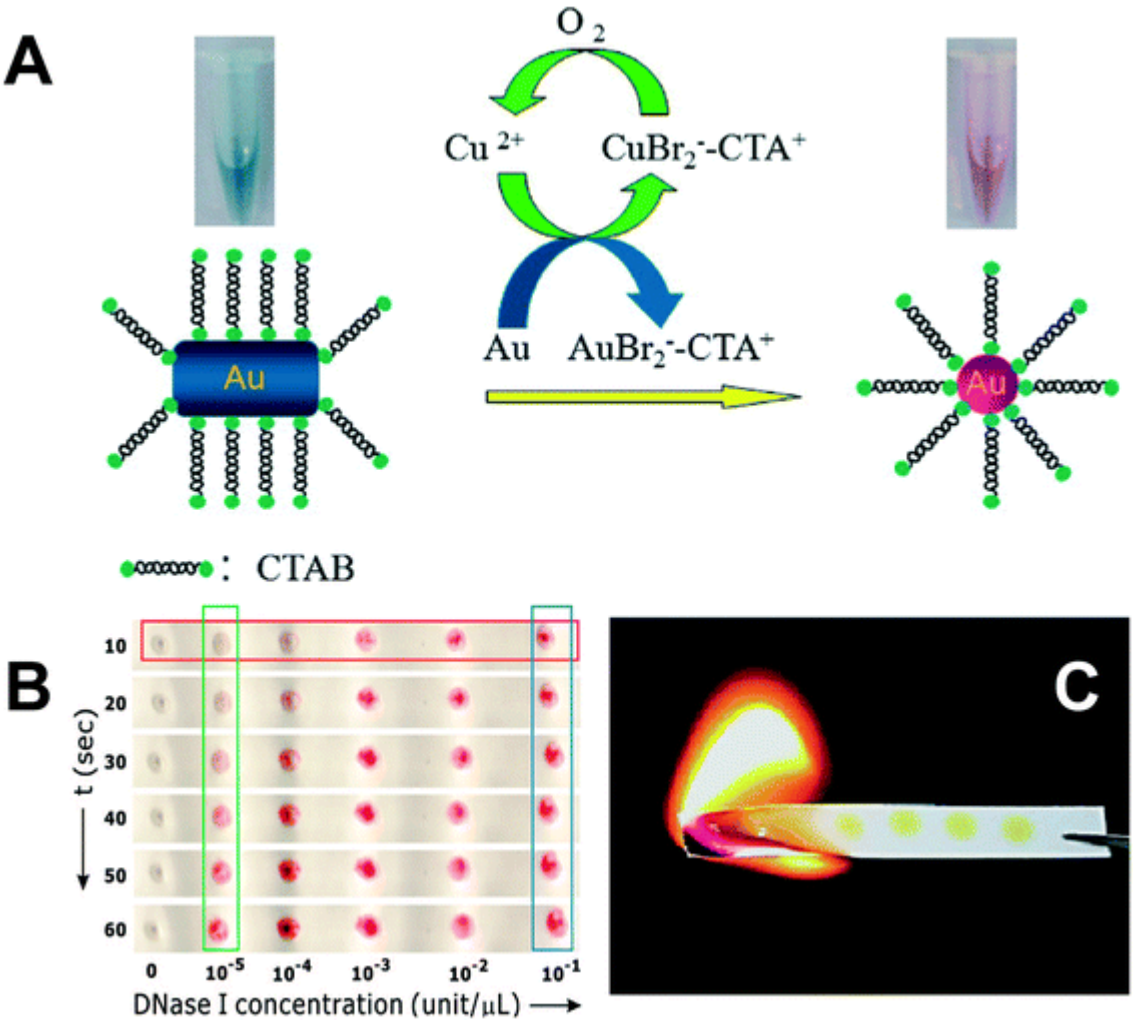

Figure A1.4. A) Schematic of colorimetric detection of Cu^{2+} by etching AuNR tips by Cu^{2+} in the presence of CTAB and HBr.[106]Reprinted with permission from Z. Zhang, Z. Chen, C. Qu and L. Chen, *Langmuir*, 2014, **30**, 3625–3630. Copyright 2014 American Chemical Society. B) DNA-hybridized AuNP aggregates on a hydrophobic paper after exposure to DNase I droplets.[108] Reprinted with permission from W. Zhao, M. M. Ali, S. D. Aguirre, M. A. Brook and Y. Li, *Anal. Chem.*, 2008, **80**, 8431–8437. Copyright 2014 American Chemical Society. C) Spent paper substrates are burnt to minimize hazardous

chemical handling.[109] Reprinted with permission from S. C. Tseng, C. C. Yu, D. Wan, H. L. Chen, L. A. Wang, M. C. Wu, W. F. Su, H. C. Han and L. C. Chen, *Anal. Chem.*, 2012, **84**, 5140–5145. Copyright 2014 American Chemical Society.

For practical field applications, paper-based colorimetric sensors may be better than suspension-based ones due to their smaller volume, longer-term stability, and convenient handling and processing. Recently it has been reported that the protocols for suspension-based colorimetric detection can also be applied on a paper substrate.[108,110] For example, DNA-hybridized AuNP aggregates that were spotted on paper can be redispersed into a droplet that contains endonuclease (DNase I), which could cleave hybridized DNA. Following endonuclease addition, the blue or black spot on paper rapidly changed color to red and this color change could be discerned by the naked eye even at low nM endonuclease concentrations (Figure. 4B).[108] It is notable that the paper used in these assays should be hydrophobic paper or surfactant-treated hydrophilic paper to avoid the rapid spread and drying of the droplet applied on the surface. In addition to drop-coated AuNP suspensions on paper, paper/AuNP composites can also be synthesized by a laser-induced thermal method. When 15 nm thin gold films coated on paper were exposed to KrF excimer laser irradiation, AuNPs (46 nm) formed on the paper surface with a high density of 318 μm^{-2}. Following immersion into cysteine solution the color of the paper changed from light yellow to dark yellow. The paper could be burnt after use, which is a simple mechanism for hazardous waste disposal (Figure. 4C).[109] Another paper-based analytical protocol has been reported for colorimetric sensing of Cu^{2+} by AgNPs functionalized with homocysteine and dithiothreitol. The LSPR peak intensity of AgNPs at 404 nm decreased while a new red-shifted band at 502 nm appeared as Cu^{2+} was

added. Consequently, the color of the paper coated with AgNPs changed from yellow to orange or green-brown. A linear response was observed for the color intensity change as a function of Cu^{2+} concentration in the range of 7.8–62.8 μM.[111] Based on these results, we are confident that paper-based colorimetric LSPR sensors should have applicability for detection of a broad range of environmental pollutants.

A1.4. SERS detection

The SERS phenomenon was first observed in 1974 when the Raman signal of pyridine adsorbed on a roughened silver electrode was substantially enhanced.[112] SERS was subsequently proposed as an analytical technique for many organic compounds using substrates such as roughed Ag electrodes or Ag films on nanospheres (AgFON).[113,114] However, the detection limits achieved with these methods are high (above 1 μM), which limits their application. In 1997, however, single molecule detection was achieved for resonant dye molecules, such as rhodamine 6G (R6G) and crystal violet (CV) using AgNP colloids as SERS substrates.[19,22] It was subsequently realized that aggregates in the colloid are responsible for the substantially enhanced Raman signal and the concept of the aforementioned SERS “hot spot”, the gap between the aggregates, was proposed.

In the past decade, numerous research efforts have been devoted to create and maximize the number of “hot spots” within SERS substrates.[116,118,119] Adding salts or organic electrolytes to gold or silver colloid suspensions can induce aggregation and generate SERS “hot spots”.[120] However, the aggregation process is random and thus hard to replicate. Recently, methods to generate highly reproducible and controllable SERS hot spots in suspension have been reported.[115,116,121,122] For example, the supermolecule

cucurbit[*n*]uril (CB[*n*]) can link AuNPs with a fixed gap of 0.9 nm and this molecule can also specifically capture target analytes within the hot spot (Figure. 5A).[115] DNA-mediated gold nanogap particles, which contain a 20 nm gold core and 11 nm gold shell linked by a gold nanobridge have recently been synthesized (Figure. 5B). Dyes located in the 1 nm gap were quantitatively detected over an ultra low concentration range of 10 fM to 1 pM. Raman mapping results demonstrate that 90% of these nanoparticles show SERS enhancement factors between 10^8 and 10^9 – a range that is sufficient for single molecule detection.[116] Despite its excellent homogeneity, this nanoparticle is more appropriate for use as a SERS tag rather than as a SERS substrate due to the difficulty associated with getting analyte chemicals to diffuse into the nanogap.

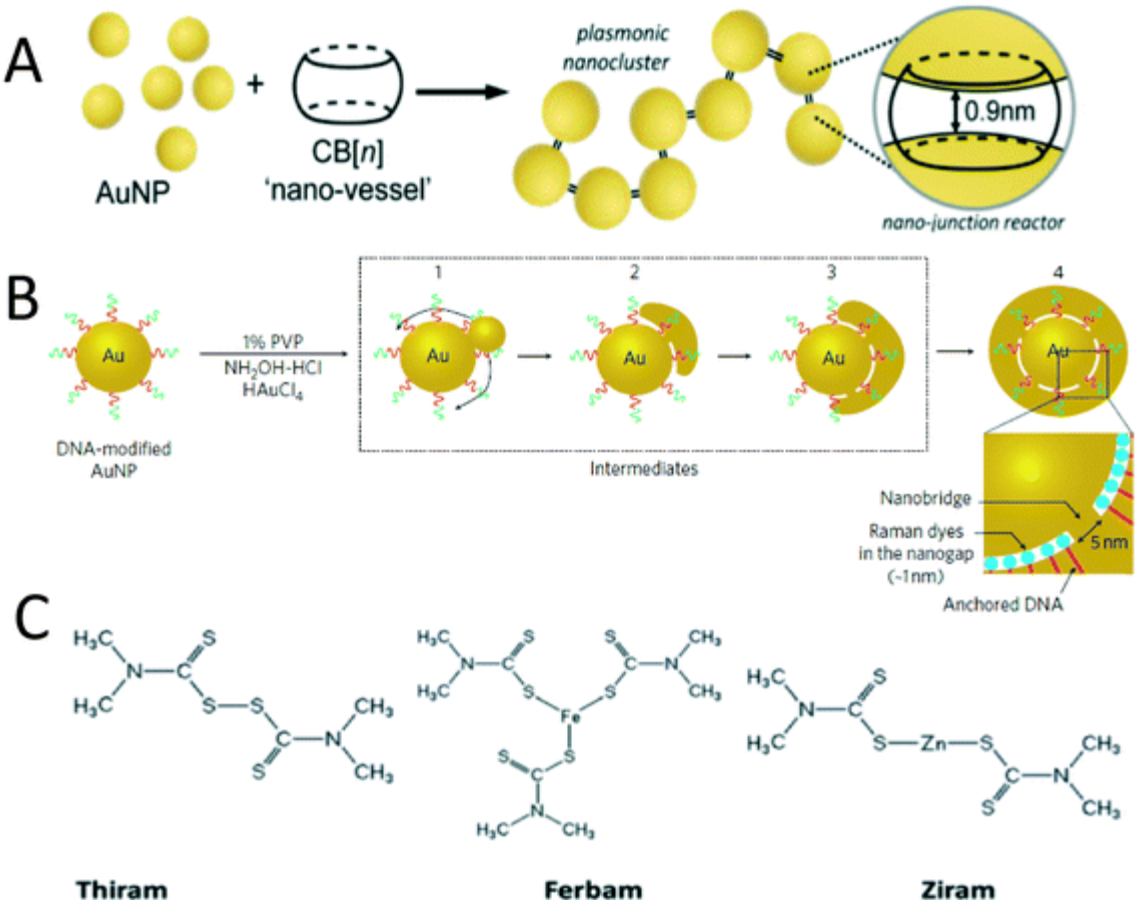

Figure A1.5. A) CN[*n*] induced AuNP aggregation with a fixed sub nanometer gap;[115] Reprinted with permission from R. W. Taylor, R. J. Coulston, F. Biedermann, S. Mahajan, J. J. Baumberg and O. A. Scherman, *Nano Lett.*, 2013, **13**, 5985–5990. Copyright 2014 American Chemical Society. B) Formation of 1 nm gap between AuNP core and shell linked with a Au nanobridge.[116] Reprinted with permission from D. K. Lim, K. S. Jeon, J. H. Hwang, H. Kim, S. Kwon, Y. D. Suh and J. M. Nam, *Nat. Nanotechnol.*, 2011, **6**, 452–460. Copyright 2014 Nature Publishing Group. C) Chemical structures of three dithiolcarbamate pesticides.[117]Reproduced from B. Saute, R. Premasiri, L. Ziegler

and R. Narayanan, *Analyst*, 2012, **137**, 5082–5087. With permission from The Royal Society of Chemistry. Copyright 2014 The Royal Society of Chemistry.

For real applications, solid SERS substrates are often considered superior to suspension-based SERS due to the long term stability and transport and handling convenience that the solid substrates provide. Extensive research efforts have been devoted to making homogeneous solid SERS substrates using approaches such as electron lithography, focused ion beam lithography, and nanosphere lithography.[13,20,33,82,123–125] These top-down methods make highly ordered plasmonic nanostructures with tunable shape, size, and particle-to-particle gap size and have very high SERS enhancement factors.[126] However, these methods, especially electron lithography, can be quite expensive and are difficult to scale up. Recently reported nanoporous gold and gold/silver nanoporous films are easy to make at large scale. After thermal treatment, the films wrinkle and create quasi-periodic nanogaps and nanotips, which act as SERS “hot spots”. With these wrinkled films, single molecule detection of R6G was achieved.[20,123] Recent studies find that covering Au nano-pyramid arrays with graphene can improve the SERS signal 10× due to the enhanced charge transfer.[127]

In contrast to the aforementioned rigid SERS substrates, flexible substrates such as paper-based SERS substrates are cheaper, easier to make, and can be applied for curvy surfaces.[128–134] A paper-based SERS swab was fabricated by simply dipping a filter paper in AuNR suspension. AuNRs were adsorbed efficiently onto the surface of filter paper due to the electrostatic attraction between the negatively charged cellulose and the positively charged CTAB-coated AuNRs. The biggest advantage of this SERS substrate is its ease of use for the collection of trace samples from a solid surface. By swabbing a glass

surface contaminated with a 140 pg 1,4-benzenedithiol (1,4-BDT) residue, the chemicals were readily adsorbed on the paper surface and their Raman spectrum was easily obtained (Figure. 6A).[129] Similarly, a star-shaped μPAD whose fingers were coated with polyelectrolyte was fabricated (Figure. 6B). This μPAD showed the capability to separate chemicals based upon their charge and to concentrate the chemicals into the small volume of the tips (Figure. 6B). For example, positively charged R6G readily moved to the finger tip coated with positively charged poly(allylamine hydrochloride), while it was retained at the entrance of the finger coated with negatively charged poly(sodium 4-styrenesulfonate). This μPAD exhibited a preconcentration factor of 10^9 for R6G and thus a super low detection limit of 100 aM was detected.[133] In addition to paper, electrospun nanofiber mats have also been used as the SERS substrate scaffold.[134,135] For example, an AgNP/PVA (poly(vinyl alcohol)) membrane was fabricated by electrospinning AgNPs and PVA mixture. The bulk material and nanofibers coated with AgNPs are shown in Figure. 6C and D, respectively. 4-mercaptobenzoic acid (4-MBA) at a concentration of 10^{-6} M was detected using this SERS substrate.[135]

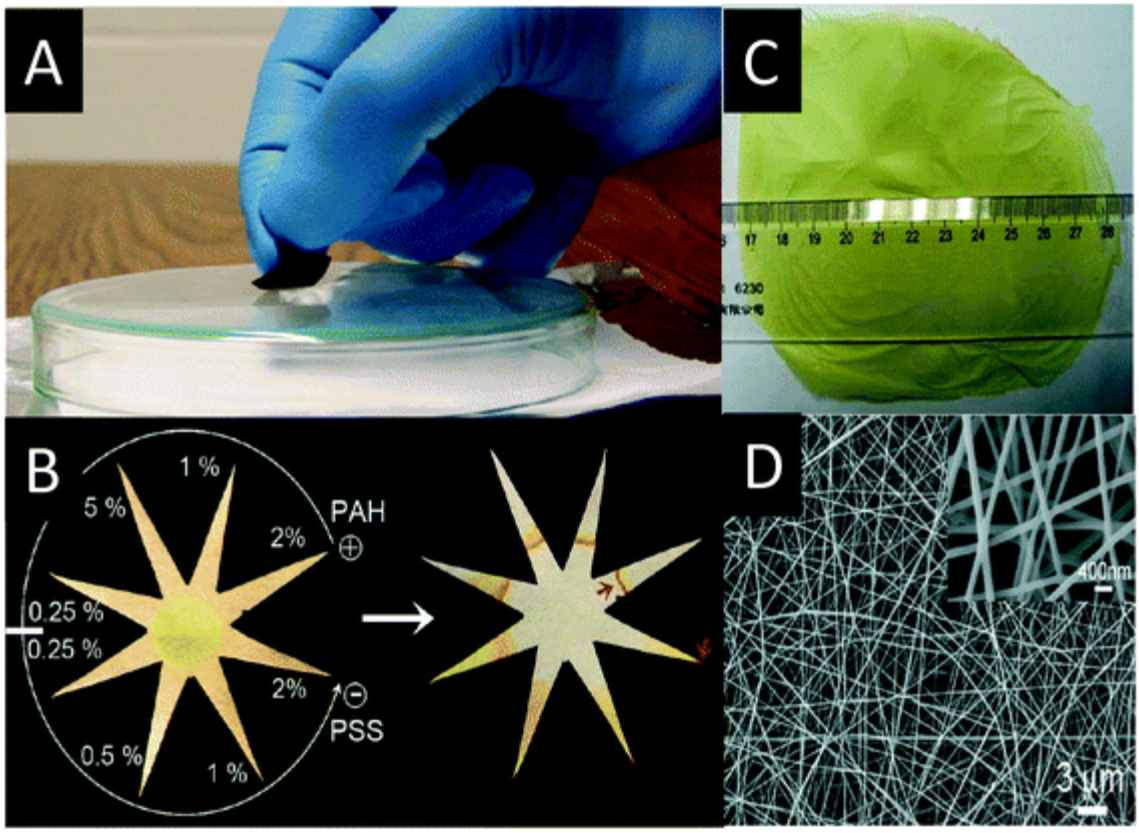

Figure A1.6. A) A glass with 1,4-BDT residue is swabbed by the paper-based SERS substrate;[129] Reprinted with permission from C. H. Lee, L. Tian and S. Singamaneni, *ACS Appl. Mater. Interfaces*, 2010, **2**, 3429–3435. Copyright 2014 American Chemical Society. B) A star-shape paper with eight fingers were coated by polyelectrolyte, which could separate and preconcentrate chemicals efficiently;[133] Reprinted with permission from A. Abbas, A. Brimer, J. M. Slocik, L. Tian, R. R. Naik and S. Singamaneni, *Anal. Chem.*, 2013, **85**, 3977–3983. Copyright 2014 American Chemical Society. C) The photo and D) SEM image of AgNP/PVA membrane fabricated by electrospinning.[135] Reprinted with permission from D. He, B. Hu, Q. F. Yao,

K. Wang and S. H. Yu, *ACS Nano*, 2009, **3**, 3993–4002. Copyright 2014 American Chemical Society.

Although significantly improved average enhancement factors (EF) have been achieved (generally greater than 10^9) for Raman active dyes and other test materials, the application of such SERS substrates for ultrasensitive detection of organic pollutants are few.[117,136–140] The reason for this is that many organic pollutants are non-resonant under the laser excitation wavelengths (>514 nm) typically used for Raman spectroscopy. Accordingly, their Raman cross-sections are generally several orders of magnitude lower than those for the resonant dyes most commonly used for SERS substrate development.

SERS detection of pesticides with high affinity to AuNPs has been reported.[117,138] Dithiolcarbamate pesticides – thiram, ferbam, and ziram were detected and differentiated by SERS using a gold nanorod suspension as the SERS substrate. The structures of these three chemically similar pesticides are shown in Figure. 5C. Each pesticide contains sulfur groups that can form covalent Au–S bonds with the AuNP surface. To obtain high SERS intensity, gold nanorods whose longitudinal LSPR was well coupled with the laser wavelength were used as the SERS substrate. The detection limits of these three pesticides are 34 nM, 26 nM, and 13 nM, respectively, well below the EPA standards (17 μM, 10 μM, 23 μM).[117] These results indicate that for organic pollutants showing high affinity with gold or silver nanoparticles, SERS detection is feasible if the LSPR of the SERS substrate matches the excitation laser wavelength. An organophosphorus pesticide – paraoxon at a concentration of 10 nM was detected using a self-assembled gold nanoparticle film. The film is made by ting methoxy-mercapto-poly(ethylene glycol) (mPEG-SH) functionalized AuNP suspension onto a solid substrate.

The AuNPs were closely packed on the substrate with 5 nm gaps. Self-assembly induced by mPEG-SH modification significantly improved the SERS intensity and homogeneity of the film.[138] This is a simple and cost-efficient method for SERS substrate fabrication. However, the author did not explain how the mPEG-SH-AuNP suspension and the analyte solution overcame the “coffee ring effect” when t on a solid substrate.

A significant challenge that has limited SERS detection of organic pollutants is not only their generally small Raman cross sections, but also their low affinity to the NP surface. Therefore, methods to enhance the affinity between pollutants and the gold/silver NP surface have been pursued to solve this problem.[141–146] One way to achieve this goal is through addition of a molecular trap on the gold/silver nanoparticle surface to specifically capture organic molecules. The thermally sensitive polymer poly-(*N*-isopropylacrylamide) (pNIPAM) was recently used as the trap for 1-naphthol (1-NOH). At a temperature of 277 K, pNIPAM exists in a swollen state, such that 1-NOH trapped within the polymer is far away from the AuNP surface, which then results in a weak SERS signal. In contrast, at a temperature of 333 K, pNIPAM shrinks to half of its swollen volume, thus bringing 1-NOH closer to the AuNP surface resulting in a substantial increase in the SERS signal.[143] This method enabled acquisition of the SERS spectrum of 1-NOH for the first time. However, the limit of detection for 1-NOH is high (10 μM). TNT was trapped on a cysteine-functionalized AuNP surface by the formation of a Meisenheimer complex with cysteine (Figure. 7A). Electrostatic attraction between Meisenheimer complex-bound AuNPs and cysteine-bound AuNPs subsequently resulted in AuNP aggregation and the generation of a number of SERS hot spots. With this method, 2 pM TNT was detected in aqueous solution.[141] TNT has also been adsorbed onto the AuNR surface by a peptide linker

containing a TNT-binding tail, a cysteine terminal, and a glycine spacer. The peptide-functionalized AuNRs were embedded in a filter paper and tested with both liquid phase and vapor phase TNT. Notably, this material could detect 10 μM TNT in a shampoo solution thus indicating its high selectivity for TNT.[147] Dithiolcarbamate calix[4]arene was also used as a linker between AgNPs and polycyclic aromatic hydrocarbons (PAHs). The cup shape calix[4]arene is able to host hydrophobic PAHs and the dithiolcarbamate on the linker increases the affinity between the linker and the nanoparticle (Figure. 7B). This novel SERS substrate can achieve a limit of detection for four PAHs (pyrene, benzo[*c*]phenanthrene, triphenylene, and coronene) in the range between 10 nM to 100 pM.[142]Calixarene-functionalized AgNP embedded in silica film was applied in a flow cell designed for *in situ* monitoring of PAHs in seawater.[148–150] Limits of detection of 100 pM and 310 pM for pyrene and anthracene were achieved when artificial sea water spiked with PAHs traveled through the flow cell.[148] A field study using this SERS substrate was conducted in the Gulf of Gdańsk (Baltic Sea). The limit of detection for 12 different PAHs was 150 ng L^{-1}, which is comparable to the results obtained *via* GC/MS, thus indicating the SERS technique has potential for monitoring pollution events *in situ*.[150] Viologens have also been used as a PAH linker. Because of their high affinity to both AgNPs and guest PAHs, viologens could induce the aggregation of AgNPs and thus further increase the SERS intensity. With this method, a detection limit of 80 pyrene molecules was obtained – this is the lowest limit of detection for pyrene ever reported.[144] The drawback of this method is the high background signal from the linker, which makes spectrum analysis challenging.

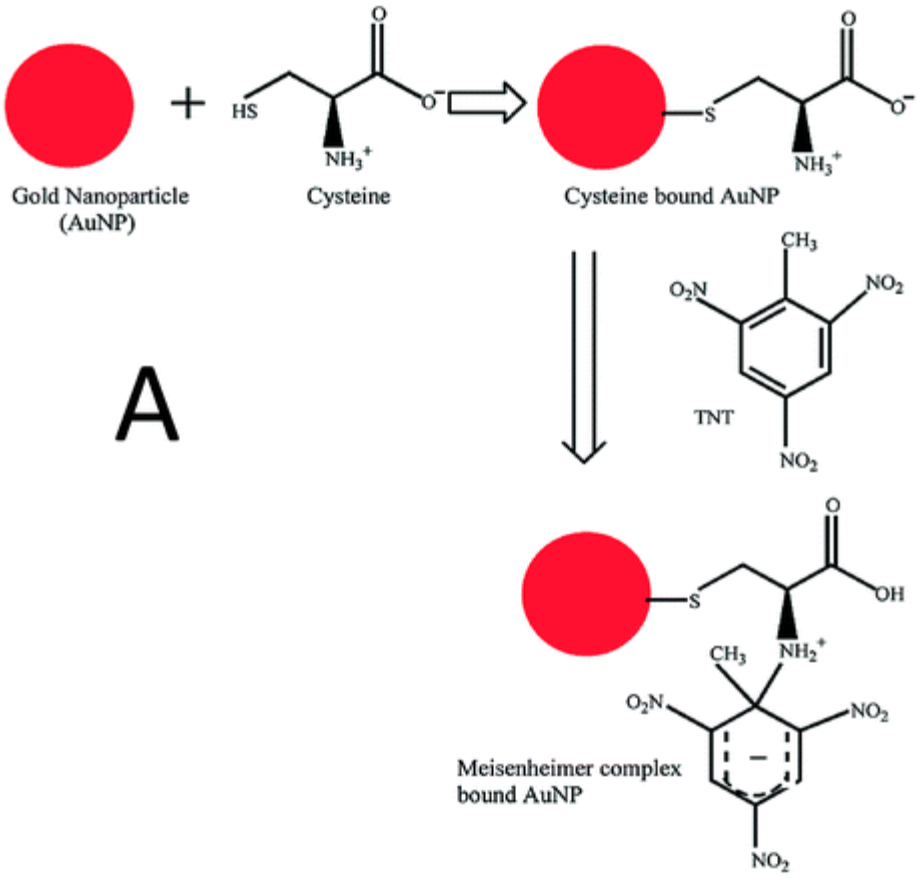
Gold Nanoparticle
(AuNP)
Cysteine
Cysteine bound AuNP
A
TNT
Meisenheimer complex
bound AuNP

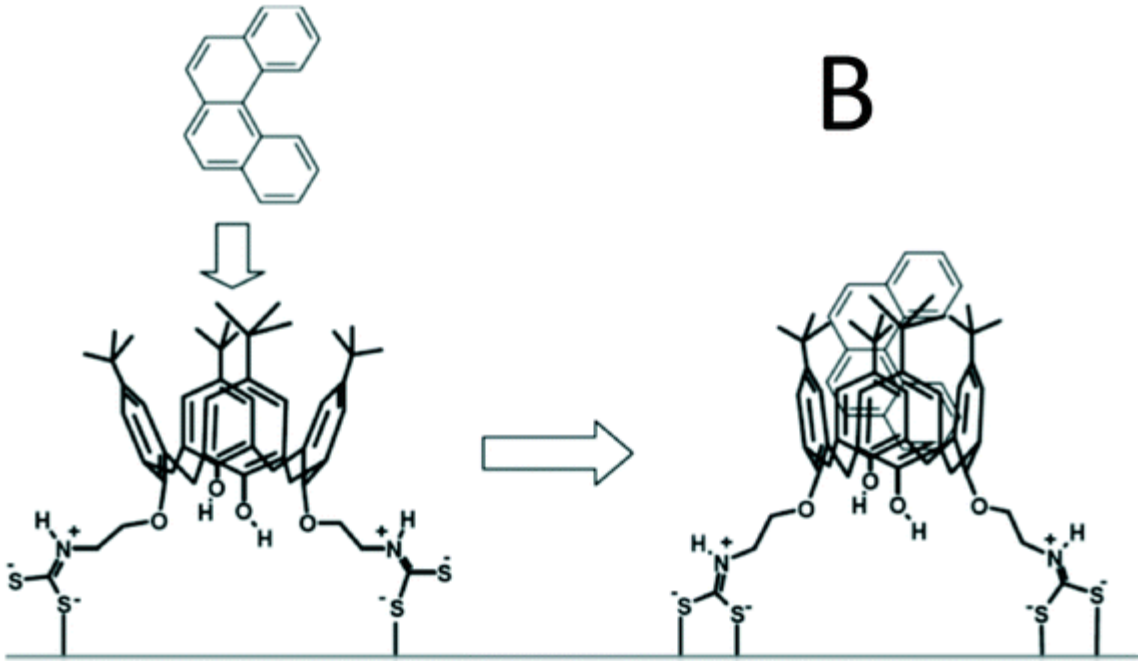
B

Figure A1.7. A) Trinitrotoluene (TNT) is captured by cysteine-functionalized AuNPs by formation of a Meisenheimer complex;[141]Reprinted with permission from S. S. Dasary, A. K. Singh, D. Senapati, H. Yu and P. C. Ray, *J. Am. Chem. Soc.*, 2009, **131**, 13806–13812. Copyright 2014 American Chemical Society. B) calix[4]arene links PAHs and AgNPs.[142] L. Guerrini, J. V. Garcia-Ramos, C. Domingo and S. Sanchez-Cortes, *Anal. Chem*., 2009, **81**, 953–960. Copyright 2014 American Chemical Society.

The SERS spectrum of the dioxin 2-benzoyldibenzo-*p*-dioxin (BDPD), a highly toxic compound, was first reported in 2009 using AgNPs loaded in poly(diallyldimethylammonium chloride) (PDDA) and poly-(acrylic acid) (PAA) film. This film was fabricated using a layer-by-layer method and subsequently impregnated with AgNPs. After drying in air, this SERS substrate showed a 5× higher Raman signal for 1-naphthalenethiol (1-NAT) than an AgNP suspension due to hot spot formation in the 3D structure. More importantly, the SERS dioxin spectrum at 10 nM was observed on this substrate although the signal was very weak.[140] This substrate works for dioxin partly because the PDDA–PAA can trap dioxin in the film thus creating the opportunity for dioxin contact with the AgNP surface. Recently, a detection limit down to three molecules was reported for atrazine detection *via* SERS.[151] This detection limit was achieved by directly adding a specific volume of 100 μM atrazine to an AgNP colloid suspension. This result demonstrates that SERS achieved similar detection limit (ppt) to sophisticated liquid chromatography-tandem mass spectroscopy (LC-MS/MS) and outperformed it due to its facile operation and fast measurement. However, this paper did not report a detailed characterization of the SERS substrate, the Raman measurement conditions, or the reproducibility of the data. The reason why the authors were able to achieve such a low

detection limit is probably the addition of high concentrations of atrazine (100 μM) that induced AgNP aggregation. More research efforts are required in this field to discuss if SERS can be used for single or few molecule detection of organic pollutants in environmentally relevant samples.

To facilitate on site pollutant detection, a portable Raman instrument integrating a SERS sensor is highly desired.[152,153] Recently such an instrument containing a silver dendrite SERS substrate was developed for pesticide detection. The large laser spot of 2 mm minimizes SERS intensity variation among parallel samples. The pesticide ferbam with concentrations of 0 ppm, 4 ppm, 7 ppm, and 14 ppm was used as reference materials indicating no risk, low risk, risk, and high risk, respectively. The self checking tests for the four references all passed, indicating this instrument shows potential for on site pesticide detection.[152] Combining microfluidic chips and SERS substrates in the portable Raman instrument is promising for real-time on site pollutant detection. With a micropillar array PDMS chip integrated in the instrument, complete mixing of the two confluents – AgNPs and pollutants (dipicolinic acid and malachite green) is achieved. Dipicolinic acid and malachite green were quantitatively detected with limits of detection of 200 ppb and 500 ppb, respectively.[153]

For larger targets, such as biomolecules, viruses, cancer cells, bacteria and protozoa, it is very difficult to directly acquire their SERS spectra by adding them to SERS substrates because they are too big to fit into the hot spots due to their large size.[155,156]Instead, a SERS tag is used to specifically bind the targets and the SERS spectrum of a Raman reporter functionalized on the SERS tag is then monitored.[93,157] Raman reporter is usually a dye having a large Raman cross section. Ideal SERS tags are able to generate strong

enough signals for single target detection. Interested readers are referred to a very good review for additional details on SERS tags.[31] Yang *et al.* fabricated a nanopillar-based SERS substrate to detect the macromolecule vasopressin, which was labeled by a Raman reporter 5-carboxytetramethylrhodamine. The nanopillar is made by depositing gold vapor onto etched silicon wafer. The coated gold film on the tip of silicon wire formed a pillar, which was functionalized with a vasopressin-specific aptamer. After exposure to vasopressin and subsequent drying, the intensified SERS signal of TAMRA was acquired due to the capillary force-driven aggregation of the nanopillars. The detection limit of vasopressin was reported to be 1 pM.[119] Recently, graphene oxide (GO) was used for SERS tag fabrication because of its capacity to significantly enhance the SERS signal.[154,158] The schematic of this SERS tag synthesis is shown in Figure. 8. Different from the traditional SERS tag fabrication, the Raman reporter – tris(2,2′-bipyridyl)ruthenium(II) chloride (Rubpy) was first adsorbed on GO and subsequently AuNPs formed by *in situ* reduction of $HAuCl_4$ on GO/Rubpy. GO was able to not only enhance the SERS signal by two fold but also improve the colloid stability by wrapping around the small nanoparticle aggregates. AuNP/GO/Rubpy was subsequently functionalized with positively charged poly(allylamine hydrochloride) (PAH), which provided amine groups to link to the recognition element glutaraldehyde (GA). GA can bind to both gram-positive and gram-negative bacteria by crosslinking with the peptidoglycan layer on their surfaces. In addition to its single cell identification capability, this SERS tag can also be used for photothermal ablation of bacteria when exposed to a 400 mW 785 nm laser. The decrease in the SERS signal can be used to monitor the bacterial ablation process (Figure. 8).[154]

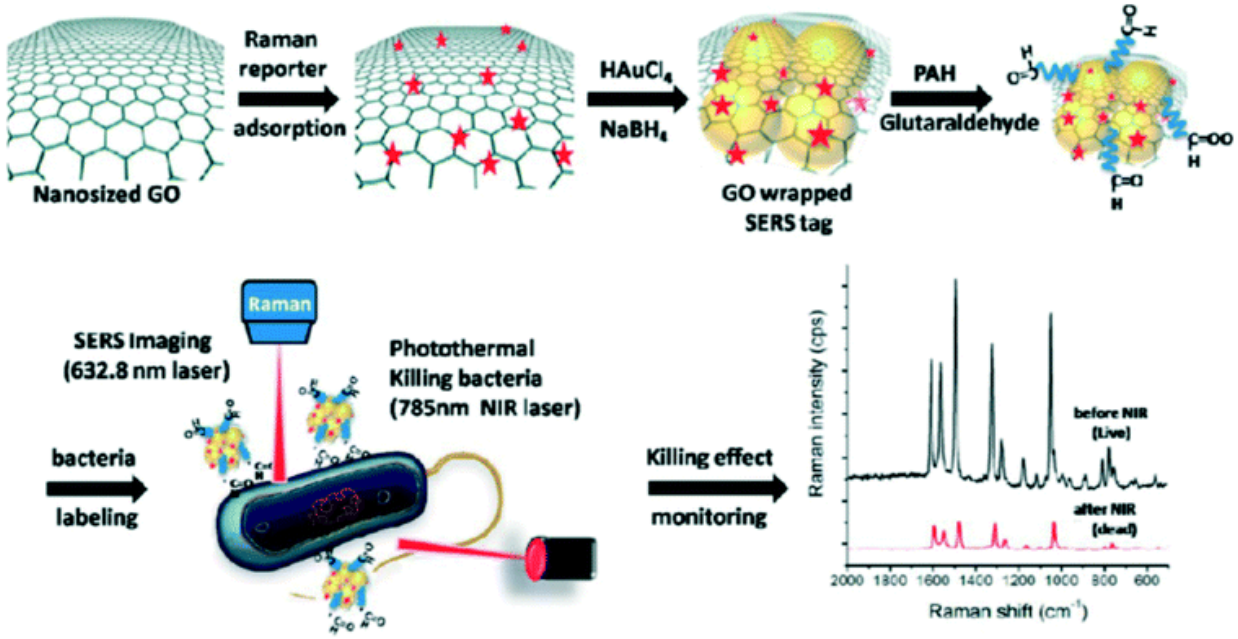

Figure A1.8. Schematic for AuNP/GO/Rubpy/GA SERS tag synthesis and its application for monitoring the photothermal ablation of bacteria.[154] Reprinted with permission from D. Lin, T. Qin, Y. Wang, X. Sun and L. Chen, *ACS Appl. Mater. Interfaces*, 2014, **6**, 1320–1329. Copyright 2014 American Chemical Society.

Although detecting large targets using SERS tags can achieve very high sensitivity, it is complex and costly to fabricate these tags. Most recently, the SERS spectrum of virus on SERS substrates without a SERS tag has been reported. This is called label-free SERS detection of virus.[159] Progress made in this promising area of research was recently summarized elsewhere.[159] Briefly, a highly sensitive and reproducible SERS substrate was fabricated by oblique angle deposition. The obtained SERS substrate contains tilted silver nanowire arrays. Virus was directly added to the SERS substrate and its SERS spectrum was readily acquired. Using this technique, three viruses – adenovirus,

rhinovirus, and HIV were distinguished and even different strains of respiratory syncytial virus (RSV) could be differentiated. This approach was also applied to measure the SERS spectrum of RSV in its infected cell lysate although the background interference is strong. These results indicate that label-free detection of virus is feasible if SERS substrates are well designed. However, the weak signal, strong background disturbance, and subtle change of spectrum between different viruses make the data analysis challenging. Principle component analysis (PCA) and other chemometic approaches are often required to differentiate the viruses from the background and from one another.

A1.5. Challenges

Although the rapid development of nanotechnology has facilitated substantial progress towards improved colorimetric and SERS detection, the high costs of sensor fabrication still impede their practical environmental applications. Development of low-cost and scalable detection platforms remains a big challenge. It is thus desirable to incorporate detection components within paper or other sustainable materials without using costly lithography techniques. Paper-based colorimetric sensors can be used at home to monitor drinking water quality by simply dipping test strips into water. However, the sensitivity and resistance of these test strips to potential interferents such as drinking water disinfectants should be improved to make such a sensor truly useful. SERS sensors have the capacity to replace the complex lab assays currently used in water and wastewater treatment plants because of their simple sample preparation and rapid detection process. Suspension-based sensors may not be appropriate for use in real water samples since the colloids may not be stable in complex water chemistries and the challenges associated with long-term storage. As noted, paper-based SERS substrates

have potential application. However, their SERS hot spot densities and affinities for specific organic pollutants currently do not meet real world application requirements. It is a considerable challenge to develop universal SERS substrates that have broad applicability to all of the organic chemicals of interest because the size, polarity, and isoelectric point of the chemicals determine their capacity to enter the hot spots on the SERS substrate. For on-site detection, portable SERS instrumentation is required and those systems currently rely only on near infrared lasers because of their ease of miniaturization. Accordingly, the SERS substrate must be optimized for application with near infrared lasers. Unfortunately, most organic pollutants are non-resonant at this laser wavelength, which makes their detection more challenging. Moreover, if we want to achieve real-time detection, the laser integration time must be very short, which further increases the difficulty. In addition to organic pollutant detection, SERS sensors also show potential for label-free pathogen detection. Since pathogens are generally too large to readily enter hot spots, the SERS substrate must have extremely high enhancement factor to make the pathogen spectrum visible. The reproducibility of SERS pathogen detection is also challenged because the contact between pathogens and Au or AgNPs may vary with time. The steps required for development of low-cost and efficient SERS substrates for pathogen detection are an ongoing area of research focus.

A1.6. Acknowledgements

Funding for this study was provided by the US National Science Foundation (NSF; CBET 1236005 and 1133736) and the Virginia Tech Institute for Critical Technology and Applied Science. Support for HW was provided by the Virginia Tech Graduate School through the Sustainable Nanotechnology Interdisciplinary Graduate Education Program (VTSuN

IGEP). Additional funding was provided by NSF and the Environmental Protection Agency under NSF Cooperative Agreement EF-0830093, Center for the Environmental Implications of NanoTechnology (CEINT). Any opinions, findings, conclusions or recommendations expressed in this material are those of the authors and do not necessarily reflect the views of the NSF or the EPA. This work has not been subjected to EPA review and no official endorsement should be inferred.

A1.7. References

1. J. Manuel, *Environ. Health Perspect.*, 2014, **122**, A214–A219
2. C. Fitzpatrick, *Water21 - Magazine of The International Water Association*, 2014
3. W. R. Mac Kenzie, N. J. Hoxie, M. E. Proctor, M. S. Gradus, K. A. Blair, D. E. Peterson, J. J. Kazmierczak, D. G. Addiss, K. R. Fox and J. B. Rose, *N. Engl. J. Med.*, 1994, **331**, 161–167
4. M. Widerström, C. Schönning, M. Lilja, M. Lebbad, T. Ljung, G. Allestam, M. Ferm, B. Björkholm, A. Hansen and J. Hiltula,*Emerging Infect. Dis.*, 2014, **20**, 581–589
5. L. B. van Alphen, F. Dorléans, A. C. Schultz, J. Fonager, S. Ethelberg, C. Dalgaard, M. Adelhardt, J. H. Engberg, T. K. Fischer and S. G. Lassen, *PLoS One*, 2014, **9**, e105053
6. A. Abbott and H. Pearson, *Nature*, 2004, **427**, 472–473
7. F. Karasek and O. Hutzinger, *Anal. Chem.*, 1986, **58**, 633A–642A
8. A. J. Haes, C. L. Haynes, A. D. McFarland, G. C. Schatz, R. P. Van Duyne and S. Zou, *MRS Bull.*, 2005, **30**, 368–375

9. A. J. Haes and R. P. Van Duyne, *Anal. Bioanal. Chem.*, 2004, **379**, 920–930

10. S. Link and M. A. El-Sayed, *J. Phys. Chem. B*, 1999, **103**, 8410–8426

11. B. Sepúlveda, P. C. Angelomé, L. M. Lechuga and L. M. Liz-Marzán, *Nano Today*, 2009, **4**, 244–251

12. J. Mock, M. Barbic, D. Smith, D. Schultz and S. Schultz, *J. Chem. Phys.*, 2002, **116**, 6755–6759

13. C. L. Haynes and R. P. Van Duyne, *J. Phys. Chem. B*, 2001, **105**, 5599–5611

14. W. L. Daniel, M. S. Han, J.-S. Lee and C. A. Mirkin, *J. Am. Chem. Soc.*, 2009, **131**, 6362–6363

15. F. Xia, X. Zuo, R. Yang, Y. Xiao, D. Kang, A. Vallée-Bélisle, X. Gong, J. D. Yuen, B. B. Hsu and A. J. Heeger, *Proc. Natl. Acad. Sci. U. S. A.*, 2010, **107**, 10837–10841

16. J. Du, B. Zhu and X. Chen, *Small*, 2013, **9**, 4104–4111

17. G. C. Schatz, M. A. Young and R. P. Van Duyne, *Surface-enhanced Raman Scattering*, Springer, 2006, pp. 19–45

18. C. L. Haynes, A. D. McFarland and R. P. V. Duyne, *Anal. Chem.*, 2005, **77**, 338 A–346 A

19. S. Nie and S. R. Emory, *Science*, 1997, **275**, 1102–1106

20. H. Liu, L. Zhang, X. Lang, Y. Yamaguchi, H. Iwasaki, Y. Inouye, Q. Xue and M. Chen, *Sci. Rep.*, 2011, **1**, 1–5

21. J. Kneipp, H. Kneipp and K. Kneipp, *Chem. Soc. Rev.*, 2008, **37**, 1052–1060 **RSC**.

22. K. Kneipp, Y. Wang, H. Kneipp, L. T. Perelman, I. Itzkan, R. R. Dasari and M. S. Feld, *Phys. Rev. Lett.*, 1997, **78**, 1667

23. E. Podstawka, Y. Ozaki and L. M. Proniewicz, *Appl. Spectrosc.*, 2005, **59**, 1516–1526

24. J. C. Costa, R. A. Ando, P. H. Camargo and P. Corio, *J. Phys. Chem. C*, 2011, **115**, 4184–4190

25. N. A. Abu Hatab, J. M. Oran and M. J. Sepaniak, *ACS Nano*, 2008, **2**, 377–385

26. R. Tan, A. Agarwal, N. Balasubramanian, D. Kwong, Y. Jiang, E. Widjaja and M. Garland, *Sens. Actuators, A*, 2007, **139**, 36–41

27. W. J. Cho, Y. Kim and J. K. Kim, *ACS Nano*, 2011, **6**, 249–255

28. A. Campion and P. Kambhampati, *Chem. Soc. Rev.*, 1998, **27**, 241–250 **RSC**.

29. K. Kneipp, H. Kneipp, I. Itzkan, R. R. Dasari and M. S. Feld, *Chem. Rev.*, 1999, **99**, 2957–2976

30. M. D. Porter, R. J. Lipert, L. M. Siperko, G. Wang and R. Narayanan, *Chem. Soc. Rev.*, 2008, **37**, 1001–1011 **RSC**.

31. Y. Wang, B. Yan and L. Chen, *Chem. Rev.*, 2012, **113**, 1391–1428

32. M. Vendrell, K. K. Maiti, K. Dhaliwal and Y. T. Chang, *Trends Biotechnol.*, 2013, **31**, 249–257

33. S. C. Luo, K. Sivashanmugan, J. D. Liao, C. K. Yao and H. C. Peng, *Biosens. Bioelectron.*, 2014, **61**, 232–240

34. R. A. Halvorson and P. J. Vikesland, *Environ. Sci. Technol.*, 2010, **44**, 7749–7755

35. B. Sharma, R. R. Frontiera, A. I. Henry, E. Ringe and R. P. Van Duyne, *Mater. Today*, 2012, **15**, 16–25

36. S. Schlücker, *Angew. Chem., Int. Ed.*, 2014, **53**, 4756–4795

37. D. Liu, Z. Wang and X. Jiang, *Nanoscale*, 2011, **3**, 1421–1433 **RSC**.

38. W. Zhao, M. A. Brook and Y. Li, *ChemBioChem*, 2008, **9**, 2363–2371

39. D. Vilela, M. C. González and A. Escarpa, *Anal. Chim. Acta*, 2012, **751**, 24–43

40. S. Su, W. Wu, J. Gao, J. Lu and C. Fan, *J. Mater. Chem.*, 2012, **22**, 18101–18110 **RSC**.

41. R. Alvarez-Puebla and L. Liz-Marzan, *Energy Environ. Sci.*, 2010, **3**, 1011–1017

42. T. Masciangioli and W. X. Zhang, *Environ. Sci. Technol.*, 2003, **37**, 102A–108A

43. C. Wang and C. Yu, *Rev. Anal. Chem.*, 2013, **32**, 1–14

44. L. Wang, W. Ma, L. Xu, W. Chen, Y. Zhu, C. Xu and N. A. Kotov, *Mater. Sci. Eng., R*, 2010, **70**, 265–274

45. P. J. Vikesland and K. R. Wigginton, *Environ. Sci. Technol.*, 2010, **44**, 3656–3669

46. S. Szunerits and R. Boukherroub, *Chem. Commun.*, 2012, **48**, 8999–9010 **RSC**.

47. J. N. Anker, W. P. Hall, O. Lyandres, N. C. Shah, J. Zhao and R. P. Van Duyne, *Nat. Mater.*, 2008, **7**, 442–453

48. J. Homola, *Chem. Rev.*, 2008, **108**, 462–493

49. R. A. Alvarez-Puebla and L. M. Liz-Marzán, *Angew. Chem., Int. Ed.*, 2012, **51**, 11214–11223

50. Y. Sun and Y. Xia, *Analyst*, 2003, **128**, 686–691 **RSC**.

51. P. Mulvaney, *Langmuir*, 1996, **12**, 788–800

52. A. Zielińska, E. Skwarek, A. Zaleska, M. Gazda and J. Hupka, *Procedia Chem.*, 2009, **1**, 1560–1566

53. S. Link and M. A. El-Sayed, *Annu. Rev. Phys. Chem.*, 2003, **54**, 331–366

54. C. J. Orendorff, T. K. Sau and C. J. Murphy, *Small*, 2006, **2**, 636–639

55. C. L. Nehl and J. H. Hafner, *J. Mater. Chem.*, 2008, **18**, 2415–2419 **RSC**.

56. L. Zhong, X. Zhou, S. Bao, Y. Shi, Y. Wang, S. Hong, Y. Huang, X. Wang, Z. Xie and Q. Zhang, *J. Mater. Chem.*, 2011, **21**, 14448–14455 **RSC**.

57. I. Blakey, Z. Merican and K. J. Thurecht, *Langmuir*, 2013, **29**, 8266–8274

58. K. A. Willets and R. P. Van Duyne, *Annu. Rev. Phys. Chem.*, 2007, **58**, 267–297

59. J. J. Storhoff, R. Elghanian, R. C. Mucic, C. A. Mirkin and R. L. Letsinger, *J. Am. Chem. Soc.*, 1998, **120**, 1959–1964

60. C. C. Huang and H. T. Chang, *Chem. Commun.*, 2007, 1215–1217 **RSC**.

61. J. Liu and Y. Lu, *Angew. Chem.*, 2006, **118**, 96–100

62. I. Mrozek and A. Otto, *J. Electron Spectrosc. Relat. Phenom.*, 1990, **54**, 895–911

63. G. Compagnini, C. Galati and S. Pignataro, *Phys. Chem. Chem. Phys.*, 1999, **1**, 2351–2353 **RSC**.

64. K. H. Su, Q. H. Wei, X. Zhang, J. Mock, D. R. Smith and S. Schultz, *Nano Lett.*, 2003, **3**, 1087–1090

65. X. Qian, X. Zhou and S. Nie, *J. Am. Chem. Soc.*, 2008, **130**, 14934–14935

66. L. Qin, S. Zou, C. Xue, A. Atkinson, G. C. Schatz and C. A. Mirkin, *Proc. Natl. Acad. Sci. U. S. A.*, 2006, **103**, 13300–13303

67. H. Im, K. C. Bantz, N. C. Lindquist, C. L. Haynes and S. H. Oh, *Nano Lett.*, 2010, **10**, 2231–2236

68. H. Wang, C. S. Levin and N. J. Halas, *J. Am. Chem. Soc.*, 2005, **127**, 14992–14993

69. K. L. Wustholz, A.-I. Henry, J. M. McMahon, R. G. Freeman, N. Valley, M. E. Piotti, M. J. Natan, G. C. Schatz and R. P. V. Duyne, *J. Am. Chem. Soc.*, 2010, **132**, 10903–10910

70. L. Fabris, A. S. D. Indrasekara, S. Meyers, S. Shubeita, L. C. Feldman and T. Gustafsson, *Nanoscale*, 2014

71. M. Potara, A. M. Gabudean and S. Astilean, *J. Mater. Chem.*, 2011, **21**, 3625–3633 **RSC**.

72. A. McLintock, C. A. Cunha-Matos, M. Zagnoni, O. R. Millington and A. W. Wark, *ACS Nano*, 2014, **8**, 8600–8609

73. G. Braun, I. Pavel, A. R. Morrill, D. S. Seferos, G. C. Bazan, N. O. Reich and M. Moskovits, *J. Am. Chem. Soc.*, 2007, **129**, 7760–7761

74. S. L. Kleinman, R. R. Frontiera, A.-I. Henry, J. A. Dieringer and R. P. Van Duyne, *Phys. Chem. Chem. Phys.*, 2013, **15**, 21–36 **RSC**.

75. A. Shiohara, Y. Wang and L. M. Liz-Marzán, *J. Photochem. Photobiol., C*, 2014, **21**, 2–25

76. N. H. Kim, S. J. Lee and M. Moskovits, *Adv. Mater.*, 2011, **23**, 4152–4156

77. R. A. Alvarez-Puebla, E. Arceo, P. J. Goulet, J. J. Garrido and R. F. Aroca, *J. Phys. Chem. B*, 2005, **109**, 3787–3792

78. L. S. Lawson, J. W. Chan and T. Huser, *Nanoscale*, 2014, **6**, 7971–7980 **RSC**.

79. K. V. Kong, U. Dinish, W. K. O. Lau and M. Olivo, *Biosens. Bioelectron.*, 2014, **54**, 135–140

80. W. Ji, N. Spegazzini, Y. Kitahama, Y. Chen, B. Zhao and Y. Ozaki, *J. Phys. Chem. Lett.*, 2012, **3**, 3204–3209

81. W. Hill and B. Wehling, *J. Phys. Chem.*, 1993, **97**, 9451–9455

82. R. Alvarez-Puebla, B. Cui, J. P. Bravo-Vasquez, T. Veres and H. Fenniri, *J. Phys. Chem. C*, 2007, **111**, 6720–6723

83. U. K. Sarkar, *Chem. Phys. Lett.*, 2003, **374**, 341–347

84. H. Yuan, A. M. Fales, C. G. Khoury, J. Liu and T. Vo-Dinh, *J. Raman Spectrosc.*, 2013, **44**, 234–239

85. D. K. Lim, I. J. Kim and J. M. Nam, *Chem. Commun.*, 2008, 5312–5314 **RSC**.

86. C. J. Murphy, T. K. Sau, A. M. Gole, C. J. Orendorff, J. Gao, L. Gou, S. E. Hunyadi and T. Li, *J. Phys. Chem. B*, 2005, **109**, 13857–13870

87. L. J. Sherry, R. Jin, C. A. Mirkin, G. C. Schatz and R. P. Van Duyne, *Nano Lett.*, 2006, **6**, 2060–2065

88. J. E. Millstone, S. Park, K. L. Shuford, L. Qin, G. C. Schatz and C. A. Mirkin, *J. Am. Chem. Soc.*, 2005, **127**, 5312–5313

89. L. Rodríguez-Lorenzo, R. A. Alvarez-Puebla, I. Pastoriza-Santos, S. Mazzucco, O. Stéphan, M. Kociak, L. M. Liz-Marzán and F. J. García de Abajo, *J. Am. Chem. Soc.*, 2009, **131**, 4616–4618

90. C. J. Orendorff, L. Gearheart, N. R. Jana and C. J. Murphy, *Phys. Chem. Chem. Phys.*, 2006, **8**, 165–170 **RSC**.

91. S. E. Bell and M. R. McCourt, *Phys. Chem. Chem. Phys.*, 2009, **11**, 7455–7462 **RSC**.

92. T. Iliescu, M. Baia and W. Kiefer, *Chem. Phys.*, 2004, **298**, 167–174

93. H. Y. Lin, C. H. Huang, W. H. Hsieh, L. H. Liu, Y. C. Lin, C. C. Chu, S. T. Wang, I. Kuo, L. K. Chau and C. Y. Yang, *Small*, 2014,**10**, 4700–4710

94. C. A. Mirkin, R. L. Letsinger, R. C. Mucic and J. J. Storhoff, *Nature*, 1996, **382**, 607–609

95. R. A. Reynolds, C. A. Mirkin and R. L. Letsinger, *J. Am. Chem. Soc.*, 2000, **122**, 3795–3796

96. D. G. Thompson, A. Enright, K. Faulds, W. E. Smith and D. Graham, *Anal. Chem.*, 2008, **80**, 2805–2810

97. L. Liu, S. Li, L. Liu, D. Deng and N. Xia, *Analyst*, 2012, **137**, 3794–3799 **RSC**.

98. D. E. Huizenga and J. W. Szostak, *Biochemistry*, 1995, **34**, 656–665

99. J. Liu and Y. Lu, *Nat. Protoc.*, 2006, **1**, 246–252

100. Z. Zhu, C. Wu, H. Liu, Y. Zou, X. Zhang, H. Kang, C. J. Yang and W. Tan, Angew. Chem., 2010, 122, 1070–1074

101. A. Sugunan, C. Thanachayanont, J. Dutta and J. Hilborn, Sci. Technol. Adv. Mater., 2005, 6, 335–340

102. J. Liu and Y. Lu, J. Am. Chem. Soc., 2003, 125, 6642–6643

103. C. Y. Lin, C. J. Yu, Y. H. Lin and W. L. Tseng, Anal. Chem., 2010, 82, 6830–6837

104. A. E. Üzer, Z. Can, I. l. Akın, E. Erçağ and R. A. Apak, Anal. Chem., 2013, 86, 351–356

105. F. M. Li, J. M. Liu, X. X. Wang, L. P. Lin, W. L. Cai, X. Lin, Y. N. Zeng, Z. M. Li and S. Q. Lin, Sens. Actuators, B, 2011, 155, 817–822

106. Z. Zhang, Z. Chen, C. Qu and L. Chen, Langmuir, 2014, 30, 3625–3630

107. G. Wang, Z. Chen, W. Wang, B. Yan and L. Chen, Analyst, 2011, 136, 174–178 RSC.

108. W. Zhao, M. M. Ali, S. D. Aguirre, M. A. Brook and Y. Li, Anal. Chem., 2008, 80, 8431–8437

109. S. C. Tseng, C. C. Yu, D. Wan, H. L. Chen, L. A. Wang, M. C. Wu, W. F. Su, H. C. Han and L. C. Chen, Anal. Chem., 2012, 84, 5140–5145

110. D. Mazumdar, J. Liu, G. Lu, J. Zhou and Y. Lu, Chem. Commun., 2010, 46, 1416–1418 RSC.

111. N. Ratnarathorn, O. Chailapakul, C. S. Henry and W. Dungchai, Talanta, 2012, 99, 552–557

112. M. Fleischmann, P. Hendra and A. McQuillan, Chem. Phys. Lett., 1974, 26, 163–166

113. T. Vo-Dinh, M. Hiromoto, G. Begun and R. Moody, Anal. Chem., 1984, 56, 1667–1670

114. M. M. Carrabba, R. B. Edmonds and R. D. Rauh, Anal. Chem., 1987, 59, 2559–2563

115. R. W. Taylor, R. J. Coulston, F. Biedermann, S. Mahajan, J. J. Baumberg and O. A. Scherman, Nano Lett., 2013, 13, 5985–5990

116. D. K. Lim, K. S. Jeon, J. H. Hwang, H. Kim, S. Kwon, Y. D. Suh and J. M. Nam, Nat. Nanotechnol., 2011, 6, 452–460

117. B. Saute, R. Premasiri, L. Ziegler and R. Narayanan, Analyst, 2012, 137, 5082–5087 RSC.

118. D. K. Lim, K. S. Jeon, H. M. Kim, J. M. Nam and Y. D. Suh, Nat. Mater., 2009, 9, 60–67

119. J. Yang, M. Palla, F. G. Bosco, T. Rindzevicius, T. S. Alstrøm, M. S. Schmidt, A. Boisen, J. Ju and Q. Lin, ACS Nano, 2013, 7, 5350–5359

120. W. Leng and P. J. Vikesland, Langmuir, 2014, 30, 8342–8349

121. S. Basu, S. Pande, S. Jana, S. Bolisetty and T. Pal, Langmuir, 2008, 24, 5562–5568

122. R. W. Taylor, T. C. Lee, O. A. Scherman, R. Esteban, J. Aizpurua, F. M. Huang, J. J. Baumberg and S. Mahajan, ACS Nano, 2011, 5, 3878–3887

123. L. Zhang, X. Lang, A. Hirata and M. Chen, ACS Nano, 2011, 5, 4407–4413

124. A. Tao, F. Kim, C. Hess, J. Goldberger, R. He, Y. Sun, Y. Xia and P. Yang, Nano Lett., 2003, 3, 1229–1233

125. T. H. Reilly, J. D. Corbman and K. L. Rowlen, Anal. Chem., 2007, 79, 5078–5081

126. Y. Jin, Adv. Mater., 2012, 24, 5153–5165

127. P. Wang, O. Liang, W. Zhang, T. Schroeder and Y. H. Xie, Adv. Mater., 2013, 25, 4918–4924

128. R. Zhang, B. B. Xu, X. Q. Liu, Y. L. Zhang, Y. Xu, Q. D. Chen and H. B. Sun, Chem. Commun., 2012, 48, 5913–5915 RSC.

129. C. H. Lee, L. Tian and S. Singamaneni, ACS Appl. Mater. Interfaces, 2010, 2, 3429–3435

130. W. Zhang, B. Li, L. Chen, Y. Wang, D. Gao, X. Ma and A. Wu, Anal. Methods, 2014, 6, 2066–2071 RSC.

131. Y. H. Ngo, D. Li, G. P. Simon and G. Garnier, Langmuir, 2012, 28, 8782–8790

132. L. Polavarapu and L. M. Liz-Marzán, Phys. Chem. Chem. Phys., 2013, 15, 5288–5300 RSC.

133. A. Abbas, A. Brimer, J. M. Slocik, L. Tian, R. R. Naik and S. Singamaneni, Anal. Chem., 2013, 85, 3977–3983

134. L. Zhang, X. Gong, Y. Bao, Y. Zhao, M. Xi, C. Jiang and H. Fong, Langmuir, 2012, 28, 14433–14440

135. D. He, B. Hu, Q. F. Yao, K. Wang and S. H. Yu, ACS Nano, 2009, 3, 3993–4002

136. H. Ko, S. Chang and V. V. Tsukruk, ACS Nano, 2008, 3, 181–188

137. P. Aldeanueva-Potel, E. Faoucher, R. N. A. Alvarez-Puebla, L. M. Liz-Marzán and M. Brust, Anal. Chem., 2009, 81, 9233–9238

138. X. Zhou, F. Zhou, H. Liu, L. Yang and J. Liu, Analyst, 2013, 138, 5832–5838 RSC.

139. B. Saute and R. Narayanan, Analyst, 2011, 136, 527–532 RSC.

140. S. Abalde-Cela, S. Ho, B. Rodríguez-González, M. A. Correa-Duarte, R. A. Álvarez-Puebla, L. M. Liz-Marzán and N. A. Kotov,Angew. Chem., 2009, 121, 5430–5433

141. S. S. Dasary, A. K. Singh, D. Senapati, H. Yu and P. C. Ray, J. Am. Chem. Soc., 2009, 131, 13806–13812

142. L. Guerrini, J. V. Garcia-Ramos, C. Domingo and S. Sanchez-Cortes, Anal. Chem., 2009, 81, 953–960

143. R. A. Álvarez-Puebla, R. Contreras-Cáceres, I. Pastoriza-Santos, J. Pérez-Juste and L. M. Liz-Marzán, Angew. Chem., Int. Ed., 2009, 48, 138–143

144. L. Guerrini, J. V. Garcia-Ramos, C. Domingo and S. Sanchez-Cortes, Anal. Chem., 2009, 81, 1418–1425

145. P. Leyton, C. Domingo, S. Sanchez-Cortes, M. Campos-Vallette and J. Garcia-Ramos, Langmuir, 2005, 21, 11814–11820

146. L. Guerrini, J. V. Garcia-Ramos, C. Domingo and S. Sanchez-Cortes, Langmuir, 2006, 22, 10924–10926

147. S. Z. Nergiz, N. Gandra, M. E. Farrell, L. Tian, P. M. Pellegrino and S. Singamaneni, J. Mater. Chem. A, 2013, 1, 6543–6549

148. A. Kolomijeca, Y. Kwon, K. Sowoidnich, R. Prien, D. Schulz-Bull and H. Kronfeldt, Proc. 21th, 2011, 859–862

149. H. Schmidt, N. Bich Ha, J. Pfannkuche, H. Amann, H.-D. Kronfeldt and G. Kowalewska, Mar. Pollut. Bull., 2004, 49, 229–234

150. J. Pfannkuche, L. Lubecki, H. Schmidt, G. Kowalewska and H.-D. Kronfeldt, Mar. Pollut. Bull., 2012, 64, 614–626

151. R. J. Rubira, S. A. Camacho, P. H. Aoki, M. D. Maximino, P. Alessio, C. S. Martin, O. N. Oliveira Jr, F. M. Fatore, F. V. Paulovich and C. J. Constantino, Colloid Polym. Sci., 2014, 1–10

152. J. Zheng, S. Pang, T. P. Labuza and L. He, Analyst, 2013, 138, 7075–7078 RSC.

153. L. XuanáQuang, G. HunáSeong and K. JunáDo, Lab Chip, 2008, 8, 2214–2219 RSC.

154. D. Lin, T. Qin, Y. Wang, X. Sun and L. Chen, ACS Appl. Mater. Interfaces, 2014, 6, 1320–1329

155. K. L. Rule and P. J. Vikesland, Environ. Sci. Technol., 2009, 43, 1147–1152

156. K. K. Maiti, U. Dinish, C. Y. Fu, J. J. Lee, K. S. Soh, S. W. Yun, R. Bhuvaneswari, M. Olivo and Y. T. Chang, Biosens. Bioelectron., 2010, 26, 398–403

157. B. Guven, N. Basaran-Akgul, E. Temur, U. Tamer and İ. H. Boyacı, Analyst, 2011, 136, 740–748 RSC.

158. S. Deng, W. Xu, J. Wang, X. Ling, J. Wu, L. Xie, J. Kong, M. S. Dresselhaus and J. Zhang, Nano Res., 2014, 7, 1271–1279

159. R. A. Tripp, R. A. Dluhy and Y. Zhao, Nano Today, 2008, 3, 31–37